

Copyright
by
William Jeffrey McCarty
2011

**The Dissertation Committee for William Jeffrey McCarty certifies that this is the
approved version of the following dissertation:**

Precursor Design for Materials Applications

Committee:

Richard A. Jones, Supervisor

Alan H. Cowley

Bradley J. Holliday

Philip D. Magnus

John G. Ekerdt

Precursor Design for Materials Applications

by

William Jeffrey McCarty, B. S.

Dissertation

Presented to the Faculty of the Graduate School of

The University of Texas at Austin

in Partial Fulfillment

of the Requirements

for the Degree of

Doctor of Philosophy

The University of Texas at Austin

December 2011

Dedication

For Bonnie

Acknowledgements

I would like to express my deepest gratitude to Professor Richard Jones for the relentless patience and guidance he has shown during the course of my graduate and undergraduate studies at UT. His wisdom, leadership and good humor have truly been inspirational, and I could not have asked for a better education. I am also grateful for the insight and advice that I have received from my committee members Professors Bradley Holliday, Alan Cowley, Philip Magnus and John Ekerdt, as well as expert guidance from Dr. Simon Humphrey. I must also thank Dr. Vincent Lynch (who might be the most patient person I know) for being such a great teacher and for his unwavering willingness to offer a helping hand. I am especially grateful to Dr. Xiaoping Yang, who has been an excellent mentor and friend from the beginning. I think we have truly learned a lot from each other over the years. My current lab mates Lauren DePue and Justin Hall have been an invaluable source of help and advice relating to research. To former Jones Group members Dr. Kyris Agapiou and Dr. Joe Rivers – you guys are great chemists and even better sloshball players. Thanks for the good times. And to all the current and former colleagues in the inorganic division with whom I have shared a beer (or two or three) over the years at Posse - it's been a pleasure knowing each of you.

I must also acknowledge the dedicated love and support that I have received from my family, not only during the past decade or so that I have in college, but for as long as I can remember. My parents and brothers have been (and still are) my greatest role models and I am forever grateful for their fostering of my love of science. And finally to my wife, my best friend, and my better half Bonnie –as with most things in my life, I could not have done this without you.

Precursor Design for Materials Applications

William Jeffrey McCarty, Ph.D.

The University of Texas at Austin, 2011

Supervisor: Richard A. Jones

The importance of platinum group metals for catalytic and microelectronic applications has prompted research into the development of novel molecular precursors for chemical vapor deposition of thin films of these metals. A variety of molecular architectures, ligand systems, as well as deposition conditions are investigated and related to the morphology and composition of the resultant films. For example, amorphous thin films of ruthenium and phosphorus alloys are deposited using single source metal hydride precursors, while use of the 3,5-di-substituted pyrazolate ligand in conjunction with various rhodium starting materials leads to a variety of different volatile monomeric and dimeric complexes. Synthesis of pyrazole and pyrazolate complexes of tungsten and palladium are also explored.

In a related research area, progress towards the development of novel synthetic routes to mesostructured transition metal phosphides and borates for Li-ion battery electrode applications is summarized. Traditional routes to these materials involve high-temperature syntheses, allowing limited control over morphology. Identification of low-temperature reaction conditions necessary to afford a desired composition, morphology and electrochemical performance of the bulk material are the main goals of this project, and results are discussed with various early transition metals.

Table of Contents

List of Tables	xii
List of Figures	xiv
List of Schemes	xviii
Chapter 1: Introduction	1
Applications of platinum group metals	1
Chemical vapor deposition	4
CVD precursor design	5
Overview and scope	11
References	13
Chapter 2: Chemical vapor deposition of amorphous ruthenium phosphorus thin films from Ru trialkylphosphite hydride complexes	18
Introduction	18
Results and discussion	22
Ruthenium hydride complexes	22
Ruthenium oxalate complexes	28
CVD of Ru(P, O) thin films	34
Post-growth annealing experiments	41
Conclusions and future studies	47
Experimental details	48
General synthesis	48
Thin film deposition studies	48
Single crystal X-ray crystallography	49
Syntheses of <i>cis</i> -H ₂ Ru(P(OR) ₃) ₄ ; R = Me (2-1), Et (2-2), ⁱ Pr (2-3)	50
Synthesis of <i>trans</i> -Cl ₂ Ru(P(OMe) ₃) ₄ (2-4)	50
Synthesis of Cl ₂ Ru ₂ (μ-η ⁴ -C ₂ O ₄)(PMe ₃) ₆ (2-5)	51
Synthesis of Cl ₂ Ru ₂ (μ-η ⁴ -C ₂ O ₄)(P(OEt) ₃) ₄ (2-6)	51
X-ray crystallographic details	53

References.....	58
Chapter 3: Synthesis, characterization and film growth studies of rhodium pyrazolate complexes	60
Introduction.....	60
Results and discussion	61
Synthesis of a mononuclear Rh(II) complex	61
Synthesis of Rh(II) paddlewheel complexes.....	70
Synthesis of rhodium acetate and trifluoroacetate pyrazole adducts ...	82
Other rhodium pyrazolate/pyrazole complexes	92
Rhodium CVD film growth and characterization	101
Conclusions.....	106
Experimental details.....	107
General synthesis	107
Thin film deposition studies.....	107
X-band EPR studies	108
Electrochemical studies	108
DFT calculations.....	109
Single crystal X-ray crystallography	109
Synthesis of $[\text{Li}(\text{THF})]_2 \text{Rh}(\mu\text{-}3,5\text{-(CF}_3)_2\text{Pz})_4$ (3-1).....	110
Synthesis of $\text{Rh}_2(\mu\text{-}3,5\text{-(CF}_3)_2\text{Pz})_4 \cdot 2 \text{H}_2\text{O}$ (3-2).....	110
Synthesis of $\text{Rh}_2(\mu\text{-}3,5\text{-(CF}_3)_2\text{Pz})_4 \cdot 2 \text{CH}_3\text{CN}$ (3-3)	111
Synthesis of $\text{Rh}_2(\mu\text{-}3,5\text{-}^t\text{Bu})_2\text{Pz})_4$ (3-4)	111
Synthesis of $\text{Rh}_2(\mu\text{-}3\text{-(CF}_3)_2\text{Pz}, 5\text{-}^t\text{BuPz})_4$ (3-5).....	112
Synthesis of $\text{Rh}_2(\mu\text{-}3\text{-(CF}_3)_2\text{Pz}, 5\text{-(CH}_3)_2\text{Pz})_4 \cdot 2 \text{CH}_3\text{CN}$ (3-6)	113
Synthesis of $\text{Rh}_2(\text{O}_2\text{CCH}_3)_4 \cdot 2 (3,5\text{-(CF}_3)_2\text{PzH})$ (3-7).....	113
Synthesis of $\text{Rh}_2(\text{O}_2\text{CCH}_3)_4 \cdot 2 (3\text{-(CF}_3)_2\text{PzH}, 5\text{-}^t\text{BuPzH})$ (3-8).....	114
Synthesis of $\text{Rh}_2(\text{O}_2\text{CCH}_3)_4 \cdot 2 (3,5\text{-}^t\text{Bu}_2\text{PzH})$ (3-9)	115
Synthesis of $\text{Rh}_2(\text{O}_2\text{CCF}_3)_4 \cdot 2 (3,5\text{-(CF}_3)_2\text{PzH})$ (3-10)	115
Synthesis of $\text{Rh}_2(\text{O}_2\text{CCF}_3)_4 \cdot 2 (3\text{-(CF}_3)_2\text{PzH}, 5\text{-}^t\text{BuPzH})$ (3-11)	116
Synthesis of $\text{Rh}_2(\text{O}_2\text{CCF}_3)_4 \cdot 2 (3,5\text{-}^t\text{Bu}_2\text{PzH})$ (3-12).....	116

Synthesis of <i>cis</i> -Cl ₂ Rh(3,5-(CF ₃) ₂ Pz)(3,5-(CF ₃) ₂ PzH) ₃ (3-13)	117
Synthesis of Rh(PMe ₃) ₃ (3-(CF ₃),5-(CH ₃)Pz) (3-14).....	117
Synthesis of Rh(PMe ₃) ₃ (3,5-(CH ₃) ₂ Pz) (3-15)	118
Synthesis of Rh(PMe ₃) ₃ (3,5-(CF ₃) ₂ Pz) (3-16)	119
X-ray crystallographic details	120
References.....	134
Chapter 4: A tungsten pyrazolate complex	138
Introduction.....	138
Results and discussion	138
Conclusions.....	143
Experimental details.....	143
General synthesis	143
Single crystal X-ray crystallography	144
Synthesis of [LiCl(Et ₂ O)] ₂ W(μ-3,5-(CF ₃) ₂ Pz) ₄ (4-1).....	144
X-ray crystallographic details	145
References.....	147
Chapter 5: Synthesis and characterization of palladium pyrazolate complexes ..	148
Introduction.....	148
Synthesis of palladium pyrazolate complexes	150
Results and discussion	150
Pyrazole adducts	150
A binary palladium pyrazolate complex	158
Conclusions and future studies	160
Experimental details.....	161
General synthesis	161
Single crystal X-ray crystallography	162
Synthesis of <i>trans</i> -Cl ₂ Pd(3-(CF ₃),5-(^t Bu)PzH) ₂ (5-1).....	162
Synthesis of <i>trans</i> -Cl ₂ Pd(3-(CF ₃),5-(CH ₃)PzH) ₂ (5-2)	163
Synthesis of Cl ₂ Pd ₂ (μ-(3-(CF ₃),5-(^t Bu)Pz)) ₂ (3-(CF ₃), 5-(^t Bu)PzH) ₂ (5-3)	164

Synthesis of $[\text{Pd}(\mu\text{-(3-(CF}_3\text{),5-(CH}_3\text{)Pz})}_2\text{)]}_3$ (5-4).....	164
X-ray crystallographic details	166
References.....	171
Chapter 6: Low-temperature synthetic routes to transition metal phosphides and borates for Li-ion battery applications.....	173
Introduction.....	173
Li-ion batteries	173
Metal phosphides	175
Synthesis of transition metal phosphides	177
Results and discussion	179
Synthesis of manganese phosphide and lithium manganese phosphide.....	179
Characterization	180
Scanning electron microscopy	180
X-ray diffraction	183
Electrochemical studies	186
Other metal systems.....	188
Iron phosphide	189
Titanium phosphide	189
Manganese and iron borates as cathode materials	189
Conclusions and future studies	193
Experimental details.....	194
General synthesis	194
Synthesis of manganese phosphide.....	194
Synthesis of mixed phase manganese phosphide ($\text{MnP} + \text{Li}_3\text{MnP}_2$).....	195
Synthesis of iron phosphide	195
Synthesis of titanium phosphide	196
Synthesis of lithium manganese borate.....	196
Synthesis of iron borate	197
References.....	198

Glossary	201
Vita	202

List of Tables

Table 2.1	Summary of deposition conditions for Ru films.....	35
Table 2.2	Crystallographic details and refinement data for 2-1 , 2-2 and 2-4	53
Table 2.3	Crystallographic details and refinement data for 2-5 and 2-6	54
Table 2.4	Selected bond lengths [\AA] and angles [$^{\circ}$] for 2-1	55
Table 2.5	Selected bond lengths [\AA] and angles [$^{\circ}$] for 2-2	55
Table 2.6	Selected bond lengths [\AA] and angles [$^{\circ}$] for 2-4	56
Table 2.7	Selected bond lengths [\AA] and angles [$^{\circ}$] for 2-5	56
Table 2.8	Selected bond lengths [\AA] and angles [$^{\circ}$] for 2-6	57
Table 3.0	Summary of deposition conditions for Rh films.....	102
Table 3.1	Crystallographic details and refinement data for 3-1 , 3-2 , and 3-3 .	120
Table 3.2	Crystallographic details and refinement data for 3-4 , 3-5 , and 3-6 .	121
Table 3.3	Crystallographic details and refinement data for 3-7 , 3-8 , and 3-9 .	122
Table 3.4	Crystallographic details and refinement data for 3-10 , 3-11 , 3-12 ..	123
Table 3.5	Crystallographic details and refinement data for 3-13 and 3-14	124
Table 3.6	Crystallographic details and refinement data for 3-15 and 3-16	125
Table 3.7	Selected bond lengths [\AA] and angles [$^{\circ}$] for 3-1	126
Table 3.8	Selected bond lengths [\AA] and angles [$^{\circ}$] for 3-2 and 3-3	127
Table 3.9	Intermolecular hydrogen bonds for 3-2 [\AA and $^{\circ}$].....	127
Table 3.10	Selected bond lengths [\AA] and angles [$^{\circ}$] for 3-4	128
Table 3.11	Selected bond lengths [\AA] and angles [$^{\circ}$] for 3-5	128
Table 3.12	Selected bond lengths [\AA] and angles [$^{\circ}$] for 3-6	129
Table 3.13	Selected bond lengths [\AA] and angles [$^{\circ}$] for 3-7	129
Table 3.14	Selected bond lengths [\AA] and angles [$^{\circ}$] for 3-8	130

Table 3.15	Selected bond lengths [\AA] and angles [$^{\circ}$] for 3-9	130
Table 3.16	Selected bond lengths [\AA] and angles [$^{\circ}$] for 3-10	130
Table 3.17	Selected bond lengths [\AA] and angles [$^{\circ}$] for 3-11	131
Table 3.18	Selected bond lengths [\AA] and angles [$^{\circ}$] for 3-12	131
Table 3.19	Intramolecular hydrogen bonds for complexes 3-7 – 3-12	131
Table 3.20	Selected bond lengths [\AA] and angles [$^{\circ}$] for 3-13	132
Table 3.21	Hydrogen bonds for 3-13 [\AA and $^{\circ}$].	132
Table 3.22	Selected bond lengths [\AA] and angles [$^{\circ}$] for 3-14	132
Table 3.23	Selected bond lengths [\AA] and angles [$^{\circ}$] for 3-15	133
Table 3.24	Hydrogen bonds for 3-15 [\AA and $^{\circ}$].	133
Table 3.25	Selected bond lengths [\AA] and angles [$^{\circ}$] for 3-16	133
Table 4.1	Crystallographic details and refinement data for 4-1	145
Table 4.2	Selected bond lengths [\AA] and angles [$^{\circ}$] for 4-1	146
Table 5.1	Crystallographic details and refinement data for 5-1 and 5-2	166
Table 5.2	Crystallographic details and refinement data for 5-3 and 5-4	167
Table 5.3	Selected bond lengths [\AA] and angles [$^{\circ}$] for 5-1	168
Table 5.4	Selected bond lengths [\AA] and angles [$^{\circ}$] for 5-2	168
Table 5.5	Selected bond lengths [\AA] and angles [$^{\circ}$] for 5-3	168
Table 5.6	Selected bond lengths [\AA] and angles [$^{\circ}$] for 5-4	169
Table 5.7	Hydrogen bonds for 5-1 [\AA and $^{\circ}$].	170
Table 5.8	Hydrogen bonds for 5-2 [\AA and $^{\circ}$].	170
Table 5.9	Hydrogen bonds for 5-3 [\AA and $^{\circ}$].	170
Table 6.1	FWHM values determined for MnP and the mixed phase material. .	185

List of Figures

Figure 1.1	A schematic of a typical MOSFET with a metal gate electrode	2
Figure 1.2	Possible decomposition pathways of β -diketonate ligands	9
Figure 1.3	Various coordination modes of the Pz ligand.....	10
Figure 2.1	A copper interconnect device formed by the damascene process	19
Figure 2.2	ORTEP diagram and partial atom numbering scheme of 2-1	24
Figure 2.3	ORTEP diagram and partial atom numbering scheme of 2-2	26
Figure 2.4	ORTEP diagram and partial atom numbering scheme of 2-4	27
Figure 2.5	ORTEP diagram and partial atom numbering scheme of 2-5	30
Figure 2.6	ORTEP diagram and partial atom numbering scheme of 2-6	32
Figure 2.7	Capped stick view of complex 2-5 (top) and 2-6 (bottom)	33
Figure 2.8	SEM images of a typical film grown from 2-1 under H_2	36
Figure 2.9	XRD patterns of a typical Ru film deposited from 2-1 under Ar and then annealed at various temperatures under dynamic vacuum.....	36
Figure 2.10	XPS survey scan (top) of a typical film deposited from 2-2 at 400 °C under H_2	38
Figure 2.11	XPS depth profiles of films deposited from 2-1 under Ar (top) and under H_2 (bottom)	40
Figure 2.12	XRD pattern of a typical Ru film deposited from 2-3 under H_2 , followed by annealing under flowing H_2 at 700 °C	42
Figure 2.13	XPS depth profiles (left) of films deposited from 2-3 under H_2	43
Figure 2.14	SEM images of a film grown from 2-3 annealed under H_2	45
Figure 2.15	EDX Quantitative Element Mapping of a typical film of Ru(P,O) annealed under H_2	46

Figure 3.1	ORTEP diagram and partial atom numbering scheme of 3-1	64
Figure 3.2	X-band EPR spectrum of complex 3-1 in frozen toluene at 78 K.....	65
Figure 3.3	Cyclic voltammogram of complex 3-1	66
Figure 3.4	DFT calculated (SOMO) (top), SOMO - 1 (middle) and SOMO - 3 (bottom) of complex 3-1	68
Figure 3.5	Energy level diagram of complex 3-1	69
Figure 3.6	ORTEP diagram and partial atom numbering scheme of 3-2	72
Figure 3.7	Intermolecular hydrogen bonding interactions of 3-2	73
Figure 3.8	ORTEP diagram and partial atom numbering scheme of 3-3	75
Figure 3.9	ORTEP diagram and partial atom numbering scheme of 3-4	77
Figure 3.10	ORTEP diagram and partial atom numbering scheme of 3-5	79
Figure 3.11	ORTEP diagram and partial atom numbering scheme of 3-6	81
Figure 3.12	ORTEP diagram and partial atom numbering scheme of 3-7	84
Figure 3.13	ORTEP diagram and partial atom numbering scheme of 3-8	85
Figure 3.14	ORTEP diagram and partial atom numbering scheme of 3-9	85
Figure 3.15	ORTEP diagram and partial atom numbering scheme of 3-10	88
Figure 3.16	ORTEP diagram and partial atom numbering scheme of 3-11	88
Figure 3.17	ORTEP diagram and partial atom numbering scheme of 3-12	89
Figure 3.18	Rh-Rh distances of $\text{Rh}_2(\text{O}_2\text{CCH}_3)_4 \cdot 2 \text{ PzH}$ and $\text{Rh}_2(\text{O}_2\text{CCF}_3)_4 \cdot 2 \text{ PzH}$ complexes	91
Figure 3.19	ORTEP diagram and partial atom numbering scheme of 3-13	94
Figure 3.20	ORTEP diagram and partial atom numbering scheme of 3-14	97
Figure 3.21	ORTEP diagram and partial atom numbering scheme of 3-15	99
Figure 3.22	ORTEP diagram and partial atom numbering scheme of 3-16	100
Figure 3.23	X-ray diffraction patterns of as-deposited Rh films	104

Figure 3.24	SEM micrograph and EDX spectrum of a typical Rh film grown from complex 3-4	104
Figure 3.25	XP survey spectrum (top) and high resolution Rh, C, and O spectra after 100 seconds of Ar ⁺ sputtering (bottom) of a representative Rh film grown from complex 3-2 at 400 °C.....	105
Figure 3.26	XPS depth profile of a Rh film grown from complex 3-2 at 400 °C showing atomic percent of Rh, C, O, and Si.....	106
Figure 4.1	ORTEP diagram and partial atom numbering scheme of 4-1	141
Figure 4.2	ORTEP diagrams of 4-1 (left) and 3-1 (right).....	142
Figure 5.0	Examples of volatile homoleptic metal pyrazolate complexes appropriate for CVD applications.....	149
Figure 5.1	ORTEP diagram and partial atom numbering scheme of 5-1	153
Figure 5.2	ORTEP diagram and partial atom numbering scheme of 5-2	154
Figure 5.3	Conformational isomers of <i>trans</i> -Cl ₂ Pd(PzH) ₂	155
Figure 5.4	ORTEP diagram and partial atom numbering scheme of 5-3	158
Figure 5.5	ORTEP diagram and partial atom numbering scheme of 5-4	160
Figure 6.1	Schematic representation of a lithium ion battery.	174
Figure 6.2	SEM images of MnP.....	182
Figure 6.3	N ₂ adsorption desorption isotherm for MnP.....	182
Figure 6.4	Powder XRD patterns of MnP annealed at different temperatures .	184
Figure 6.5	Powder XRD patterns of the mixed phase material (Li ₃ MnP ₂ + MnP) annealed at different temperatures	185
Figure 6.6	Initial discharge capacity of (MnP + Li ₃ MnP ₂) annealed at different temperatures.....	187

Figure 6.7	Comparison of the 6 th discharge cycles of MnP (blue) and the mixed phase material (red).....	188
Figure 6.8	XRD pattern of LiMnBO ₃ annealed at 400 °C for 4 hr.	191
Figure 6.9	Electrochemical behavior of amorphous iron borate (top) and material annealed to 400 °C (bottom).....	192

List of Schemes

Scheme 2.1	Synthesis of ruthenium phosphite complexes.....	23
Scheme 2.2	Synthesis of ruthenium oxalate complexes.....	29
Scheme 3.1	Synthesis of $[\text{Li}(\text{THF})]_2 \text{Rh}(\mu\text{-}3,5\text{-(CF}_3)_2\text{Pz})_4$ (3-1).....	62
Scheme 3.2	Synthesis of rhodium(II) paddlewheel complexes.....	70
Scheme 3.3	Synthesis of rhodium acetate pyrazole adducts.	83
Scheme 3.4	Synthesis of rhodium trifluoroacetate pyrazole adducts.	87
Scheme 3.5	Synthesis of <i>cis</i> - $\text{Cl}_2\text{Rh}(3,5\text{-(CF}_3)_2\text{Pz})(3,5\text{-(CF}_3)_2\text{PzH})_3$ (3-13).....	93
Scheme 3.6	Synthesis of rhodium trimethylphosphine pyrazolate complexes. ..	96
Scheme 4.1	Synthesis of $[\text{LiCl}(\text{Et}_2\text{O})]_2\text{W}(\mu\text{-}3,5\text{-(CF}_3)_2\text{Pz})_4$ (4-1).	139
Scheme 5.1	Synthesis of palladium pyrazolate complexes.	151

Chapter 1: Introduction

APPLICATIONS OF PLATINUM GROUP METALS

Thin films of platinum group metals have proven useful in a wide variety of applications due to their desirable chemical, optical and electronic properties. The catalytic activity exhibited by these metals has been exploited for use in heterogeneous hydrocarbon conversion reactions,¹⁻⁵ in automobile catalytic converters,⁶ as well as in nitric oxide reduction processes.⁷⁻⁸ Several noble metals such as rhodium, ruthenium, palladium and platinum have been utilized in catalytic hydrogen gas production.⁹⁻¹⁰ Due to their high reflectivity, platinum group metals are well suited for certain optical coating applications¹¹⁻¹² and their relative chemical inertness also makes them attractive for protective and anti-corrosion coatings.¹³ They also find use as electrode materials for gas sensing applications.¹⁴⁻¹⁶

Applications of thin films of platinum group metals in the microelectronics industry include use as electrodes in metal-oxide semiconductor field effect transistor (MOSFET) devices as well as Cu seed layers and diffusion barriers in copper interconnect devices. These applications are directly driven by the progressive exponential increase in the number of transistors that may be inexpensively implemented on an integrated circuit (IC) – a trend described as Moore's Law.¹⁷ The scale-down of IC components has prompted the use of novel materials to replace SiO₂ as a dielectric material in order to maintain high current density and low leakage currents. Oxides of the early transition metals such as HfO₂, Ta₂O₅, and ZrO₂ have been widely studied as alternative high-κ dielectrics for use in IC devices.¹⁸

Polycrystalline Si has traditionally been used as the gate electrode material in MOSFETs and SiO₂ as the gate dielectric, but further scale-down of device dimensions

has necessitated replacement of SiO₂ with high- κ dielectric materials (Figure 1.1). This has led to several compatibility issues, as silicon exhibits poor adhesion to most high- κ dielectrics.¹⁸⁻¹⁹ Furthermore, the high electrical resistivity of Si has prompted research into its replacement as a gate electrode with alternative highly conductive materials that have high work functions. Several platinum group metals fulfill these requirements and show promise for use in future metal-gate MOSFET devices for the 22 nm node and onward. For example, Ru, Ir and Pt films grown on HfO₂ exhibit work functions in the range of 4.6 - 5.3 eV, which are compatible values for integration with *p* type MOSFETs.²⁰⁻²³ Thin films of Ru and Pd have been shown to have good adhesion to HfO₂ surfaces and are stable at elevated temperatures of 500 - 800 °C.^{24,25} Ruthenium appears to be the most promising platinum group metal for gate electrode applications, as there are no metal - dielectric interface issues such as reactivity or interdiffusion.²² Thin films of conductive RuO₂ have also been investigated as gate electrode materials.²⁶

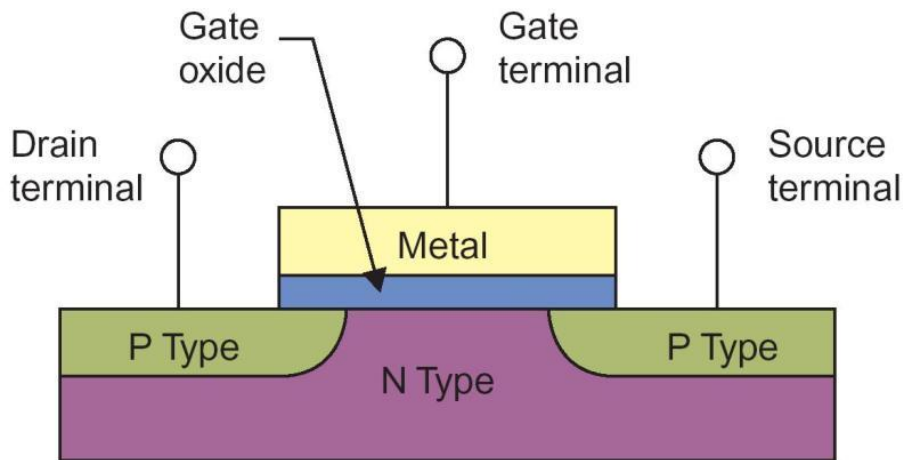


Figure 1.1 A schematic of a typical MOSFET with a metal gate electrode.

Copper has replaced aluminum as the dominant interconnect material for IC devices due to its lower resistivity, although electromigration of Cu into lower layer dielectric material is problematic as this diminishes the electrical properties of the interconnect. This is prevented by the deposition of a thin film of material between the copper and dielectric that acts as a diffusion barrier. Tantalum nitride has been extensively studied for use as a diffusion barrier material²⁷ but requires the deposition of an additional Cu seed layer in order to facilitate Cu electrochemical deposition (ECD), as copper cannot be directly electroplated onto metal nitrides because of poor adhesion. Therefore, alternating layers of TaN, Ta and then Cu must be deposited by ALD or CVD prior to copper electroplating.²⁸ This multistep process is time and energy intensive and thus exploration of alternative materials for Cu diffusion barriers is an area of current interest.

Platinum group metals are potentially attractive materials for combined copper diffusion barriers and seed layers as they exhibit low resistivities, adhere well to Si, Cu and most dielectric materials, resist oxidation under acidic electroplating conditions, and are able to be deposited as very thin films with good conformality.²⁹ Ruthenium is a potential material for a combined seed layer and diffusion barrier as it shows good adhesion and low solubility with copper at elevated temperatures. Though some reports^{28,30,32} show promising results as a diffusion barrier, Ru is generally thought to be limited in this application due to the propensity for formation of highly directional grain boundaries that allow for fast electromigration of Cu ions. This issue, along with potential solutions, will be further addressed in the proceeding chapter. Palladium has been studied as a seed layer for ECD of copper, though it has limited use as a diffusion barrier because of its relatively high solubility with copper.³³⁻³⁴

CHEMICAL VAPOR DEPOSITION

Metal-organic chemical vapor deposition (MOCVD) has been used extensively as a method for depositing high purity thin films of metals, metal oxides, and semiconductor materials for a variety of applications. Because highly conformal thin films with good step coverage may be obtained with this technique, MOCVD is well suited for silicon-based microelectronic applications in which features with high aspect ratios such as trenches or vias must be coated uniformly. In contrast, physical vapor deposition (PVD) techniques commonly employ either sputtering or evaporation to cover the surfaces, and are considered line-of-sight deposition techniques.³⁵ These processes may not be suitable for certain applications as they tend to exhibit directional film coverage, resulting in poor step coverage. Other potential advantages of CVD are high deposition rates, low deposition temperatures, and high film purity.³⁶

The details of CVD processes may vary greatly (e.g., hot or cold wall reactor, atmospheric or low pressure, plasma assisted, etc.) with the conditions dependent on the application, but all CVD processes share three common features.^{37,38} First, the precursor is introduced into the deposition chamber in the gaseous phase. This may be accomplished with the aid of an inert or reactive carrier gas flow or by thermal vaporization (or both). Next, in the deposition chamber, energy is supplied either in the form of heat or a reactive plasma or laser in order to afford deposition of the precursor. At this step, the precursor decomposes through a series of complex chemical reactions that may involve pyrolysis, oxidation, reduction, etc. resulting in the formation of thin films from elements in the precursor. The final step is the efficient removal of gaseous reaction by-products from the deposition chamber by means of a vacuum exhaust system. In all stages of the process, fine control over experimental conditions (temperature, flow rate, pressure, etc.) is possible, making the CVD technique highly versatile and useful for

the study of physical properties that control the kinetics and thermodynamics of film growth.

CVD PRECURSOR DESIGN

The choice of an appropriate precursor for thin film deposition depends not only on the requirement that it contains the elements of interest, but also on a number of other desired film properties such as purity, morphology and associated cost. Research and development of CVD precursors for specific applications and CVD conditions has led to a wide variety of molecular precursors, exhibiting diverse chemistry. There are, however, several common chemical properties that are required for ideal MOCVD precursors.

The chemical composition of resultant thin films from a CVD process is of great importance, especially in applications such as catalysis and microelectronics, where small amounts of impurities have significant (and usually detrimental) effects on reactivity or electronic properties of the films. While physical conditions of the deposition process, as well as use of co-reactants or reactive carrier gases have been demonstrated to influence the purity of the resultant film,⁷⁶ the chemistry of the precursor itself fundamentally controls which elements may or may not be present. The high deposition temperatures of CVD processes commonly leads to unwanted decomposition of ancillary components of the precursor, resulting in incorporation of impurities in the film. This can be avoided by minimizing unwanted elements in the precursor molecules as well as utilizing molecular frameworks that decompose in a predictable manner. For example, decomposition of binary metal carbonyl complexes usually involves cleavage of the M-C bond, leaving zerovalent metal and volatile carbon monoxide as decomposition products. Use of other neutral, two electron donor molecules as ligands results in clean bond cleavage and no

reduction or oxidation of the metal center. Metal alkyl complexes may undergo more complicated decomposition pathways involving intramolecular β -hydride elimination reactions. In this case, M-C bond cleavage is accomplished cleanly by formation of an alkene and an M-H bond.

Multicomponent or mixed-metal materials are frequently obtained by use of two separate precursor sources. For example, GaAs films may be deposited from simultaneous decomposition of GaMe₃ and AsH₃.³⁹ Film composition is inconsistent, however, as the exact gas-phase stoichiometry of the reagents is dependent on the physical deposition conditions and is difficult to control. Use of single source precursors gives greater control over stoichiometry as well as simplifies the CVD process. Several multi-nuclear complexes [Me₂Ga(μ -As'Bu₂)]₂, [Et₂Ga(μ -As'Bu₂)]₂ and Ga(As'Bu₂)₃ have proven to be attractive single-source alternatives for deposition of GaAs thin films.⁴⁰⁻⁴² Other single-source precursors have been used to deposit thin films of metal phosphides⁴³ and metal nitrides.⁴⁴

The volatility of a CVD precursor influences the total amount of energy required for the deposition process, and is an important consideration for scale-up manufacturing procedures. Ideally, the vaporization temperature of a given complex should be well below the temperature at which it decomposes in order to minimize premature deposition in the CVD reactor. The physical state of the precursor before entering the vapor phase has also been shown to influence film properties, as liquid CVD precursors often show a more evenly saturated vapor stream due to the ability to introduce the precursor from an aerosol spray or a bubbler.⁴⁸

Several factors have been shown to influence the volatility of MOCVD precursors. Use of small molecules as ligands lowers the molecular weight of the metal complex and increases volatility. Examples of low molecular weight complexes suitable

for CVD applications include homoleptic metal carbonyl complexes⁴⁵ such as $\text{Ni}(\text{CO})_4$, $\text{Fe}(\text{CO})_5$, and $\text{Mn}_2(\text{CO})_{10}$ as well as metal phosphine complexes⁴⁶ such as $\text{Pd}(\text{PF}_3)_4$ and $\text{Pt}(\text{PF}_3)_4$. These complexes have the added advantage of the central metal being in the zero oxidation state, and no additional reducing agent is needed to deposit thin metal films. Binary metal halide complexes such as WF_6 and HfCl_4 have high volatilities and are suitable for use as CVD precursors and usually require deposition in the presence of a reactive carrier gas to cleanly reduce the metal.⁴⁷ Binary complexes incorporating heavier halogens are less common as these tend to show decreased volatility, though there are exceptions (SnCl_4 , TiCl_4 , TiI_4).^{47,48} Other ligands utilized in CVD precursors include η^3 -allyl,⁴⁹ methyl,⁵⁰ hydride,⁵¹ alkoxide⁵² and dialkylamine moieties.⁵³

Reduction of intermolecular forces such as van der Waals interactions or hydrogen bonding between precursor molecules serves as an effective method to increase volatility, as these forces tend to result in bridged coordination networks or higher molecular weight adducts. Filling the coordination sphere of the metal with bulky or perfluorinated ligands shields the positively charged metal center and ensures the formation of monomeric species, despite the sometimes significant increase in molecular weight due to the relatively large ligands. For example, the series of chromium acetylacetonate complexes $\text{Cr}(\text{acac})_3$, $\text{Cr}(\text{tfac})_3$, and $\text{Cr}(\text{hfac})_3$ are shown to have vapor pressures that increase with replacement of CH_3 functionalities with CF_3 .⁵⁴ Similarly, the volatility of a series of metal alkoxide complexes has been shown to directly relate to the length of the alkyl chain, increasing in the order $\text{M}(\text{OEt})_n < \text{M}(\text{O}^i\text{Pr})_n < \text{M}(\text{O}^t\text{Bu})_n$ due to increased shielding of the positively charged metal center.⁵⁵

Other desirable properties for CVD precursors include high purity, stability under normal storage conditions and low toxicity.³⁷ Furthermore, it is advantageous to develop synthetic schemes that involve as few steps as possible in order to increase overall yield

and decrease production cost. This is especially important for development of precursors that contain relatively expensive platinum group metals. In order to address the aforementioned issues, the synthetic strategies employed for the research discussed in this dissertation were developed using relatively inexpensive starting materials and simple synthetic routes, as well as investigating complexes without direct C or O bonds.

β -diketonate ligands have been used extensively in precursor synthesis for the CVD of transition metals,^{56,57} rare earth metals,⁵⁸ as well as alkali earth metals.⁵⁹ Increased volatility may be imparted to the resultant metal complex by incorporation of bulky substituents onto the backbone of the ligand. Furthermore, the preferred bidentate coordination mode of the ligand serves to fill the coordination sphere and thus shield the positively charged metal center. These ligands may also bridge multiple metal centers, forming low-volatility multinuclear complexes, e.g. $[\text{Sr}(\text{thd})]_3$ (thd = 2,2,6,6-tetramethylheptane-3,5-dionate).⁶⁰ Use of chelating donor molecules, such as pentamethylethylenediamine⁶¹ or triglyme⁶², break up the metal clusters and form monomeric species that show improved volatility.

The relatively high thermal stability of β -diketonate complexes often requires higher temperatures to afford decomposition. This may lead to significant C, O or F contamination in the resultant film, as the rate of ligand decomposition competes with precursor decomposition. An example of various decomposition pathways of various substituted β -diketonate complexes is presented in Figure 1.2. Mechanistic studies^{63,64} have shown that decomposition of complexes in which the ligands lack β -hydrogens (a) decompose by successive loss of $t\text{Bu}$ moieties followed by loss of the C_3O_2 fragment, resulting in the deposition of pure metal. An alternative pathway exists for complexes in which the ligand has β -hydrogens. In this case (b) β -hydrogen transfer results in the facile loss of ligand and formation of a metal-hydroxy species. As O incorporation in the

resultant film may hinder certain properties, β -diketonate ligands are not appropriate for all applications.

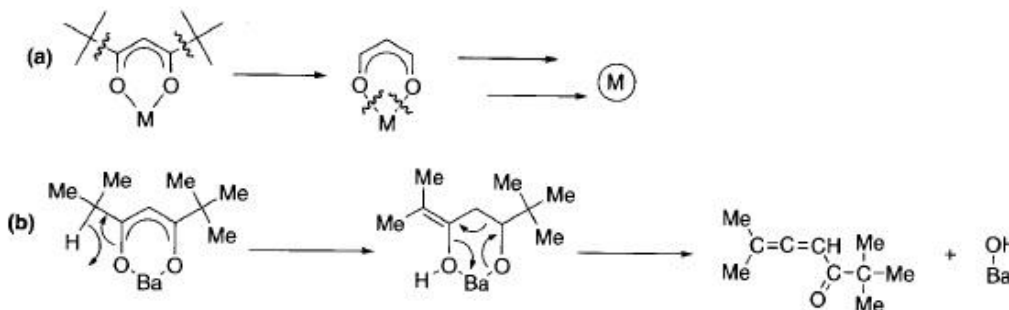


Figure 1.2 Possible decomposition pathways of β -diketonate ligands

An attractive alternative to β -diketonates for CVD applications is the related pyrazolate (Pz) class of compounds. These may be prepared in most cases by the acid-catalyzed reaction of hydrazine hydrate with the corresponding β -diketone. Similar in molecular weight, ease of preparation and handling, as well as substitutional variety, the pyrazolate ligand has several advantages compared to β -diketonate ligands for CVD precursor applications. First, the replacement of oxygen atoms with nitrogen eliminates direct M-O bonds in metal precursor complexes, a feature advantageous for highly reactive metal surfaces or other applications where the incorporation of oxygen impurities in the deposited film is undesirable. Second, the closure of the diketone molecule into a five-membered pyrazole ring allows for a larger variety of coordination modes (Figure 1.3).^{65,68} For example, the ligand may function as a neutral two electron donor by coordination to metal centers through the N2 nitrogen atom on the ring, while deprotonation allows the possibility of η^2 coordination to a single metal center as in $\text{Fe}(\text{tBu}_2\text{Pz})_3$ ⁶⁶ or bridging η^2 coordination, as seen in $[\text{Os}(\text{CO})_3(3,5\text{-(CF}_3)_2\text{Pz})]_2$.⁶⁷

Coordination in an η^5 half-sandwich fashion in $(\text{Cp}^*)\text{Ru}(\eta^5\text{-Me}_2\text{Pz})$ has also been demonstrated with this ligand.⁶⁹

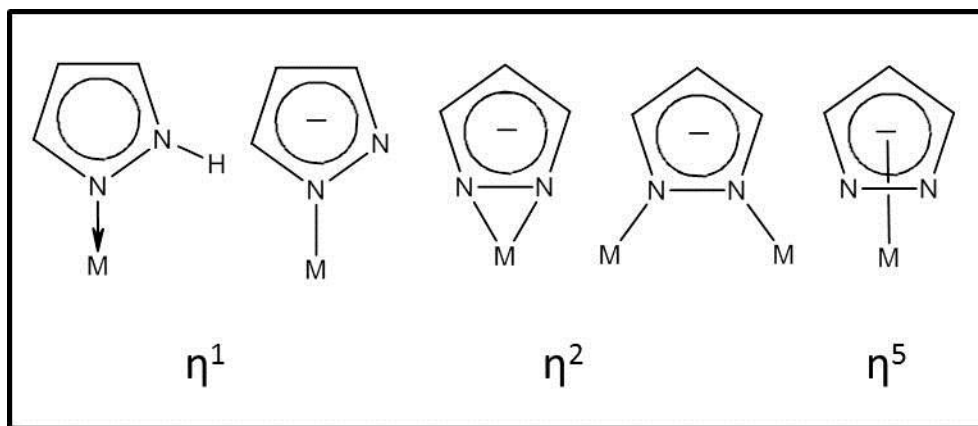


Figure 1.3 Various coordination modes of the Pz ligand.

Several examples of pyrazolate complexes have been studied in these laboratories and by others for use as CVD precursors. For instance, tungsten dialkylamido derivatives with Pz ligands have been investigated for the deposition of tungsten nitride films.⁷⁰ $[\text{Ru}(\text{CO})_3(3,5\text{-(CF}_3)_2\text{Pz})]_2$ has been used to deposit thin films of Ru and RuO_2 at temperatures of 400-450 °C.⁷¹ Dias, *et al.* have studied homoleptic pyrazolate complexes of the form $[\text{M}(3,5\text{-(CF}_3)_2\text{Pz})]_3$ ($\text{M} = \text{Ag}$ or Au),^{72,73} while research in these laboratories have yielded a number of late transition metals complexes suitable for CVD applications.^{74,75}

OVERVIEW AND SCOPE

This dissertation is organized into six chapters, with this introductory section comprising the initial chapter in order to provide general background information on the techniques and to clearly outline the research motivations of the present work. Chapter two highlights advances in the chemical vapor deposition of amorphous ruthenium phosphorus alloys. A series of novel and known complexes containing trialkylphosphine and trialkylphosphite molecules as ligands have been synthesized and evaluated for their potential use as volatile single source CVD reagents. Thin films grown with these compounds were characterized by X-ray diffraction (XRD), X-ray photoelectron spectroscopy (XPS), and scanning electron microscopy (SEM). Control of deposition conditions was obtained with a horizontal hot-wall vapor deposition chamber constructed to allow the option of varying carrier gasses. The chemistry of the precursor complexes themselves plays a large role in determining the composition and morphology of the resultant films.

Chapter three examines synthetic strategies and deposition conditions used to evaluate a series of rhodium containing precursor complexes for the CVD of rhodium thin films. In this section, several series of mononuclear and dinuclear Rh complexes covering a range of molecular architectures were synthesized using a series of symmetrically and asymmetrically substituted pyrazole and pyrazolate ligands. Several complexes were found to sublime at mild temperatures, a direct result of the functional groups of the substituted pyrazolate, and were further studied for use as CVD precursors. Emphasis is placed not only on the purity of the resultant films or the volatility of the precursor, but also on the ease and yield of the preparative procedure necessary to synthesize the complexes, as well as their stability in ambient conditions. Optimization of

these later two properties is an important issue for the development of novel precursors for the relatively expensive noble metals.

Chapter four outlines the synthesis of a homoleptic tungsten pyrazolate complex. Modern methods for tungsten thin film deposition involve the use of WF_6 and a reactive carrier gas such as H_2 or SiH_4 . High quality W films are produced, though a drawback is the formation of corrosive HF gas, which limits this precursor combination for some applications. Due to the importance of tungsten thin films for applications in microelectronic devices, volatile CVD precursors are needed as an alternative.

Chapter five outlines the synthesis of a series of palladium pyrazolate complexes, synthesized with the aim of use as volatile CVD reagents. As with the synthetic strategies involved with the rhodium precursors mentioned above, a variety of variously substituted pyrazolate ligands were investigated to determine the effect on precursor volatility as well as film properties. A major feature of the synthetic scheme followed in this chapter is the rational removal of direct metal-halide bonds from the precursors, resulting in homoleptic palladium pyrazolate complexes.

In chapter six, the focus of research changes from CVD source reagents to synthesis and characterization of bulk materials with useful electrochemical properties for Li-ion battery electrode applications. Novel low-temperature synthetic methods are outlined that result in facile formation of transition metal phosphides, phosphates, borates, and oxides. The materials are characterized primarily by XRD and electron microscopy, and the physical properties are related to electrochemical performance. The convenient, low-temperature preparative method, as well as the potential to fine tune the morphology of the material provides an attractive alternative to existing high-temperature methods for these types of materials.

REFERENCES

1. Serp, P.; Chateau, L.; Feurer, R.; Kiennemann, A.; Kalck, P. *J. Mol. Catal. A* **1998**, *136*, 269.
2. Dal Santo, V.; Mondelli, C.; De Grandi, V.; Gallo, A.; Recchia, S.; Sordelli, L.; Psaro, R. *Appl. Catal. A – Gen.* **2008**, *346*, 126.
3. Breen, J. P.; Burch, R.; Gomez-Lopez, J.; Griffin, K.; Hayes, M. *Appl. Catal. A* **2004**, *268*, 267.
4. Kennedy, D. R.; Webb, G.; Jackson, S. D.; Lennon, D. *Appl. Catal. A* **2004**, *259*, 109.
5. Waterhouse, G. I. N.; Bowmaker, G. A.; Metson, J. B. *Appl. Catal. A* **2004**, *266*, 257.
6. Shelef, M.; McCabe, R. W. *Catal. Today* **2000**, *62*, 35.
7. Amiridis, M. D.; Mihut, C.; Maciejewski, M.; Baiker, A. *Top. Catal.* **2004**, *28*, 141.
8. Richter, M.; Fricke, R.; Eckelt, R. *Catal. Lett.* **2004**, *94*, 115.
9. Liguras, D. K.; Kondarides, D. I.; Verykios, X. E. *Appl. Catal. B* **2003**, *43*, 345.
10. Ghenciu, A. F. *Curr. Opin. Solid St. M.* **2002**, *6*, 389.
11. Marot, L.; De Temmerman, G.; Thommen, V.; Mathys, D.; Oelhafen, P. *Surf. Coat. Tech.* **2008**, *202*, 2837.
12. Hemphill, R.; Hurwitz, M.; Pelizzo, M. G. *Appl. Optics* **2003**, *42*, 5149.
13. Igumenov, I. K.; Gelfond, N. V.; Galkin, P. S.; Morozova, N. B.; Fedotova, N. E.; Zharkova, G. I.; Shipachev, V. I.; Reznikova, E. F.; Ryabtsev, A. D.; Kotsupalo, N. P.; Titarenko, V. I.; Dikov, Y. P.; Distler, V. V.; Buleev, M. I. *Desalination* **2001**, *136*, 273.
14. Briand, D.; Van der Schoot, B.; de Rooij, N. F.; Sundgren, H.; Lundström, I. *J. Microelectromech. S.* **2000**, *9*, 303.
15. Zimmer, M.; Burgmair, M.; Scharnagl, K.; Karthigeyan, A.; Doll, T.; Eisele, I. *Sensor Actuat. B-Chem.* **2001**, *80*, 174.

16. (a) Kuban, P.; Berg, J. M.; Dasgupta, P. K. *Anal. Chem.* **2004**, 76, 2561–2567. (b) Renzas, J. R.; Somorjai, G. A. *J. Phys. Chem. C* **2010**, 114, 17660.
17. Moore, G. E. *Electronics* **1965**, 38, 4.
18. Wilk, G. D.; Wallace, R. M.; Anthony, J. M. *J. Appl. Phys.* **2001**, 89, 5243.
19. Youm, M.; Sim, H. S.; Jeon, H.; Kim, S.-I.; Kim, Y. T. *Jpn. J. Appl. Phys.* **2003**, 42, 5010.
20. Schaeffer, J. K.; Samavedam, S. B.; Gilmer, D. C.; Dhandapani, V.; Tobin, P. J.; Mogab, J.; Nguyen, B.-Y.; White, Jr. B. E.; Dakshina-Murthy, S.; Rai, R. S.; Jiang, Z.-X.; Martin, R.; Raymond, M. V.; Zavala, M.; La, L. B.; Smith, J. A.; Garcia, R.; Roan, D.; Kottke, M.; Gregory, R. B. *J. Vac. Sci. Technol. B* **2003**, 21, 11.
21. Schaeffer, J. K.; Fonseca, L. R. C.; Samavedam, S. B.; Liang, Y.; Tobin, P. J.; White, B. E. *Appl. Phys. Lett.* **2004**, 85, 1826.
22. Dey, S. K.; Goswami, J.; Gu, D.; de Waard, H.; Marcus, S.; Werkhoven, C. *Appl. Phys. Lett.* **2004**, 84, 1606.
23. Ľapajna, M.; Písečný, P.; Lupták, R.; Hušeková, K.; Frölich, K.; Harmatha, L.; Hooker, J. C.; Roozeboom, F.; Jergel, J. *Mater. Sci. Semicond. Process.* **2004**, 7, 271.
24. Fillot, F.; Chenevier, B.; Maîtrejean, S.; Audier, M.; Chaudouët, P.; Bochu, B.; Sénateur, J. P.; Pisch, A.; Mourier, T.; Monchoix, H.; Guillaumot, B.; Passemar, G. *Microelectron. Eng.* **2003**, 70, 384.
25. Zhong, H.; Heuss, G.; Suh, Y.-S.; Misra, V.; Hong, S.-N. *J. Electron. Mater.* **2001**, 30, 1493.
26. Zhong, H.; Heuss, G.; Misra, V.; Luan, H.; Lee, C.-H.; Kwong, D.-L. *Appl. Phys. Lett.* **2001**, 78, 1134.
27. Kwon, J.-D.; Jeong, S.-J.; Kang, J.-W.; Kim, D.-G.; Kim, J.-K.; Rha, J.-J.; Nam, K.-S.; Kwon, S.-H. *J. Electrochem. Soc.* **2009**, 156, H832.
28. Liu, C. H.; Wang, Y.; Liu, B.; An, Z.; Song, Z. X.; Xu, K. W. *J. Phys. D: Appl. Phys.* **2011**, 44, 075302.

29. Lane, M. W.; Murray, C. E.; McFeely, F. R.; Vereecken, P. M.; Rosenberg, R. *Appl. Phys. Lett.* **2003**, 83, 2330–2332.
30. Chyan, O.; Arunagiri, T. N.; Ponnuswamy, T. *J. Electrochem. Soc.* **2003**, 150, C347–C350.
31. Chen, C.-W.; Jeng, J.-S.; Chen, J.-S. *J. Electrochem. Soc.* **2010**, 157, H997.
32. Fang, J. S.; Lin, J. H.; Chen, B. Y.; Chin, T. S. *J. Electrochem. Soc.* **2011**, 158, H97.
33. Kim, J. J.; Kim, S.-K.; Kim, Y. S. *J. Electrochem. Soc.* **2004**, 151, C97–C101.
34. Wang, Z.; Yaegashi, O.; Sakaue, H.; Takahagi, T.; Shingubara, S. *Jpn. J. Appl. Phys.*, **2003**, 42, L1223–L1225.
35. Lee, H. *J Micromech. Microeng.* **2006**, 16, 557.
36. Seshan, K. *Handbook of Thin-Film Deposition Processes and Techniques*; Noyes: Norwich, NY, **2002**.
37. Dobkin, D. M.; Zuraw, M. K. *Principles of Chemical Vapor Deposition*; KluwerAcademic: Dordrecht, **2003**.
38. Hierso, J.-C.; Feurer, R.; Kalck, P. *Coordin. Chem. Rev.* **1998**, 178-180, 1811.
39. Beach, D. B. *IBM J. Res. Develop.* **1990**, 34, 796.
40. Cowley, A. H.; Jones, R. A. *Angew. Chem. Int. Edit.* **1989**, 28, 1208.
41. Cowley, A. H.; Jones, R. A. *Polyhedron* **1994**, 13, 1149.
42. Ekerdt, J. G.; Sun, Y. M.; Jackson, M. S.; Lakhotia, V.; Pacheco, K. A.; Koschmieder, S. U.; Cowley, A. H.; Jones, R. A. *J. Cryst. Growth* **1992**, 124, 158.
43. Cowley, A. H.; Jones, R. A. *Angew. Chem. Int. Edit.* **1998**, 28, 1208.
44. Chiu, H.-T. *Mater. Res. Soc. Symp. P.* **1992**, 250, 317.
45. Pierson, H. O. *Handbook of chemical vapor deposition (CVD): principles, technology, and applications 2nd ed.*; William Andrew, **1999**.
46. Kruck, T.; Baur, K. *Angew. Chem. Int. Edit.* **1965**, 4, 521.

47. Kodas, T. *The Chemistry of Metal CVD*; Wiley-VCH, **1994**.
48. Jones, A. C.; Hitchman, M. L. *Chemical Vapour Deposition Precursors, Processes and Applications*; RSC Publishing, **2009**.
49. Cohan, J. S.; Yuan, H.; Williams, R. S.; Zink, J. I. *Applied Physics Letters* **1992**, *60*, 1402.
50. Yuan, Z.; Jiang, D.; Naftel, S. J.; Sham, T. K.; Puddephatt, R. J. *Chem. Mater.* **1994**, *6*, 2151.
51. Park, S.; Lim, S.; Choi, H. *Chem. Mater.* **2006**, *18*, 5150.
52. Baxter, D. V.; Chisholm, M. H.; Doherty, S.; Gruhn, N. E. *Chem. Commun.* **1996**, 1129.
53. Lappert, M. F.; Power, P. P.; Sanger, A. R.; Srivastava, R. C. *Metal and Metalloid amides*; Ellis Horwood, **1980**.
54. Herrmann, W. A.; Huber, N.W.; Runte, O. *Angew. Chem. Int. Edit.* **1995**, *34*, 2187.
55. Jones, A.C. *Chem. Vapor Depos.* **1998**, *4*, 169.
56. Lai, W. G.; Xie, Y.; Griffin, G. L. *J. Electrochem. Soc.* **1991**, *138*, 3499.
57. Lee, D.-J.; Kang, S.-W.; Rhee, S.-W. *Thin Solid Films* **2002**, *413*, 237.
58. Edleman, N. L.; Wang, A.; Belot, J. A.; Metz, A. W.; Babcock, J. R.; Kawaoka, A. M.; Ni, J.; Metz, M. V.; Flaschenriem, C. J.; Stern, C. L.; Liable-Sands, L. M.; Rheingold, A. L.; Markworth, P. R.; Chang, R. P. H.; Chudzik, M. P.; Kannewurf, C. R.; Marks, T. J. *Inorg. Chem.* **2002**, *41*, 5005-5023.
59. Schulz, D. L.; Hinds, B. J.; Stern, C. L.; Marks, T. J. *Inorg. Chem.* **1993**, *32*, 249.
60. Brooks, J.; Davies, H. O.; Leedham, T. J.; Jones, A. C.; Steiner, A. *Chem. Vap. Deposition.* **2000**, *6*, 66.
61. Timmer, K.; Spee, K.; Mackor, A.; Meinema, H. A.; Spek, A. L.; Van der Sluis, P. *Inorg. Chim. Acta* **1991**, *190*, 109.
62. Roeder, J. F.; Baum, T. H.; Bilodeau, S. M.; Stauff, G. T.; Ragaglia, C.; Russell,

- M. W.; Van Buskirk, P. C. *Adv. Mater. Opt. Electr.* **2000**, *10*, 145.
63. Luten, H. A.; Rees, W. S.; Goedken, V. L. *Chem. Vap. Deposition.* **1996**, *2*, 149.
 64. Gordon, R. G.; Barry, S.; Broomhall-Dillard, R. N. R.; Teff, D. J. *Adv. Mater. Opt. Electr.* **2000**, *10*, 201.
 65. Halcrow, M. A. *Dalton Trans.* **2009**, *12*, 2059.
 66. Mosch-Zanetti, N. C.; Kratzner, R.; Lehmann, C.; Schneider, T. R.; Uson, I. *Eur. J. Inorg. Chem.* **2000**, *13*; (b) K. R. Gust, J. E. Knox, M. J. Heeg, H. B. Schlegel and C. H. Winter, *Angew. Chem., Int. Ed.*, 2002, *41*, 1591.
 67. Chi, Y.; Yu, H.-L.; Ching, W.-L.; Liu, C.-S.; Chen, Y.-L.; Chou, T.-Y.; Peng, S.-M.; Lee, G.-H. *J. Mater. Chem.* **2002**, *12*, 1363.
 68. Trofimenko, S. *Chem Rev.* **1972**, *72*, 497.
 69. Perera, J. R.; Heeg, M. J.; Schlegel, H. B.; Winter, C. H. *J. Am. Chem. Soc.* **1999**, *121*, 4536.
 70. El-Kadri, O. M.; Heeg, M. J.; Winter, C. H. *J. Organomet. Chem.* **2009**, *694*, 3902.
 71. Song, Y.-H.; Chen, Y.-L.; Chi, Y.; Liu, C.-S.; Ching, W.-L.; Kai, J.-J.; Chen, R.-S.; Huang, Y.-S.; Carty, A. J. *Chem. Vapor Depos.* **2003**, *9*, 162.
 72. Dias, H. V. R.; Gamage, C. S. P. *Angew. Chem., Int. Edit.* **2007**, *46*, 2192.
 73. Dias, H. V. R.; Gamage, C. S. P.; Keltner, J.; Diyabalanage, H. V. K.; Omari, I.; Eyobo, Y.; Dias, N. R.; Roehr, N.; McKinney, L.; Poth, T. *Inorg. Chem.* **2007**, *46*, 2979.
 74. Waheed, A.; Jones, R. A.; Agapiou, K.; Yang, X.; Moore, J. A.; Ekerdt, J. G. *Organometallics* **2007**, *26*, 6778.
 75. Wang, Z.; Abernethy, C. D.; Cowley, A. H.; Jones, J. N.; Jones, R. A.; Macdonald, C. L.B.; Zhang, L. *J. Organomet. Chem.* **2003**, *666*, 35.
 76. Kumar, R.; Puddephatt, R. J. *Can. J. Chemistry* **1991**, *69*, 108.

Chapter 2: Chemical vapor deposition of amorphous ruthenium phosphorus thin films from Ru trialkylphosphite hydride complexes

INTRODUCTION

The advent of Moore's Law in the mid 1960's initially served as a forecast concerning the exponential growth of the number of transistors able to be inexpensively placed on an integrated circuit (IC), and has since become the basis of production goals and research and development targets for many segments of the microelectronics industry. As the trend continues, miniaturization of IC components will require ever more innovative solutions in manufacturing processes and material development. The number of transistors implemented in integrated circuits from the 22 nm technology node onward will jump from hundreds of millions to several billion, and each of these will require metal interconnects.¹ Copper is considered an attractive alternative to aluminum as an interconnect material due to its lower resistivity (ca. 1.7 $\mu\Omega\text{cm}$ vs. 2.8 $\mu\Omega\text{cm}$ for Al) and improved resistance to electromigration.² When summed over billions of separate connections, the lower resistivity of Cu is extremely important for lowering interconnect resistance-capacitance (RC) delay and significantly enhancing overall device performance.

The ubiquitous replacement of aluminum with copper as the preferred interconnect metal in microelectronic devices in the late 1980's ushered in a new set of fabrication challenges that led to significant long-term changes in semiconductor manufacturing processes. Formation of aluminum interconnects was accomplished by deposition of aluminum over the entire wafer and then patterning with reactive ion etching.¹ Analogous fabrication processes were not successful with copper, and various CVD and PVD techniques were limited by low precursor volatility and poor film conformality. Thus a new fabrication method was developed which involves filling of

trenches and vias of patterned dielectric with Cu via electrochemical deposition (ECD). This procedure, known as the damascene process, involves three steps (Figure 2.1). First, a thin film of a diffusion barrier material is deposited over a patterned trench in the dielectric in order to prevent interdiffusion of Cu into the dielectric. In order to promote adhesion of the interconnect, this step is followed by the deposition of a thin Cu seed layer. The trench is then quickly filled with Cu with good coverage by ECD. This step overfills the feature and a final step of chemical mechanical polishing (CMP) is required to remove excess metal and flatten the wafer surface for the next patterning step.

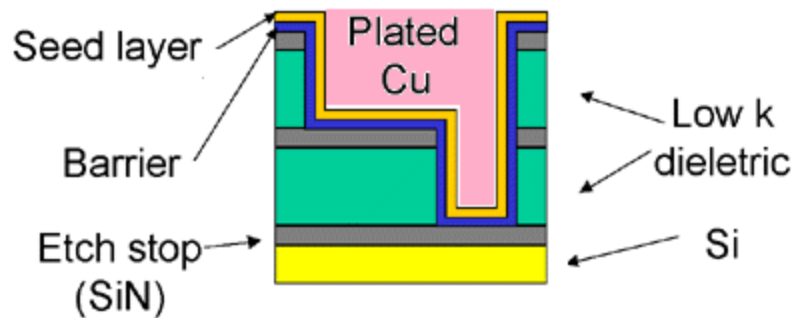


Figure 2.1 A cross-sectional view of a typical copper interconnect device formed by the damascene process.

The most serious problem associated with copper as an interconnect material is its ability to electromigrate through the SiO_2 dielectric, thus degrading device performance.³ This issue is addressed by the inclusion of an interstitial layer of a material between the copper and dielectric that acts as a diffusion barrier and prevents intermixing. Ideal materials for this role exhibit low resistivity, high thermal stability and good adhesion to both copper and silicon. There is a great deal of interest in early transition metal nitrides such as TiN, HfN and ZrN to act as barriers, while TaN in particular has become a widely used and commercially accepted barrier.⁴ One drawback of the use of TaN, however, is

the requirement of successive layers of PVD-grown TaN, Ta and Cu for the complete formation of the barrier layer. Thus the potential of this multilayer solution may be limited as ever-decreasing feature size of IC components will require thinner and more conformal diffusion barriers.

Ruthenium is a viable alternative to TaN based diffusion barriers due to its high conductivity and chemical inactivity with copper and silicon.⁵ Furthermore films of Ru adhere well to silicon and can be directly electroplated with copper.⁶ However, ruthenium films tend to grow with columnar crystalline domains oriented perpendicular to the film surface, presenting efficient paths for copper migration.⁷ Use of amorphous thin films as barrier layers would eliminate problems associated with grain boundary or stacking fault formation, as amorphous materials exhibit no long range order. Control over microstructure of deposited films leading to microcrystalline or amorphous films may improve the diffusion barrier properties.

Previous studies performed in these laboratories,⁸ with the single source CVD precursor *cis*-H₂Ru(PMe₃)₄, have revealed a strong dependence on film morphology with precursor chemistry. Thin films of Ru grown from this precursor show phosphorus incorporation in amounts of up to 20 % due to decomposition of PMe₃ ligands in the precursor. Furthermore, heteroatom incorporation is believed to interfere with crystallite formation, as all as-deposited films are X-ray amorphous, showing no long range order. X-ray photoelectron spectroscopy (XPS) studies revealed information about the chemical states of the elements within the film, and support the formulation of a Ru(P) alloy in which both Ru and P are in an elemental, zero valent state.

As an extension of the results obtained previously, a series of ruthenium hydride complexes were synthesized with various phosphorus donor ligands for use as single source CVD precursors. Coordination complexes incorporating trialkylphosphite

(P(OR)₃) ligands with several different R-groups were studied in order to determine the effect of precursor ligand chemistry on film morphology and composition. Trialkylphosphite ligands were chosen as the P donor ligands for the precursor complexes for several reasons. They are generally more air stable and less expensive than corresponding trialkylphosphines - important considerations for scale up manufacturing processes. Furthermore thermal decomposition pathways of phosphites have been shown to be similar to that of phosphines,⁹ affording the possibility of control over the amount of P incorporation into films deposited from precursors utilizing these ligands. For example, decomposition via P-O bond cleavage may result in higher levels of P in the film, while minimizing C incorporation. Phosphite ligands contain oxygen, however and there exists the possibility for oxygen incorporation into resultant films, though the specific decomposition pathway likely depends strongly on physical deposition conditions. There exist several examples of trialkylphosphite derivatives of copper,^{10a} cobalt,^{10b} and nickel¹¹ that have been used as CVD reagents for the deposition of pure metal.

An additional strategy employed for the Ru precursors studied in this chapter is use of the oxalate (C₂O₄²⁻) ligand to fill the coordination sphere of the metal. Metal oxalate complexes are known to thermally decompose by a reductive elimination pathway that results in the evolution of two moles of CO₂ per oxalate.¹² Reduction of the metal center and facile formation of a relatively inert gaseous byproduct make this an attractive ligand for many CVD applications. The oxalate ligand (ox) is able to bridge two metal centers, though monomeric transition metal complexes are known, e.g. Pt(ox)(PEt₃)₂¹³ and [NEt₄]₂[W(ox)(CO)₄].¹⁴ A series of dicopper(I) oxalate complexes of the form (Cu(L))₂(μ-ox) (L = alkene or alkyne) have been shown to exhibit high vapor pressures and sublime without decomposition upon gentle heating.¹⁵ Analogous

ruthenium oxalate complexes with phosphine or phosphite ligands may serve as potentially useful CVD precursors for amorphous Ru(P) alloys.

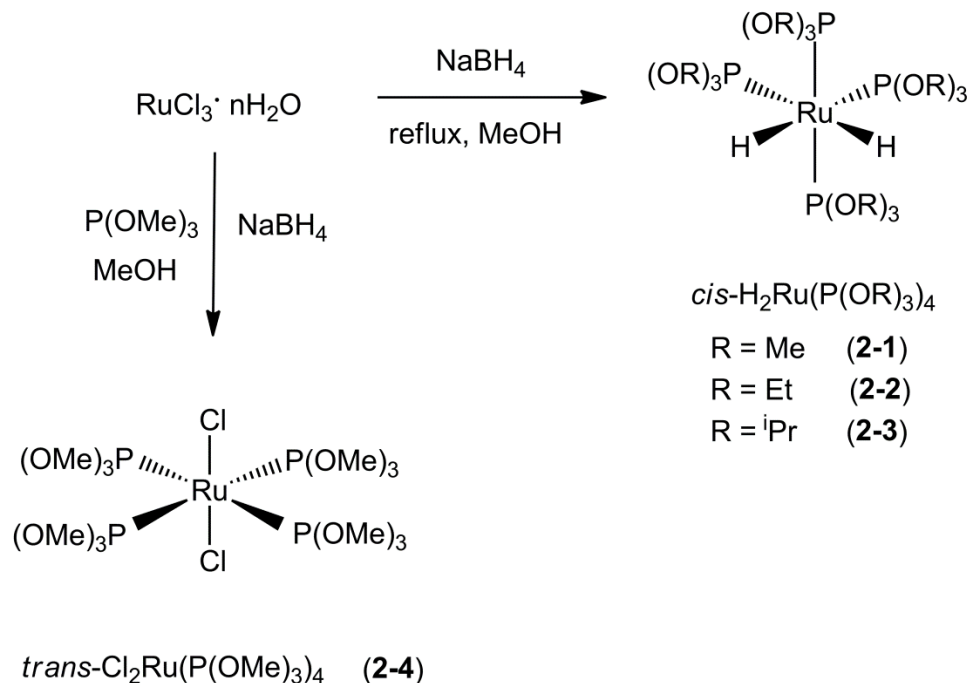
RESULTS AND DISCUSSION

The objective of the research summarized in this chapter is to develop volatile Ru complexes for use as single source molecular precursors for CVD of amorphous ruthenium phosphorus alloys. Key properties of the precursors are that they vaporize without decomposition at moderate temperatures, and that they incorporate phosphorus-containing functionality as ligands to provide a source of P in the resultant thin film. Ruthenium hydride complexes of the form *cis*-H₂Ru(P(OR)₃)₄ were synthesized and structurally characterized by single crystal X-ray diffraction methods and were further tested as CVD precursors in a home-built hot-wall CVD reactor. Morphology and composition of thin films grown from these precursors were studied by X-ray diffraction and X-ray photoelectron spectroscopy. Furthermore the synthesis and structural characterization of two novel Ru-containing complexes with bridging oxalate ligands is described. While these complexes remained involatile, they provide useful insight into synthetic approaches for metal oxalate complexes and provide a foundation for future development of volatile complexes appropriate for CVD.

Ruthenium hydride complexes

The *cis*-ruthenium hydride complexes H₂Ru(P(OR)₃)₄ (R = Me (**2-1**), Et (**2-2**), ^{*i*}Pr (**2-3**)) were first synthesized by Muetterties, *et al.* more than 30 years ago but were not structurally characterized.¹⁶ In the present work, all three complexes were synthesized by a slight modification of the method previously reported (shown in Scheme 2.1). The

crude products consisted of flaky off-white solids that were purified by sublimation under reduced pressure (10^{-2} Torr). X-ray quality crystals of complexes **2-1** and **2-2** were grown by cooling a hexane/methanol solution to $-30\text{ }^{\circ}\text{C}$, though similar recrystallization attempts led only to microcrystalline powder for complex **2-3**. Large colorless crystals of **2-3** were obtained by slow heating under vacuum in a zone sublimator, but were not suitable for X-ray crystallography. The identity of all three complexes were confirmed by comparison of NMR and IR spectral data with that previously reported.



Scheme 2.1 Synthesis of ruthenium phosphite complexes.

The crystal structure of **2-1** is shown in Figure 2.2. Selected bond lengths and angles are presented in Table 2.4, while additional crystallographic details are listed in Table 2.2. The complex crystallizes in the triclinic space group *P1* with six molecules per

unit cell. The central Ru ion of the complex is six-coordinate with a *cis*-configuration of the hydride ligands. The hydride hydrogen atoms were located as peaks in reasonable locations on a difference Fourier map and included without refinement. The position of the hydride ligands is further established by the approximate see-saw molecular geometry formed by the four trimethylphosphite ligands. The two P atoms of the mutually *trans* phosphite ligands form an angle of ca. 154°, while the other two P(OMe)₃ ligands form a mutual angle of 95°, leaving room for the coordination of the relatively small hydride ligands. The two phosphite ligands coordinated *trans* to the hydrides exhibit a slightly longer average Ru-P bond length (2.281(11) Å, av.) compared to the other two phosphite ligands (2.260(10) Å, av.), reflecting the *trans*-directing influence of the hydride ligands. Infrared and NMR spectroscopic data for **2-1** are consistent with previously reported data.¹⁶

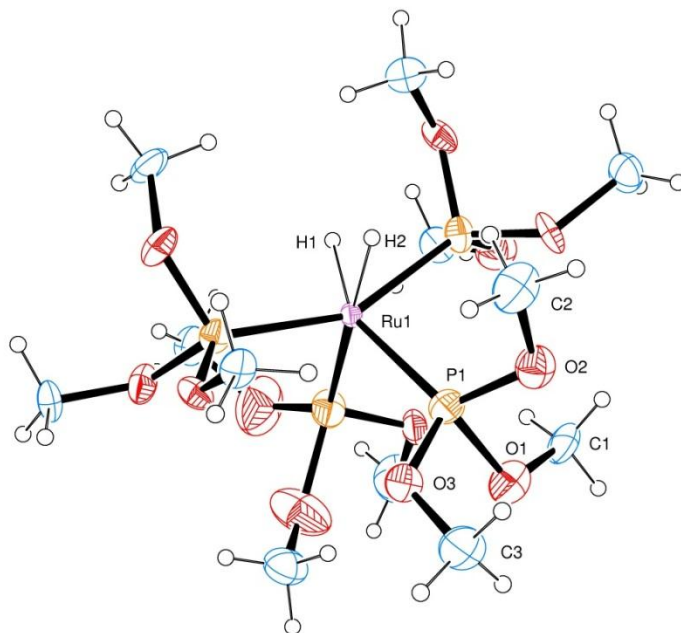


Figure 2.2 ORTEP diagram and partial atom numbering scheme of *cis*-H₂Ru(P(OMe)₃)₄ (**2-1**). Thermal ellipsoids are drawn at the 30% probability level.

Complex **2-2** was synthesized similarly to complex **2-1**, but using triethylphosphite as the phosphorus containing ligand. The crystal structure of **2-2** is shown in Figure 2.3. Selected bond lengths and angles are presented in Table 2.5, while additional crystallographic details are summarized in Table 2.2. Complex **2-2** crystallizes in the triclinic space group $P\bar{1}$ with four independent molecules in the unit cell. The compound is isostructural to complex **2-1**, with the phosphite ligands arranged in a similar see-saw geometry about the central ruthenium ion and the hydride atoms located *cis* to each other. The P-Ru-P angle for the ligands *trans* to the hydrides ($98(2)^\circ$) is significantly larger than that for the ligands *cis* to the hydrides ($152(1)^\circ$). As in complex **2-1**, a slight *trans*-directing influence of the hydride ligands is observed for complex **2-2** (Ru-P_{*cis*} = 2.25(3) Å, av.; Ru-P_{*trans*} = 2.27(1) Å, av. for the P(OEt)₃ ligands *cis* and *trans* to the hydride atoms, respectively). Infrared and NMR spectroscopic data for **2-2** are consistent with those previously reported.¹⁶

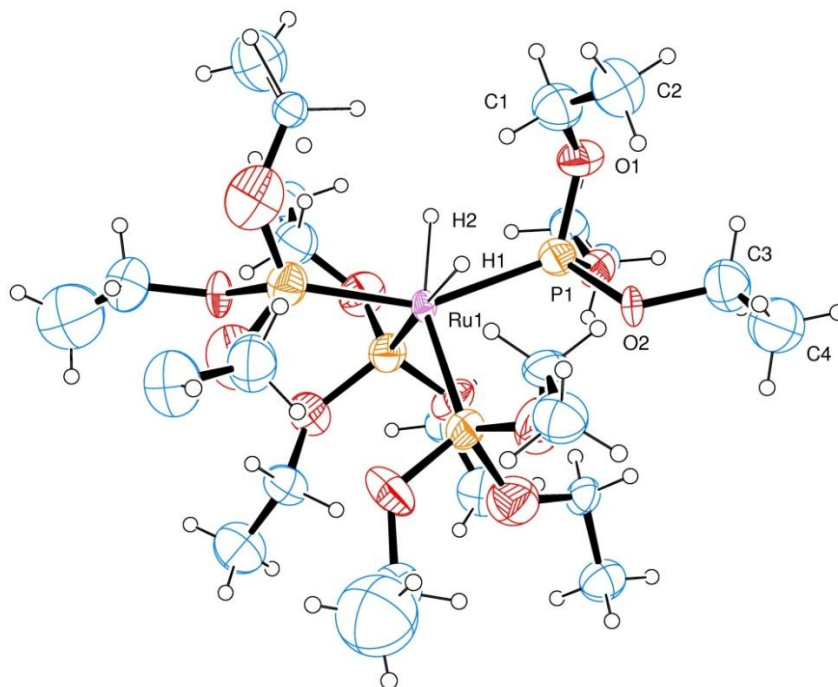


Figure 2.3 ORTEP diagram and partial atom numbering scheme of *cis*-H₂Ru(P(OEt)₃)₄ (**2-2**). Thermal ellipsoids are drawn at the 30% probability level.

The complex *trans*-Cl₂Ru(P(OMe)₃)₄ was isolated as an intermediate in the synthesis of **2-1**, and although the preparation and spectral characterization of this compound has been previously reported,¹⁶ surprisingly, it has not been structurally characterized by single crystal X-ray diffraction. The complex is not suitable for use as a CVD precursor because of the two metal coordinated chloride ions, but these may be easily exchanged by other functional groups more appropriate for CVD applications. For example, further reaction of this complex with NaBH₄ in methanolic solution results in the *cis*- ruthenium dihydride complex **2-1**. Additionally, salt exchange reactions with a number of small anionic ligands such as pyrazolate, β-diketonate, or oxalate moieties may lead to volatile monomeric species. Thus complex **2-4** remains an interesting and

useful molecular platform for the development of volatile single source Ru CVD precursors.

Reaction of excess triethylphosphite and NaBH₄ with RuCl₃ • nH₂O in methanol gave *trans*-Cl₂Ru(P(OMe)₃)₄ (**2-4**) in high yield as a bright yellow solid, which may be recrystallized from hexane/methanol at -30 °C. The X-ray crystal structure of complex **2-4** is shown in Figure 2.4, while selected bond lengths and angles are listed in Table 2.6. Other crystallographic details are listed in Table 2.2.

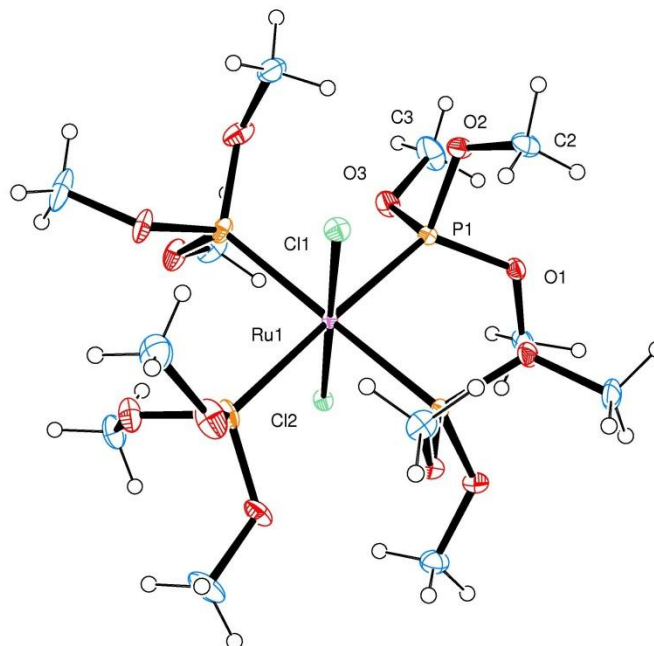


Figure 2.4 ORTEP diagram and partial atom numbering scheme of Cl₂Ru(P(OMe)₃)₄ (**2-4**). Thermal ellipsoids are drawn at the 30% probability level.

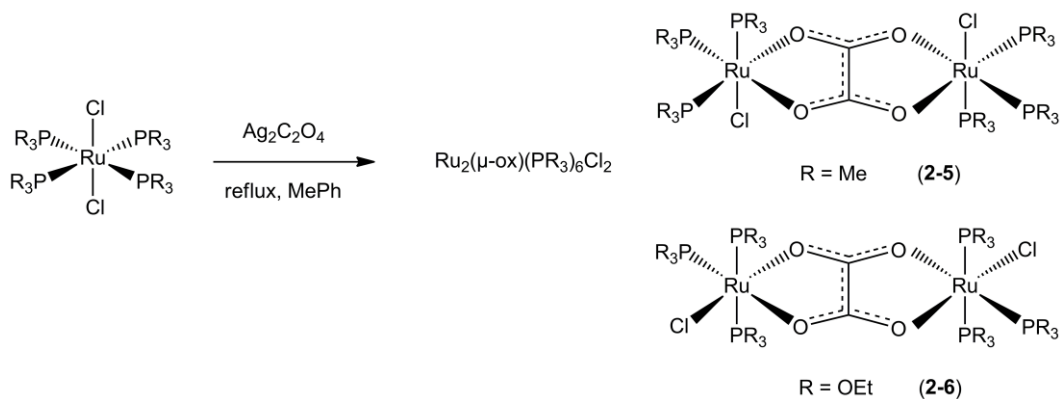
Complex **2-4** crystallizes in the centrosymmetric space group *P*2₁/*n* with four molecules per unit cell. Two chloride ligands are coordinated to the central ruthenium atom in a *trans* configuration, giving the complex approximate *D*_{4h} symmetry. The average Ru-P distance of 2.325(30) Å is slightly longer than that found in complexes **2-1**

and **2-2**, and is typical for ruthenium phosphite complexes.¹⁷ While the angular separation of the phosphite ligands is almost exactly 90°, they are not co-planar. The average *trans* P-Ru-P angle of 175(1)° results in a slight distortion of the four phosphite ligands from a square planar geometry which allows for steric relief of the bulky ligands. Infrared and NMR spectroscopic data for **2-4** are consistent with previously reported data.¹⁶

Ruthenium oxalate complexes

The reaction of potassium oxalate (K₂C₂O₄) with *cis*-Cl₂Ru(PMe₃)₄ in a 1:1 molar ratio was attempted in order to obtain Ru(ox)(PMe₃)₄, a six-coordinate, 18 electron Ru(II) complex. The proposed mononuclear complex was not obtained, however, and the main reaction product proved to be the dinuclear oxalate-bridged species Cl₂Ru₂(μ-ox)(PMe₃)₆ (**2-5**). In order to drive the reaction to favor substitution of both chloride ions on each Ru with oxalate, the reaction was repeated with two modifications: (i) Ag₂(ox) was used as the oxalate salt, with the rationale being utilization of the higher lattice energy of AgCl vs KCl as a stronger enthalpic driving force, and (ii) the reaction was performed in refluxing toluene in order to increase the solubility of Ag₂(ox) (Scheme 2.2). Silver oxalate is light and shock sensitive, and is thermally unstable at temperatures above 140 °C,¹⁸ and, it was hypothesized that refluxing toluene (b.p. 110 °C) would increase the solubility of the oxalate in the reaction mixture without affording significant decomposition. The reaction was conducted by refluxing in the dark for several hours, during which time the strongly colored yellow solution became more pale and eventually colorless (Scheme 2.2). Upon filtration, extraction of the product into THF, and cooling to -30 °C, colorless X-ray quality crystals of **2-5** were isolated. The product is virtually insoluble in hexane, but dissolves in polar aprotic solvents such as THF, toluene, and methylene chloride. The X-

ray crystal structure and partial atom numbering scheme of **2-5** is shown in Figure 2.5. Selected bond lengths and distances are presented in Table 2.7, and additional crystallographic details are listed in Table 2.3.



Scheme 2.2 Synthesis of ruthenium oxalate complexes.

Complex **2-5** crystallizes in the triclinic space group $P\bar{1}$ with two molecules per unit cell. The structure consists of two ruthenium centers bridged by one oxalate ligand through the μ - 1, 2, 3, 4 bridging mode common for this ligand. A C_2 axis runs along the C-C bond of the bridging oxalate ligand, giving the complex approximate C_{2h} overall symmetry. The PMe_3 ligands are arranged such that four are coordinated in the $\text{Ru}_2(\text{ox})$ plane and two coordinate above and below this plane, respectively, *trans* to two metal-coordinated chloride ligands. The two Cl atoms are bent away from the PMe_3 groups, towards the less sterically hindering oxalate ligand ($\text{Cl(1)-Ru(1)-O(1)} = 81.05^\circ$).

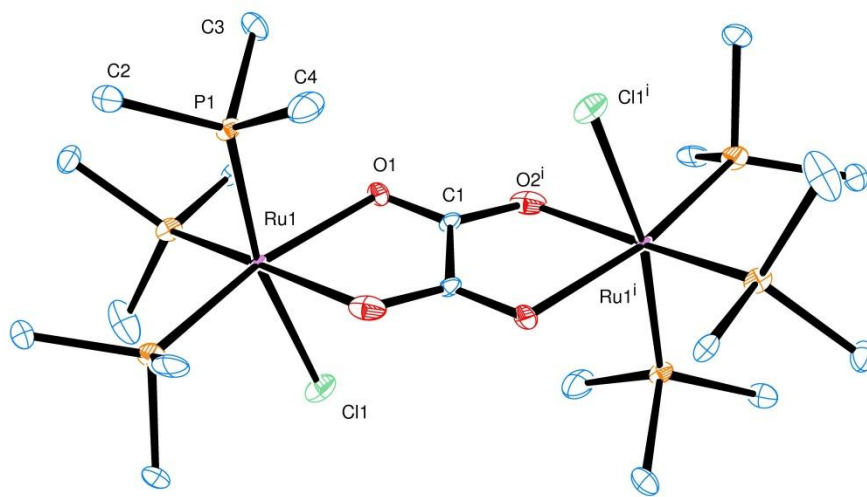


Figure 2.5 ORTEP diagram and partial atom numbering scheme of $\text{Cl}_2\text{Ru}_2(\mu\text{-ox})(\text{PMe}_3)_6$ (**2-5**). Thermal ellipsoids are drawn at the 30% probability level. Hydrogen atoms have been omitted for clarity.

Each ruthenium(II) ion in complex **2-5** is stabilized by ligand field stabilization energy (18 electron, d^6) and remains inert to further substitution of chloride. Many dinuclear Ru(II) phosphine complexes of this type exist with a variety of bridging ligands.¹⁹ Because *cis*- $\text{Cl}_2\text{Ru}(\text{PMe}_3)_4$ is highly soluble in hydrocarbons as well as polar organic solvents, it is present in far excess in the reaction mixture, and thus elevated temperatures were required to increase the concentration of the relatively insoluble oxalate salt. This may have had the effect of driving the loss of PMe_3 from the final reaction product. Addition of excess PMe_3 to the reaction mixture, however, had no effect on the product obtained, and it should be noted that $(\text{PMe}_3)\text{AgCl}$ was recovered in varying amounts as a soluble byproduct. Thus, loss of PMe_3 from the Ru coordination complex may be facilitated by formation of the stable silver-trimethylphosphine adduct.

The ^1H NMR spectrum of **2-5** in CD_2Cl_2 consists of three equal intensity doublets ($J_{\text{P-H}} = 9$ Hz) centered at 1.45, 1.41, and 1.32 ppm, corresponding to the protons of the

PMe₃ ligands. This suggests a slight magnetic inequality of the four PMe₃ groups in the Ru₂(ox) plane of the molecule. The ³¹P NMR spectrum is consistent with the solid state molecular structure. A doublet centered at 25.5 ppm (*J*_{P-P} = 38.9 Hz) corresponds to the four coordinated PMe₃ ligands in the Ru₂(ox) plane, while a triplet appears at 22.8 ppm (*J*_{P-P} = 40.0 Hz), corresponding to the two PMe₃ groups *trans* to the chloride ligands. The infrared spectrum of **2-5** shows a strong absorption at 1612 cm⁻¹, indicative of the asymmetric CO stretch of the oxalate ligand. The symmetric stretch is apparent at 1414 cm⁻¹ as a band of medium intensity.

Under similar reaction conditions for the preparation of **2-5**, but with the use of triethylphosphite as the P-containing ligand, complex **2-6** was isolated as pale yellow crystals from toluene at -30 °C (Scheme 2.2). The X-ray crystal structure of **2-6** is shown in Figure 2.6. Selected bond lengths and angles as well as additional crystallographic data are presented in Tables 2.6 and 2.3, respectively. Complex **2-6** crystallizes in the triclinic space group *P* $\bar{1}$ with one molecule in the unit cell. Two ruthenium ions are bridged by an oxalate ligand, and are each further coordinated by three triethylphosphite ligands as well as a chloride ion. Interestingly, the arrangement of the phosphorus-containing ligands around the Ru two centers in complex **2-6** is different from that observed in **2-5**. This *meridonal* arrangement of P(OEt)₃ ligands in complex **2-6** places the chloride ion in the Ru₂(ox) plane, *trans* to the oxalate ligand. The Ru-Cl bond distance is ca. 0.1 Å shorter in complex **2-6** than complex **2-5**, a result of the weaker *trans* directing effect of the oxalate ligand compared to PMe₃ (Ru(1)-Cl(1) = 2.491(3) Å for **2-5**; Ru(1)-Cl(1) = 2.4037(9) Å for **2-6**). The average Ru-P bond length of the two mutually *trans* P(OEt)₃ ligands (av. 2.335(9) Å) is ca. 0.1 Å longer than the Ru-P distance of the P(OEt)₃ ligand *trans* to the oxalate functionality (2.2072(9) Å).

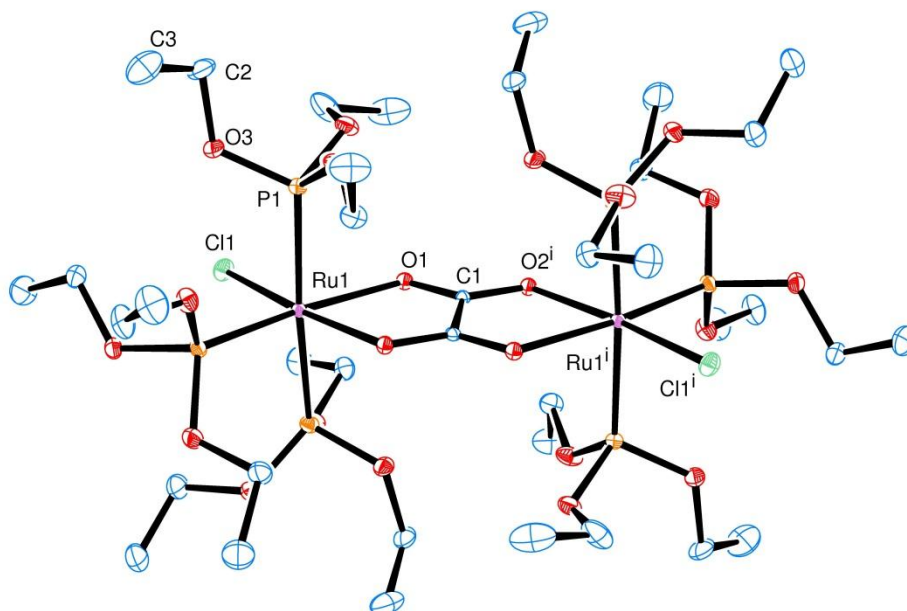


Figure 2.6 ORTEP diagram and partial atom numbering scheme of $\text{Cl}_2\text{Ru}_2(\mu\text{-ox})(\text{P}(\text{OEt})_3)_6$ (**2-6**). Thermal ellipsoids are drawn at the 30% probability level. Hydrogen atoms have been omitted for clarity.

An illustration of the key differences in the coordination geometries of complexes **2-5** and **2-6** is shown in Figure 2.7. Interestingly, the bridging oxalate ligand is slightly angled with respect to the two Ru centers in complex **2-5** ($\text{Ru-centroid}_{\text{O-O-centroid}_{\text{C-C}}} = 165.81(9)^\circ$), while the $\text{Ru}_2(\text{ox})$ coordination geometry is almost perfectly planar in **2-6** ($\text{Ru-centroid}_{\text{O-O-centroid}_{\text{C-C}}} = 177.88(9)^\circ$). This is likely a result of the different steric requirements of $\text{P}(\text{OEt})_3$ as compared to the slightly more bulky PMe_3 ligand (cone angle of 109° for $\text{P}(\text{OEt})_3$ vs. 118° for PMe_3).

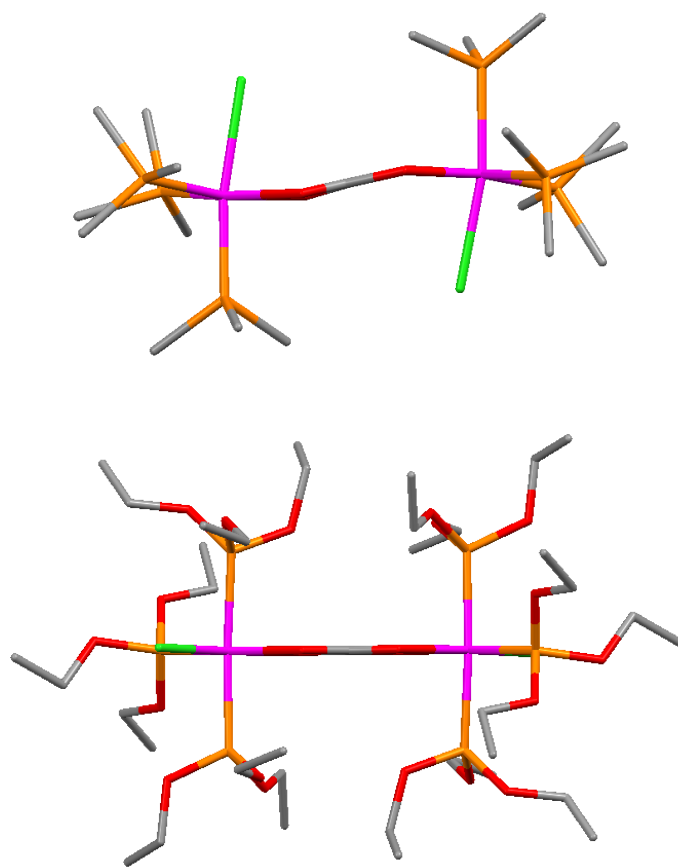


Figure 2.7 Capped stick view of complex **2-5** (top) and **2-6** (bottom) along the C-C bonding axis of the bridging oxalate ligand. Ruthenium (pink), phosphorus (orange), oxygen (red), carbon (gray), chlorine (green) are shown with hydrogen atoms omitted for clarity.

The ^1H NMR spectrum of **2-6** in C_6D_6 shows two regions of multiplets centered at 0.76 ppm and 3.62 ppm in a 3:2 ratio, corresponding to the methyl and methylene protons of each $\text{P}(\text{OEt})_3$ ligand. The $^{31}\text{P}\{^1\text{H}\}$ NMR spectrum shows a well resolved doublet at 145.8 ppm ($J_{\text{P-P}} = 19$ Hz) and a triplet centered at 148.3 ppm ($J_{\text{P-P}} = 42$ Hz), reflecting the two distinct magnetic environments of the triethylphosphite ligands. The infrared

spectrum of **2-6** shows sharp bands at 1669 cm^{-1} and 1419 cm^{-1} , which correspond to the asymmetric and symmetric CO stretch of the bridging oxalate ligand, respectively.

The dinuclear complexes **2-5** and **2-6** show limited volatility, each decomposing before subliming under vacuum (sealed ampoule, 10^{-2} Torr). Replacement of the coordinated chloride ions by ligands more appropriate for CVD applications may enhance the volatility of the complexes. Additionally, utilization of bidentate phosphine ligands such as dimethylphosphino ethane (dmpe) or dimethylphosphino methane (dmpm) may help facilitate formation of a monomeric metal-oxalate complex by avoiding the loss of a monodentate phosphine (or phosphite) group.

CVD of Ru(P, O) thin films

Thin films of Ru were grown from complexes **2-1**, **2-2**, and **2-3** at various temperatures in a horizontal hot-wall CVD reactor with ultra-high purity argon or hydrogen as the carrier gas. In a typical deposition, a saturator tube was charged with approximately 10-20 mg of sample and the gas flow rate was varied to allow for optimal film growth. Each precursor was heated to a temperature deemed adequate to sufficiently volatilize the complex, while the deposition chamber was maintained at the lowest temperature in which deposition occurred. Sublimation and deposition temperature were found to increase with precursor molecular weight. A summary of deposition conditions and film composition is presented in Table 2.1.

Precursor	R	Carrier Gas	Precursor	Deposition	Pressure	Film Composition (at. %)			
		Flow (sccm)	Temp. (°C)	Temp. (°C)	(Torr)	Ru	P	O	C
2-1	Me	Ar (10)	85	350	1.0	40	37	18	< 5
2-1	Me	H ₂ (13)	85	350	1.2	23	27	48	< 2
2-2	Et	Ar (10)	110	400	1.0	51	31	16	< 2
2-2	Et	H ₂ (10)	110	400	1.0	41	25	32	< 2
2-3	ⁱ Pr	H ₂ (10)	120	420	1.0	34	21	42	< 3

Table 2.1 Summary of deposition conditions and film composition for Ru films. Film composition was determined by XPS.

All deposited films appeared lustrous with a silver or golden hue and adhered well to the substrate (Si(100) with native oxide) as determined by the Scotch tape test. As shown in Figure 2.8 for a typical film grown from **2-1**, scanning electron microscopy (SEM) revealed relatively smooth surfaces of uniform thickness (50 – 100 nm) and a lack of large crystalline grains. X-ray reflectivity measurements of selected films corroborate this range for film thickness. All as-deposited films were amorphous in nature, as indicated by the lack of diffraction peaks present in the *ex situ* X-ray diffraction patterns taken immediately after film growth (Figure 2.9).

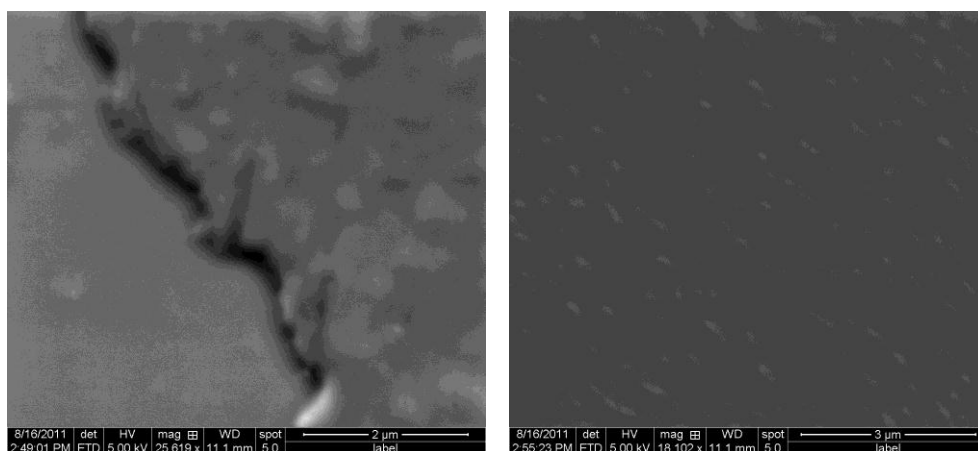


Figure 2.8 SEM images of a typical film grown from **2-1** under H_2 .

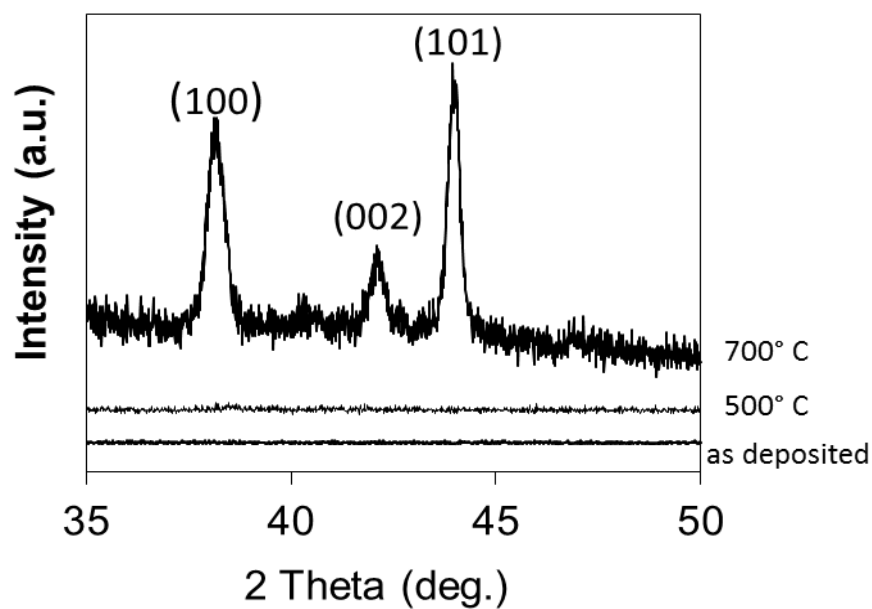


Figure 2.9 XRD patterns of a typical Ru film deposited from **2-1** under Ar and then annealed at various temperatures under dynamic vacuum. The patterns are vertically shifted for comparison.

Compositional analysis of each film was performed by *ex-situ* X-ray photoelectron spectroscopy (XPS). Figure 2.10 shows an XPS survey scan (top) and high resolution spectral regions (bottom) for a typical film grown from $\text{H}_2\text{Ru}(\text{P}(\text{OEt})_3)_4$ (**2-2**) at 400 °C under H_2 . Peaks corresponding to Ru, P, O, and C were present in all films, with no traces of Cl impurities from the precursor synthesis. After brief (30 sec.) sputtering with Ar^+ to remove adventitious surface C and O contamination present from exposure to atmosphere, the nature of the chemical states of the elements of interest were probed in more detail from high resolution data. Peaks with binding energies (BE) of 280.1 eV and 284.3 eV were observed for all films and correspond to the 3*d* doublet for elemental Ru.^{21a} These peaks were found to be slightly asymmetric for all films, with lower intensity shoulders appearing at higher BE for both peaks of the doublet. The shoulders are centered at BE 280.8 eV and 284.9 eV, which is within range of the literature value^{21b} for the binding energy of the Ru 3*d* doublet in RuO_2 ($3d_{5/2} = 280.7 - 281.0$ eV; $3d_{3/2} = 284.9 - 285.2$ eV). This indicates that the films contain ruthenium in two distinct chemical environments; i.e. zero valent Ru comprising the majority of the films as well as small contributions from oxidized Ru (possibly from RuO_2 , $\text{Ru}(\text{PO}_4)_3$, etc.).

Oxygen was present in varying amounts for all films, likely a result of ligand decomposition. At least two distinct chemical environments for O could be reasonably modeled with peak fitting, with broad peaks appearing at BE 532.8 eV and 531.4 eV. The chemical state of P was found to be similar to that observed in $\text{Ru}(\text{P})$ films deposited from *cis*- $\text{H}_2\text{Ru}(\text{PMe}_3)_4$ previously.⁸ Three phosphorus peaks were present in two distinct regions, with a well resolved doublet at lower BE corresponding to elemental phosphorus ($2p_{1/2} = 130.6$ eV; $2p_{3/2} = 129.7$ eV) as well as a broad, lower intensity peak centered at 133.4 eV corresponding to oxidized phosphorus. No maxima were observed at BE lower than 129.7 eV, indicating a lack of phosphidic phosphorus (P^{3-}) in the as-deposited film.

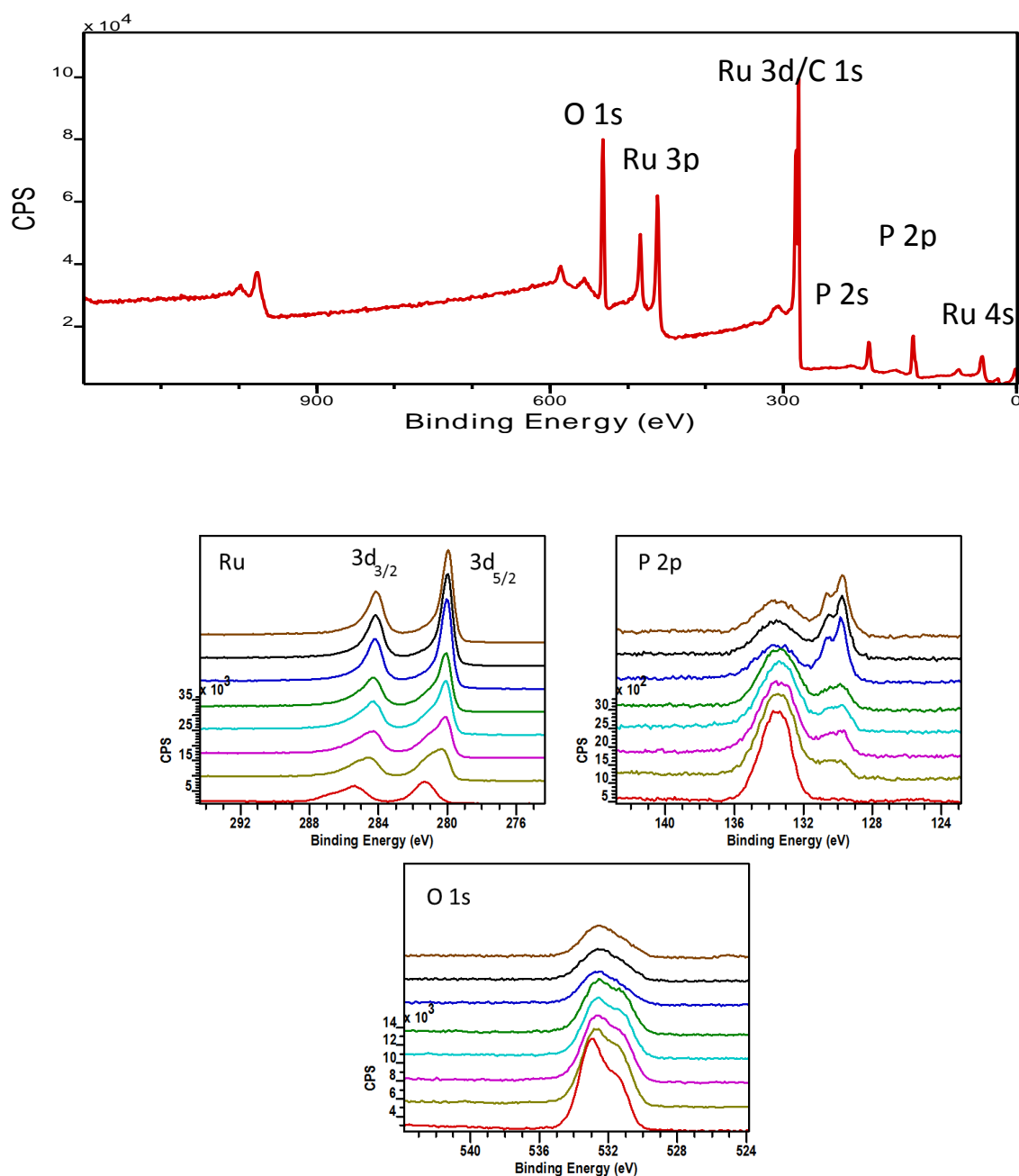


Figure 2.10 XPS survey scan (top) of a typical film deposited from 2-2 at 400 °C under H₂. High resolution scans (bottom) for Ru, P, and O obtained from depth profiling. The bottom red scans correspond to the film surface, with sputtering ascending in 1 minute increments.

The carbon content was found to be low for all films despite relatively high P and O content. It should be noted that the C 1s primary photoelectron peak at 384.5 eV directly overlaps with the Ru $3d_{3/2}$ peak located at 284.3 eV, thus making direct measurement of C content virtually impossible. The Ru $3d_{5/2}$ peak, however, does not overlap with the C signal. Therefore carbon content was estimated by constraining the peak area of the Lorentzian-Gaussian curves used to fit the experimental Ru $3d$ doublet to a 3:2 ratio, which corresponds to the theoretical value for peak height due to spin-orbit interactions of d -electrons. Assuming that the Ru $3d_{5/2}$ signal is due only to Ru and that the C 1s peak only overlaps the Ru $3d_{3/2}$ peak, the difference in area of the curve fitting data and experimental data corresponds to the atomic percentage of carbon. For all films, the C content was estimated to be below 5%.

XPS depth profiling revealed an uneven distribution of elements throughout the films. For all films, C and O content was greater near the film surface undoubtedly due to adventitious contamination resulting from exposure to the atmosphere. Gentle Ar⁺ sputtering drastically lowered the presence of these elements. Further sputtering was continued in 30 sec. intervals for up to 3 minutes to investigate the atomic composition throughout the films. Oxygen content was observed to decrease while Ru and P content generally increased throughout the thickness of the films. Depth profiles also clearly display key differences in composition of the films due to differing deposition conditions as well as post-deposition thermal treatment. For example, the two depth profiles shown in Figure 2.11 illustrate the difference in composition in two films grown from the same precursor (**2-1**) but under different deposition conditions (Ar carrier gas vs. H₂). Contrary to our hypothesis that use of H₂ as a reactive carrier gas would reduce C and O impurities, films grown under H₂ generally showed lower Ru content than films grown with the same precursor and at the same temperature with Ar as a carrier gas. This is

interesting because it is essentially opposite to the effect observed for the Rh pyrazolate precursors which will be described in Chapter 3. A hydrogen saturated atmosphere may hinder reductive elimination of H₂ from the metal-hydride precursors, thus preventing the initial formation of an open coordination site for the metal to adsorb to the surface of the substrate. Difficulty in producing pure films of Ru with H₂ as a carrier gas has been observed with β -diketonato and β -ketoiminato precursors.²²

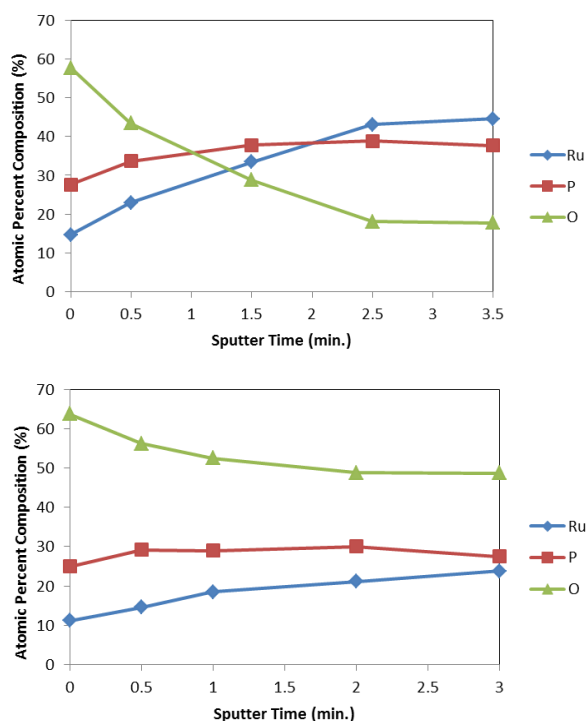


Figure 2.11 XPS depth profiles of films deposited from **2-1** under Ar (top) and under H₂ (bottom).

Post-growth annealing experiments

The morphology as well as composition of the deposited films were found to vary depending on specific annealing conditions. The films remained amorphous upon heating to 500 °C for 3 hr. and then began to crystallize upon further heating to 700 °C. Films annealed under dynamic vacuum showed peaks at $2\theta = 38.6, 42.4,$ and 44.2° , associated with the (100), (002), and (101) diffraction planes of hcp Ru, respectively, indicating a microcrystalline morphology (Figure 2.9). Crystallite size was estimated to be between 50 and 75 nm from the Scherrer equation²⁰ using the two most intense reflections. It should be noted that film strain as well as instrumental effects may also influence XRD peak broadening and is not accounted for using this equation, and thus the numbers presented represent a lower estimate of crystallite size. No diffraction peaks corresponding to crystalline phases of RuO₂ were detected for any film. Interestingly, thermal treatment of the films under flowing H₂ resulted in a change in film composition along with an increase in particle size. A typical X-ray diffraction pattern of a film grown from **2-3** under H₂, and then annealed at 700 °C under flowing H₂ is presented in Figure 2.12, and shows intense peaks corresponding to diffraction planes of polycrystalline RuP (PDF # 01-074-6494). The formation of binary RuP under reducing conditions may be a result of reaction of surface oxide with H₂ to form water. The ability to control film composition as well as morphology by varying the thermal treatment conditions has potential for formation of a variety of binary phases of ruthenium phosphide – the chemical and electrical properties of which remain largely unexplored.

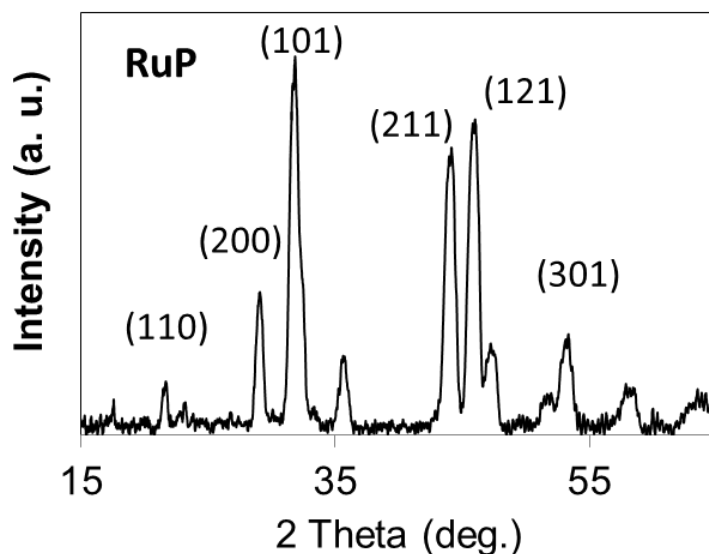


Figure 2.12 XRD pattern of a typical Ru film deposited from **2-3** under H_2 , followed by annealing under flowing H_2 at 700 °C.

XPS depth profiling was used to compare the composition of pre- and post-annealed films. Figure 2.13 shows depth profiles of a film deposited from **2-3** with hydrogen as a carrier gas without annealing (top) and after annealing under flowing H_2 at 700 °C (bottom). The oxygen content throughout the thickness of the annealed film is substantially reduced after 3 minutes of Ar^+ sputtering, while the Ru:P ratio remains approximately constant at c.a. 1.8:1. Changes in the chemical states of the elements due to the formation of RuP upon annealing were monitored by peak positions in the XPS spectra. A shift of 0.4 eV towards lower BE was observed for the P 2*p* doublet, indicating the formation of phosphidic P^{3-} , while the broad peak centered at 133 eV corresponding to oxidized phosphorus is not present in the annealed films. This is consistent with the drastic reduction in oxygen content in the H_2 annealed films. Interestingly, no apparent BE shift of the Ru 3*d* peak from Ru(0) to Ru (III) was observed upon annealing, though it should be noted that such a shift associated with formation of RuP may be small.

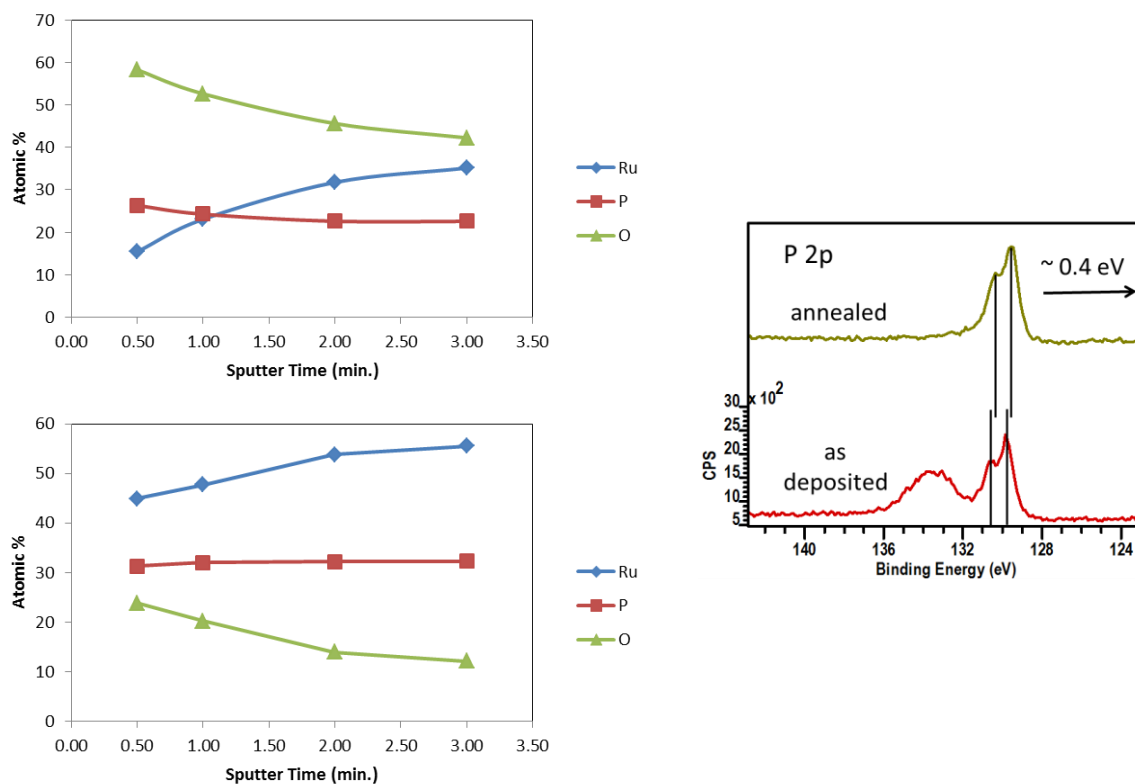


Figure 2.13 XPS depth profiles (left) of films deposited from **2-3** under H_2 . The top scan shows compositional analysis of an as-deposited amorphous film, while the bottom scan is from a film annealed at 700 °C in flowing H_2 . The HR-XPS spectrum (right) illustrates the shift in BE of the P 2p peak upon formation of RuP, and the disappearance of the broad peak corresponding to oxidized phosphorus that occurs upon annealing in H_2 .

The films annealed under vacuum showed no visible change in morphology upon heating, while films annealed under flowing H_2 exhibited broad cracking features over the length of the film, as shown in Figure 2.14. This was accompanied by a darkening and loss of luster upon formation of crystalline RuP. Elemental mapping through energy dispersive X-ray spectroscopy (EDX) of the cracked films revealed an uneven distribution of Ru, P, O and Si across the surface of the films. As shown in Figure 2.15, ruthenium and phosphorus are concentrated primarily within the deposited film, while silicon and oxygen signals arise mostly from the interstitial space between portions of the deposited film corresponding to the Si/SiO₂ substrate onto which the film was deposited. This anisotropic surface distribution of elements suggests that the Si and O content within the film is overestimated as determined by XPS, which has a rather large spot size of approximately 300 x 700 μm .

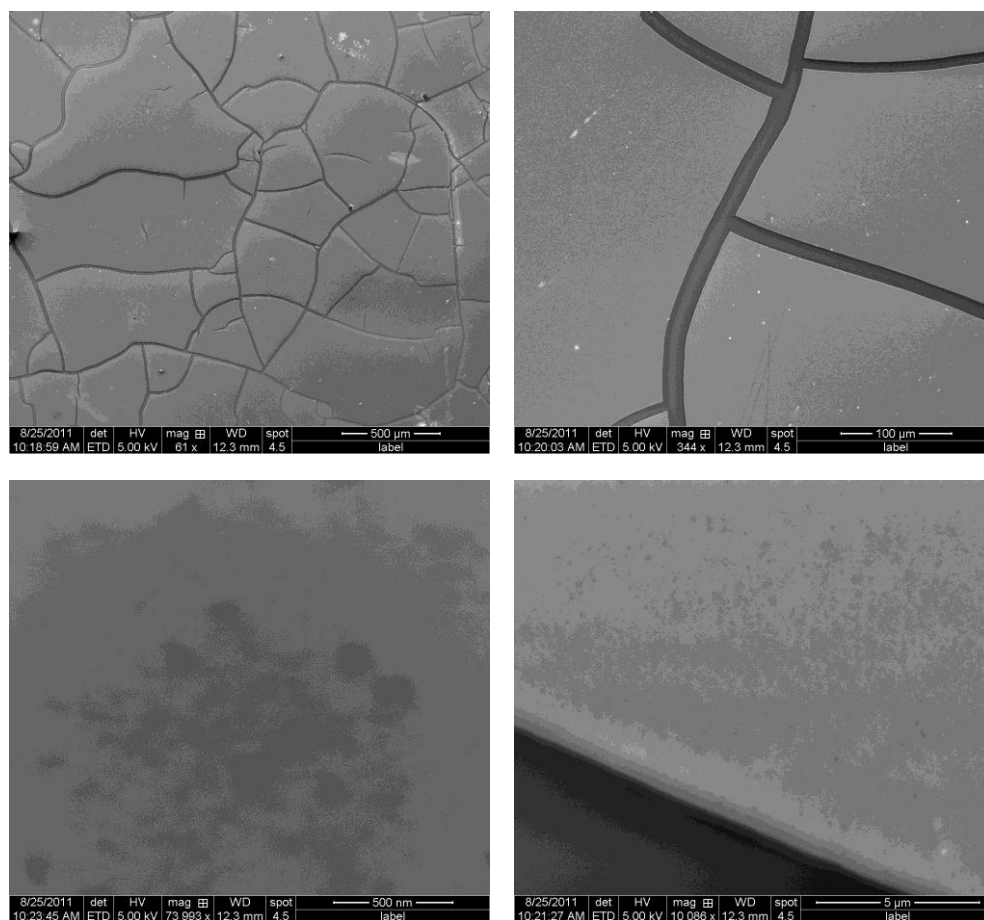


Figure 2.14 SEM images of a typical film grown from 2-3 annealed under flowing H₂.

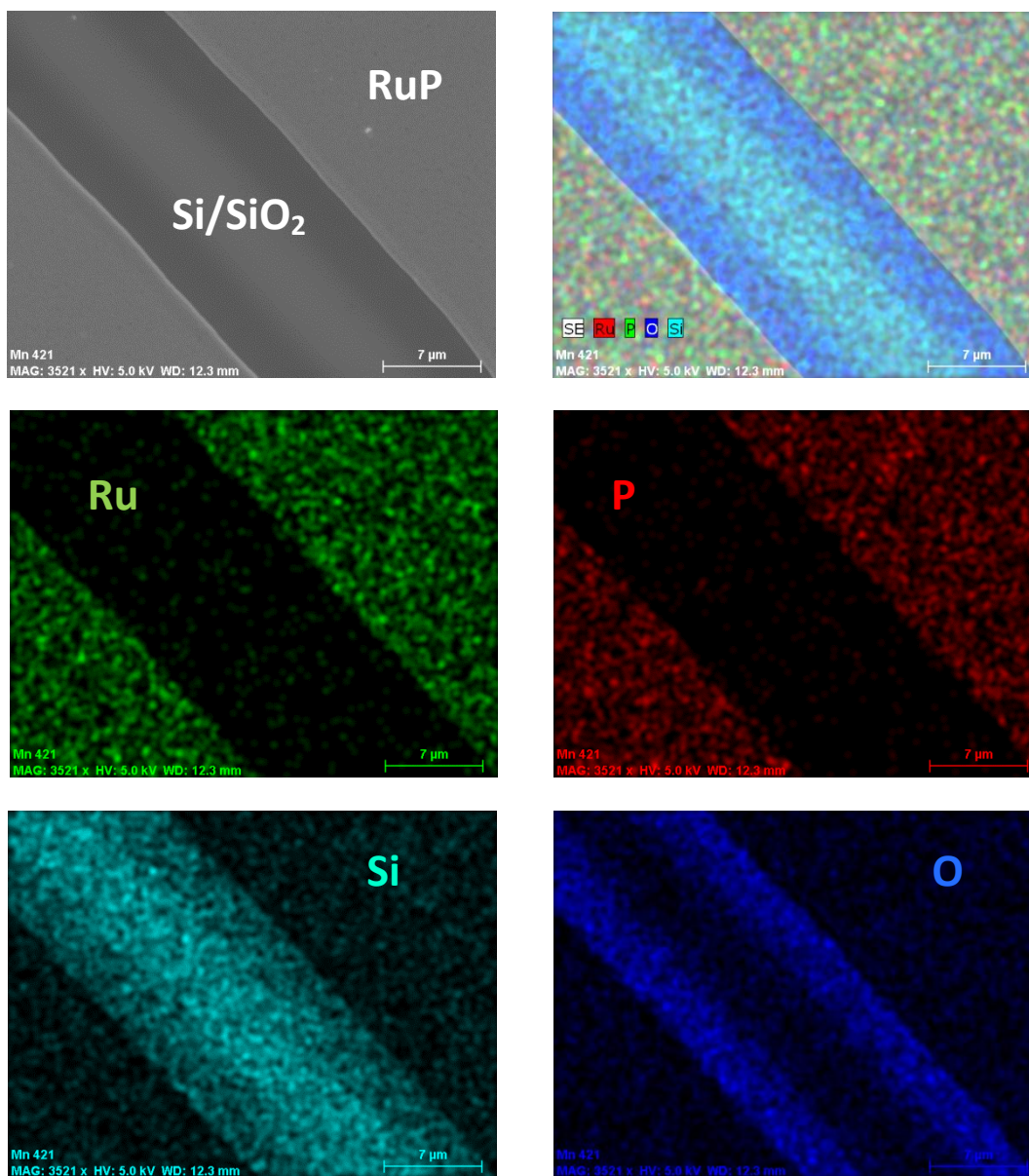


Figure 2.15 EDX Quantitative Element Mapping of a typical film of Ru(P,O) annealed under flowing H₂ to give polycrystalline RuP, showing the relative locations of the Ru, P, Si and O within the film. Ru and P are more concentrated in the thin film, while Si and O contributions primarily arise from the silicon substrate.

CONCLUSIONS AND FUTURE STUDIES

It has been demonstrated that a series of ruthenium phosphite hydride complexes are suitable for use as CVD precursors for deposition of films of amorphous ruthenium-phosphorus alloys. In all cases, the as-deposited films were X-ray amorphous and contained Ru and P in the zero oxidation state. XPS analysis revealed the presence of small amounts of oxidized ruthenium and phosphorus in the films as well. The composition of the films was found to depend on ligand chemistry as well as deposition conditions. Films grown from $\text{H}_2\text{Ru}(\text{P}(\text{OEt})_3)_4$ (**2-2**) generally showed higher Ru content, and, surprisingly, the use of H_2 as a reactive carrier gas had the effect of increasing the relative concentration of P and O for all films. Further film growth studies are needed to optimize deposition conditions with these complexes, as well as elucidate the effects of morphology and composition on conductive properties of the resultant films. The diffusion barrier capabilities of the Ru(P) films are of importance in Cu interconnect applications and thus should be further investigated. Additionally, detailed mechanistic studies would be helpful in understanding the chemical process by which both the Ru and P attain a zero valent state upon deposition. Ruthenium oxalate complexes were also studied as CVD precursor candidates, and their isolation and characterization has helped to develop the chemistry of the Ru-oxalate system in general and this work may be of use in further attempts to obtain viable CVD precursors.

EXPERIMENTAL DETAILS

General synthesis

Unless otherwise noted, all reactions were performed under a dry, oxygen-free nitrogen atmosphere or under vacuum using standard Schlenk line and dry box techniques. All solvents were dried prior to use by distillation from molten sodium or sodium benzophenone ketyl under nitrogen. $\text{Ag}_2(\text{ox})$,¹³ $\text{Cl}_2\text{Ru}(\text{PMe}_3)_4$ ^{16c} and $\text{Cl}_2\text{Ru}(\text{P}(\text{OEt})_3)_4$ ^{16b} were prepared according to literature procedures. Trimethylphosphite, triethylphosphite and tri(isopropyl)phosphite were purchased and used without further purification. Microanalyses (C,H,N) were performed by Galbraith Laboratories of Knoxville, TN or QTI Labs of Whitehouse, NJ. Melting points were determined in sealed capillaries under N_2 (1 atm.) on an Electrothermal Melting Point apparatus and are uncorrected. ESI mass spectra were collected on a Finnigan MAT TSQ 700 mass spectrometer. NMR spectra were recorded on a Varian 300 Unity Plus spectrometer (300 MHz at 298 K). Chemical shifts are referenced to the deuterated solvent. Infrared spectra were taken on a Nicolet IR 200 FTIR spectrometer between KBr plates.

Thin film deposition studies

Films were grown in a horizontal, hot-wall CVD reactor consisting of a 2" diameter Pyrex tube heated by a tube furnace. The precursor was heated in a saturator tube connected to the deposition assembly by VCR and Swagelok connections. Ultra high purity (99.999%) hydrogen or argon was used as the carrier gas at flow rates of 5-50 sccm controlled by a Fathom Technologies mass flow controller, with the overall pressure of the system maintained between 0.5 and 2 Torr. The temperature of the precursor was controlled by an oil bath, while the lines were heated separately with

insulated heating tape. Films were grown on Si(100) wafers with native oxide cut into approximately 1 cm × 1 cm squares. The wafers were prepared by sequentially sonicating in hexane, isopropanol, and DI water, and then drying at 120 °C for 1 hour. XPS measurements were carried out on a Kratos AXIS Ultra DLD (monochromatic Al K α), and depth profiling was achieved by sputtering the film with 4 kV Ar⁺. X-ray diffraction patterns were collected on a Bruker Nonius D8 ADVANCE diffractometer. Film thicknesses were determined using cross-sectional SEM (Hitachi S-5500 and FEI Quanta 650).

Single crystal X-ray crystallography

All crystals were covered in mineral oil and mounted on a nylon thread loop. Crystallographic data were collected on either a Nonius Kappa CCD diffractometer using a graphite monochromator with MoK α radiation ($\lambda = 0.71073 \text{ \AA}$) at reduced temperature using an Oxford Cryostream low temperature device or a Rigaku AFC12 diffractometer with a Saturn 724+ CCD using a graphite monochromator with MoK α radiation at reduced temperature using a Rigaku XStream low temperature device. Data reduction was performed with either DENZO-SMN or Rigaku Americas Corporation's Crystal Clear version 1.40. All structures were solved by direct methods using SIR2004 and refined by full-matrix least squares on F^2 with anisotropic displacement parameters for the non-H atoms using SHELXL-97. Hydrogen atoms on carbon were calculated in idealized positions with isotropic displacement parameters set to $1.2 \times U_{eq}$ of the attached atom ($1.5 \times U_{eq}$ for methyl hydrogen atoms). The function $\sum w(|F_o|^2 - |F_c|^2)^2$, was minimized, where $w = 1/[(\sigma(F_o))^2 + (0.0528*P)^2 + (0.685*P)]$ and $P = (|F_o|^2 + 2|F_c|^2)/3$. Neutral atom scattering factors and values used to calculate the linear absorption

coefficient are from the International Tables for X-ray Crystallography. All figures were generated using SHELXTL/PC.

Syntheses of *cis*-H₂Ru(P(OR)₃)₄; R = Me (2-1), Et (2-2), ⁱPr (2-3)

The three phosphite hydride complexes **2-1**, **2-2**, and **2-3** were prepared using a modified literature procedure.¹⁶ In a typical synthesis, a mixture of RuCl₃ • nH₂O (2.6 g, 0.01 mol) and P(OR)₃ (25 mL, excess) was stirred until the reaction subsided and the color turned red-brown. Sodium borohydride (2 g, 0.053 mol) was added and the mixture heated gently until the color turned off-white. Excess phosphite was then removed *in vacuo*. The residue was heated gently for 20 minutes in the presence of THF, ethanol, and NaBH₄ (3 g, 0.079 mol). The volatile products were removed under vacuum and the sticky residue was extracted into toluene (50 mL), and the mixture filtered. Evaporation of the filtrate led to off-white solid, which was purified by sublimation (10⁻² Torr) at temperatures between 120 – 160 °C for the three complexes. The recovered solids were then recrystallized from methanol (-30 °C) to yield large, colorless crystals. Yields typically ranged from 50 – 60 %.

Synthesis of *trans*-Cl₂Ru(P(OMe)₃)₄ (2-4)

This complex was prepared using a modified literature procedure.¹⁶ A mixture of RuCl₃ • nH₂O (0.26 g, 0.001 mol) and trimethylphosphite (2.5 mL, excess) was stirred for 15 min. The solution turned dark red and evolved heat. Addition of NaBH₄ (1.0 g, 0.026 mol) in THF (50 mL) initiated a color change from red to brown to green. This heterogeneous solution was stirred for 45 minutes and then the solvent and excess phosphite were removed *in vacuo*. The yellow green residue was extracted into

methylene chloride (100 mL) and then filtered. Solvent was removed *in vacuo* and the residue was extracted into hexane (100 mL) and then filtered. The yellow filtrate was cooled to -30 °C and the resulting yellow crystals were collected and dried *in vacuo*. Isolated: 0.45 g, 70 %.

Synthesis of $\text{Cl}_2\text{Ru}_2(\mu\text{-}\eta^4\text{-C}_2\text{O}_4)(\text{PMe}_3)_6$ (**2-5**)

To a suspension of silver oxalate (0.09 g, 0.3 mmol) in toluene (25 mL) was added $\text{Cl}_2\text{Ru}(\text{PMe}_3)_4$ (0.149 g, 0.3 mmol) dissolved in toluene (50 mL). The flask was wrapped in foil and brought to reflux under N_2 for 3 hours. During this time, the color of the reaction mixture became much paler yellow and a white/gray precipitate formed. The mixture was cooled to room temperature and filtered. The solvent was removed *in vacuo*, and the pale yellow residue was consecutively extracted into methylene chloride (100 mL) and THF (100 mL) and filtered through a short bed of Celite (2 cm). The volume of the THF extract was reduced to c.a. 10 mL and the flask cooled to -30 °C to give large colorless crystals of **2-5**. Isolated: 0.05 g, 41 %; mp 126-130 °C (dec.); ^1H -NMR (300 MHz, δ , CD_2Cl_2): 1.45 (d, $J_{\text{P-H}} = 9.8$ Hz, 18 H), 1.41 (d, $J_{\text{P-H}} = 8.2$ Hz, 18 H), 1.32 (d, $J_{\text{P-H}} = 9.0$ Hz, 18 H); $^{31}\text{P}\{^1\text{H}\}$ -NMR (CDCl_3): δ 25.5 (d, $J_{\text{P-P}} = 38.9$ Hz), 22.8 (t, $J_{\text{P-P}} = 40.0$ Hz); FT-IR (KBr, cm^{-1}): 2963 (s), 2908 (s), 1938 (w), 1612 (s), 1414 (m), 1260 (s), 1093 (br, s), 1019 (br, s), 943 (m), 787 (s), 668 (w). Calcd. for $\text{C}_{20}\text{H}_{54}\text{Cl}_2\text{O}_4\text{P}_6\text{Ru}_2$: C, 29.38; H, 6.66 %. Found: C, 26.53; H, 6.58 %.

Synthesis of $\text{Cl}_2\text{Ru}_2(\mu\text{-}\eta^4\text{-C}_2\text{O}_4)(\text{P}(\text{OEt})_3)_4$ (**2-6**)

To a suspension of silver oxalate (0.118 g, 0.14 mmol) in toluene (25 mL) was added $\text{Cl}_2\text{Ru}(\text{P}(\text{OEt})_3)_4$ (0.043 g, 0.14 mmol) dissolved in toluene (50 mL). The flask was

wrapped in foil and brought to reflux under N₂ for 3 hours. The yellow heterogeneous solution was cooled to room temperature and filtered. The solvent was removed *in vacuo*, and the residue was consecutively extracted into methylene chloride (100 mL) and THF (100 mL) and filtered through a short bed of Celite (2 cm). The volume of the THF extract was reduced to c.a. 10 mL and the flask cooled to -30 °C to give light yellow crystals of **2-6**. Isolated: 0.032 g, 34 %; mp 156-170 °C (slow dec.); ¹H-NMR (300 MHz, δ, C₆D₆): 3.62 (m, 36 H), 0.75 (m, 54 H); ³¹P{¹H}-NMR (C₆D₆): δ 148.4 (t, *J*_{P-P} = 42.0 Hz), 145.7 (d, *J*_{P-P} = 19.1 Hz); FT-IR (KBr, cm⁻¹): 2982 (m), 2915 (m), 1977 (w), 1669 (m), 1521 (w), 1499 (w), 1259 (vs), 1210 (s), 1119 (s), 1003 (m), 949 (vs), 858 (w), 754(m). Calcd. for C₃₈H₉₀Cl₂O₂₂P₆Ru₂: C, 33.56; H, 6.82 %. Found: C, 33.67; H, 7.19 %.

X-RAY CRYSTALLOGRAPHIC DETAILS

Table 2.2 Crystallographic details and refinement data for **2-1**, **2-2** and **2-4**.

	2-1	2-2	2-4
Empirical formula	C ₁₂ H ₃₈ O ₁₂ P ₄ Ru	C ₂₄ H ₆₂ O ₁₂ P ₄ Ru	C ₄₈ H ₁₄₄ Cl ₈ O ₄₈ P ₁₆ Ru ₄
Formula weight	599.37	767.69	2673.03
Temperature	153(2) K	153(2) K	100(2) K
Wavelength	0.71073 Å	0.71073 Å	0.71073 Å
Crystal system	triclinic	triclinic	monoclinic
Space group	<i>P</i> 1	<i>P</i> $\bar{1}$	<i>P</i> 2 ₁ / <i>n</i>
Unit cell dimensions	a = 10.000(2) Å b = 19.007(4) Å c = 20.695(4) Å α = 78.84(3)° β = 87.29(3)° γ = 79.76(3)°	a = 11.465 Å b = 18.064 Å c = 18.784 Å α = 100.57° β = 99.47° γ = 96.97°	a = 18.165 Å b = 20.207 Å c = 28.696 Å α = 90° β = 90.20° γ = 90°
Volume	3797.4(13) Å ³	3725.7 Å ³	10533.1 Å ³
Z	6	4	4
Density (calculated)	1.573 Mg/m ³	1.369 Mg/m ³	1.686 Mg/m ³
Absorption coefficient	0.921 mm ⁻¹	0.643 mm ⁻¹	1.092 mm ⁻¹
F(000)	1860	1624	5472
Theta range for data collection	3.01 to 25.00°	1.12 to 25.00°	3.01 to 27.48°
Index ranges	-11 ≤ h ≤ 11, -20 ≤ k ≤ 22, -24 ≤ l ≤ 24	-13 ≤ h ≤ 13, -21 ≤ k ≤ 21, -21 ≤ l ≤ 22	-23 ≤ h ≤ 23, -26 ≤ k ≤ 26, -37 ≤ l ≤ 37
Reflections collected	22839	21319	193887
Independent reflections	22839 [R(int) = 0.0000]	12988 [R(int) = 0.0491]	24118 [R(int) = 0.0867]
Data / restraints / parameters	22839 / 1048 / 1567	12988 / 483 / 729	24118 / 0 / 1117
Goodness-of-fit on F ₂	1.008	1.525	0.836
Final R ^a indices [I > 2σ(I)]	R ₁ = 0.0785 wR ₂ = 0.2083	R ₁ = 0.1386 wR ₂ = 0.3739	R ₁ = 0.0526 wR ₂ = 0.1228
R ^a indices (all data)	R ₁ = 0.1097 wR ₂ = 0.2440	R ₁ = 0.1997 wR ₂ = 0.4233	R ₁ = 0.0704 wR ₂ = 0.1340
Largest diff. peak and hole	3.472 and -1.195 e.Å ⁻³	5.973 and -1.449 e.Å ⁻³	2.270 and -0.759 e.Å ⁻³

^a R₁ = $\sum_{\text{hkl}}(|F_o| - |F_c|) / \sum_{\text{hkl}} |F_o|$; wR₂ = $[\sum w(|F_o| - |F_c|)^2 / \sum w|F_o|^2]^{1/2}$

Table 2.3 Crystallographic details and refinement data for **2-5** and **2-6**.

	2-5	2-6
Empirical formula	C ₂₀ H ₅₄ Cl ₂ O ₄ P ₆ Ru ₂	C ₃₈ H ₉₀ Cl ₂ O ₂₂ P ₆ Ru ₂
Formula weight	817.49	1367.96
Temperature	153(2) K	153(2) K
Wavelength	0.71073 Å	0.71073 Å
Crystal system	triclinic	triclinic
Space group	<i>P</i> $\bar{1}$	<i>P</i> $\bar{1}$
Unit cell dimensions	a = 11.442 Å b = 11.786 Å c = 15.184 Å α = 69.48° β = 82.13° γ = 89.94°	a = 9.910 Å b = 12.421 Å c = 14.367 Å α = 103.12° β = 101.32° γ = 113.04°
Volume	1897.3 Å ³	1502.6 Å ³
Z	2	1
Density (calculated)	1.431 Mg/m ³	1.501 Mg/m ³
Absorption coefficient	1.211 mm ⁻¹	0.819 mm ⁻¹
F(000)	836	706
Theta range for data collection	3.09 to 27.36°	3.02 to 25.00°
Index ranges	-13 ≤ h ≤ 14, -15 ≤ k ≤ 14, -19 ≤ l ≤ 19	-11 ≤ h ≤ 11, -14 ≤ k ≤ 13, -16 ≤ l ≤ 17
Reflections collected	11913	8480
Independent reflections	8128 [R(int) = 0.0545]	5242 [R(int) = 0.0324]
Refinement method	Full-matrix least-squares on F ²	Full-matrix least-squares on F ²
Data / restraints / parameters	8128 / 204 / 307	5242 / 210 / 316
Goodness-of-fit on F ²	1.653	1.017
Final R ^a indices [I > 2σ(I)]	R ₁ = 0.1626 wR ₂ = 0.4051	R ₁ = 0.0390 wR ₂ = 0.0653
R ^a indices (all data)	R ₁ = 0.1869 wR ₂ = 0.4210	R ₁ = 0.0621 wR ₂ = 0.0723
Largest diff. peak and hole	17.817 and -2.974 e.Å ⁻³	0.605 and -0.448 e.Å ⁻³

^a R₁ = $\sum_{\text{hkl}} (|F_o| - |F_c|) / \sum_{\text{hkl}} |F_o|$; wR₂ = $[\sum w(|F_o| - |F_c|)^2 / \sum w|F_o|^2]^{1/2}$

Table 2.4 Selected bond lengths [Å] and angles [°] for **2-1**.

Ru(1)-P(2)	2.252(2)	P(2)-Ru(1)-P(5)	96.65(9)
Ru(1)-P(5)	2.278(3)	P(2)-Ru(1)-P(1)	154.75(9)
Ru(1)-P(1)	2.278(2)	P(5)-Ru(1)-P(1)	98.28(9)
Ru(1)-P(3)	2.288(3)	P(2)-Ru(1)-P(3)	101.79(9)
P(5)-O(1B)	1.442(3)	O(1B)-P(5)-O(5)	109.3(2)
P(5)-O(5)	1.625(6)	O(1B)-P(5)-O(2B)	86.69(13)
P(5)-O(2B)	1.681(3)	O(5)-P(5)-O(2B)	97.5(2)
O(11)-C(3)	1.425(9)	O(1B)-P(5)-Ru(1)	126.35(16)
C(11)-O(6)	1.419(10)	O(5)-P(5)-Ru(1)	112.1(2)
O(16)-C(3B)	1.402(6)	O(2B)-P(5)-Ru(1)	119.17(12)
		C(15)-O(12)-P(1)	123.9(5)
		C(3)-O(11)-P(2)	124.8(5)
		C(3B)-O(16)-P(1)	124.3(4)
		C(¹ H)-O(9)-P(3)	122.6(4)

Table 2.5 Selected bond lengths [Å] and angles [°] for **2-2**.

Ru(1)-P(3)	2.260(3)	P(3)-Ru(01)-P(4)	152.06(14)
Ru(1)-P(4)	2.261(3)	P(3)-Ru(01)-P(6)	96.25(13)
Ru(1)-P(6)	2.274(4)	P(4)-Ru(01)-P(6)	102.52(12)
Ru(1)-P(5)	2.274(4)	P(3)-Ru(01)-P(5)	101.17(13)
P(3)-O(23)	1.598(10)	O(20)-P(3)-O(23)	98.2(6)
P(3)-O(24)	1.617(12)	O(20)-P(3)-O(24)	103.5(6)
P(4)-O(13)	1.599(10)	O(23)-P(3)-O(24)	93.3(6)
O(11)-C(35)	1.404(15)	O(20)-P(3)-Ru(1)	114.3(4)
O(12)-C(66)	1.47(2)	O(23)-P(3)-Ru(1)	124.4(5)
O(13)-C(52)	1.420(16)	O(24)-P(3)-Ru(1)	118.9(5)
		C(35)-O(11)-P(4)	122.8(8)
		C(66)-O(12)-P(6)	121.4(10)
		C(52)-O(13)-P(4)	122.2(9)
		C(39)-O(14)-P(5)	121.6(8)

Table 2.6 Selected bond lengths [\AA] and angles [$^\circ$] for **2-4**.

C(1)-O(1)	1.448(6)	C(1)-O(1)-P(1)	120.9(4)
C(2)-O(2)	1.441(6)	C(2)-O(2)-P(1)	119.7(3)
C(3)-O(3)	1.403(7)	C(3)-O(3)-P(1)	122.7(4)
O(1)-P(1)	1.585(4)	O(1)-P(1)-O(3)	98.5(2)
O(2)-P(1)	1.597(4)	O(1)-P(1)-O(2)	103.0(2)
O(3)-P(1)	1.590(4)	O(3)-P(1)-O(2)	98.6(2)
P(1)-Ru(1)	2.3160(12)	O(1)-P(1)-Ru(1)	111.10(14)
P(2)-Ru(1)	2.3310(12)	O(3)-P(1)-Ru(1)	119.41(16)
P(3)-Ru(1)	2.3224(12)	O(2)-P(1)-Ru(1)	122.62(16)
P(4)-Ru(1)	2.3182(11)	P(1)-Ru(1)-P(4)	88.27(4)
Cl(1)-Ru(1)	2.4317(11)	P(1)-Ru(1)-P(3)	176.04(5)
Cl(2)-Ru(1)	2.4257(11)	P(1)-Ru(1)-P(2)	90.84(5)
		P(1)-Ru(1)-Cl(1)	91.77(4)
		P(1)-Ru(1)-Cl(2)	88.58(4)
		Cl(2)-Ru(1)-Cl(1)	179.58(4)

Table 2.7 Selected bond lengths [\AA] and angles [$^\circ$] for **2-5**.

C(11)-P(2)	1.827(13)	O(1)-C(1)-O(2)#1	124.7(10)
C(12)-P(4)	1.829(13)	O(1)-C(1)-C(1)#1	119.0(13)
C(13)-P(4)	1.848(12)	O(2)-C(1)-C(1)#2	115.6(13)
P(1)-Ru(1)	2.243(3)	O(2)#2-C(1)-C(1)#2	117.9(13)
P(2)-Ru(1)	2.253(3)	C(2)-P(1)-C(3)	101.7(6)
P(3)-Ru(1)	2.241(3)	C(2)-P(1)-C(1)	101.2(6)
C(1)-O(1)	1.228(15)	C(2)-P(1)-Ru(2)	111.5(5)
C(1)-O(1)#1	1.264(15)	C(1)-P(1)-Ru(2)	115.7(4)
C(1)-C(1)#1	1.57(2)	O(1)-Ru(1)-O(2)	77.7(3)
Ru(1)-O(1)	2.159(9)	O(1)-Ru(1)-P(2)	90.0(2)
Ru(1)-O(2)	2.183(8)	O(1)-Ru(1)-P(3)	167.5(2)
Ru(1)-Cl(1)	2.491(3)	O(2)-Ru(1)-P(3)	170.0(2)
		P(1)-Ru(1)-P(2)	96.29(11)
		P(1)-Ru(1)-P(3)	95.64(11)
		P(3)-Ru(1)-Cl(1)	94.81(11)
		P(2)-Ru(1)-Cl(1)	88.05(11)
		P(1)-Ru(1)-Cl(1)	167.88(12)

Symmetry transformations used to generate equivalent atoms:

#1 -x+1,-y,-z #2 -x+2,-y+1,-z

Table 2.8 Selected bond lengths [\AA] and angles [$^\circ$] for **2-6**.

Ru(1)-O(1)	2.121(2)	O(1)-Ru(1)-P(2)	96.07(6)
Ru(1)-P(2)	2.2072(9)	O(1)-Ru(1)-O(1)#1	76.83(8)
Ru(1)-O(1)	2.210(2)	P(3)-Ru(1)-O(1)	172.81(6)
Ru(1)-P(3)	2.3278(9)	O(1)-Ru(1)-P(1)	90.55(6)
Ru(1)#1-P(4)#1	2.3425(9)	P(2)-Ru(1)-P(3)	92.98(3)
Ru(1)-Cl(1)	2.4037(9)	O(1)-Ru(1)-P(2)	88.28(6)
P(1)-O(3)	1.590(3)	O(1)#1-Ru(1)-Cl(1)	170.58(6)
P(1)-O(4)	1.594(2)	P(2)-Ru(1)-Cl(1)	93.19(3)
P(1)-O(5)	1.599(2)	O(3)-P(1)-O(4)	105.79(14)
O(3)-C(2)	1.447(4)	O(4)-P(1)-O(5)	99.70(12)
O(4)-C(4)	1.440(4)	O(3)-P(1)-O(5)	97.01(13)
O(5)-C(6)	1.446(4)	O(1)-C(1)-O(1)#1	124.9(3)
C(2)-C(3)	1.462(6)	O(1)-C(1)-C(1)#1	117.4(4)
C(4)-C(5)	1.500(5)		
C(6)-C(7)	1.486(5)		

Symmetry transformations used to generate equivalent atoms: #1 -x+1,-y,-z

REFERENCES

1. (a) Pratt, A. "Overview of the use of Copper Interconnects in the Semiconductor Industry," Advanced Energy Briefing **2004**, http://www.advanced-energy.com/upload/File/White_Papers/SL-ELECTROPLATING-270-01.pdf (b) International Technology Roadmap for Semiconductors, 2008 Update, <http://public.itrs.net>
2. *CRC Handbook of Chemistry and Physics*, 92th ed.; CRC Press: Boca Raton, 2011-2012; pp. 12-41.
3. (a) Istratov, A. A.; Flink, C.; Hieslmair, H.; Weber, E. R. *Phys. Rev. Lett.* **1998**, *81*, 1243. (b) McBrayer, J. D.; Swanson, R. M.; Sigmon, T. W. *J. Electrochem. Soc.* **1986**, *133*, 1242. (c) Shacham-Diamand, Y.; Dedhia, A.; Hoffstetter, D.; Oldham, W. G. *J. Electrochem. Soc.* **1993**, *140*, 2427. (d) Lanckmans, F.; Maex, K. *Microelectron. Eng.* **2002**, *60*, 125.
4. (a) Han, C-H.; Cho, K-N.; Oh, J-E.; Paek, S-H.; Park, C-S; Lee, S-I; Lee, M. Y.; Lee, J. G. *Jap. J. Appl. Phys. Pt 1*, **1998**, *37*, 2646. (b) Lin, J.; Lee, C. *J. Electrochem. Soc.* **1999**, *146*, 3466.
5. Mudholkar, M.S.; Thompson, L.T. *J. Appl. Phys.* **1995**, *77*, 5138.
6. (a) Fix, R.; Gordon, R.G.; Hoffman, D.M. *Thin Solid Films* **1996**, *288*, 116. (b) Roberson, S.L.; Finello, D.; Davis, R.F. *Thin Solid Films* **1998**, *324*, 30.
7. Damayanti, M.; Sritharan, T.; Gan, Z. H.; Mhaisalkar, S. G.; Jiang, N.; Chan, L. *J. Electrochem. Soc.* **2006**, *153*, J41.
8. (a) Shin, J.; Waheed, A.; Agapiou, K.; Winkenwerder, W.A.; Kim, H.-W.; Jones, R.A.; Hwang, G.S.; Ekerdt, J.G. *J. Am. Chem. Soc.* **2006**, *128*, 16510. (b) Shin, J.-H.; Waheed, A.; Winkenwerder, W. A.; Kim, H.-W.; Agapiou, K.; Jones, R. A.; Hwang, G. S.; Ekerdt, J. G. *Thin Solid Films* **2007**, *515*, 5298. (c) Shin, J.; Kim, H.-W.; Agapiou, K.; Jones, R. A.; Hwang, G. S.; Ekerdt, J. G. *J. Vac.Sci. Technol. A* **2008**, *26*, 974.
9. Li, Y.-X.; Koper, O.; Atteya, M.; Klabunde, K.J. *Chem. Mater.* **1992**, *4*, 323.
10. (a) Mothes, R.; Rueffer, T.; Shen, Y.; Jakob, A.; Walfort, B.; Petzold, H.; Schulz, S. E.; Ecke, R.; Gessnerb, T.; Lang, H. *Dalton Trans.* **2010**, *39*, 11235. (b) Park, S; Choi, H. *Chem. Mater.* **2003**, *15*, 3121.
11. Choi, H; Park, S; Kim, T.H. *Chem. Mater.* **2003**, *15*, 3735.

12. (a) Itoh, M.; Kakuta, T.; Nagaoka, M.; Koyama, Y.; Sakamoto, M.; Kawasaki, S.; Umeda, N.; Kurihara, M. *J. Nanosci. Nanotechnol.* **2009**, *9*, 6655. (b) Navaladian, S.; Viswanathan, B.; Viswanath, R.; Varadarajan, T. *Nanoscale Res. Lett.* **2007**, *2*, 44.
13. Paonessa, R.S.; Prignano, A.L.; Troglor, W.C. *Organometallics* **1985**, *4*, 647.
14. Darensbourg, D.J.; Chojnacki, J.A.; Reibenspies, J.H. *Inorg. Chem.* **1992**, *31*, 3428.
15. Koehler, K.; Eichhorn, J.; Meyer, F.; Vidovic, D. *Organometallics* **2003**, *22*, 4426.
16. (a) Meakin, P.; Muetseries, E. L.; Jesson, J. P. *J. Am. Chem. Soc.* **1973**, *95*, 75. (b) Gerlach, D. H.; Peet, W. G.; Muettersies, E. L. *J. Am. Chem. Soc.* **1972**, *94*, 4545. (c) Jones, R. A.; Real, F. M.; Wilkinson, G.; Galas, A. M. R.; Hursthouse, M. B.; Malik, K. M. A. *J. Chem. Soc., Dalton Trans.* **1980**, 511.
17. (a) Frank, K.G.; Selegue, J.P. *Acta Cryst. C* **1991**, *C47*, 35. (b) Albertin, G.; Antoniutti, S.; Bordignon, E.; Pelizzi, G.; Vitali, F. *J. Organomet. Chem.* **1988**, *353*, 229. (c) Koyama, T.; Koide, Y.; Matsumoto, K. *Inorg. Chem.* **1999**, *38*, 3241.
18. Boldyrev, V.V. *Thermochim. Acta.* **2002**, *388*, 63.
19. Chan, H. Y. H.; Takoudis, C. G.; Weaver, M. J. *J. Catal.* **1997**, *172*, 336.
20. (a) Scherrer, P. *Zsigmondy's Kolloidchemie*, 3rd. ed.; Verlag: Berlin, 1920. (b) Warren, B. E. *X-Ray Diffraction*, Dover Publications: Mineola, 1990.
21. (a) Feldman, L.C.; Mayer, J.W. *Fundamentals of Surface and Thin Film Analysis*; North Holland: New York, 1986. (b) Chan, H.Y.H.; Takoudis, C.G.; Weaver, M.J. *J. Catal.* **1997**, *172*, 336.
22. (a) Sandhu, G.S. *Thin Solid Films* **1998**, *320*, 1. (b) Aoyama, T.; Kiyotoshi, M.; Yamazaki, S.; Eguchi, K. *Jpn. J. Appl. Phys.* **1999**, *38*, 2194. (c) Choi, E.-S.; Lee, J.-C.; Hwang, J.-S.; Park, J.B.; Yoon, S.-G. *J. Electrochem. Soc.* **1999**, *146*, 4189. (d) Matsui, Y.; Hiratani, M.; Nabatame, T.; Shimamoto, Y.; Kimura, S. *Electrochem. Solid St.* **2001**, *4*, C9.
23. Mazzetto, S. E.; Gambardella, M. T.; Santos, R. H. A.; Lopes, L. G. F. ; Franco, D. W. *Polyhedron* **1999**, *18*, 979.

Chapter 3: Synthesis, characterization and film growth studies of rhodium pyrazolate complexes

INTRODUCTION

Thin films of rhodium are used as reflective¹ and catalytic² coatings, as diffusion barriers and interconnect layers in microelectronic devices,³ and in chemical sensing applications.⁴ Typically the volatile organometallic precursors studied for the chemical vapor deposition (CVD) of rhodium films contain acetylacetonato,⁵ η^5 -cyclopentadienyl and allyl ligands,⁶ which have direct Rh-O or Rh-C bonds, and thus pose a possible source for film contamination by O or C. Also, the synthesis of precursors which feature multiple varieties of ligands to fill the coordination sphere of the metal tend to involve low-yield, multistep syntheses. Both of these issues are of concern for CVD coating applications where the goal is the production of low-cost, high-purity films.

The pyrazolate ligand exhibits a wide variety of coordination modes and there is a rich chemistry of the *d*-block transition metals which involve this ligand and its substituted analogs.⁷ There have been limited reports of the use of the 3,5-di-substituted pyrazolate moiety (Pz) as a promising ligand for volatile precursors for CVD of transition metal thin films.⁸ This class of ligand has advantages for use in CVD precursor applications for several reasons. First, bulky or perfluorinated substituents at the 3- and 5-positions of the ring serve to preclude hydrogen bonding interactions, thus increasing the volatility of metal complexes which incorporate the ligand. Additionally, most substituted pyrazoles display relatively high thermal stability, which should lead to low levels of impurities in the grown film. The use of a reactive carrier gas such as H₂ during film deposition may enhance the reductive elimination pathway of the metal coordinated pyrazolate ligand by reforming free pyrazole. Indeed it has been demonstrated that the use of hydrogen as carrier gas for Rh thin film CVD from organometallic precursors

produces films of higher purity.^{6a}

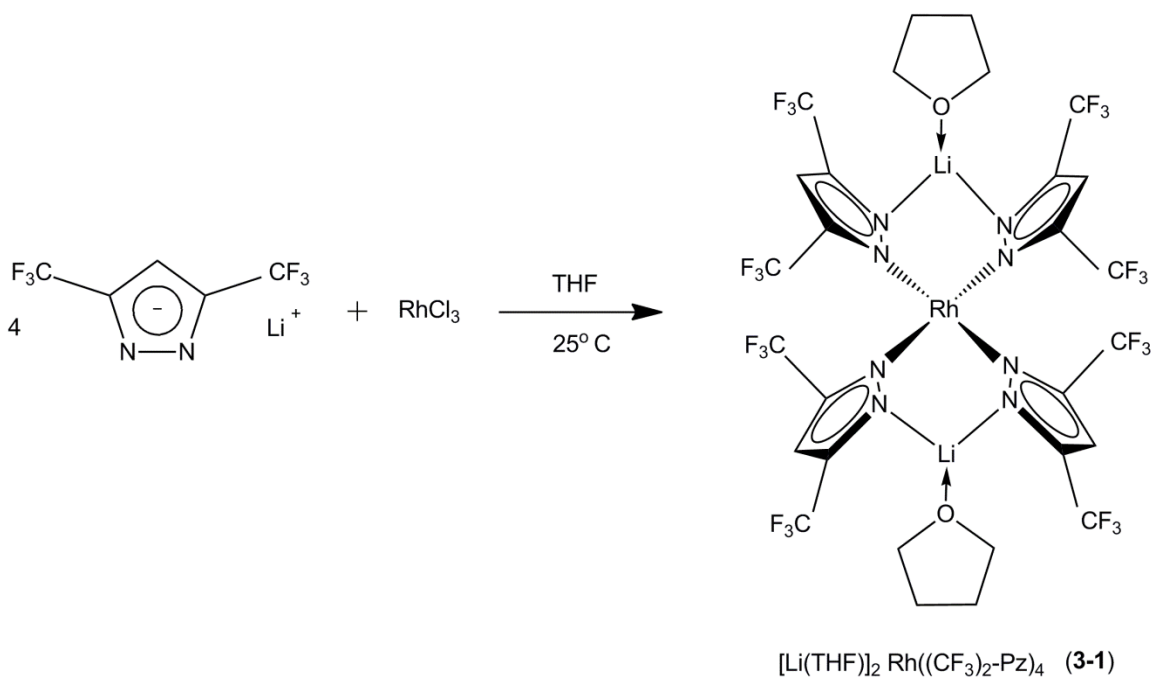
This chapter describes the synthesis and structural characterization of a series of Rh pyrazolate complexes, some of which were further evaluated as precursors for the CVD of Rh thin films. Several different pyrazolate moieties were investigated with varying functional groups substituted at the 3- and 5- positions in order to study the effect of steric and electronic properties of the ligands on precursor volatility and film composition. The general synthetic approach for the majority of the reactions described involved a salt exchange reaction of an anhydrous rhodium salt (acetate or chloride) with either the lithium or sodium salt of the pyrazole ligand. Coordination of pyrazole to Rh centers in a dative fashion through the N2 atom on the ring was also investigated. The rhodium pyrazolate complexes described herein present interesting possibilities for CVD applications due to their air and thermal stability, high-yielding synthesis, and high metal to ligand ratio. Finally, the results of the CVD of rhodium films from selected complexes are reported.

RESULTS AND DISCUSSION

Synthesis of a mononuclear Rh(II) complex

Despite the propensity to bridge multiple metal centers through both nitrogen atoms, coordination of pyrazolate molecules to a single metal center in a bidentate η^2 mode is common for alkaline earth metals, lanthanides and early transition metals.^{7b} This coordination mode is less common for electron rich metals of Group 8 and later, however, and there exist a limited number of examples.¹¹ It was hypothesized that the reaction of anhydrous RhCl_3 with four equivalents of 3,5-(CF_3)₂PzLi in THF would result

in a stable, six-coordinate 18-electron rhodium pyrazolate complex of the formula $\text{Rh}(\eta^2\text{-Pz})_3$. The product of the reaction, however, was air sensitive, paramagnetic $[\text{Li}(\text{THF})]_2 \text{Rh}(\mu\text{-3,5-(CF}_3)_2\text{Pz})_4$ (**3-1**) shown in Scheme 3.1.



Scheme 3.1 Synthesis of $[\text{Li}(\text{THF})]_2 \text{Rh}(\mu\text{-3,5-(CF}_3)_2\text{Pz})_4$ (**3-1**).

The product may be recrystallized from hexane, forming deliquescent, air sensitive crystals. The exact nature of the reducing agent is unclear, but may involve oxidation of the pyrazolate ligand, which, due to its solubility in THF, is present in large excess throughout the course of the reaction. The formation of **3-1** is remarkable since diamagnetic dinuclear complexes featuring bridging pyrazolate groups as well as ancillary ligands such as Cp^* ,⁹ COD ,^{8a,10} PR_3 and MeCN ²² are known for Rh(I) , Rh(II) and Rh(III) .¹² Although the first example of a four coordinate, square planar Rh(II)

complex, $[n\text{-Bu}_4\text{N}]_2[\text{Rh}(\text{maleonitriledithiolate})_2]$ was reported many years ago by Gray and coworkers,¹³ there have been relatively few examples of well characterized mononuclear Rh(II) compounds. These include those based on porphyrins,¹⁴ pyridyl ligands,¹⁵ 1,4,7-trithiacyclononane,¹⁶ tris(2,4,6-trimethoxyphenyl-phosphine),¹⁷ aryls,¹⁸ hydrotris (pyrazolyl) borates,^{19a} and bisphosphine two-legged piano-stool ligands.^{19b}

The central Rh atom of **3-1** resides on a crystallographic inversion center and has a nearly square planar coordination geometry ($\text{N}(1)\text{-Rh-N}(4) = 89.71^\circ$, $\text{N}(1)\text{-Rh-N}(4A) = 90.29^\circ$) as shown in Figure 3.1. The two unique 3,5-(CF_3)₂Pz groups also bind a Li^+ ion with their outer N atoms and give each half of the molecule a boat-like configuration with a dihedral angle between the two 3,5-(CF_3)₂Pz rings of 75.5° . A single THF molecule is bound to each three-coordinate Li. The N-Li bond distances average 1.998 (4) Å. The two unique Rh-N bond lengths are 2.041 (2) Å (Rh-N(1)) and 2.038 (2) Å (Rh-N(4)), which are slightly shorter than those typically observed in both mononuclear and dinuclear Rh(I) and Rh(III) pyrazolate complexes, which all have Rh-N distances of ca. 2.1 Å. (based on the mean Rh-N bond distance for 258 structures of rhodium pyrazolate complexes deposited in the Cambridge Structural Database). Although the Rh center is four coordinate, the solid state structure also revealed four (CF_3) fluorine atoms that occupy open coordination sites above and below the RhN_4 plane, which may serve to enhance the stability of the complex by preventing coordination of nucleophiles to the metal center. The unique Rh...F non-bonded distances are 3.009 Å (Rh(1)...F(2)) and 3.114 Å (Rh(1)...F(11)).

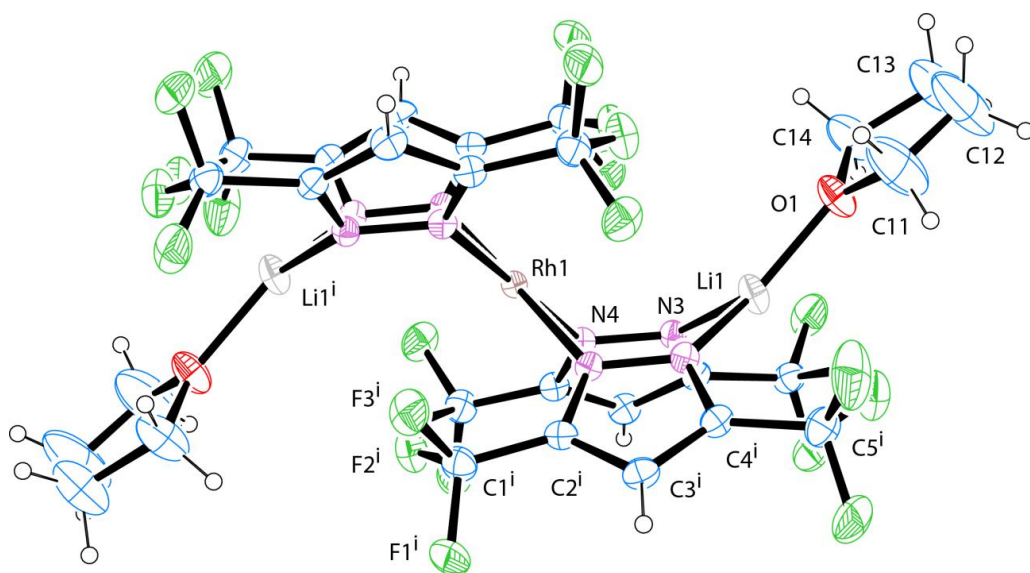


Figure 3.1 ORTEP diagram and partial atom numbering scheme of $[\text{Li}(\text{THF})]_2 \text{Rh}(\mu\text{-}3,5\text{-(CF}_3)_2\text{Pz)}_4$ (**3-1**). Thermal ellipsoids are drawn at the 30% probability level.

Complex **3-1** was studied in more detail using EPR, cyclic voltammetry and by DFT calculations. The X-band EPR spectrum of **3-1** in frozen toluene at 78 K is indicative of a paramagnetic complex with rhombic symmetry (Figure 3.2) with three well separated g values centered at $g_1 = 2.079$, $g_2 = 2.007$, and $g_3 = 1.968$. Hyperfine splitting is observed as two broad shoulders on the central g_2 feature, though the resolution is too poor to definitively assign coupling to ^{14}N ($I = 1$) or ^{103}Rh ($I = 1/2$). Similar hyperfine and g anisotropy has been observed in other low symmetry Rh(II) systems.²¹

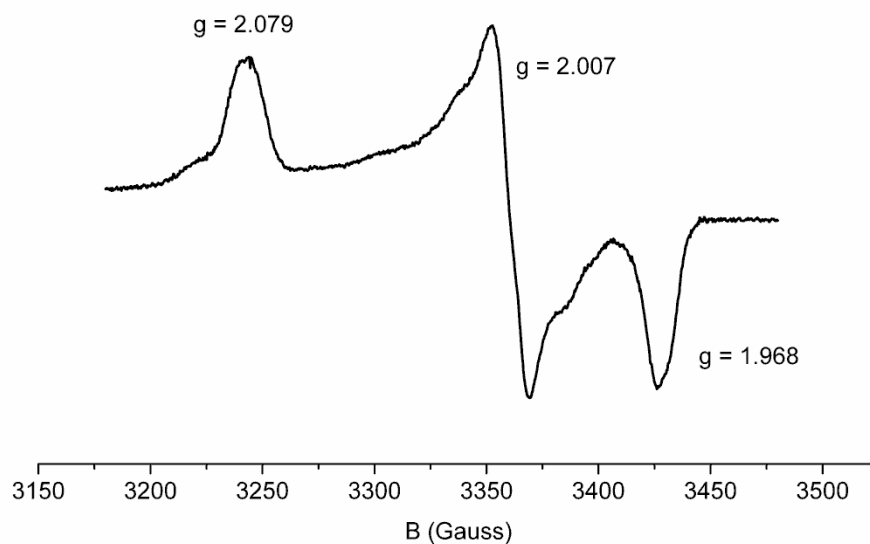


Figure 3.2 X-band EPR spectrum of complex **3-1** in frozen toluene at 78 K.

Electrochemical studies of **3-1** in acetonitrile revealed three separate redox processes, as shown in the cyclic voltammogram in Figure 3.3. The forward scan exhibits a large reduction wave **a** with a cathodic peak potential of -1.98 V, and two oxidation waves **b** ($E_{pa} = -1.32$ V) and **c** ($E_{pa} = -0.59$ V) are present when the potential is reversed. The reduction peak **a** is an irreversible process involving conversion of the 15 electron Rh(II) complex to a 16 electron Rh(I) species accompanied by significant structural rearrangement. The more cathodic oxidation wave **b** is related to the initial reduction of the species, as it appears only after the potential is first driven past ca. -1.8 V. This may correspond to the oxidation of a species generated by a disproportionation reaction upon reduction of the original Rh(II) complex. Evidence of structural rearrangement of the initial species is given by the gradual appearance of a redox couple attributable to free

pyrazole after several cycles. Peak **c**, which also lacks a corresponding reduction wave, corresponds to the irreversible oxidation of the Rh(II) species to a more stable Rh(III) complex.

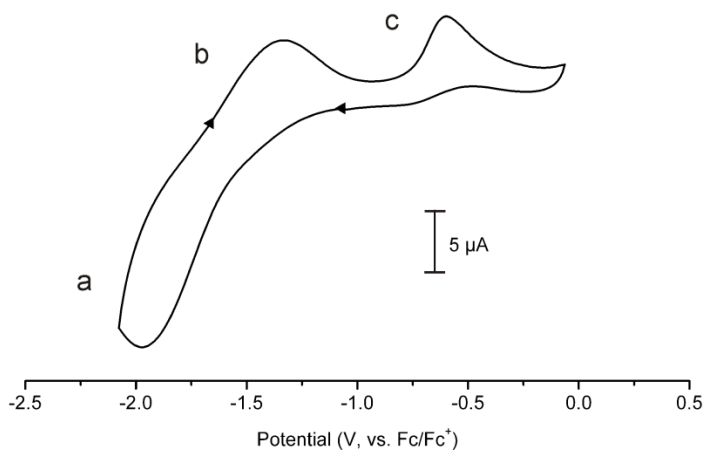


Figure 3.3 Cyclic voltammogram of complex **3-1** measured at 200 mV s^{-1} in acetonitrile solution with $0.1 \text{ M [TBA][PF}_6\text{]}$, showing a reduction peak (**a**) followed by two oxidation processes (**b**) and (**c**). Potentials are referenced to $[\text{Cp}_2\text{Fe}]^{0/+}$.

The electronic nature of **3-1** was investigated by DFT methods using a geometry optimized model, and the resulting frontier orbitals of the complex are shown in Figure 3.4. The metal $d_{x^2-y^2}$ orbital is directly involved in σ -bonding with the four ligands, forming a low energy bonding and a high energy anti-bonding interaction (SOMO + 2). Two of the metal d orbitals (d_{xy} , d_{yz}) are involved in bonding interactions with π^* MOs of the four pyrazolate ligands, while the remaining two d orbitals (d_{xz} , d_{z^2}) are not symmetry matched to ligand orbitals, and thus remain essentially non-bonding. The ordering of the orbitals in the ground state electron configuration differs from what is commonly observed in mononuclear square planar Rh(II) porphyrin systems ($((d_{xy})^2 (d_{xz}, d_{yz})^4 (d_{z^2})^1)$),

in which the unpaired electron is confined to a metal based d_{z^2} orbital.^{14a} The reason for the difference is due to the nature of the bonding interactions of the metal d orbitals with the π^* orbitals of the ligands (Figure 3.5). Because of the tilted orientation of each pyrazolate ring with respect to the xy plane of the complex (121°), overlap of ligand based π^* orbitals with the d_{xy} orbital on the metal is much more extensive, whereas overlap with the d_{xz} and d_{z^2} orbitals is diminished. Thus, the energy difference between the bonding and anti-bonding $d_{xy} + L_{\pi^*}$ interaction increases significantly, while MOs formed with d_{xz} and d_{z^2} contributions remain relatively unmixed. The result of this interaction is the splitting of the degeneracy of the d_{xz} and d_{yz} orbitals and placement of the unpaired electron in a $d_{xy} + L_{\pi^*}$ antibonding orbital of relatively high energy with substantial ligand and metal character. Complex **3-1** was not further investigated for CVD applications due to its extreme air and moisture sensitivity as well as its poor volatility.

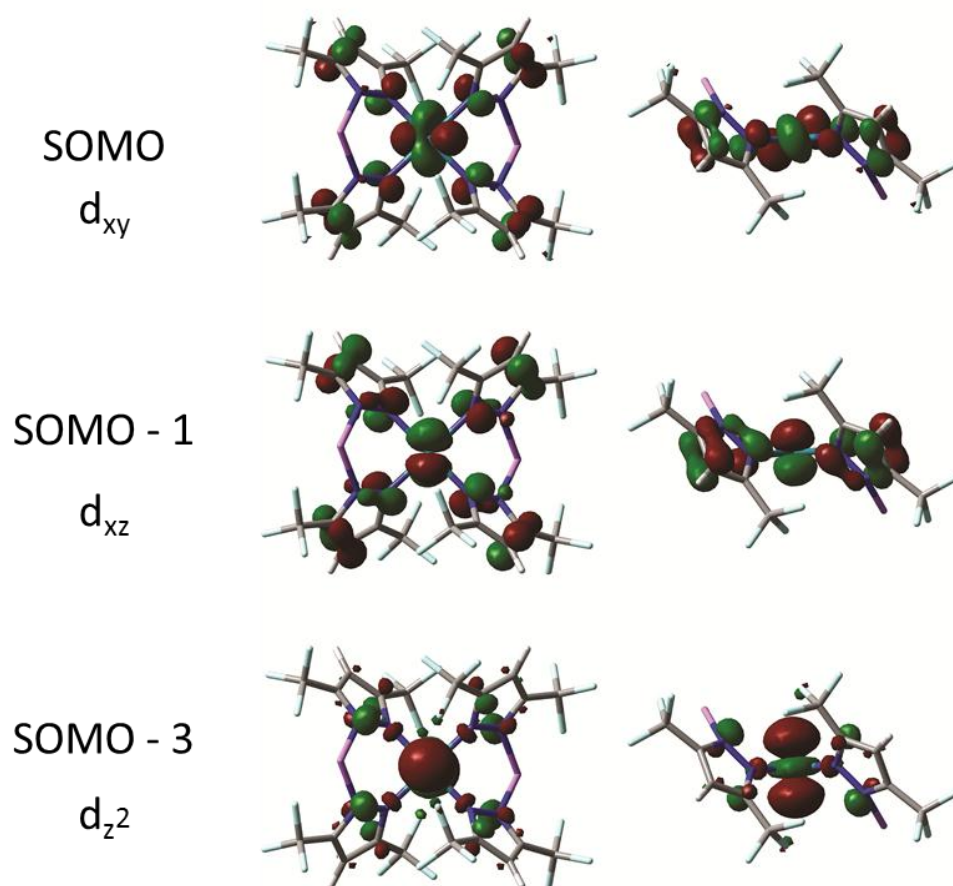


Figure 3.4 Top and side views of DFT calculated singularly occupied molecular orbital (SOMO) (top), SOMO - 1 (middle) and SOMO - 3 (bottom) of complex **3-1** shown with an isovalue of 0.04.

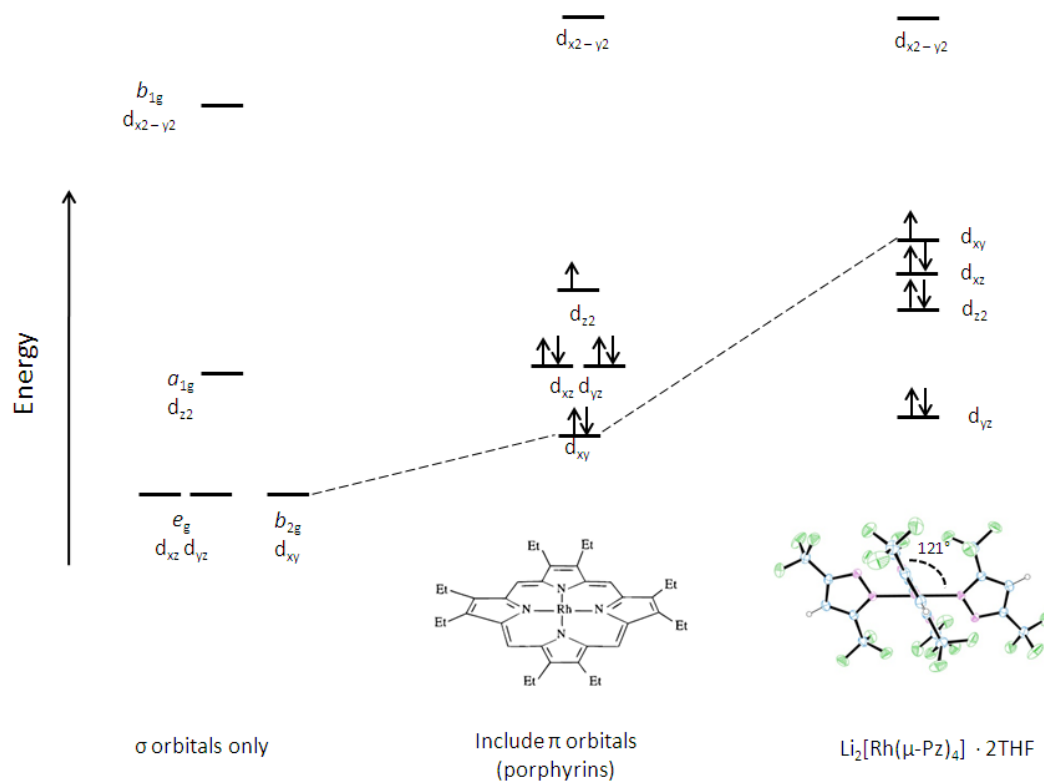
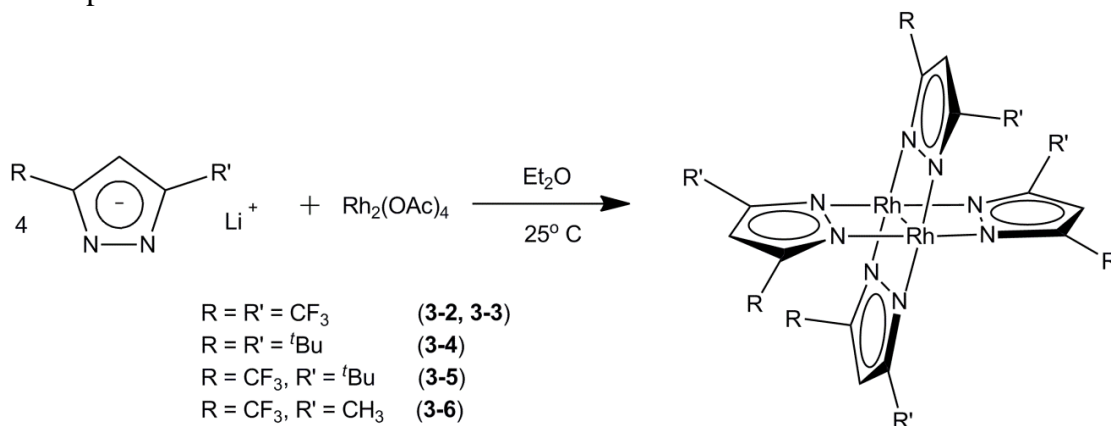


Figure 3.5 Energy level diagram of a metal in a D_{4h} coordination environment (left), a typical Rh porphyrin radical system (middle), and complex **3-1** (right). The twisted orientation of the pyrazolate ligands with respect to the Rh-N₄ plane is responsible for the reordering of the molecular orbitals.

Synthesis of Rh(II) paddlewheel complexes

In order to take advantage of the propensity of the pyrazolate ligand to bridge multiple metal centers, an alternative metal containing scaffold was chosen for further reactions with pyrazolate ligands. $\text{Rh}_2(\text{OAc})_4$ was chosen because it has been shown to undergo facile, single-step substitution reactions with a variety of ligands.²⁵ It is air stable, and is one of the least expensive commercially available salts of rhodium. Furthermore, because it is dinuclear, resultant volatile complexes contain a higher metal to ligand ratio. This may be an important factor in industrial scale reactions. The general synthetic scheme for the series of rhodium pyrazolate paddlewheel complexes studied in this chapter is outlined in Scheme 3.2 below.



Scheme 3.2 Synthesis of rhodium(II) paddlewheel complexes.

Reaction of anhydrous $\text{Rh}_2(\text{OAc})_4$ with four equivalents of the corresponding lithiated pyrazolate in diethyl ether at -78°C produces complexes **3-2**, **3-3**, **3-4**, **3-5**, and **3-6** in good yields. Use of THF as the solvent and the sodium salts of the corresponding pyrazoles (from NaH and PzH) gave identical products for each reaction. Though the reactions were generally high yielding, incomplete substitution products of the form

$\text{Rh}_2(\text{OAc})_x(\text{Pz})_y$ were spectroscopically detected in small amounts in the crude reaction mixtures, thus requiring purification of the products either by crystallization from hexanes at $-30\text{ }^\circ\text{C}$ or alternatively by sublimation of the crude reaction products under reduced pressure at temperatures ranging from $140 - 210\text{ }^\circ\text{C}$. Slow heating of the crude products in sealed quartz tubes in a zone sublimator facilitated the growth of large, high quality crystals suitable for X-ray diffraction studies. The solid state structures of complexes **3-2**, **3-3**, **3-4**, **3-5**, and **3-6** reveal that they are isostructural, consisting of two Rh(II) centers bridged by four pyrazolate units in the classic paddlewheel configuration most commonly found for dinuclear Rh(II) carboxylate complexes. The only other known dinuclear Rh-bridged pyrazolate system of this type is the 3,5-(Me)₂Pz analog reported by Wilkinson and co-workers,²² while a tin pyrazolate complex of this type is also known.²³

Complex **3-2** was isolated as a red solid from the reaction of 3,5-(CF₃)₂PzLi with rhodium acetate in Et₂O. Crystals suitable for X-ray diffraction studies were grown by sublimation in a sealed quartz tube at $140\text{ }^\circ\text{C}$ under reduced pressure. The complex crystallizes in the monoclinic space group $P2_1/n$ with one half molecule in the asymmetric unit and two molecules per unit cell. The X-ray crystal structure of **3-2** is presented in Figure 3.6, and selected bond lengths and angles are listed in Table 3.8. An inversion center resides midway between the two Rh atoms, leading to crystallographically imposed planarity of the pyrazolate ligands with respect to the Rh-Rh bond. The short Rh-Rh interaction of $2.343(11)\text{ \AA}$ is indicative of a strong single bond, while the Rh-N bond distances range from $2.056(6)$ to $2.060(6)\text{ \AA}$ and are typical of both mononuclear and bridged rhodium pyrazolate complexes. The hydrogen atoms of the axially coordinated water molecules were found in the electron difference map and refined isotropically with fixed O-H distances of 0.807 \AA and 0.805 \AA for H(1) and H(2).

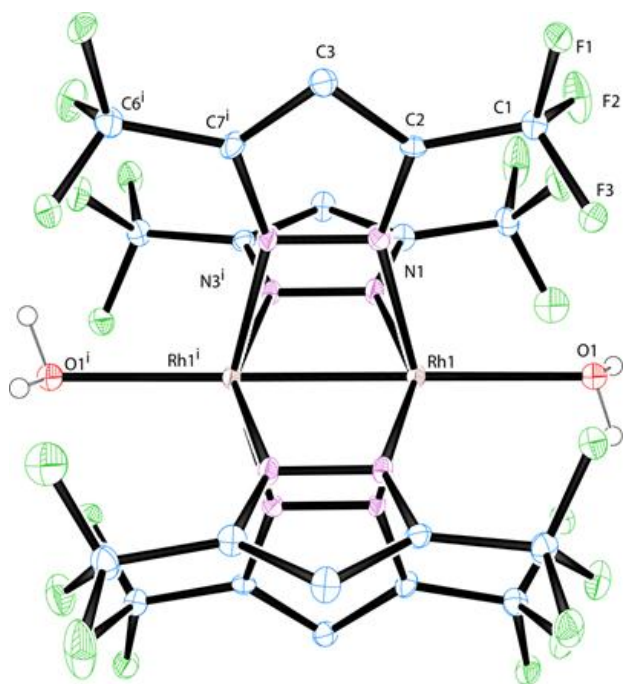


Figure 3.6 ORTEP diagram and partial atom numbering scheme of $\text{Rh}_2(\mu\text{-}3,5\text{-(CF}_3)_2\text{Pz)}_4 \cdot 2 \text{H}_2\text{O}$ (**3-2**). Thermal ellipsoids are drawn at the 30% probability level. Hydrogen atoms have been omitted from the pyrazolate ligands for clarity.

The oxygen atoms of the water molecules on adjacent $\text{Rh}_2(\text{Pz})_4$ units in the lattice are sufficiently close to each other to suggest intermolecular hydrogen bonding through $\text{O}\cdots\text{O}$ linkages ($\text{O}(1)\cdots\text{O}(1)^i = 2.915(4) \text{ \AA}$). However the $\text{O}\cdots\text{H}\cdots\text{F}$ distances of $2.487(2) \text{ \AA}$ and $2.611(2) \text{ \AA}$ for $\text{H}(1)\cdots\text{F}(3)^i$ and $\text{H}(2)\cdots\text{F}(2)^i$, respectively, as well as the large average $\text{O}\cdots\text{H}\cdots\text{F}$ angle of $123.35(14)^\circ$ indicate significant electrostatic interaction of the water molecules with fluorine atoms on neighboring pyrazolate ligands. As shown in Figure 3.7, this hydrogen bonding interaction results in packing of the crystals into one-dimensional coordination networks of $\text{Rh}_2(\text{Pz})_4(\text{H}_2\text{O})_2$ molecules.

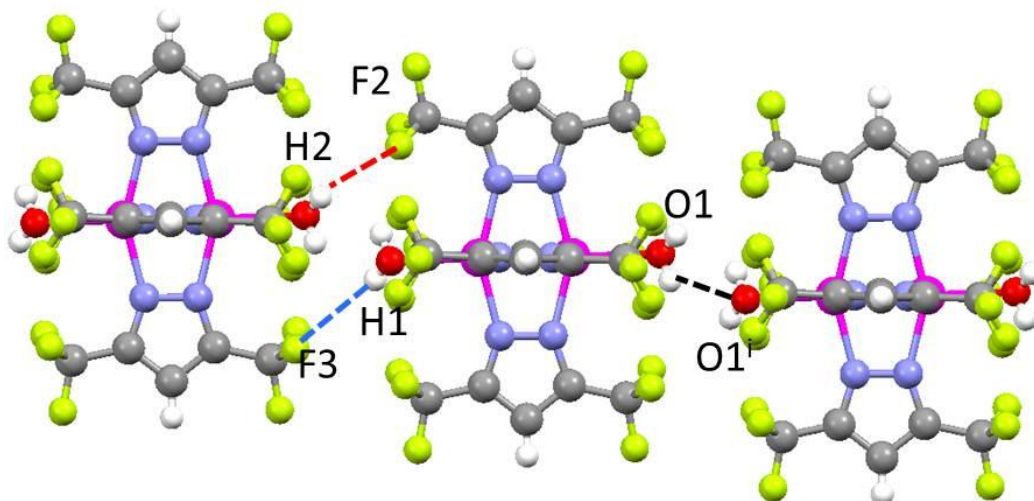


Figure 3.7 Intermolecular hydrogen bonding interactions of **3-2**.

Spectroscopic data supports the crystallographically determined molecular configuration, with two singlets observed in the ^1H NMR spectrum corresponding to protons on the Pz ligands and on the axially coordinated water molecules. One resonance was observed in the ^{19}F NMR spectrum, indicating a single coordination environment for the magnetically equivalent CF_3 fluorine atoms. A broad band in the infrared spectrum at 3600 cm^{-1} is indicative of O-H stretches from the axially coordinated water molecules.

Addition of acetonitrile to a hexane solution of **3-2** led to an immediate color change from orange red to yellow, and large yellow crystals of **3-3** were obtained by slow evaporation of the solvent. The solid state structure of **3-3** is shown in Figure 3.8 and key

bond lengths and angles are listed in Table 3.8. The molecule has nearly identical metrical parameters to the water adduct (**3-2**), although the Rh-Rh bond length for **3-3** is slightly longer than that in **3-2** (Rh-Rh: 2.353(3) Å). One possible explanation for this lengthening is the difference in σ donating ability of acetonitrile vs. water. Better overlap of the ligand orbitals with the σ^* LUMO of the complex, which is antibonding with respect to the Rh-Rh interaction and occupies the area along the rotational axis of the complex, would result in a relative weakening of the Rh-Rh interaction in **3-3** vs. **3-2**. The effect of axial ligand basicity on Rh-Rh bond length for di-rhodium complexes is well established,^{20,25,29,30} and will be further discussed in this chapter in relation to the rhodium carboxylate complexes **3-7**, **3-8**, **3-9**, **3-10**, and **3-12** (see below).

The ^1H NMR spectrum of **3-3** shows two singlets at 6.30 ppm and 2.68 ppm corresponding to pyrazole and acetonitrile proton resonances, respectively, while the ^{19}F NMR spectrum shows a single resonance at -61.62 ppm. The infrared spectrum of **3-3** resembles that of **3-2**, though the band corresponding to the symmetric C-N stretch for the coordinated acetonitrile molecules is weak and appears to be obscured by the doublet arising from atmospheric carbon dioxide ($\nu_{\text{asym}} = 2360, 2340 \text{ cm}^{-1}$). Other di-rhodium complexes with coordinated acetonitrile show absorptions in this region.

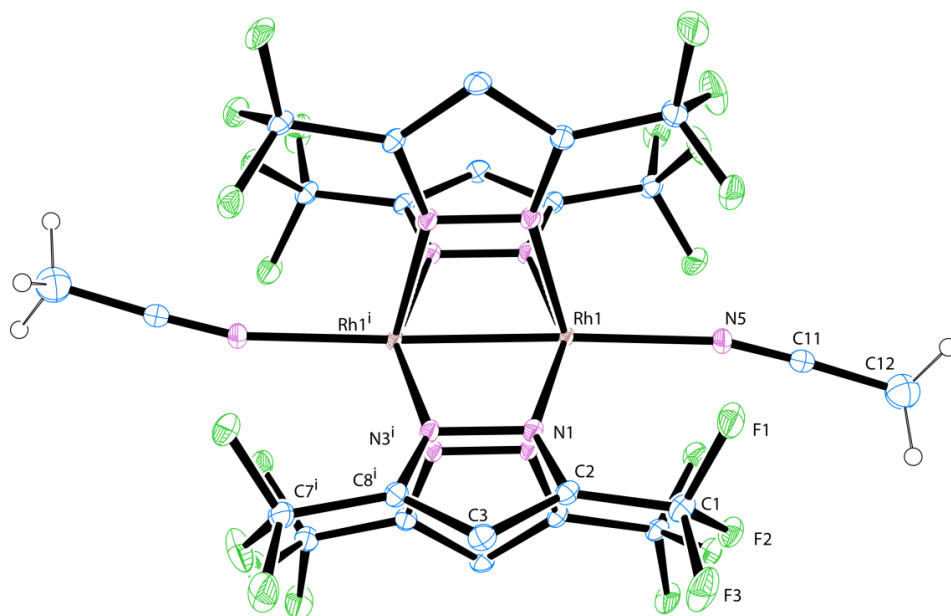


Figure 3.8 ORTEP diagram and partial atom numbering scheme of $\text{Rh}_2(\mu\text{-}3,5\text{-(CF}_3)_2\text{Pz)}_4 \cdot 2 \text{CH}_3\text{CN}$ (**3-3**). Thermal ellipsoids are drawn at the 30% probability level. Hydrogen atoms on the pyrazolate ligands have been omitted for clarity.

Although it was not possible to isolate the binary dinuclear complex $\text{Rh}_2((\text{CF}_3)_2\text{Pz})_4$ without axial donor ligands, loss of both H_2O and MeCN from **3-2** and **3-3** was observed by CI mass spectrometry. Peaks at m/e 1018 ($\text{M}^+ - 2 \text{H}_2\text{O}$) and 998 ($\text{M}^+ - 2 \text{H}_2\text{O} - \text{F}$) dominate the spectrum of **3-2**, with a very low intensity signal at m/e 1034, representing coordination of one water molecule to the parent ion. Similarly, the CI mass spectrum of the acetonitrile adduct **3-3** shows peaks corresponding loss of one (m/e 1059) and both (m/e 1018) coordinated solvent molecules.

Interaction of four equivalents of 3,5-(^tBu)₂PzLi with Rh₂(OAc)₄ in Et₂O leads to a forest green solution containing **3-4**. Complex **3-4** crystallizes in the monoclinic space group *C2/c* with four molecules per unit cell (Figure 3.9). Each 3,5-(^tBu)₂Pz ligand is tilted slightly such that the pyrazolate rings are not perfectly co-linear with the Rh-Rh bond (angle between two opposite pyrazolate rings 19.8° av.). This deviation from *D*_{4h} symmetry is seen in other similar dinuclear systems with sterically demanding ligands,²⁴ and likely allows for better packing of the large ^tBu groups around the Rh₂ core. The Rh-N distances are similar to those found in complexes **3-2** and **3-3**. Other key bond lengths and angles are listed in Table 3.10.

The Rh-Rh bond distance of 2.305(8) Å observed in **3-4** is the shortest reported for a quadruply-bridged dinuclear Rh(II)-Rh(II) complex. In fact, all of the dirhodium paddlewheel complexes studied in this chapter exhibit short Rh-Rh bond lengths compared to other quadruply bridged Rh(II) compounds which have carboxylato or hydroxypyridine ligands where the Rh-Rh bond length ranges from 2.350-2.550 Å.²⁵ The remarkably short Rh-Rh interaction in **3-4** may be a result of several factors. The common μ -exobidentate coordination mode of the pyrazolate ligand is capable of supporting a wide range of M-M separations, depending on the metal. Additionally, the bulky ^tBu groups of **3-4** sterically hinder coordination of small σ donor molecules at the open axial sites of each Rh atom, preventing donation of electron density into the $\sigma^*_{\text{Rh-Rh}}$ LUMO of the molecule. Complex **3-4** did not form adducts which could be isolated when dissolved in a variety of donor solvents such as THF, acetonitrile, and acetone.

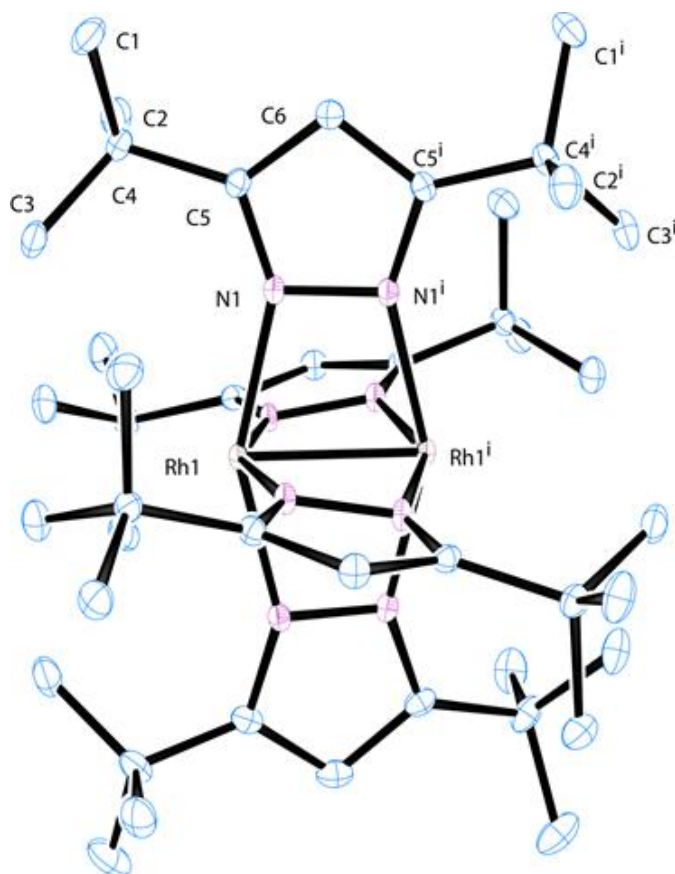


Figure 3.9 ORTEP diagram and partial atom numbering scheme of $\text{Rh}_2(\mu\text{-}3,5\text{-}(t\text{Bu})_2\text{Pz})_4$ (**3-4**). Thermal ellipsoids are drawn at the 30% probability level. Hydrogen atoms have been omitted for clarity.

In order to probe the steric and electronic effects of the pyrazolate ligand on $\text{Rh}_2(\text{Pz})_4$ species, the asymmetrically substituted pyrazoles (3-(CF_3),5-($t\text{Bu}$))PzH and (3-(CF_3),5-(CH_3))PzH, were used for the synthesis of complexes **3-5** and **3-6**, respectively. Complex **3-5** crystallizes in the tetragonal space group $I4_1/a$ with four molecules per unit cell. The solid state structure of the complex is shown in Figure 3.10 and selected bond lengths and angles are listed in Table 3.11. Additional crystallographic details are presented in Table 3.2. The pyrazolate ligands adopt an alternating configuration so that

CF₃ and ^tBu groups are adjacent to each other and this presumably minimizes steric interactions. Of related interest are the examples of Rh₂(mhp)₄ complexes (mhp = anion of 2-hydroxy-6-methyl-pyridine) in which three of the ligands are oriented in the same direction.²⁶ The observed 3:1 ligand arrangement of these complexes is a result of steric constraints imposed by the coordination of either ligand or solvent at only one of the axial sites.

The Rh atoms of complex **3-5** reside on a twofold rotation axis, and are bisected by an inversion center, giving the molecule S₄ symmetry. The Rh-N distances for the nitrogen atoms closest to the CF₃ substituent on each ligand are longer than at the opposite nitrogen (Rh(1) - N(1) = 2.071(11) Å, Rh(1) - N(2) = 2.023(12) Å). The significant contraction of only one Rh-N bond is explained by electronic effects of the substituents on the pyrazole ring. The strongly electron withdrawing CF₃ group at the 3-position of the ring preferentially enhances the basicity of the distal nitrogen, causing a stronger, shorter Rh-N interaction.²⁷ The unequal Rh-N bond lengths causes a slight tilting of each ligand with respect to the Rh-Rh bonding axis (Rh(1) - N(1) - C(2) = 150.39° is slightly more obtuse than Rh(1)ⁱ - N(2)ⁱ - C(4)ⁱ = 146.08°). This tilting is also favored on steric grounds, as the alternating orientation of the pyrazolate ligands allows for relief of steric strain imposed by the bulky substituents. As in complex **3-4**, the lack of coordinated donor ligands in the axial positions of **3-5** leads to a remarkably short Rh-Rh interaction (2.308(3) Å).

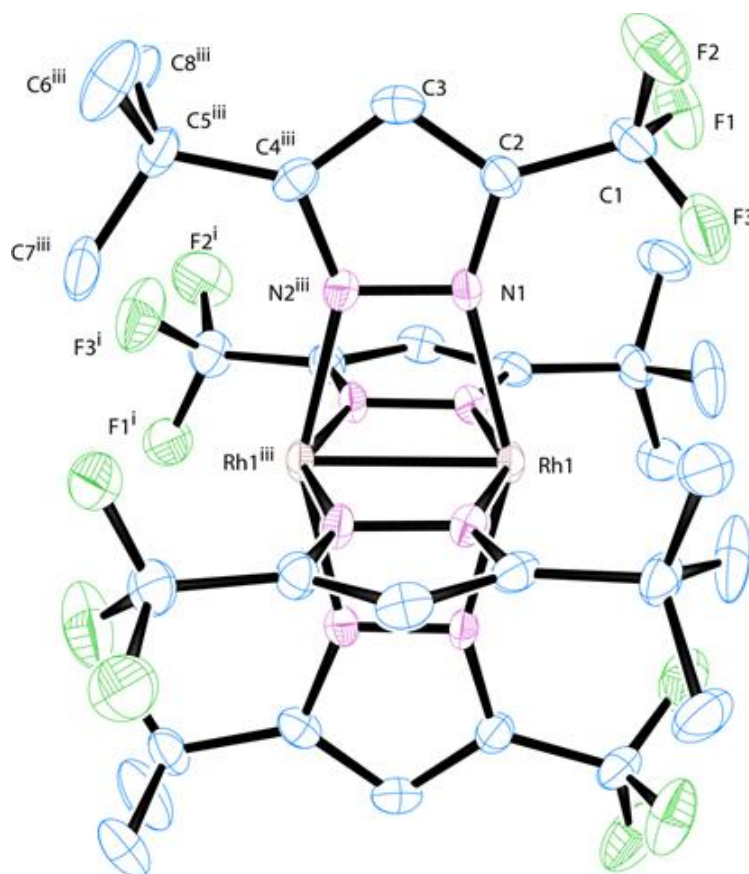


Figure 3.10 ORTEP diagram and partial atom numbering scheme of $\text{Rh}_2(\mu\text{-}3\text{-(CF}_3\text{)},5\text{-(tBu)Pz})_4$ (**3-5**). Thermal ellipsoids are drawn at the 30% probability level. Hydrogen atoms have been omitted for clarity.

The ^1H NMR spectrum of **3-5** in CDCl_3 shows the expected 9:1 ratio of tBu : aromatic Pz proton resonances, while the ^{19}F NMR spectrum reveals a singlet at -58.8 ppm, indicative of one coordination environment for the fluorine atoms of the CF_3 groups. Chemical ionization mass spectral analysis of the complex shows $m/e = 970$ (M^+) as the highest peak, with a smaller peak at $m/e = 951$ indicating loss of one fluorine atom.

Complex **3-6** is formed from the reaction of (3-(CF₃),5-(CH₃))PzLi with Rh₂(OAc)₄ in Et₂O. Sublimation of the reaction product led to a microcrystalline green solid that changed color to purple upon standing under an inert atmosphere. Despite repeated attempts to crystallize Rh₂((3-(CF₃),5-(CH₃))Pz)₄ from a variety of solvents, only the acetonitrile solution yielded crystals upon slow evaporation. Complex **3-6** crystallizes in the triclinic space group *P1* with two molecules per unit cell. The structure is shown in Figure 3.11 and selected bond lengths and angles are presented in Table 3.12. Additional crystallographic details are listed in Table 3.2.

The Rh-Rh and Rh-N distances of complex **3-6** are similar to those observed in complex **3-3**. Similarly to the other asymmetrically substituted analog **3-5**, there is a significant difference in the two unique Rh-N bond lengths (Rh1-N1 = 2.035(10) Å, Rh1-N2 = 2.056(9) Å), with the shorter interaction arising from the more basic nitrogen atom that is distal from the CF₃ functionality on the ring forming a stronger bonding interaction with one of the rhodium ions. Because there is less of a steric difference between CF₃ and CH₃ groups substituted on the ring, this Rh-N discrepancy is less likely influenced by sterics and more a result of electronic factors of the pyrazolate ligand.

In contrast to the alternating ligand arrangement observed in **3-5**, each ligand of complex **3-6** faces the same direction as an adjacent ligand such that two neighboring ligands have CF₃ groups facing one direction along the Rh-Rh axis and the other ligand pair has CF₃ functionalities facing the other direction. This arrangement is likely driven by steric interactions with the coordinated acetonitrile molecules. Unfortunately no analogous structure could be isolated for the complex lacking axially coordinated ligands for comparison.

The ¹H NMR of complex **3-6** shows peaks in a 3:1 ratio for the methyl and aromatic protons of the four bridging pyrazolate ligands at 2.20 ppm and 5.70 ppm,

respectively. A broad resonance at 2.61 ppm corresponds to the two coordinated acetonitrile ligands. The signals for the pyrazolate ligands each show a single sharp peak surrounded by several closely spaced signals of lower intensity, indicating the existence of isomers of the complex present in solution. A similar complex pattern is observed in the ^{19}F NMR spectrum, which consists of weak signals between -60.78 ppm and -60.55 ppm, with a sharp, high intensity signal centered at -60.67 ppm.

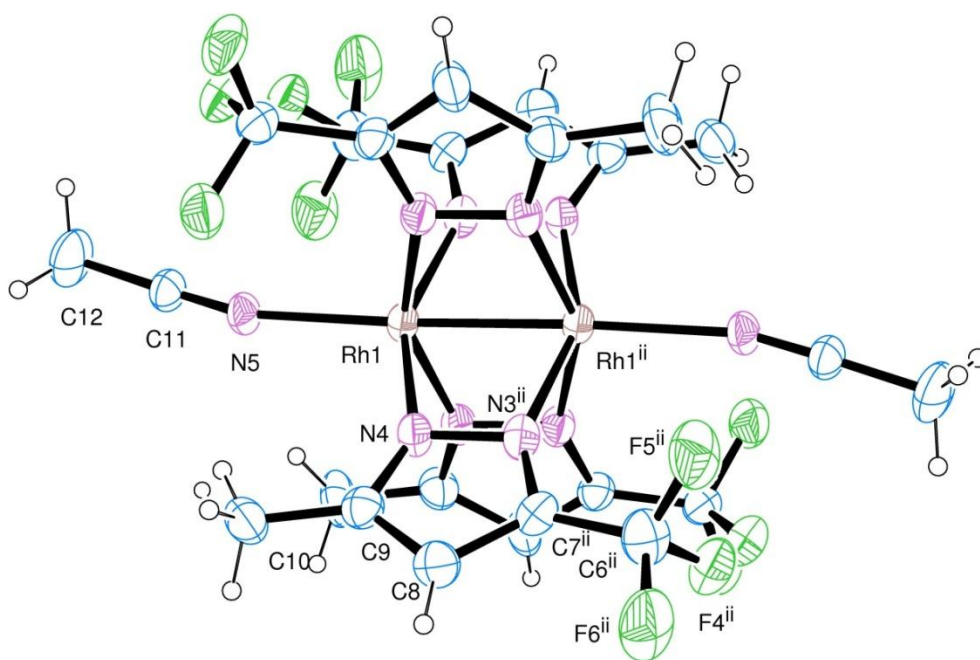
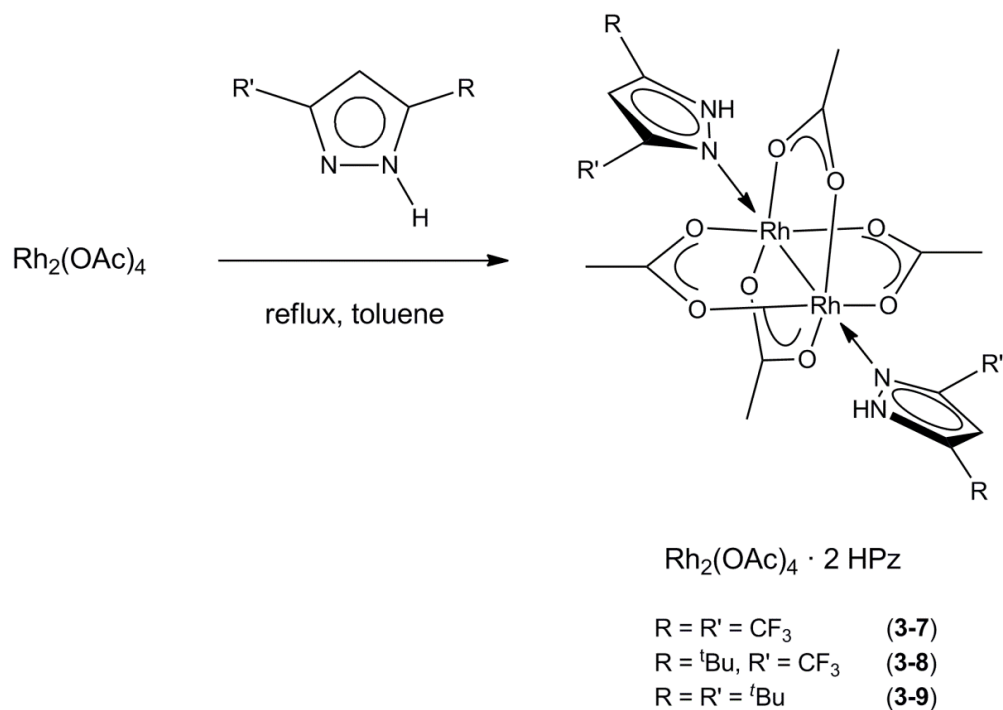


Figure 3.11 ORTEP diagram and partial atom numbering scheme of $\text{Rh}_2(\mu\text{-}3\text{-(CF}_3\text{)},5\text{-(CH}_3\text{)Pz})_4 \cdot 2 \text{CH}_3\text{CN}$ (**3-6**). Thermal ellipsoids are drawn at the 30% probability level.

The volatility of complexes **3-2**, **3-3**, **3-4**, **3-5**, and **3-6** were tested by heating each complex in a sealed ampoule under vacuum (10^{-2} Torr). Complexes **3-2**, **3-4**, and **3-5** sublimed without decomposition at 140 °C, 180 °C, and 210 °C, respectively, and were further investigated for use as CVD reagents (discussed below), while complexes **3-3** and **3-6** were not thermally stable under these conditions.

Synthesis of rhodium acetate and trifluoroacetate pyrazole adducts

The series of reactions outlined in Scheme 3.2 are suitable for producing the described rhodium paddlewheel complexes **3-2**, **3-3**, **3-4**, **3-5**, and **3-6** in good yield (60-90%), though incomplete substitution products of the form $\text{Rh}_2(\text{OAc})_x(\text{Pz})_{4-x}$ were spectroscopically detected in small amounts for each reaction. In previous reports, several different dirhodium(II) paddlewheel complexes have been isolated from the direct reaction of the free ligand with rhodium acetate at elevated temperatures. These carboxylate exchange reactions are facile, high-yielding, and eliminate the need to first prepare a Li^+ or Na^+ salt of the bridging ligand. Examples include $\text{Rh}_2(\text{mhp})_4$ (mhp = anion of methylhydroxypyridine)²⁶ and $\text{Rh}_2(\text{O}_2\text{CCF}_3)_4$.²⁸ Thus in an effort to increase yield and eliminate the formation of these involatile partially substituted products, the direct reaction of rhodium acetate with excess free pyrazole at elevated temperatures was attempted. All of the substituted pyrazoles used in this study sublime at elevated temperatures at atmospheric pressure, so direct reaction of molten ligand with $\text{Rh}_2(\text{OAc})_4$ was not possible. Instead, the starting reagents were refluxed in high boiling non polar solvents such as toluene (b.p. 110 °C) and decane (b.p. 174 °C) in order to drive the reaction. The products isolated from this series of reactions, however, were rhodium acetate-pyrazole adducts of the form $\text{Rh}_2(\text{OAc})_4 \cdot 2 \text{PzH}$, as presented in Scheme 3.3.



Scheme 3.3 Synthesis of rhodium acetate pyrazole adducts.

For complexes **3-7**, **3-8**, and **3-9**, the reaction mixture turned a deep purple (indicative of a rhodium acetate - amine adduct) and did not change color further. Filtration and slow evaporation of the solvent resulted in dark purple crystals of each of the products. The X-ray crystal structures of complexes **3-7**, **3-8**, and **3-9** are shown in Figures 3.12, 3.13 and 3.14, respectively. Selected bond lengths and angles for each complex are presented in Tables 3.13, 3.14 and 3.15, while additional crystallographic details are listed together in Table 3.3. The three complexes are isostructural in the solid state, consisting of a central $\text{Rh}_2(\text{OAc})_4$ core with two axially coordinated pyrazole molecules. For each complex, the two oppositely coordinated pyrazole molecules are

coplanar and face different directions, imposing C_{2v} symmetry on each molecular unit. The Rh-O bond distances and angles are typical for bridged dinuclear carboxylate complexes of this type. The metrical parameters show small variations upon changing the pyrazole ligand, with Rh-Rh = 2.4046(13) Å and Rh-N = 2.319(6) Å for complex **3-7**, Rh-Rh = 2.3948(8) Å and Rh-N = 2.318(4) Å for complex **3-8**, and Rh-Rh = 2.4059(6) Å and Rh-N = 2.322(3) Å for complex **3-9**.

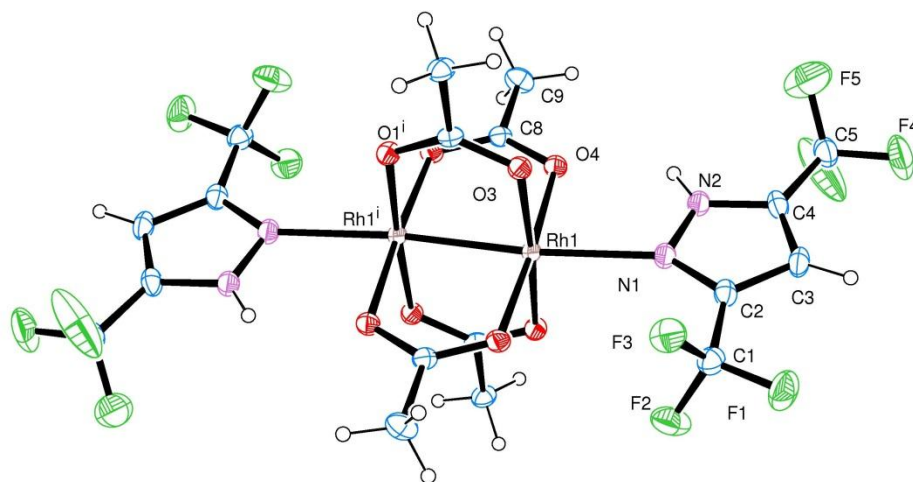


Figure 3.12 ORTEP diagram and partial atom numbering scheme of $\text{Rh}_2(\text{O}_2\text{CCH}_3)_4 \cdot 2$ (3,5-(CF_3) $_2\text{PzH}$) (**3-7**). Thermal ellipsoids are drawn at the 30% probability level.

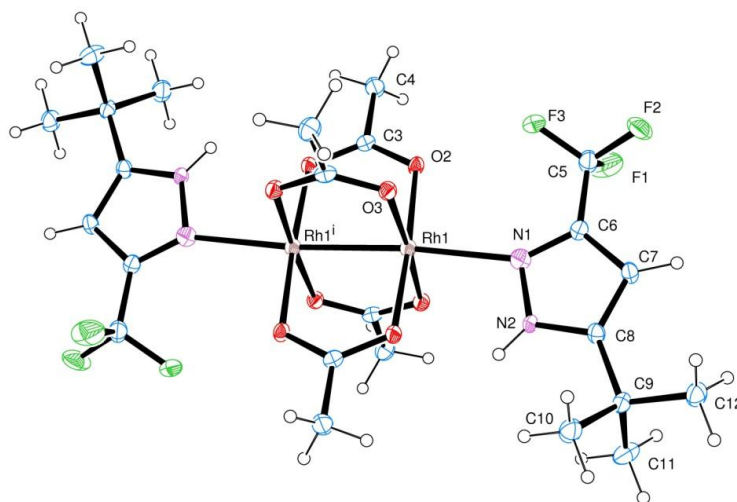


Figure 3.13 ORTEP diagram and partial atom numbering scheme of $\text{Rh}_2(\text{O}_2\text{CCH}_3)_4 \cdot 2$ (3-(CF_3),5-($t\text{Bu}$)PzH) (**3-8**). Thermal ellipsoids are drawn at the 30% probability level.

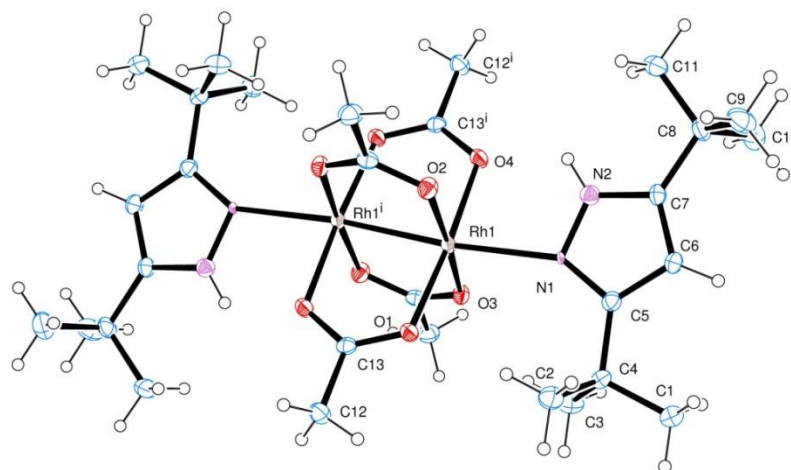


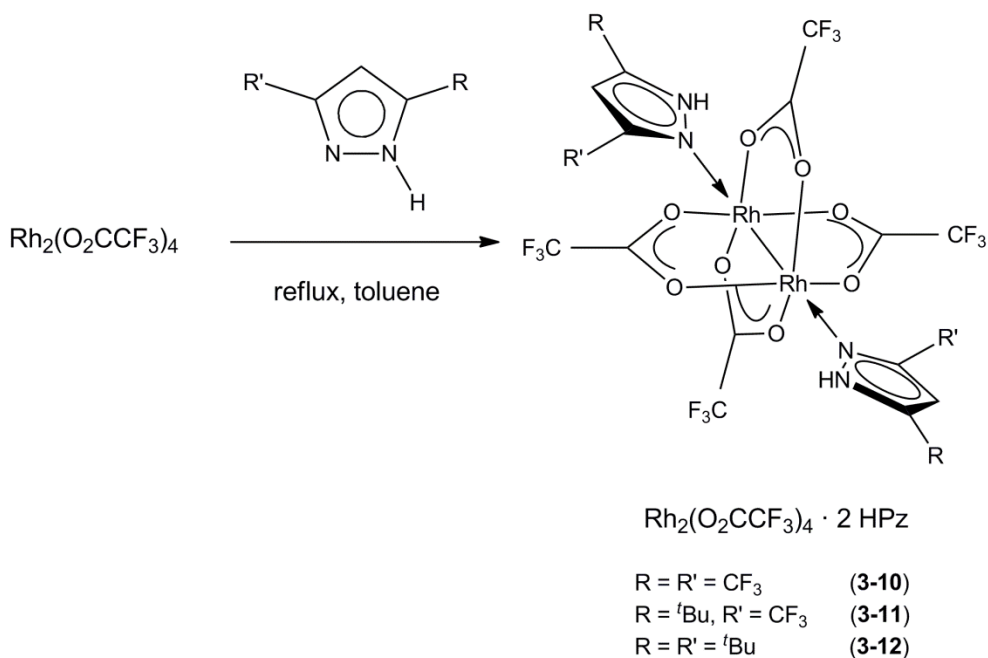
Figure 3.14 ORTEP diagram and partial atom numbering scheme of $\text{Rh}_2(\text{O}_2\text{CCH}_3)_4 \cdot 2$ (3,5-($t\text{Bu}$)₂PzH) (**3-9**). Thermal ellipsoids are drawn at the 30% probability level.

Intramolecular hydrogen bonding interactions between the pyrazole N-H hydrogen and the oxygen atoms of the acetate ligands are apparent from the solid state structures of complexes **3-7**, **3-8**, and **3-9**. For all complexes, the pyrazole hydrogen atoms were located on the Fourier difference map and refined isotropically at a fixed distance of N-H = 0.86 Å. A list of the bond distances and angles of the hydrogen bonding interactions for the complexes is presented in Table 3.18. These H-bonding interactions serve to stabilize the complexes by formation of a five-membered ring consisting of O and Rh atom from Rh₂(OAc)₄ and both N atoms and a H atom from the pyrazole. This also has the effect of bringing each pyrazole molecule closer to one acetate group, slightly distorting the Rh-Rh-N angle from linearity (e.g. N(1)-Rh(1)-Rh(1)ⁱ = 173.74(10)° for **3-7**).

¹H NMR spectral data show sharp singlets from the aromatic N-H protons as well as the acetate CH₃ protons. The simplicity of the spectra indicates fast rotation of the pyrazole ligand about the Rh-N axis in solution, leading to a single chemical environment for the ligands. Very broad N-H resonances were located between 9-12 ppm for all three complexes. Intramolecular hydrogen bonding is further supported by the appearance of bands in the infrared spectrum located at a somewhat lowered frequency for the characteristic N-H stretch of amines. Sharp bands are observed at 3229 cm⁻¹, 3295 cm⁻¹ and 3345 cm⁻¹ for complexes **3-7**, **3-8** and **3-9**, respectively.

The complexes of the type Rh₂(OAc)₄ • 2 PzH show limited volatility, as the adducts decompose with loss of pyrazole upon heating under vacuum. However it was hypothesized that axially coordinated pyrazole adducts of this type with a more volatile rhodium carboxylato core may have more attractive properties for CVD applications. This is the rationale for the reaction outlined in Scheme 3.4, in which Rh₂(O₂CCF₃)₄, which sublimates at 280 °C, was chosen as the reagent for a series of reactions to form

complexes **3-10**, **3-11**, and **3-12**. The complexes were synthesized from the reaction of two equivalents of pyrazole with rhodium trifluoroacetate in toluene. Filtration and slow evaporation of solvent led to large deep purple X-ray quality crystals.



Scheme 3.4 Synthesis of rhodium trifluoroacetate pyrazole adducts.

The crystal structures of complexes **3-10**, **3-11**, and **3-12** are shown in Figures 3.15, 3.16 and 3.17, respectively. Select bond lengths and angles are presented in Tables 3.16, 3.17 and 3.18, while further crystallographic details are listed together in Table 3.4. Complexes **3-10**, **3-11**, and **3-12** are isostructural with complexes **3-7**, **3-8**, and **3-9**, consisting of a $\text{Rh}_2(\text{O}_2\text{CCF}_3)_4$ core with two pyrazole molecules axially coordinated. Similar intramolecular hydrogen bonding between the pyrazole N-H hydrogens and one oxygen atom of an acetate group are present in complexes **3-10**, **3-11**, and **3-12**, and relevant bond lengths and angles of these interactions are listed in Table 3.19.

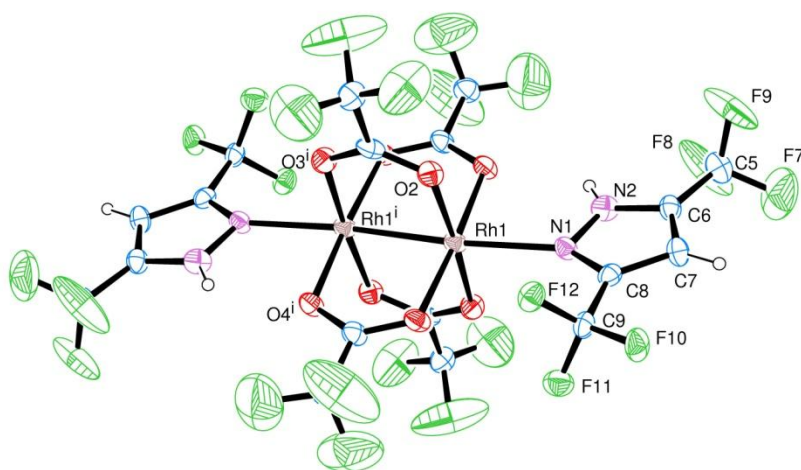


Figure 3.15 ORTEP diagram and partial atom numbering scheme of $\text{Rh}_2(\text{O}_2\text{CCF}_3)_4 \cdot 2$ (3,5-(CF_3) $_2\text{PzH}$) (**3-10**). Thermal ellipsoids are drawn at the 30% probability level.

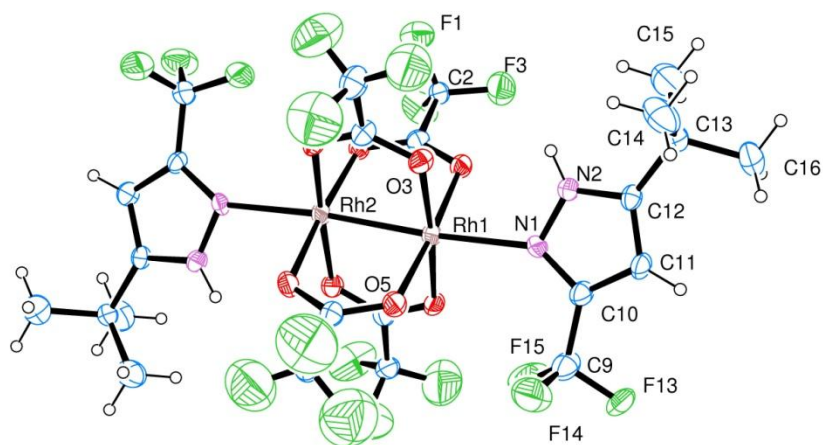


Figure 3.16 ORTEP diagram and partial atom numbering scheme of $\text{Rh}_2(\text{O}_2\text{CCF}_3)_4 \cdot 2$ (3-(CF_3),5-($t\text{Bu}$)PzH) (**3-11**). Thermal ellipsoids are drawn at the 30% probability level.

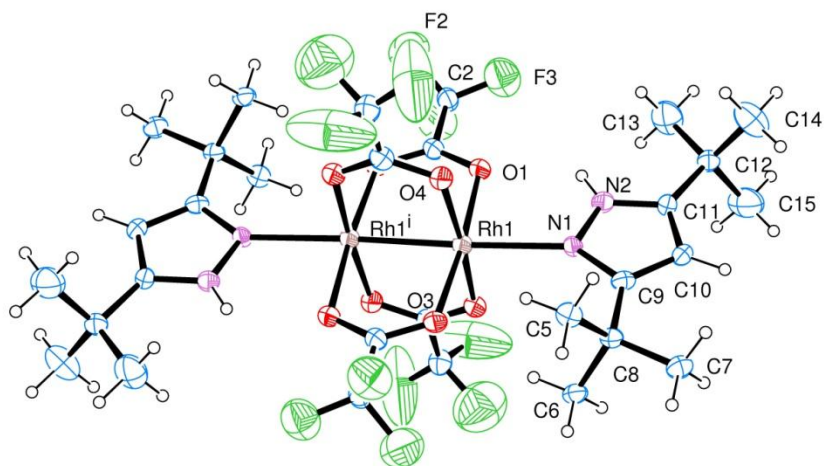


Figure 3.17 ORTEP diagram and partial atom numbering scheme of $\text{Rh}_2(\text{O}_2\text{CCF}_3)_4 \cdot 2$ (3,5- $^t\text{Bu}_2\text{PzH}$) (**3-12**). Thermal ellipsoids are drawn at the 30% probability level.

The strength of the Rh-Rh interaction for Rh_2^{4+} bridged complexes has been shown to be sensitive to the nature of the axially coordinating ligand L. Based on structural data from several studies of rhodium carboxylate complexes with various σ donors, an approximately linear correlation has been shown to exist between Rh-Rh bond length and pK_b of the axially coordinated ligand.^{20,29} This observed trend is rationalized based on *trans*- theory for a M-M-L system involving a simple σ donor L, which predicts a weakening of the M-M bond as the M-L bond strength is increased.²⁰ While this explanation is sufficient for simple σ donor molecules, the matter is complicated by ligands that participate in π -back donation with the metal or are sterically bulky enough to influence the bridging carboxylate moieties, and thus the Rh-Rh bond. Examples of molecules which deviate significantly from the linear relationship include phosphorus and sulfur containing donor molecules, which coordinate through large, diffuse orbitals that are able to achieve better overlap with the σ^* LUMO of $\text{Rh}_2(\text{OAc})_4$.^{30a} In addition,

some heterocyclic aromatic nitrogen-containing ligands such as acridine and phenazine have been hypothesized to create a nondegeneracy of the Rh-based frontier orbitals via π interactions with the aromatic ligand ring system, leading to a higher energy HOMO and a lengthening of the Rh-Rh interaction.^{30b}

The series of substituted pyrazole ligands studied in this chapter show a range of basicities due to the electron withdrawing (CF_3) and electron donating ($t\text{Bu}$) groups at the 3- and 5- positions on the ring, and it is instructive to note the trends in Rh-Rh distance of the $\text{Rh}_2(\text{OAc})_4 \cdot 2 \text{PzH}$ adducts as a function of the substitution of the pyrazole as well as the nature of the bridging carboxylate ligands. The basicities of the (3-R, 5-R')Pz molecules increase in the order $(\text{CF}_3)_2\text{PzH} < (t\text{Bu}, \text{CF}_3)\text{PzH} < (t\text{Bu})_2\text{PzH}$, with all three pyrazoles showing relatively weak acidity. The 3,5-bis(trifluoromethyl) moiety is the strongest acid, as a formal negative charge placed on the Pz ring upon deprotonation is more easily stabilized by the electron withdrawing (CF_3) substituents at the 3- and 5- positions of the ring. Assuming minimal steric effects, a near linear relationship is predicted for Rh-Rh distance with increased ligand basicity for complexes of the form $\text{Rh}_2(\text{O}_2\text{CCH}_3)_4 \cdot 2 \text{PzH}$ (**3-7**, **3-8**, and **3-9**) and $\text{Rh}_2(\text{O}_2\text{CCF}_3)_4 \cdot 2 \text{PzH}$ (**3-10**, **3-11**, and **3-12**), and this is generally what is observed (Figure 3.18). The lone deviation is the Rh-Rh distance found for complex **3-7**, which is somewhat longer than expected. The trend is more pronounced for the dirhodium trifluoroacetate adducts, as mentioned above, and all three values are within the expected range for coordination of N-donor adducts.

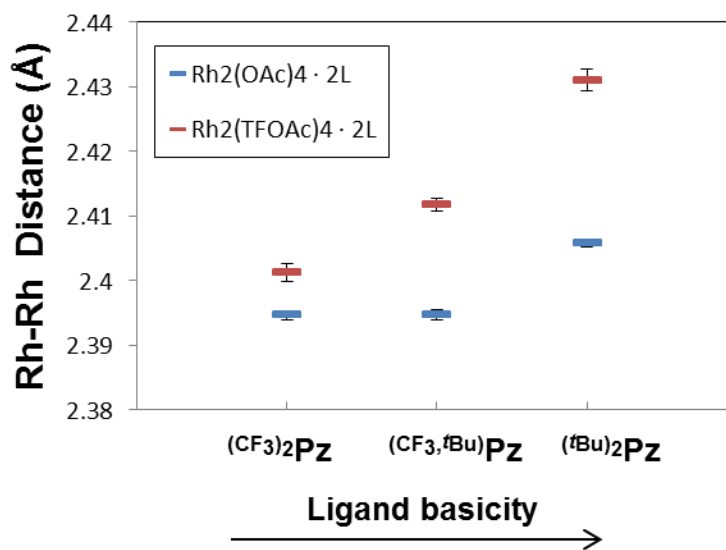


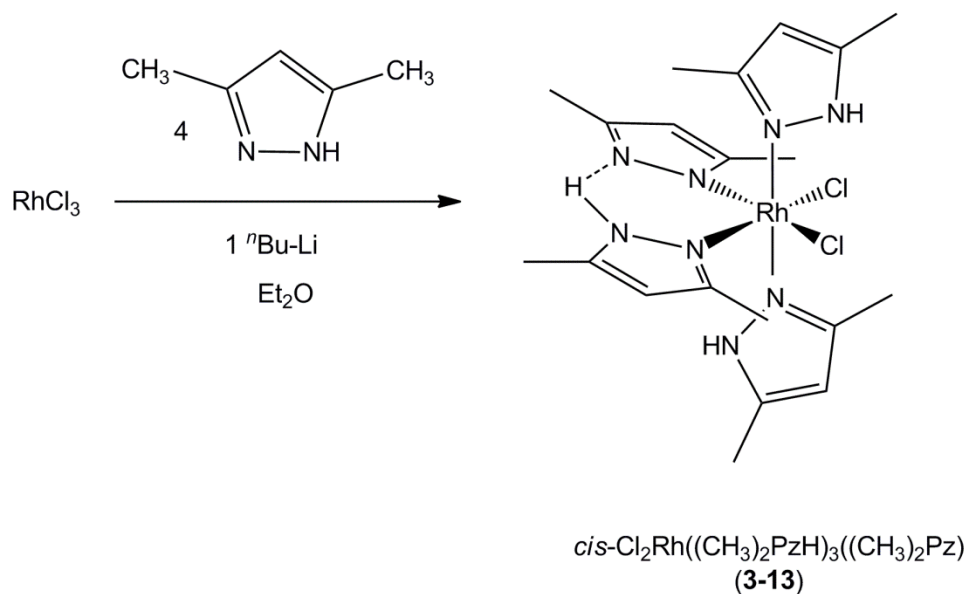
Figure 3.18 Rh-Rh distances of Rh₂(OAc)₄ · 2 PzH complexes (blue) and Rh₂(O₂CCF₃)₄ · 2 PzH complexes (red) as a function of basicity of the axial ligands. The error bars on the distances are $\pm 1\sigma$.

It is noteworthy that the nitrogen atom of the asymmetrically substituted pyrazole ligands that is directly coordinated to the metal in complexes **3-8** and **3-11** is the one proximal to the CF₃ functionality. This is a direct result of tautomeric equilibrium of the free ligand in which the electron withdrawing nature of the perfluoroalkyl group causes an increase in basicity of the distal nitrogen of the ring, and thus a preference for the proton to reside on this nitrogen. This behavior is established for this and other pyrazole ligands with electron withdrawing and electron donating substituents at the 3- and 5-position of the ring.^{27,31} This allows a certain degree of predictability over the structure of the coordination product formed from the reaction of asymmetrically substituted pyrazoles and pyrazolates with metal centers.

The melting points of the rhodium trifluoroacetate adducts were found to be 148-150 °C for complex **3-10**, 136-138 °C for complex **3-11**, and 145-146 °C for complex **3-12** (1 atm. N₂), and all complexes sublimed without decomposition at reduced pressure (10⁻² Torr) between 120 – 130 °C. This enhanced volatility arises from the ability of the two pyrazole molecules to fill the otherwise open axial coordination sites of each Rh₂(O₂CCF₃)₄ core, which prevents intermolecular H-bonding interactions at the Lewis acidic metal centers and keeps the complexes monomeric. It has been shown that anhydrous Rh₂(O₂CCF₃)₄ is Lewis acidic enough to form linear, one-dimensional coordination adducts with itself, in the absence of other coordinating small molecules.³² This extended polymeric network serves to lower the volatility of rhodium trifluoroacetate (subl. 280 °C, 10⁻² Torr). Thus despite an increase in molecular weight of between 50 - 60% by reaction with two pyrazole molecules, the sublimation temperature of rhodium trifluoroacetate is lowered by almost 160 °C, making complexes **3-10**, **3-11**, and **3-12** viable precursors for the chemical vapor deposition of Rh thin films.

Other rhodium pyrazolate/pyrazole complexes

Addition of four equivalents of 3,5-dimethylpyrazole to a stirred solution of anhydrous RhCl₃ in THF followed by the addition of one equivalent of *n*-butyllithium at -78 °C affords the mixed pyrazole-pyrazolate complex **3-13**. The X-ray crystal structure of the complex is shown in Figure 3.19, while a list of bond lengths and angles are presented in Table 3.20. Further crystallographic details are shown in Table 3.5.



Scheme 3.5 Synthesis of *cis*-Cl₂Rh(3,5-(CF₃)₂Pz)(3,5-(CF₃)₂PzH)₃ (**3-13**).

Complex **3-13** crystallizes in the monoclinic space group $P2_1/c$ and the asymmetric unit consists of one *cis*-Cl₂Rh(PzH)₃(Pz) unit along with one molecule of toluene. The central Rh atom lies at the center of a *pseudo* octahedral field with two pyrazole molecules coordinated above and below the approximate square plane formed by two chloride ligands and two Pz ligands that are linked via hydrogen bonding (N(3)-H(1)⋯N(5) = 2.563(5) Å, 145(5)°). This type of intramolecular hydrogen bonding has been observed in other pyrazolate metal complexes and prevents the possibility of η^2 coordination to the metal. The Rh-Cl and Rh-N distances are similar to other Rh(III) pyrazolate complexes.³³

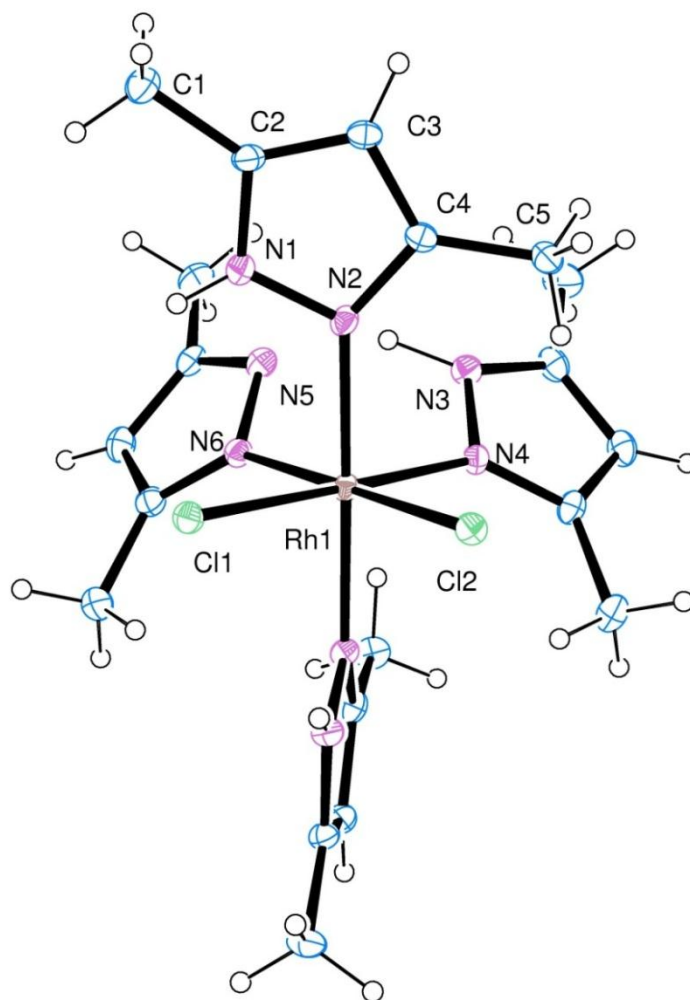


Figure 3.19 ORTEP diagram and partial atom numbering scheme of *cis*-Cl₂Rh(3,5-(CF₃)₂Pz)(3,5-(CF₃)₂PzH)₃ (**3-13**). Thermal ellipsoids are drawn at the 30% probability level. Toluene solvent molecule of crystallization omitted for clarity.

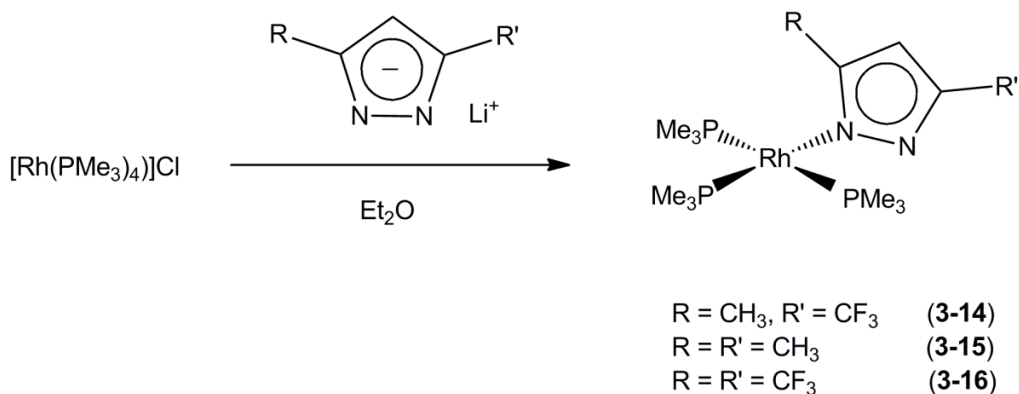
The ¹H NMR spectrum of **3-13** in d₈-toluene shows resonances at 5.73 ppm and 5.66 ppm corresponding to the aromatic proton of the coordinated pyrazole and

pyrazolate ligands. Four broad resonances at 2.32 ppm, 2.08 ppm, 1.59 ppm and 0.93 ppm correspond to methyl groups of the two mutually *trans* PzH ligands, while two sharp peaks at 2.12 ppm and 1.82 ppm correspond to pairs of methyl groups of the two mutually *cis* ligands that interact via hydrogen bonding. Broad resonances shifted downfield at 11.2 ppm and 13.90 ppm indicate pyrazole N-H and N-H \cdots H protons, respectively. The IR spectrum of **3-13** shows a broad medium intensity band centered at 3450 cm⁻¹ as well as a sharp, strong band at 3381 cm⁻¹ corresponding to the characteristic N-H stretching frequency. The melting point of complex **3-13** is 113-114 °C (sealed tube under 1 atm. N₂).

Several volatile transition metal complexes with tertiary phosphine ligands have been studied for the CVD of thin films of the corresponding metal. Examples include Pt(PF₃)₄, Pd(Me)₂(PEt₃)₂, H₂Fe(PMe₃)₄, and Rh(Cp)(PF₃)₂.³⁴ Phosphines are well suited as ligands for vapor deposition precursors due to their relatively low molecular weight and ability to impart volatility on the resultant metal complex. Furthermore use of phosphines to fill the coordination sphere of the metal eliminates direct M-C and M-O bonds, reducing the possibility of film contamination from these two elements. The chemistry of rhodium trialkylphosphine complexes is extensive, spurred by potential applications in homogeneous catalysis, while the development of these complexes for CVD of Rh films remains relatively unexplored. As a continuation of an effort to develop low molecular weight complexes of Rh and Ru with phosphine ligands, complexes **3-14**, **3-15** and **3-16** were explored for potential use as CVD reagents.

Complexes **3-14**, **3-15** and **3-16** were prepared similarly from the reaction of [Rh(PMe₃)₄]Cl with one molar equivalent of 3-R, 5-R'PzLi in Et₂O at -78 °C as shown in Scheme 3.6. Filtration of insoluble LiCl from the supernatant and recrystallization from hexane gave all three products as light yellow crystalline solids in high yields (60-80%).

All three complexes are air and moisture sensitive and react quickly in solution and in the solid state upon exposure to atmosphere.



Scheme 3.6 Synthesis of rhodium trimethylphosphine pyrazolate complexes.

Complex **3-14** crystallizes in the space group $P2_1/c$ with four molecules per unit cell. The geometry of the central Rh atom is a distorted *pseudo* square plane. The two mutually *trans* trimethylphosphine ligands are skewed away from the coordinated Pz ligand ($\text{P}(1) - \text{Rh} - \text{P}(2) = 165.602(17)^\circ$) in order to relieve steric strain, while the $\text{N}(1) - \text{Rh} - \text{P}(3)$ angle is $176.49(4)^\circ$. The Rh – P distances for the two mutually *trans* ligands are longer ($2.3089(4)$ Å, av.) than that of the Rh – P(3) interaction ($2.2294(4)$ Å). This difference is attributable to the *trans* influence of the more π -basic pyrazolate ligand and is common in many square planar phosphine complexes of this type. The Rh – N distance of $2.0971(14)$ Å is typical of other reported Rh(I) amine complexes, and it is noteworthy that the nitrogen atom in the asymmetrically substituted pyrazolate that is bound to the metal is the one distal to the CF_3 group.

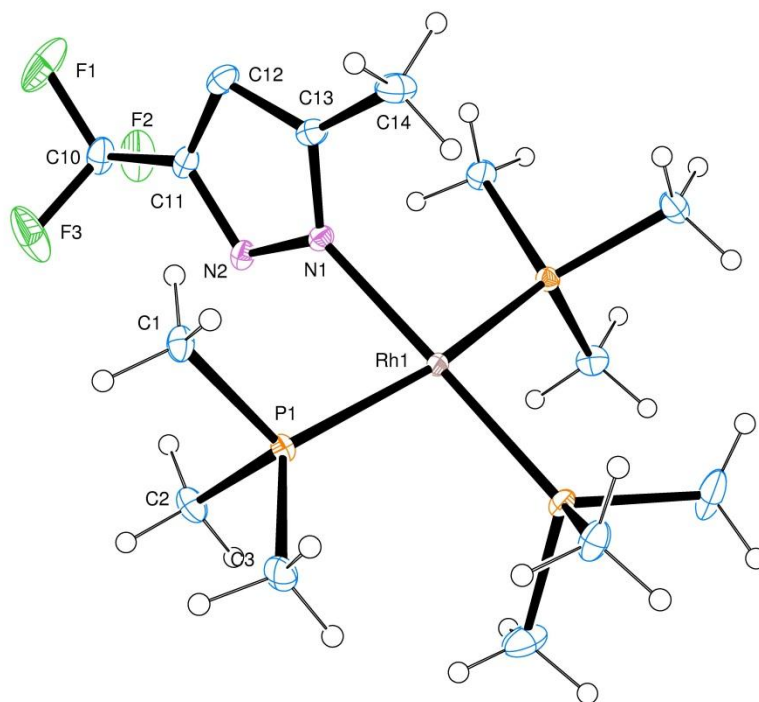


Figure 3.20 ORTEP diagram and partial atom numbering scheme of $\text{Rh}(\text{PMe}_3)_3(3\text{-(CF}_3\text{)}, 5\text{-(CH}_3\text{)Pz})$ (**3-14**). Thermal ellipsoids are drawn at the 30% probability level.

The ^1H NMR spectrum of **3-14** in C_6D_6 shows two resonances at 0.77 ppm and 0.94 ppm corresponding to the mutually *trans* PMe_3 ligands and the PMe_3 ligand *trans* to the pyrazolate ligand, respectively. Singlets farther downfield at 2.45 ppm and 6.58 ppm arise from the methyl protons and the aromatic protons on the pyrazolate ligand, respectively. The ^{31}P NMR spectrum consists of a doublet of triplets centered at -3.75 ppm ($J_{\text{P-Rh}} = 148.0$ Hz, $J_{\text{P-P}} = 46.5$ Hz) and a doublet of doublets at -11.40 ppm ($J_{\text{Rh-P}} = 135.8$ Hz, $J_{\text{P-P}} = 44.3$ Hz). These resonances appear in a 1:2 ratio and correspond to the PMe_3 ligand *trans* to the pyrazolate ligand and the two mutually *trans* PMe_3 ligands, respectively. A singlet in the ^{19}F NMR spectrum at -58.8 ppm corresponds to the CF_3

functionality on the pyrazolate ligand. Complex **3-14** was found to sublime at 72 °C under reduced pressure (sealed tube, 10^{-2} Torr).

Similarly to complex **3-14**, complex **3-15** was isolated as yellow crystals from the reaction of $[\text{Rh}(\text{PMe}_3)_4]\text{Cl}$ with one equivalent of 3,5- $(\text{CH}_3)_2\text{PzLi}$ in Et_2O at -78 °C. The X-ray crystal structure is presented in Figure 3.21, while crystallographic details are given in Table 3.6 and selected bond lengths and angles are given in Table 3.23. Complex **3-15** crystallizes in the triclinic space group with $P\bar{1}$ with one independent molecule in the asymmetric unit and two in the unit cell. The complex is isostructural with complex **3-14**, with the central Rh coordinated to three PMe_3 molecules as well as a Pz ligand. A difference in Rh – P bond lengths is found in complex **3-15** as well, with Rh – P = 2.226(2) Å for the PMe_3 group *trans* to the Pz ligand and Rh – P = 2.313(2) Å for the mutually *trans* PMe_3 groups.

Each asymmetric unit contains a $\text{Rh}(\text{PMe}_3)_3(\text{Pz})$ moiety as well as one molecule of free pyrazole. This free ligand interacts with the metal complex via H-bonding interactions with the metal bound pyrazolate ligand. A list of hydrogen-bond lengths and angles found in complex **3-15** is presented in Table 3.24. This intermolecular hydrogen bonding is present solution as confirmed by the ^1H NMR spectrum of **3-15**. Four equal intensity singlets appear in the range of 2.10 ppm – 2.36 ppm and correspond to the four different chemical environments for the methyl groups of the pyrazolate and pyrazole molecules. A doublet centered at 1.40 ppm and a multiplet at 1.51 ppm arise due to the PMe_3 group *trans* to the pyrazolate ligand and the two PMe_3 groups mutually *trans* to each other, respectively. Two resonances in the $^{31}\text{P}\{^1\text{H}\}$ NMR - a doublet of triplets centered at 7.33 ppm ($J_{\text{P-Rh}} = 139.6$ Hz, $J_{\text{P-P}} = 28.2$ Hz) and a doublet of doublets at -8.19 ppm ($J_{\text{P-Rh}} = 83.9$ Hz, $J_{\text{P-P}} = 28.2$ Hz) appear in a 1:2 ratio and represent the PMe_3 ligand *trans* to the pyrazolate and the mutually *trans* PMe_3 ligands, respectively. A broad band

in the IR spectrum of **3-15** centered at 3398 cm^{-1} is indicative of an N-H stretch. The complex sublimes under reduced pressure (sealed tube, 10^{-2} Torr) at $104\text{--}105\text{ }^{\circ}\text{C}$.

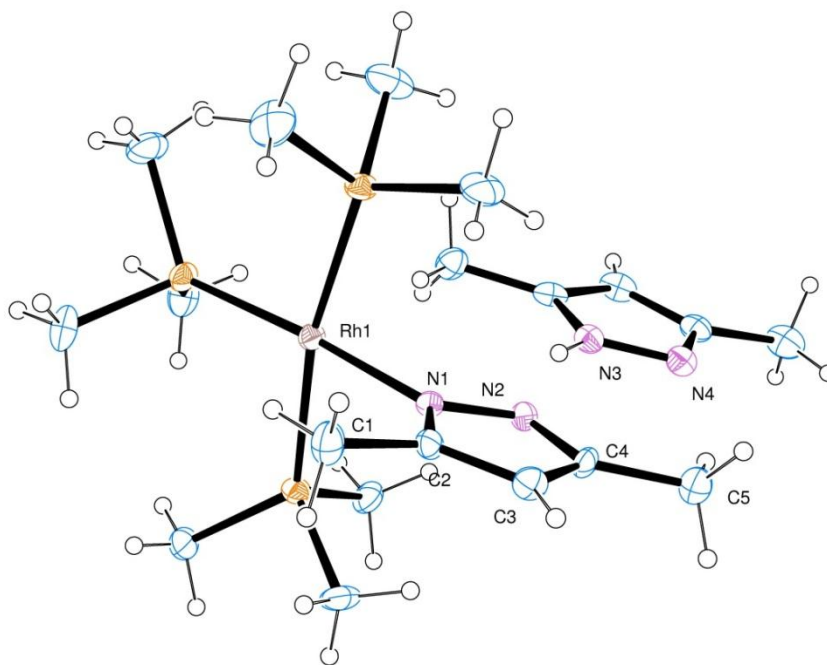


Figure 3.21 ORTEP diagram and partial atom numbering scheme of $\text{Rh}(\text{PMe}_3)_3(3,5\text{-(CH}_3)_2\text{Pz)} \cdot (3,5\text{-(CH}_3)_2\text{PzH)}$ (**3-15**). Thermal ellipsoids are drawn at the 30% probability level.

Complex **3-16** was synthesized and structurally characterized previously in these laboratories by the addition of six equivalents of PMe_3 to $[\text{Rh}(\mu\text{-}3,5\text{-(CF}_3)_2\text{Pz})(\text{COD})]_2$ in toluene.³⁵ As an alternative synthesis in this work, the complex was synthesized by the salt exchange reaction of $[\text{Rh}(\text{PMe}_3)_4]\text{Cl}$ with $3,5\text{-(CF}_3)_2\text{PzLi}$ in Et_2O at $-78\text{ }^{\circ}\text{C}$ as outlined in Scheme 3.6. ^1H and $^{31}\text{P}\{^1\text{H}\}$ NMR spectroscopic data and melting point ($100\text{--}103\text{ }^{\circ}\text{C}$ (subl.) at 10^{-2} Torr in a sealed tube) confirm the identity of $\text{Rh}(\text{PMe}_3)_3(\text{Pz})$ as the major product of the reaction.

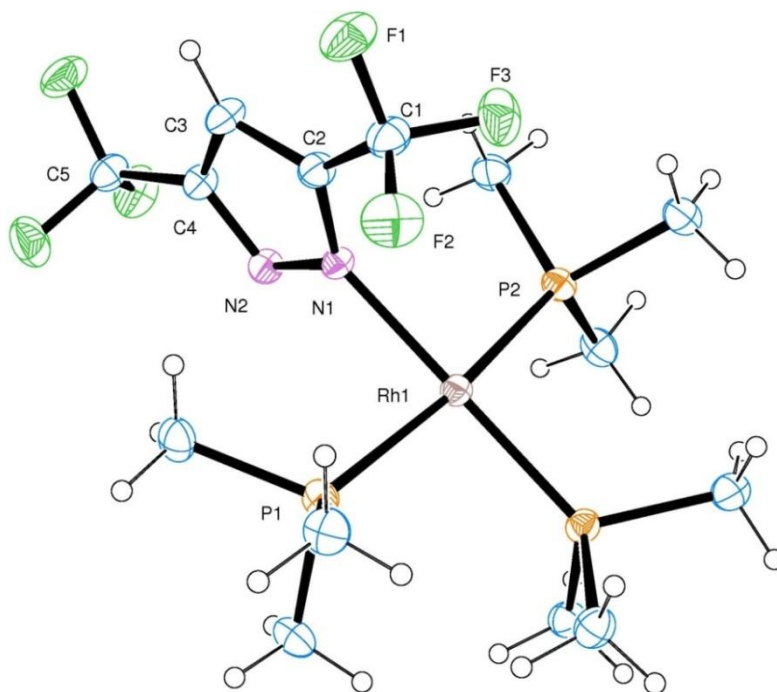


Figure 3.22 ORTEP diagram and partial atom numbering scheme of $\text{Rh}(\text{PMe}_3)_3(3,5\text{-(CF}_3)_2\text{Pz)}$ (**3-16**). Thermal ellipsoids are drawn at the 30% probability level.

There is very little variation in the metric parameters of the three complexes of the form $\text{Rh}(\text{PMe}_3)_3(\text{Pz})$. One interesting exception is the distance of the Rh-N bond formed between the central rhodium ion and the coordinating nitrogen atom of the pyrazolate ion observed for each complex. This distance is observed to lengthen as the basicity of the pyrazolate ligand decreases in the order $(\text{CH}_3)_2\text{Pz} > (\text{CF}_3, \text{CH}_3)\text{Pz} > (\text{CF}_3)_2\text{Pz}$ upon progressive incorporation of electron withdrawing (CF_3) functionality onto the Pz ring. The corresponding Rh-N bond lengths are 2.078(4) Å, 2.0971(14) Å, and 2.108(3) Å for **3-15**, **3-14** and **3-16**, respectively.

Complexes **3-14**, **3-15** and **3-16** were tested for use as CVD precursors as they all exhibited low sublimation temperatures under reduced pressure. However this was limited by their extreme reactivity, as preliminary results indicated significant decomposition upon heating under flowing H₂ in the CVD reactor and subsequently an insufficient amount of precursor vapor reached the deposition zone to afford film growth. Thus further deposition studies of these and similar complexes will likely require the use of an inert carrier gas, or alternatively a co-deposition system in which H₂ is introduced at the deposition stage.

Rhodium CVD film growth and characterization

Complexes **3-2**, **3-4**, and **3-5** showed appreciable volatility at 10⁻² Torr, and were further investigated for deposition experiments. Typical CVD experimental conditions and compositions of Rh thin films are shown in Table 3.0 which also contains data on films grown from other precursors in previous studies for comparison. All deposition experiments were performed in a horizontal hot-wall CVD reactor with ultra-high purity hydrogen as the carrier gas. In a typical deposition, a saturator tube was charged with approximately 10-20 mg of sample and the gas flow rate was varied to allow for optimal film growth. Each precursor was heated to a temperature deemed adequate to sufficiently volatilize the complex, while the deposition chamber was maintained at the lowest temperature in which deposition occurred.

All three precursors produced lustrous films that adhered well to the substrate. Typical X-ray diffraction patterns of films deposited under H₂ are shown in Figure 3.23. Broad peaks observed at 2 Θ = 41° and 47° correspond to the (111) and (200) planes of ccp Rh, respectively. Crystallite size was estimated for each film from the Scherrer

equation using the two most intense reflections, and was found to be between 8 and 12 nm. Complex **3-5** showed a significantly higher sublimation temperature than **3-2** and **3-4**, and required a higher temperature to affect deposition. The film deposited from complex **3-5** showed a slight increase in grain size due to the higher deposition temperature of 550 °C.

Precursor	Carrier gas	Precursor Temp.(°C)	Deposition Temp.(°C)	Film Composition (at. %)			Ref.
				Rh	C	O	
3-2	H ₂	140	400	91	5	4	this work
3-4	H ₂	180	400	82	15	3	this work
3-5	H ₂	210	550	72	24	4	this work
Rh ₂ (μ-Cl) ₂ (CO) ₄	H ₂	-	180	91	7	2	6a
RhCp(CO) ₂	H ₂	-	180	89	7	4	6a
RhCp(COD)	H ₂	-	230	97	3	0	6a
Rh(allyl)(CO) ₂	H ₂	-	180	94	6	0	6a
Rh(allyl) ₃	H ₂	-	130	96	4	0	6a
Rh(acac) ₃	O ₂	-	250	96	2	2	6c

Table 3.0 Summary of deposition conditions and film composition for Rh films deposited in this work as well as from other precursors suitable for CVD of Rh thin films.

Film thicknesses and morphology were investigated by X-ray reflectivity measurements as well as cross-sectional SEM. Figure 3.24 shows the surface morphology of a typical film deposited from complex **3-4**. Average grain size for all films is estimated to be 30-50 nm from HR-SEM images. X-ray photoelectron spectra of the films (Figure 3.25) determined the positions of the Rh $3d_{3/2}$ and $3d_{5/2}$ peaks at 311.9 eV and 307.2 eV, respectively, which are in good agreement with the binding energy for elemental rhodium. The peaks show very little asymmetry, indicative of a single electronic

environment for the metal. Low intensity peaks in the carbon and oxygen regions were detected throughout the thickness of the films. The C 1s peak consists of two well-resolved peaks corresponding to graphitic (higher BE) and carbidic (lower BE) carbon, though evidence for Rh-C bonding was not detected from BE shift in the Rh 3*d* region.

Depth profiling of the films revealed a significant drop off of carbon and oxygen after ca. 100 seconds of gentle Ar⁺ sputtering, indicating that the major source for these elements was adventitious surface adsorption from handling in the atmosphere. However both elements were present in the range of 5 – 24 at. % for carbon and 3 - 4 at. % for oxygen throughout the interior of the films. Nitrogen and fluorine 1s peaks were not apparent, indicating that N and F content is below the detection limit for all films. Though oxygen contamination remained approximately constant for each film, the carbon content of the film grown from complex **3-2** (5 at. %) was noticeably lower compared to the films grown from **3-4** and **3-5** (15 and 24 at. %, respectively). It seems likely that the increased mol. % carbon in films grown from **3-4** and **3-5** is due to the presence of the ^tBu groups in their Pz ligands. However, despite not having the highest mol % carbon in the precursor, the film from complex **3-5** showed the highest levels of carbon. This could be due to the higher deposition temperature required to afford film growth for **3-5**. At the higher temperature an increased level of ligand decomposition should be expected.

As shown in the depth profile in Figure 3.26, further sputtering revealed the very gradual appearance of a signal due to Si concomitant with a diminishing signal due to Rh. Furthermore the appearance and slow increase in intensity of a small shoulder of higher BE on the Rh 3*d* feature indicates a change in chemical environment for the metal corresponding to the dissolution of Rh into the Si of the substrate.

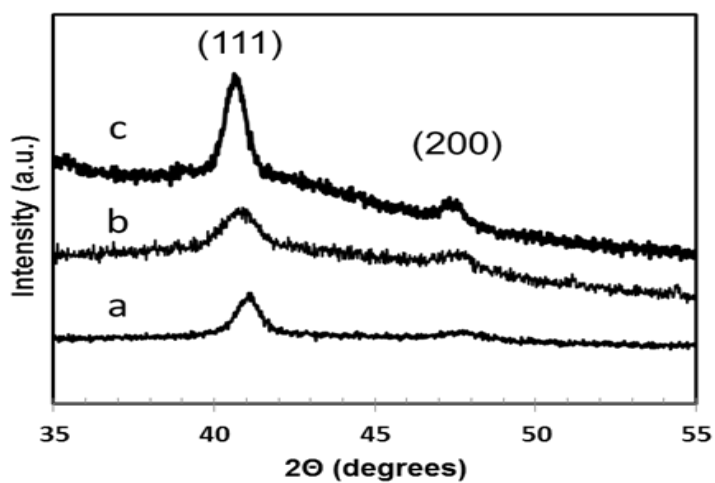


Figure 3.23 X-ray diffraction patterns of as-deposited Rh films grown from complexes **3-2** (a), **3-4** (b), and **3-5** (c). The patterns are vertically shifted for comparison.

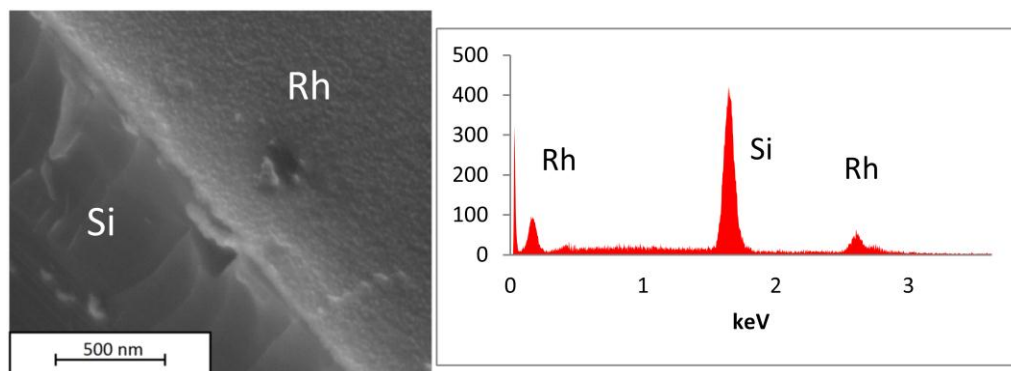


Figure 3.24 SEM micrograph and EDX spectrum of a typical Rh film grown from complex **3-4**.

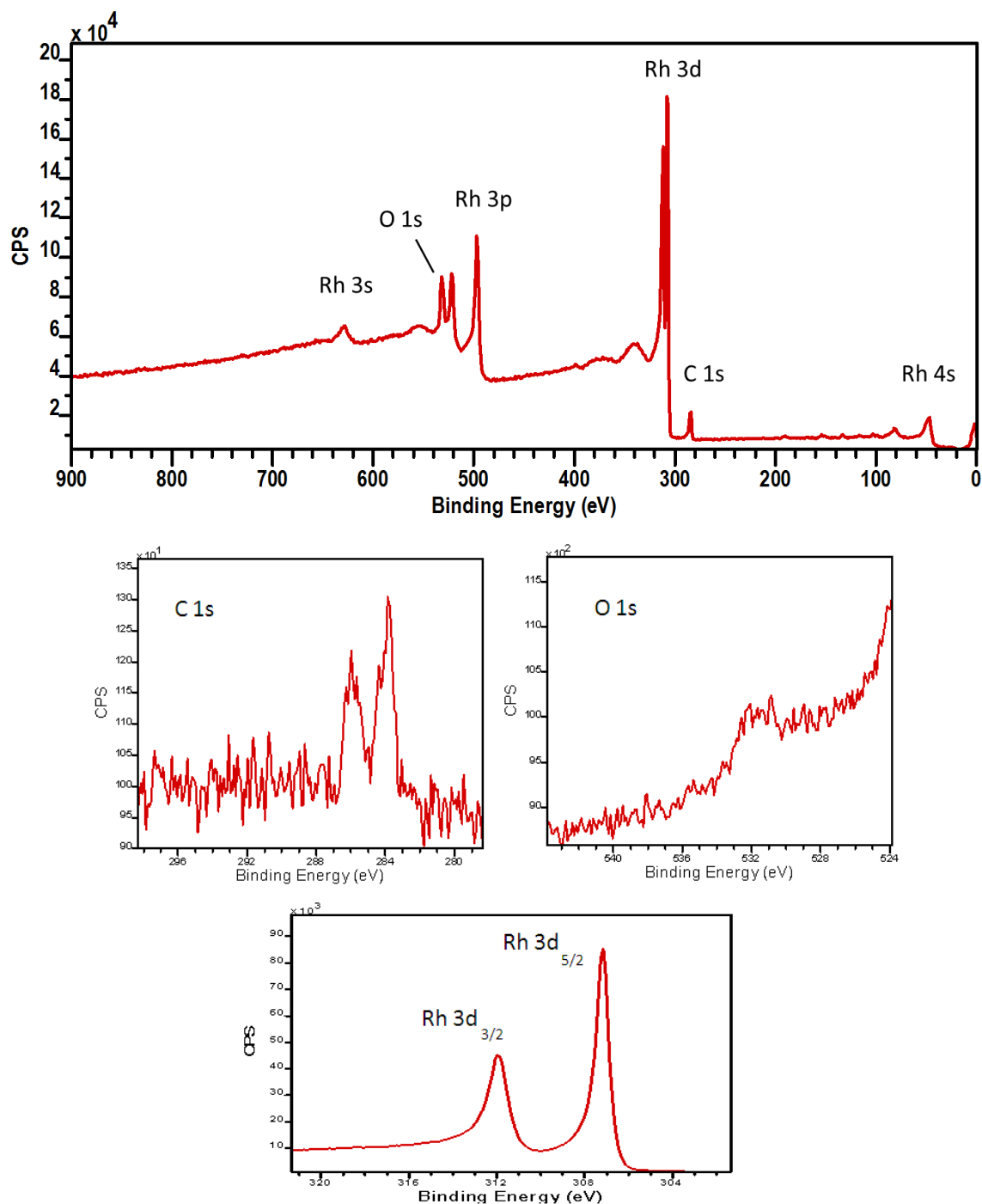


Figure 3.25 XP survey spectrum (top) and high resolution Rh, C, and O spectra after 100 seconds of Ar^+ sputtering (bottom) of a representative Rh film grown from complex **3-2** at 400 °C.

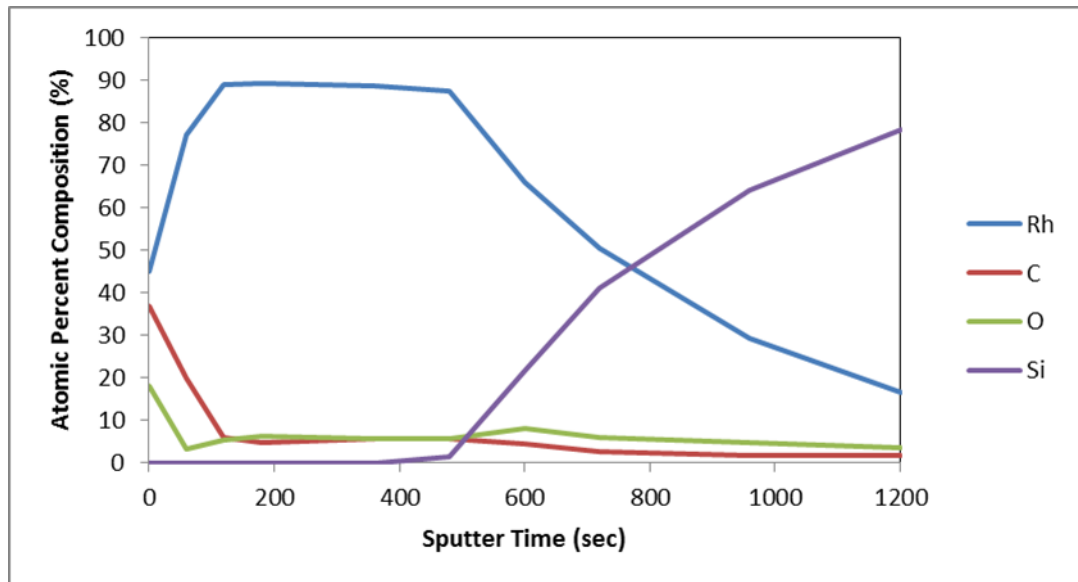


Figure 3.26 XPS depth profile of a Rh film grown from complex **3-2** at 400 °C showing atomic percent of Rh, C, O, and Si.

CONCLUSIONS

Several homoleptic and heteroleptic rhodium pyrazolate complexes have been synthesized and structurally characterized. A rare example of mononuclear Rh(II) complex forms from the interaction of anhydrous RhCl_3 with $3,5\text{-(CF}_3)_2\text{PzLi}$. Under similar preparative procedures, but with $\text{Rh}_2(\text{OAc})_4$ as the starting rhodium reagent, several novel diamagnetic Rh(II) paddlewheel complexes were isolated. Variation of the substituents at the 3 and 5 positions of the pyrazolate ligand drastically affects the thermal properties of the resulting metal complexes. Complexes **3-2**, **3-3**, **3-4**, and **3-5** were evaluated for their use as low-pressure CVD precursors, and successfully produced rhodium thin films when deposited at various temperatures using H_2 as a carrier gas.

EXPERIMENTAL DETAILS

General synthesis

Unless otherwise noted, all reactions were performed under a dry, oxygen-free nitrogen atmosphere or under vacuum using standard Schlenk line and dry box techniques. All solvents were dried prior to use by distillation from molten sodium or sodium benzophenone ketyl under nitrogen. 3,5-bis(trifluoromethyl) pyrazole,³⁶ 3,5-di-*tert*-butylpyrazole,³⁷ 3-trifluoromethyl, 5-methyl pyrazole,²⁷ and 3-trifluoromethyl, 5-*tert*-butyl pyrazole³⁸ were prepared according to literature procedures. Microanalyses (C, H, N) were performed by Galbraith Laboratories of Knoxville, TN or QTI Labs of Whitehouse, NJ. Melting points were determined in sealed capillaries under N₂ (1 atm.) on an Electrothermal Melting Point apparatus and are uncorrected. ESI mass spectra were collected on a Finnigan MAT TSQ 700 mass spectrometer. NMR spectra were recorded on a Varian 300 Unity Plus spectrometer (300 MHz at 298 K). Chemical shifts are referenced to the deuterated solvent. Infrared spectra were taken on a Nicolet IR 200 FTIR spectrometer between KBr plates.

Thin film deposition studies

Films were grown in a horizontal, hot-wall CVD reactor consisting of an approximately 2" diameter Pyrex tube heated by a tube furnace. The precursor was heated in a saturator tube connected to the deposition assembly by VCR and Swagelok type connections. Ultra high purity hydrogen (99.999%) was used as the carrier gas at flow rates of 5-50 sccm controlled by a Fathom Technologies mass flow controller, with the overall pressure of the system maintained between 0.5 and 2 Torr. The temperature of the precursor was controlled by an oil bath, while the lines were heated separately with

insulated heating tape. Films were grown on Si(100) wafers with native oxide cut into approximately 1 cm × 1 cm squares. The wafers were prepared by sequentially sonicating in hexane, isopropanol, and DI water, and then drying at 120 °C for 1 hour. XPS measurements were carried out on a Kratos AXIS Ultra DLD (monochromatic Al K α), and depth profiling was achieved by sputtering the film with 4 kV Ar⁺. X-ray diffraction patterns were collected on a Bruker Nonius D8-ADVANCE. Film thicknesses were determined using cross-sectional SEM (Hitachi S-5500, FEI Quanta 650).

X-band EPR studies

EPR data were collected on a Bruker EMX Pro with a liquid nitrogen cooled cryostat. Samples dissolved in dry, degassed toluene were transferred to a quartz EPR tube and quickly frozen and immediately used.

Electrochemical studies

All electrochemical studies of complex **3-1** were performed in 0.1 M [TBA][PF₆] in methylene chloride or acetonitrile under a nitrogen atmosphere in a dry-box using a GPES system from Eco. Chemie B. V. Cyclic voltammograms were recorded against a ferrocene external standard with a Ag/AgNO₃ non-aqueous reference electrode, a Pt button working electrode (1.6 mm diameter), and a Pt wire coil counter electrode.

DFT calculations

All calculations were performed with the Gaussian 03 suite of programs.³⁹ Initial atomic coordinates from the X-ray crystallographic data were input and the geometry was optimized using the B3LYP hybrid density functional method⁴⁰ with the LANL2DZ basis set.⁴¹ A single point energy calculation was performed at the same level of theory on the geometry optimized structures to produce graphical representations of molecular orbitals (all calculated with a 0.04 isovalue).

Single crystal X-ray crystallography

All crystals were covered in mineral oil and mounted on a nylon thread loop. Crystallographic data were collected on either a Nonius Kappa CCD diffractometer using a graphite monochromator with MoK α radiation ($\lambda = 0.71073\text{\AA}$) at reduced temperature using an Oxford Cryostream low temperature device or a Rigaku AFC12 diffractometer with a Saturn 724+ CCD using a graphite monochromator with MoK α radiation at reduced temperature using a Rigaku XStream low temperature device. Data reduction was performed with either DENZO-SMN or Rigaku Americas Corporation's Crystal Clear version 1.40. All structures were solved by direct methods using SIR2004 and refined by full-matrix least squares on F^2 with anisotropic displacement parameters for the non-H atoms using SHELXL-97. Hydrogen atoms on carbon were calculated in idealized positions with isotropic displacement parameters set to $1.2 \times U_{eq}$ of the attached atom ($1.5 \times U_{eq}$ for methyl hydrogen atoms). The function $\sum w(|F_o|^2 - |F_c|^2)^2$, was minimized, where $w = 1/[(\sigma(F_o))^2 + (0.0528 \cdot P)^2 + (0.685 \cdot P)]$ and $P = (|F_o|^2 + 2|F_c|^2)/3$. Neutral atom scattering factors and values used to calculate the linear absorption coefficient are from the International Tables for X-ray Crystallography. All figures were generated using SHELXTL/PC.

Synthesis of $[\text{Li}(\text{THF})]_2 \text{Rh}(\mu\text{-3,5-(CF}_3)_2\text{Pz})_4$ (3-1)

A solution of *n*-butyllithium (0.95 mL, 1.6 M) in hexane was added dropwise to a solution of 3,5-bis(trifluoromethyl)pyrazole (0.31 g, 1.51 mmol) in THF (25 mL) at -78 °C. This was allowed to warm to room temperature and was then stirred for 3 hours. This solution was added dropwise to a heterogeneous solution of anhydrous RhCl_3 (from 0.1 g $\text{RhCl}_3 \cdot n\text{H}_2\text{O}$ (0.38 mmol) dried with 0.2 mL SOCl_2) in diethyl ether (50 mL). The resulting reaction mixture was stirred for 12 h at room temperature. During this time, the color of the mixture changed from red to dark yellow. The mixture was then filtered. The filtrate was evaporated to dryness under vacuum and the residue was extracted with hexane (3×10 mL). The extracts were combined and X-ray quality crystals were grown by slow evaporation of this yellow solution under N_2 . Isolated: 0.18 g, 44 %; mp 126-127 °C. (dec.); $^1\text{H-NMR}$ (300 MHz, δ , CDCl_3): 6.59 (s, br, Pz-*H*), 3.46 (s, br, $\text{THF-CH}_2\text{O}$), 1.85 (s, br, THF-CH_2); $^{19}\text{F}\{^1\text{H}\}\text{-NMR}$ (CDCl_3): δ -60.7 (s, br), -61.2 (s, br); FT-IR (KBr, cm^{-1}): 1016 (s), 1128 (m), 1261 (w), 2964 (w), 1379 (m), 1450 (m); HRMS (chemical ionization) m/e 1005 [$\text{M}^+ - \text{CF}_3$], 859 [$\text{M}^+ - \text{CF}_3 - 2 \text{ THF}$], 769 [$\text{M}^+ - 2\text{CF}_3 - 2 \text{ THF} - \text{Li}$].

Synthesis of $\text{Rh}_2(\mu\text{-3,5-(CF}_3)_2\text{Pz})_4 \cdot 2 \text{ H}_2\text{O}$ (3-2)

A solution of *n*-butyllithium (0.8 mL, 1.6 M) in hexane was added dropwise to a solution of 3,5-bis(trifluoromethyl)pyrazole (0.24 g, 1.17 mmol) in diethyl ether (25 mL) at -78 °C. This was allowed to warm to room temperature, and was stirred for 3 hours. This solution was then added dropwise to a heterogeneous solution of anhydrous rhodium acetate (0.13 g, 0.29 mmol) in diethyl ether (50 mL). The resulting reaction mixture was stirred for 12 h at room temperature, and then filtered. The filtrate was evaporated to dryness under vacuum and the yellow brown residue was extracted with hexane (3×10 mL) and then filtered through a short bed of Celite (2 cm). Orange X-ray quality crystals

were grown from this solution at -30 °C. Suitable crystals may also be grown by sublimation under vacuum at 140 °C in a sealed glass tube. Isolated: 0.19 g, 64 %; mp 139-141 °C. (subl., 10⁻² Torr); ¹H-NMR (300 MHz, δ, CDCl₃): 6.37 (s), 1.58 (s, br); ¹⁹F{¹H}-NMR (CDCl₃): δ -61.80 (s); FT-IR (KBr, cm⁻¹): 3601 (w), 3159 (w), 2920 (m, br), 2851 (m), 2117 (s), 1260 (m), 1138 (m), 1021 (m). HRMS (chemical ionization) *m/e*: 1017.8278 [M⁺ - 2 H₂O], 998.8300 [M⁺ - F - 2 H₂O]. Calcd. for C₂₀H₈F₂₄N₈O₂Rh₂: C, 23.59; H, 0.40; N, 11.01 %. Found: C, 22.56; H, 0.42; N, 11.36 %.

Synthesis of Rh₂(μ-3,5-(CF₃)₂Pz)₄ · 2 CH₃CN (3-3)

To a solution of 0.050 g of **3-2** in hexane (10 mL) was added dry, degassed acetonitrile (1 mL). The orange solution immediately turned yellow. Yellow block crystals developed after slow evaporation of this solution. Isolated: 0.48 g, 90 %; mp 219 - 220 °C. (1 atm. N₂, dec.); ¹H-NMR (300 MHz, δ, CDCl₃): 6.30 (s, 4 H), 2.68 (s, 6 H); ¹⁹F{¹H}-NMR (CDCl₃): δ -61.62 (s); FT-IR (KBr, cm⁻¹): 2917 (w), 1538 (m), 1493 (m), 1272 (s), 1222 (s), 1132 (s), 1021 (s), 811 (m). HRMS (chemical ionization) *m/e*: 1058.8578 [M⁺ - H₃CCN], 1039.8574 [M⁺ - H₃CCN - F], 1017.8280 [M⁺ - 2 H₃CCN]. Calcd. for C₂₄H₁₀F₂₄N₁₀Rh₂: C, 26.20; H, 0.92; N, 12.73 %. Found: C, 26.17; H, 0.67; N, 12.83 %.

Synthesis of Rh₂(μ-3,5-(^{*t*}Bu)₂Pz)₄ (3-4)

A solution of *n*-butyllithium (1.5 mL, 1.6 M) in hexane was added dropwise to a solution of 3,5-di-*tert*-butylpyrazole (0.424 g, 2.35 mmol) in diethyl ether (25 mL) at -78 °C. This was allowed to warm to room temperature and was further stirred for 3 hours. This solution was then added dropwise to a heterogeneous suspension of anhydrous

rhodium acetate (0.254 g, 0.57 mmol) in diethyl ether (50 mL). After several minutes of stirring, the color of the mixture became forest green and more homogeneous. The resulting reaction mixture was stirred for 12 h at room temperature and was then filtered. The filtrate was evaporated to dryness under vacuum and the residue was extracted with hexane (3 × 10 mL) and then filtered through a short bed of Celite (2 cm). Green X-ray quality crystals were grown from this solution at -30 °C. Suitable crystals may also be grown by sublimation under vacuum at 180 °C in a sealed glass tube. Isolated: 0.40 g, 75 %; mp 180-182 °C. (subl., 10⁻² Torr); ¹H-NMR (300 MHz, δ, CD₂Cl₂): 5.92 (s, 4 H), 1.29 (s, 72 H); FT-IR (KBr, cm⁻¹): 2943 (m, br), 1412 (m), 1352 (m), 1217 (w). HRMS (chemical ionization) *m/e*: 922.4295 [M⁺]. Calcd. for C₄₄H₇₆N₈Rh₂: 922.4303.

Synthesis of Rh₂(μ-3-(CF₃),5-(^tBu)Pz)₄ (3-5)

A solution of *n*-butyllithium (1.2 mL, 1.6 M) in hexane was added dropwise to a solution of 3-trifluoromethyl, 5-*tert*butylpyrazole (0.34 g, 1.89 mmol) in diethyl ether (25 mL) at -78 °C. This was allowed to warm to room temperature and was further stirred for 3 hours. This solution was then added dropwise to a heterogeneous solution of anhydrous rhodium acetate (0.19 g, 0.43 mmol) in diethyl ether (50 mL). The resulting reaction mixture was stirred for 12 h at room temperature, and was then filtered. The filtrate was evaporated to dryness under vacuum and the brown residue was extracted with hexane (3 × 10mL) and filtered through a short bed of Celite (2 cm). Green X-ray quality crystals were grown from this solution after one week at -30 °C. Isolated: 0.31 g, 72 %; mp 210-212 °C. (subl., 10⁻² Torr); ¹H-NMR (300 MHz, δ, CDCl₃): 5.85 (s, 4 H), 1.34 (s, 36 H); ¹⁹F{¹H}-NMR (CDCl₃): δ -58.71 (s); FT-IR (KBr, cm⁻¹): 2920 (w), 1701 (m), 1256 (s), 1121 (s). HRMS (chemical ionization) *m/e*: 970.1292 [M⁺], 955.1057 [M⁺ -

CH₃], 951.1306 [M⁺ - F]. Calcd. for C₃₂H₄₀F₁₂N₈Rh₂: C, 39.60; H, 4.15; N, 11.55 %. Found: C, 41.08; H, 4.21; N, 11.50 %.

Synthesis of Rh₂(μ-3-(CF₃),5-(CH₃)Pz)₄ · 2 CH₃CN (3-6)

A solution of *n*-butyllithium (1.4 mL, 1.6 M) in hexane was added dropwise to a solution of 3-trifluoromethyl, 5-methylpyrazole (0.33 g, 2.2 mmol) in diethyl ether (25 mL) at -78 °C. This was allowed to warm to room temperature and was further stirred for 3 hours. This solution was then added dropwise to a heterogeneous solution of anhydrous rhodium acetate (0.237 g, 0.54 mmol) in diethyl ether (50 mL). The resulting reaction mixture was stirred for 12 h at room temperature, and was then filtered. The filtrate was evaporated to dryness under vacuum and the dark residue was extracted with hexane (3 × 10 mL) and filtered through a short bed of Celite (2 cm). Solvent was evaporated to dryness, leaving a green solid. The residue was taken up in dry, degassed acetonitrile and yellow X-ray quality crystals were grown from this solution after one week at -30 °C. Isolated: 0.19 g, 45 %; mp 145-147 °C. (1 atm. N₂, dec.); ¹H-NMR (300 MHz, δ, CDCl₃): 5.72-5.63 (m, 4 H), 2.57 (s, 3 H), 2.54 (s, 3 H), 2.15-2.07 (m, 12 H); ¹⁹F{¹H}-NMR (CDCl₃): δ -60.34 - -60.84 (m); FT-IR (KBr, cm⁻¹): 2930 (w), 1576 (w), 1430 (w), 1240 (s), 1164 (m), 1121 (s), 1003 (m), 791 (w). MS (chemical ionization) *m/e*: 843 [M⁺ - CH₃CN], 802 [M⁺ - 2 CH₃CN], 783 [M⁺ - 2 CH₃CN - F].

Synthesis of Rh₂(O₂CCH₃)₄ · 2 (3,5-(CF₃)₂PzH) (3-7)

To a suspension of anhydrous Rh₂(O₂CCH₃)₄ (0.1 g, 0.22 mmol) in toluene (50 mL) was added a solution of 3,5-bis(trifluoromethyl)pyrazole (0.092 g, 0.45 mmol) in toluene (50 mL). The mixture was heated to reflux under N₂ and gradually turned purple

and became more homogeneous. The mixture was cooled and filtered and X-ray quality crystals were recovered in several crops from the slow evaporation of this solution. Isolated: 0.18 g, 99 %; mp 128-141 °C. (10^{-2} Torr, gradual decomp.); ^1H -NMR (300 MHz, δ , CDCl_3): 7.19 (s, 2 H), 1.93 (s, 12 H); $^{19}\text{F}\{^1\text{H}\}$ -NMR (CDCl_3): δ -61.18 (s); FT-IR (KBr, cm^{-1}): 3229 (w), 3112 (w), 1599 (s), 1500 (w), 1410 (s), 1311 (m), 1264 (s), 1233 (w), 1154 (s), 1084 (m), 987 (s), 867 (m), 696 (m). MS (chemical ionization) m/e : 803 [M^+]. Calcd. for $\text{C}_{18}\text{H}_{16}\text{F}_{12}\text{N}_4\text{O}_8\text{Rh}_2$: C, 25.43; H, 1.90; N, 6.59 %. Found: C, 25.40; H, 1.64; N, 7.46 %.

Synthesis of $\text{Rh}_2(\text{O}_2\text{CCH}_3)_4 \cdot 2$ (3-(CF_3),5-($t\text{Bu}$)PzH) (3-8)

To a suspension of anhydrous $\text{Rh}_2(\text{O}_2\text{CCH}_3)_4$ (0.1 g, 0.22 mmol) in toluene (50 mL) was added a solution of 3-(trifluoromethyl),5-(*tert*-butyl)pyrazole (0.087 g, 0.45 mmol) in toluene (50 mL). The mixture was heated to reflux under N_2 and gradually turned purple and became more homogeneous. The mixture was cooled and filtered and X-ray quality crystals were recovered in several crops from the slow evaporation of this solution. Isolated: 0.17 g, 92 %; 133-136 °C. (10^{-2} Torr, gradual decomp.); ^1H -NMR (300 MHz, δ , CDCl_3): 6.67 (s, 2 H), 1.91 (s, 12 H), 1.45 (s, 18 H); $^{19}\text{F}\{^1\text{H}\}$ -NMR (CDCl_3): δ -61.09 (s); FT-IR (KBr, cm^{-1}): 3295 (m), 2972 (m), 1600 (s), 1564 (w), 1497 (m), 1435 (m), 1404 (m), 1348 (w), 1258 (s), 1182 (w), 1139 (s), 1086 (w), 1003 (m), 985 (m), 810 (m), 694 (m). MS (chemical ionization) m/e : 827 [M^+]. Calcd. for $\text{C}_{24}\text{H}_{34}\text{F}_6\text{N}_4\text{O}_8\text{Rh}_2$: C, 34.88; H, 4.15; N, 6.78 %. Found: C, 35.73; H, 4.10; N, 7.06 %.

Synthesis of $\text{Rh}_2(\text{O}_2\text{CCH}_3)_4 \cdot 2$ (3,5-*t*-Bu₂PzH) (3-9)

To a suspension of anhydrous $\text{Rh}_2(\text{O}_2\text{CCH}_3)_4$ (0.1 g, 0.22 mmol) in toluene (50 mL) was added a solution of 3,5-di-*tert*-butylpyrazole (0.81 g, 0.45 mmol) in toluene (50 mL). The mixture was heated to reflux under N_2 and gradually turned purple and became more homogeneous. The mixture was cooled and filtered and X-ray quality crystals were recovered in several crops from the slow evaporation of this solution. Isolated: 0.165 g, 91 %; 127-131 °C. (10^{-2} Torr, gradual decomp.); ^1H -NMR (300 MHz, δ , CDCl_3): 6.20 (s, 2 H), 1.89 (s, 12H), 1.48 (s, 36 H); FT-IR (KBr, cm^{-1}): 3345 (m), 2961 (m), 2868 (w), 1597 (s), 1558 (m), 1340 (s), 1363 (w), 1138 (w), 993 (s), 900 (s), 796 (m), 725 (s). MS (chemical ionization) m/e : 803 [M^+]. Calcd. for $\text{C}_{30}\text{H}_{52}\text{N}_4\text{O}_8\text{Rh}_2$: C, 44.90; H, 6.53; N, 6.98 %. Found: C, 43.39; H, 6.23; N, 6.58 %.

Synthesis of $\text{Rh}_2(\text{O}_2\text{CCF}_3)_4 \cdot 2$ (3,5-(CF_3)₂PzH) (3-10)

To a solution of anhydrous $\text{Rh}_2(\text{O}_2\text{CCF}_3)_4$ (0.1 g, 0.15 mmol) in methylene chloride (20 mL) was added 3,5-bis(trifluoromethyl)pyrazole (0.062 g, 0.30 mmol) in methylene chloride (20 mL). The dark green solution immediately turned purple and became more homogeneous. The mixture was filtered and X-ray quality crystals were recovered in several crops from the slow evaporation of this solution. Isolated: 0.15 g, 93 %; mp 148-150 °C (1 atm. N_2); 125-128 °C. (subl. 10^{-2} Torr); ^1H -NMR (300 MHz, δ , CDCl_3): 7.09 (s); $^{19}\text{F}\{^1\text{H}\}$ -NMR (CDCl_3): δ -58.71 (s); FT-IR (KBr, cm^{-1}): 3350 (w), 1652 (s), 1435 (m), 1351 (w), 1259 (m), 1307 (s), 1154 (s), 1073 (m), 989 (m), 844 (m), 714 (w). HRMS (chemical ionization) m/e : 1065.7767 [M^+]. Calcd. for $\text{C}_{18}\text{H}_4\text{F}_{24}\text{N}_4\text{O}_8\text{Rh}_2$: 1065.7756. Anal. Calcd. for $\text{C}_{18}\text{H}_4\text{F}_{24}\text{N}_4\text{O}_8\text{Rh}_2$: C, 20.28; H, 0.38; N, 5.26 %. Found: C, 18.65; H, 0.37; N, 5.43 %.

Synthesis of $\text{Rh}_2(\text{O}_2\text{CCF}_3)_4 \cdot 2$ (3-(CF_3),5-($t\text{-Bu}$)PzH) (3-11)

To a solution of anhydrous $\text{Rh}_2(\text{O}_2\text{CCF}_3)_4$ (0.1 g, 0.15 mmol) in methylene chloride (20 mL) was added 3-(trifluoromethyl),5-(*tert*-butyl)pyrazole (0.058 g, 0.30 mmol) in methylene chloride (20 mL). The dark green solution immediately turned purple and became more homogeneous. The mixture was filtered and X-ray quality crystals were recovered in several crops from the slow evaporation of this solution. Isolated: 0.12 g, 78 %; mp 136-138 °C (1 atm. N_2); 120-123 °C. (subl. 10^{-2} Torr); ^1H -NMR (300 MHz, δ , CDCl_3): 6.69 (s, 2 H), 1.45 (s, 18 H); $^{19}\text{F}\{^1\text{H}\}$ -NMR (CDCl_3): δ -61.69 (s, br), -74.95 (s); FT-IR (KBr, cm^{-1}): 3356 (m), 2971 (m), 1653 (s), 1497 (m), 1435 (m), 1257 (s), 1193 (s), 1141 (s), 989 (s), 863 (m), 814 (m), 711 (w). HRMS (chemical ionization) m/e : 1041.9253 [M^+]. Calcd. for $\text{C}_{24}\text{H}_{22}\text{F}_{18}\text{N}_4\text{O}_8\text{Rh}_2$: 1041.9260. Anal. calcd. for $\text{C}_{24}\text{H}_{22}\text{F}_{18}\text{N}_4\text{O}_8\text{Rh}_2$: C, 27.66; H, 2.13; N, 5.38 %. Found: C, 27.96; H, 1.75; N, 5.38 %.

Synthesis of $\text{Rh}_2(\text{O}_2\text{CCF}_3)_4 \cdot 2$ (3,5- $t\text{-Bu}_2$ PzH) (3-12)

To a solution of anhydrous $\text{Rh}_2(\text{O}_2\text{CCF}_3)_4$ (0.1 g, 0.15 mmol) in methylene chloride (20 mL) was added 3,5-di-*tert*-butylpyrazole (0.55 g, 0.30 mmol) in methylene chloride (20 mL). The dark green solution immediately turned purple and became more homogeneous. The mixture was filtered and X-ray quality crystals were recovered in several crops from the slow evaporation of this solution. Isolated: 0.13 g, 84 %; mp 145-146 °C (1 atm. N_2); 122-123 °C. (subl. 10^{-2} Torr); ^1H -NMR (300 MHz, δ , CDCl_3): 6.32 (s, 2 H), 1.46 (s, 36 H); $^{19}\text{F}\{^1\text{H}\}$ -NMR (CDCl_3): δ -74.95 (s); FT-IR (KBr, cm^{-1}): 3424 (s), 2964 (s), 2908 (m), 2871 (m), 1654 (s), 1562 (m), 1436 (s), 1366 (w), 1196 (s), 1164 (s), 1024 (w), 863 (w), 738 (m). HRMS (chemical ionization) m/e : 1018.0797 [M^+],

999.0808 [M⁺ - F]. Calcd. for C₃₀H₄₀F₁₂N₈O₈Rh₂: 1018.0765. Anal. calcd. for C₃₀H₄₀F₁₂N₄O₈Rh₂: C, 35.38; H, 3.96; N, 5.50 %. Found: C, 35.46; H, 3.60; N, 5.41 %.

Synthesis of *cis*-Cl₂Rh(3,5-(CF₃)₂Pz)(3,5-(CF₃)₂PzH)₃ (3-13)

To a suspension of anhydrous RhCl₃ (from 0.115 g RhCl₃ • nH₂O dried with 0.25 mL SOCl₂) in diethyl ether (50 mL) was added a solution of 3,5-dimethylpyrazole (0.167 g, 1.74 mmol) in THF (50 mL). A heterogeneous brown yellow mixture resulted. After stirring at room temperature for 1 hour, the mixture was cooled on a dry ice-acetone bath, and one molar eq. *n*-butyllithium (0.27 mL, 1.6M in hexane) was added. The solution immediately became yellow and more homogeneous. This was allowed to warm to room temperature and then stirred overnight. The solvent was removed completely *in vacuo* and the yellow residue was dissolved in dry, degassed toluene (100 mL). This was filtered and the solvent volume reduced *in vacuo*, and yellow crystals formed upon cooling this solution to -30 °C. Isolated: 0.16 g, 66 %; mp 113-114 °C. (1 atm. N₂); ¹H-NMR (300 MHz, δ, CDCl₃): 14.1 (br s, 1 H), 11.35 (br s, 1 H), 5.84 (s, 2 H), 5.78 (s, 2 H), 2.44 (s, 3 H), 2.23 (s, 6 H), 2.19 (s, 3 H), 1.94 (s, 6 H), 1.71 (s, 3 H), 1.05 (s, 3 H); FT-IR (KBr, cm⁻¹): 3390 (br, m), 3381 (m), 2984 (s), 2925 (w), 1576 (s), 1413 (m), 1277 (s), 1188 (w), 1149 (w), 1051 (m), 797 (m), 744 (s). Calcd. for C₂₇H₃₉Cl₂N₈Rh: C, 49.90; H, 6.05; N, 17.25 %. Found: C, 48.12; H, 5.83; N, 17.28 %.

Synthesis of Rh(PMe₃)₃(3-(CF₃),5-(CH₃)Pz) (3-14)

A solution of *n*-butyllithium (0.2 mL, 1.6 M) in hexane was added dropwise to a solution of 3-trifluoromethyl, 5-methylpyrazole (0.044 g, 0.29 mmol) in diethyl ether (25 mL) at -78 °C. This was allowed to warm to room temperature and was further stirred

for 3 hours. This solution was then added dropwise to a solution of $[\text{Rh}(\text{PMe}_3)_4]\text{Cl}$ (0.129 g, 0.29 mmol) in diethyl ether (100 mL). The resulting reaction mixture was stirred for 12 h at room temperature, and was then filtered. The filtrate was evaporated to dryness under vacuum and the yellow residue was extracted with hexane (3×10 mL) and filtered through a short bed of Celite (2 cm). X-ray quality crystals were grown from this solution after one week at -30 °C. Isolated: 0.1 g, 78 %; mp $72\text{--}73$ °C. (subl., 10^{-2} Torr); ^1H -NMR (300 MHz, δ , C_6D_6): 6.58 (s, 1 H), 2.45 (s, 3 H), 0.94 (d, $J = 7.0$ Hz, 9 H), 0.77 (s, 18 H); $^{19}\text{F}\{^1\text{H}\}$ -NMR (C_6D_6): δ -58.75 (s); $^{31}\text{P}\{^1\text{H}\}$ -NMR (C_6D_6): δ -3.75 (dt, $J_{\text{P-Rh}} = 148.0$ Hz, $J_{\text{P-P}} = 46.5$ Hz), -11.40 (dd, $J_{\text{Rh-P}} = 135.8$ Hz, $J_{\text{P-P}} = 44.3$ Hz); FT-IR (KBr, cm^{-1}): 2980 (w), 2916 (m), 1523 (w), 1486 (w), 1418 (m), 1302 (w), 1283 (w), 1237 (s), 1154 (m), 1108 (s), 949 (s), 857 (w), 771 (m), 668 (w). Calcd. for $\text{C}_{14}\text{H}_{31}\text{F}_3\text{N}_2\text{P}_3\text{Rh}$: C, 35.01; H, 6.51; N, 5.83 %. Found: C, 32.76; H, 6.19; N, 5.38 %.

Synthesis of $\text{Rh}(\text{PMe}_3)_3(3,5\text{-(CH}_3)_2\text{Pz})$ (3-15)

A solution of *n*-butyllithium (0.2 mL, 1.6 M) in hexane was added dropwise to a solution of 3,5-dimethylpyrazole (0.032 g, 0.33 mmol) in diethyl ether (25 mL) at -78 °C. This was allowed to warm to room temperature and was further stirred for 3 hours. This solution was then added dropwise to a solution of $[\text{Rh}(\text{PMe}_3)_4]\text{Cl}$ (0.147 g, 0.33 mmol) in diethyl ether (100 mL). The resulting reaction mixture was stirred for 12 h at room temperature, and was then filtered. The filtrate was evaporated to dryness under vacuum and the yellow residue was extracted with hexane (3×10 mL) and filtered through a short bed of Celite (2 cm). X-ray quality crystals were grown from this solution after one week at -30 °C. Isolated: 0.06 g, 33 %; mp $104\text{--}105$ °C. (subl. 10^{-2} Torr); ^1H -NMR (300 MHz, δ , C_6D_6): 5.59 (s, 1 H), 5.47 (s, 1 H), 2.36 (s, 3 H), 2.31 (s, 3 H), 2.27 (s, 3 H), 2.10

(s, 3 H), 1.50 (m, 18 H), 1.40 (d, $J = 10.6$ Hz, 9 H); $^{31}\text{P}\{^1\text{H}\}$ -NMR (C_6D_6): δ 7.32 (dt $J_{\text{P-Rh}} = 139.6$ Hz, $J_{\text{P-P}} = 28.9$ Hz), -8.23 (dd, $J_{\text{Rh-P}} = 83.9$ Hz, $J_{\text{P-P}} = 28.3$ Hz); FT-IR (KBr, cm^{-1}): 3398 (br, m), 2965 (w), 2914 (m), 1419 (m), 1286 (m), 950 (s), 801 (w), 734 (w).

Synthesis of $\text{Rh}(\text{PMe}_3)_3(3,5\text{-(CF}_3)_2\text{Pz)}$ (3-16)

A solution of *n*-butyllithium (0.2 mL, 1.6 M) in hexane was added dropwise to a solution of 3,5-bis(trifluoromethyl)pyrazole (0.067 g, 0.33 mmol) in diethyl ether (25 mL) at -78 °C. This was allowed to warm to room temperature and was further stirred for 3 hours. This solution was then added dropwise to a solution of $[\text{Rh}(\text{PMe}_3)_4]\text{Cl}$ (0.147 g, 0.33 mmol) in diethyl ether (100 mL). The resulting reaction mixture was stirred for 12 h at room temperature, and was then filtered. The filtrate was evaporated to dryness under vacuum and the yellow residue was extracted with hexane (3×10 mL) and filtered through a short bed of Celite (2 cm). X-ray quality crystals were grown from this solution after one week at -30 °C. Isolated: 0.14 g, 80 %; mp $100\text{--}103$ °C. (subl. 10^{-2} Torr); ^1H -NMR (300 MHz, δ , C_6D_6): 6.88 (s, 1 H), 1.02 (m, 9 H), 0.77 (m, 18 H); ^{19}F -NMR (C_6D_6): δ -58.71 (s), -60.05 (s); $^{31}\text{P}\{^1\text{H}\}$ -NMR (C_6D_6) δ -0.63 (dt, $J_{\text{P-Rh}} = 155.4$ Hz, $J_{\text{P-P}} = 46.3$ Hz), -10.80 (dd, $J_{\text{P-Rh}} = 142.2$ Hz, $J_{\text{P-P}} = 46.1$ Hz).

X-RAY CRYSTALLOGRAPHIC DETAILS

Table 3.1 Crystallographic details and refinement data for **3-1**, **3-2**, and **3-3**.

	3-1	3-2	3-3
Empirical formula	C ₂₈ H ₂₀ F ₂₄ Li ₂ N ₈ O ₂ Rh	C ₂₀ H ₈ F ₂₄ N ₈ O ₂ Rh ₂	C ₁₂ H ₅ F ₁₂ N ₅ Rh
Formula weight	1073.31	1054.16	550.12
Temperature	153(2) K	153(2) K	100(2) K
Wavelength	0.71073 Å	0.71073 Å	0.71073 Å
Crystal system	monoclinic	monoclinic	triclinic
Space group	<i>P</i> 2 ₁ / <i>n</i>	<i>P</i> 2 ₁ / <i>n</i>	<i>P</i> $\bar{1}$
Unit cell dimensions	a = 11.439(2) Å b = 9.2437(18) Å c = 19.437(4) Å α = 90° β = 106.65(3)° γ = 90°	a = 9.2451(11) Å b = 18.048(2) Å c = 9.3478(11) Å α = 90° β = 103.683(3)° γ = 90°	a = 9.359(2) Å b = 9.434(3) Å c = 10.913(2) Å α = 109.56(5)° β = 102.23(5)° γ = 92.58(5)°
Volume	1969.1(7) Å ³	1515.5(3) Å ³	880.2 Å ³
Z	2	2	2
Density (calculated)	1.810 Mg/m ³	2.310 Mg/m ³	2.076 Mg/m ³
Absorption coefficient	0.588 mm ⁻¹	1.277 mm ⁻¹	1.101 mm ⁻¹
F(000)	1054	1012	530
Theta range for data collection	3.11 to 25.00°	3.01 to 27.48°	3.01 to 27.46°
Index ranges	-13 ≤ h ≤ 13, -10 ≤ k ≤ 10, -23 ≤ l ≤ 23	-11 ≤ h ≤ 11, -23 ≤ k ≤ 23, -12 ≤ l ≤ 12	-12 ≤ h ≤ 12, -14 ≤ k ≤ 14
Reflections collected	6382	27098	25948
Independent reflections	3460 [R(int) = 0.0196]	3456 [R(int) = 0.0441]	4017 [R(int) = 0.0281]
Refinement method	Full-matrix least-squares on F ²	Full-matrix least-squares on F ²	Full-matrix least-squares on F ²
Data / restraints / parameters	3460 / 200 / 295	3456 / 0 / 255	4017 / 0 / 272
Goodness-of-fit on F ²	1.078	1.098	0.988
Final R ^a indices [I > 2σ(I)]	R ₁ = 0.0339 wR ₂ = 0.0820	R ₁ = 0.0260 wR ₂ = 0.0559	R ₁ = 0.0207 wR ₂ = 0.0494
R ^a indices (all data)	R ₁ = 0.0461 wR ₂ = 0.0882	R ₁ = 0.0292 wR ₂ = 0.0573	R ₁ = 0.0222 wR ₂ = 0.0500
Largest diff. peak and hole	0.630 and -0.435 e.Å ⁻³	0.449 and -0.542 e.Å ⁻³	0.563 and -0.468 e.Å ⁻³

^a R₁ = $\sum_{\text{hkl}} (|F_o| - |F_c|) / \sum_{\text{hkl}} |F_o|$; wR₂ = $[\sum w(|F_o| - |F_c|)^2 / \sum w|F_o|^2]^{1/2}$

Table 3.2 Crystallographic details and refinement data for **3-4**, **3-5**, and **3-6**.

	3-4	3-5	3-6
Empirical formula	C ₄₄ H ₇₆ N ₈ Rh ₂	C ₃₂ H ₄₀ F ₁₂ N ₈ Rh ₂	C ₂₆ H ₂₅ F ₁₂ N ₁₁ Rh ₂
Formula weight	922.95	970.54	925.39
Temperature	153(2) K	100(2) K	100(2) K
Wavelength	0.71073 Å	0.71073 Å	0.71073 Å
Crystal system	monoclinic	tetragonal	triclinic
Space group	<i>C</i> 2/ <i>c</i>	<i>I</i> 4 ₁ / <i>a</i>	<i>P</i> $\bar{1}$
Unit cell dimensions	a = 15.823(3) Å b = 15.106(3) Å c = 21.085(4) Å α = 90° β = 110.28(3)° γ = 90°	a = 19.3600(10) Å b = 19.3600(10) Å c = 10.1730(5) Å α = 90° β = 90° γ = 90°	a = 10.7267(7) Å b = 12.1650(8) Å c = 14.0561(9) Å α = 78.699(2)° β = 78.635(2)° γ = 82.113(2)°
Volume	4727.2(16) Å ³	3812.9(3) Å ³	1754.1(2) Å ³
Z	4	4	2
Density (calculated)	1.297 Mg/m ³	1.691 Mg/m ³	1.752 Mg/m ³
Absorption coefficient	0.735 mm ⁻¹	0.960 mm ⁻¹	1.041 mm ⁻¹
F(000)	1944	1944	912
Theta range for data collection	3.15 to 25.00°	2.26 to 27.53°	3.00 to 27.48°
Index ranges	-18 ≤ h ≤ 18, -16 ≤ k ≤ 17, -25 ≤ l ≤ 25	-25 ≤ h ≤ 18, -22 ≤ k ≤ 24, -13 ≤ l ≤ 13	-13 ≤ h ≤ 13, -15 ≤ k ≤ 15, -17 ≤ l ≤ 18
Reflections collected	7478	9981	26161
Independent reflections	4143 [R(int) = 0.0245]	2188 [R(int) = 0.0862]	8027 [R(int) = 0.0979]
Max. and min. transmission	0.8914 and 0.8375	0.9626 and 0.9272	0.9596 and 0.8941
Refinement method	Full-matrix least-squares on F ²	Full-matrix least-squares on F ²	Full-matrix least-squares on F ²
Data / restraints / parameters	4143 / 0 / 246	2188 / 66 / 151	8027 / 2 / 463
Goodness-of-fit on F ²	1.078	1.107	1.062
Final R ^a indices [I > 2σ(I)]	R ₁ = 0.0247 wR ₂ = 0.0536	R ₁ = 0.0590 wR ₂ = 0.1153	R ₁ = 0.0933 wR ₂ = 0.2454
R ^a indices (all data)	R ₁ = 0.0437 wR ₂ = 0.0599	R ₁ = 0.1327 wR ₂ = 0.1435	R ₁ = 0.1470 wR ₂ = 0.2806
Largest diff. peak and hole	0.325 and -0.472 e.Å ⁻³	2.067 and -0.778 e.Å ⁻³	3.681 and -1.082 e.Å ⁻³

^a R₁ = $\sum_{\text{hkl}} (|F_o| - |F_c|) / \sum_{\text{hkl}} |F_o|$; wR₂ = $[\sum w(|F_o| - |F_c|)^2 / \sum w|F_o|^2]^{1/2}$

Table 3.3 Crystallographic details and refinement data for **3-7**, **3-8**, and **3-9**.

	3-7	3-8	3-9
Empirical formula	C ₉ H ₈ F ₆ N ₂ O ₄ Rh	C ₁₂ H ₁₇ F ₃ N ₂ O ₄ Rh	C ₁₅ H ₂₆ N ₂ O ₄ Rh
Formula weight	425.08	413.19	401.29
Temperature	153(2) K	153(2) K	153(2) K
Wavelength	0.71073 Å	0.71073 Å	0.71073 Å
Crystal system	monoclinic	triclinic	monoclinic
Space group	<i>P</i> 2 ₁ / <i>c</i>	<i>P</i> $\bar{1}$	<i>P</i> 2 ₁ / <i>c</i>
Unit cell dimensions	a = 8.242 Å b = 20.147 Å c = 8.353 Å α = 90° β = 90.36° γ = 90°	a = 7.782 Å b = 8.499 Å c = 12.643 Å α = 70.65° β = 87.64° γ = 75.74°	a = 14.049 Å b = 8.380 Å c = 15.490 Å α = 90° β = 95.24° γ = 90°
Volume	1387 Å ³	763.9 Å ³	1816.0 Å ³
Z	4	1	4
Density (calculated)	2.036 Mg/m ³	0.898 Mg/m ³	1.468 Mg/m ³
Absorption coefficient	1.320 mm ⁻¹	0.584 mm ⁻¹	0.958 mm ⁻¹
F(000)	828	207	828
Theta range for data collection	2.02 to 32.28°	1.71 to 27.49°	2.64 to 27.49°
Index ranges	-11 ≤ h ≤ 11, -29 ≤ k ≤ 29, -12 ≤ l ≤ 11	-10 ≤ h ≤ 10, -11 ≤ k ≤ 11, -13 ≤ l ≤ 16	-18 ≤ h ≤ 18, -10 ≤ k ≤ 10, -18 ≤ l ≤ 20
Reflections collected	35734	5913	13675
Independent reflections	4646 [R(int) = 0.1294]	3451 [R(int) = 0.0325]	4155 [R(int) = 0.0532]
Refinement method	Full-matrix least-squares on F ²	Full-matrix least-squares on F ²	Full-matrix least-squares on F ²
Data / restraints / parameters	4646 / 0 / 199	3451 / 132 / 200	4155 / 126 / 194
Goodness-of-fit on F ²	1.196	1.237	1.133
Final R ^a indices [I > 2σ(I)]	R ₁ = 0.0737 wR ₂ = 0.1915	R ₁ = 0.0547 wR ₂ = 0.1286	R ₁ = 0.0423 wR ₂ = 0.1053
R ^a indices (all data)	R ₁ = 0.1014 wR ₂ = 0.2244	R ₁ = 0.0866 wR ₂ = 0.1701	R ₁ = 0.0772 wR ₂ = 0.1415
Largest diff. peak and hole	1.672 and -1.673 e.Å ⁻³	1.359 and -1.412 e.Å ⁻³	1.624 and -1.623 e.Å ⁻³

^a $R_1 = \sum_{\text{hkl}} (|F_o| - |F_c|) / \sum_{\text{hkl}} |F_o|$; $wR_2 = [\sum w(|F_o| - |F_c|)^2 / \sum w|F_o|^2]^{1/2}$

Table 3.4 Crystallographic details and refinement data for **3-10**, **3-11**, and **3-12**.

	3-10	3-11	3-12
Empirical formula	C ₁₈ H ₄ F ₂₄ N ₄ O ₈ Rh ₂	C ₂₄ H ₂₀ F ₁₈ N ₄ O ₈ Rh ₂	C ₁₅ H ₂₄ F ₆ N ₂ O ₄ Rh
Formula weight	1066.07	1040.26	513.27
Temperature	153(2) K	153(2) K	153(2) K
Wavelength	0.71073 Å	0.71073 Å	0.71073 Å
Crystal system	monoclinic	monoclinic	monoclinic
Space group	<i>C2/c</i>	<i>P2₁/c</i>	<i>P2₁/n</i>
Unit cell dimensions	a = 21.525 Å	a = 17.043 Å	a = 9.265 Å
	b = 14.776 Å	b = 11.685 Å	b = 9.862 Å
	c = 9.251 Å	c = 18.009 Å	c = 20.964 Å
	α = 90°	α = 90°	α = 90°
	β = 100.82°	β = 97.27°	β = 91.79°
Volume	γ = 90°	γ = 90°	γ = 90°
	2890.0 Å ³	3557.6 Å ³	1914.6 Å ³
Z	4	4	4
Density (calculated)	2.450 Mg/m ³	1.942 Mg/m ³	1.781 Mg/m ³
Absorption coefficient	1.351 mm ⁻¹	1.072 mm ⁻¹	0.973 mm ⁻¹
F(000)	2040	2032	1036
Theta range for data collection	1.68 to 27.52°	2.08 to 27.47°	3.02 to 26.43°
Index ranges	-27 ≤ h ≤ 27, -	-22 ≤ h ≤ 22, -	-11 ≤ h ≤ 11, -
	18 ≤ k ≤ 19, -11 ≤ l ≤ 11	15 ≤ k ≤ 14, -23 ≤ l ≤ 23	12 ≤ k ≤ 12, -26 ≤ l ≤ 26
Reflections collected	5692	14248	7085
Independent reflections	3214 [R(int) = 0.0354]	8007 [R(int) = 0.0553]	3875 [R(int) = 0.0962]
Refinement method	Full-matrix least-squares on F ²	Full-matrix least-squares on F ²	Full-matrix least-squares on F ²
Data / restraints / parameters	3214 / 0 / 253	8007 / 336 / 505	3875 / 156 / 253
Goodness-of-fit on F ²	0.988	1.103	1.072
Final R ^a indices [I > 2σ(I)]	R ₁ = 0.0738	R ₁ = 0.0842	R ₁ = 0.0897
	wR ₂ = 0.1923	wR ₂ = 0.2168	wR ₂ = 0.2154
R ^a indices (all data)	R ₁ = 0.1217	R ₁ = 0.1588	R ₁ = 0.1739
	wR ₂ = 0.2483	wR ₂ = 0.2811	wR ₂ = 0.2655
Largest diff. peak and hole	1.530 and -1.831 e.Å ⁻³	2.042 and -2.165 e.Å ⁻³	1.266 and -1.484 e.Å ⁻³

^a $R_1 = \sum_{\text{hkl}} (|F_o| - |F_c|) / \sum_{\text{hkl}} |F_o|$; $wR_2 = [\sum w(|F_o| - |F_c|)^2 / \sum w|F_o|^2]^{1/2}$

Table 3.5 Crystallographic details and refinement data for **3-13** and **3-14**.

	3-13	3-14
Empirical formula	C _{21.60} H _{30.40} Cl _{1.60} N _{6.40} Rh _{0.80}	C ₁₄ H ₃₁ F ₃ N ₂ P ₃ Rh
Formula weight	518.77	480.23
Temperature	153(2) K	100(2) K
Wavelength	0.71073 Å	0.71073 Å
Crystal system	monoclinic	monoclinic
Space group	<i>P</i> 2 ₁ / <i>c</i>	<i>P</i> 2 ₁ / <i>c</i>
Unit cell dimensions	a = 10.456(2) Å b = 14.182(3) Å c = 20.158(4) Å $\alpha = 90^\circ$ $\beta = 96.92(3)^\circ$ $\gamma = 90^\circ$	a = 9.742 Å b = 19.723 Å c = 11.755 Å $\alpha = 90^\circ$ $\beta = 109.48^\circ$ $\gamma = 90^\circ$
Volume	2967.3(10) Å ³	2129.3 Å ³
Z	5	4
Density (calculated)	1.452 Mg/m ³	1.498 Mg/m ³
Absorption coefficient	0.787 mm ⁻¹	1.051 mm ⁻¹
F(000)	1340	984
Theta range for data collection	1.76 to 31.30°	3.03 to 27.48°
Index ranges	-15 ≤ h ≤ 10, -19 ≤ k ≤ 19, -29 ≤ l ≤ 29	-12 ≤ h ≤ 12, -25 ≤ k ≤ 25, -15 ≤ l ≤ 15
Reflections collected	20210	37130
Independent reflections	8377 [R(int) = 0.0507]	4879 [R(int) = 0.0315]
Refinement method	Full-matrix least-squares on F ²	Full-matrix least-squares on F ²
Data / restraints / parameters	8377 / 0 / 347	4879 / 18 / 208
Goodness-of-fit on F ²	1.112	1.072
Final R indices [I > 2σ(I)]	R1 = 0.0595 wR2 = 0.1486	R1 = 0.0218 wR2 = 0.0551
R indices (all data)	R1 = 0.0786 wR2 = 0.1691	R1 = 0.0236 wR2 = 0.0560
Largest diff. peak and hole	0.948 and -1.728 e.Å ⁻³	0.507 and -0.335 e.Å ⁻³

$$^a R_1 = \sum_{hkl} (|F_o| - |F_c|) / \sum_{hkl} |F_o|; wR_2 = [\sum w(|F_o| - |F_c|)^2 / \sum w|F_o|^2]^{1/2}$$

Table 3.6 Crystallographic details and refinement data for **3-15** and **3-16**.

	3-15	3-16
Empirical formula	C ₁₉ H ₄₂ N ₄ P ₃ Rh	C ₁₄ H ₂₈ F ₆ N ₂ P ₃ Rh
Formula weight	522.39	534.20
Temperature	100(2) K	100(2) K
Wavelength	0.71073 Å	0.71073 Å
Crystal system	triclinic	monoclinic
Space group	<i>P</i> 1	<i>P</i> 2 ₁ / <i>c</i>
Unit cell dimensions	a = 9.189 Å b = 12.277 Å c = 12.791 Å α = 77.53° β = 72.40° γ = 72.65°	a = 12.148(2) Å b = 9.865(2) Å c = 19.534(4) Å α = 90° β = 104.61(3)° γ = 90°
Volume	1300.3 Å ³	1036.6(9) Å ³
Z	2	4
Density (calculated)	1.334 Mg/m ³	1.567 Mg/m ³
Absorption coefficient	0.853 mm ⁻¹	1.015 mm ⁻¹
F(000)	548	1080
Theta range for data collection	1.69 to 27.52°	2.98 to 25.00°
Index ranges	-11 ≤ h ≤ 9, -15 ≤ k ≤ 15, -16 ≤ l ≤ 16	-14 ≤ h ≤ 14, -11 ≤ k ≤ 10, -23 ≤ l ≤ 23
Reflections collected	9602	6426
Independent reflections	5918 [R(int) = 0.0531]	3954 [R(int) = 0.0344]
Refinement method	Full-matrix least-squares on F ²	Full-matrix least-squares on F ²
Data / restraints / parameters	5918 / 0 / 244	3954 / 0 / 235
Goodness-of-fit on F ²	1.135	1.071
Final R ^a indices [I > 2σ(I)]	R1 = 0.0574 wR2 = 0.1195	R1 = 0.0393 wR2 = 0.0791
R ^a indices (all data)	R1 = 0.1291 wR2 = 0.1862	R1 = 0.0662 wR2 = 0.0904
Largest diff. peak and hole	1.070 and -1.243 e.Å ⁻³	1.069 and -0.801 e.Å ⁻³
^a R ₁ = Σ _{hkl} (F _o - F _c) / Σ _{hkl} F _o ; wR ₂ = [Σ w(F _o - F _c) ² / Σ w F _o ²] ^{1/2}		

Table 3.7 Selected bond lengths [Å] and angles [°] for **3-1**.

Rh(1)-N(4)	2.037(3)
Rh(1)-N(1)	2.041(3)
Li(1)-O(1)	1.860(7)
Li(1)-N(2)#1	1.993(6)
Li(1)-N(3)	2.004(7)
N(2)-Li(1)#1	1.993(6)
N(1)-N(2)	1.350(4)
N(3)-N(4)	1.358(4)
N(4)-Rh(1)-N(1)	90.29(10)
N(4)#1-Rh(1)-N(1)	89.71(10)
N(1)-Rh(1)-N(1)#1	180.00(19)
N(4)#1-Rh(1)-N(4)	180.0(2)
O(1)-Li(1)-N(3)	126.0(3)
O(1)-Li(1)-N(2)#1	133.2(4)
N(2)#1-Li(1)-N(3)	97.4(3)
N(2)-N(1)-Rh(1)	120.33(19)
N(3)-N(4)-Rh(1)	118.9(2)
N(1)-N(2)-Li(1)#1	121.7(3)
N(4)-N(3)-Li(1)	123.4(3)

Symmetry transformations used to generate equivalent atoms: #1 -x,-y,-z

Table 3.8 Selected bond lengths [Å] and angles [°] for **3-2** and **3-3**.

3-2			3-3		
<i>Bond lengths</i>	Rh(1)-N(3)	2.047(6)	Rh(1)-N(3)	2.0545(17)	
	Rh(1)-N(4)	2.052(6)	Rh(1)-N(4)	2.0601(16)	
	Rh(1)-N(2)	2.055(6)	Rh(1)-N(2)	2.0606(16)	
	Rh(1)-N(1)	2.058(6)	Rh(1)-N(1)	2.0640(17)	
	Rh(1)-O(1)	2.288(5)	Rh(1)-N(5)	2.1480(17)	
	Rh(1)-Rh(1)'	2.3408(11)	Rh(1)-Rh(1)#1	2.3533(3)	
	N(1)-N(3)'	1.364(8)	N(5)-C(11)	1.140(3)	
	N(4)-N(2)'	1.374(8)	C(11)-C(12)	1.459(4)	
			N(4)-N(2)#1	1.358(2)	
<i>Bond angles</i>	N(3)-Rh(1)-N(4)	86.9(2)	N(3)-Rh(1)-N(4)	86.82(7)	
	N(4)-Rh(1)-N(2)	152.8(2)	N(4)-Rh(1)-N(2)	152.05(7)	
	N(4)-Rh(1)-N(1)	86.5(2)	N(4)-Rh(1)-N(1)	86.54(7)	
	N(3)-Rh(1)-O(1)	102.3(2)	N(3)-Rh(1)-N(5)	104.54(7)	
	N(3)-Rh(1)-Rh(1)'	76.15(16)	N(2)-Rh(1)-N(5)	101.91(7)	
	N(2)-Rh(1)-Rh(1)'	76.92(16)	N(3)-Rh(1)-Rh(1)#1	76.30(5)	
	O(1)-Rh(1)-Rh(1)'	177.65(13)	N(2)-Rh(1)-Rh(1)#1	75.86(5)	
	N(3)'-N(1)-Rh(1)	103.2(4)	N(5)-Rh(1)-Rh(1)#1	177.62(5)	
			C(11)-N(5)-Rh(1)	167.17(17)	
			N(5)-C(11)-C(12)	177.2(2)	

Symmetry transformations used to generate equivalent atoms: ' -x,-y,-z; #1 -x+1,-y,-z+1

Table 3.9 Intermolecular hydrogen bonds for **3-2** [Å and °].

D-H...A	d(D-H)	d(H...A)	d(D...A)	<(DHA)
O(1)-H(1) ...F(3) ⁱ	0.8050(18)	2.4866(15)	03.082(2)	131.76(14)
O(1)-H(2) ...F(2) ⁱ	0.8050(18)	2.6108(15)	3.039(2)	114.94(14)
O(1)-H(1) ...O(1) ⁱ	0.8072(19)	2.7511(18)	2.915(4)	93.59(13)

Symmetry transformations used to generate equivalent atoms: i -x,-y,-z.

Table 3.10 Selected bond lengths [Å] and angles [°] for **3-4**.

Rh(1)-N(3)	2.059(2)
Rh(1)-N(4)	2.061(2)
Rh(1)-N(2)	2.058(2)
Rh(1)-N(1)	2.064(2)
Rh(1)-Rh(1)#1	2.3045(8)
N(4)-N(2)#1	1.384(3)
N(3)-N(3)#1	1.373(4)
N(1)-N(1)#1	1.381(4)
N(3)-Rh(1)-N(4)	86.90(9)
N(3)-Rh(1)-N(1)	153.45(7)
N(4)-Rh(1)-N(1)	87.15(9)
N(2)-Rh(1)-N(3)	86.70(9)
N(1)-Rh(1)-Rh(1)#1	76.81(6)
N(2)-Rh(1)-Rh(1)#1	76.75(6)
N(2)-Rh(1)-N(4)	153.64(7)
N(1)#1-N(1)-Rh(1)	102.46(6)
N(2)#1-N(4)-Rh(1)	102.23(13)

Symmetry transformations used to generate equivalent atoms: #1 -x,y,-z+1/2;

Table 3.11 Selected bond lengths [Å] and angles [°] for **3-5**.

Rh(1)-N(2)	2.023(12)
Rh(1)-N(1)	2.071(11)
Rh(1)-Rh(1)#2	2.306(3)
N(1)-N(2)#2	1.372(14)
N(2)-Rh(1)-N(1)#1	87.3(5)
N(1)-Rh(1)-N(1)#1	152.7(6)
N(2)-Rh(1)-N(1)	86.7(5)
C(2)-N(1)-Rh(1)	151.5(10)
C(4)-N(2)-Rh(1)	145.3(11)

N(2)-Rh(1)-Rh(1)#2	77.2(3)
N(1)-Rh(1)-Rh(1)#2	76.4(3)
N(1)#3-N(2)-Rh(1)	104.4(8)
N(2)#2-N(1)-Rh(1)	102.0(9)
Symmetry transformations used to generate equivalent atoms: #1 -x+2,-y+1/2,z; #2 y+3/4,-x+5/4,-z+5/4; #3 -y+5/4,x-3/4,-z+5/4	

Table 3.12 Selected bond lengths [Å] and angles [°] for **3-6**.

N(1)-N(2)#1	1.364(12)	N(1)-C(2)-C(3)	110.4(10)
N(1)-Rh(1)	2.056(9)	N(1)-C(2)-C(1)	120.4(11)
N(2)-Rh(1)	2.035(10)	N(2)-Rh(1)-N(4)	86.4(4)
Rh(1)-Rh(1)#1	2.3511(16)	N(2)-Rh(1)-N(1)	152.1(3)
Rh(2)-Rh(2)#2	2.3501(15)	N(4)-Rh(1)-N(1)	86.7(4)
		N(1)-Rh(1)-N(5)	102.9(3)
		N(3)-Rh(1)-Rh(1)#1	76.3(2)
		N(5)-Rh(1)-Rh(1)#1	177.4(3)
Symmetry transformations used to generate equivalent atoms: #1 -x-1,-y,-z-1 #2 -x,-y+1,-z			

Table 3.13 Selected bond lengths [Å] and angles [°] for **3-7**.

Rh(1)-O(2)	2.047(4)	O(2)-Rh(1)-O(1)	90.33(16)
Rh(1)-O(4)	2.046(4)	O(4)-Rh(1)-O(1)	89.58(16)
Rh(1)-O(3)	2.043(4)	O(3)-Rh(1)-O(1)	176.41(14)
Rh(1)-O(1)	2.046(4)	O(2)-Rh(1)-N(1)	98.86(17)
Rh(1)-N(1)	2.295(5)	O(4)-Rh(1)-N(1)	84.82(17)
Rh(1)-Rh(1)#1	2.3947(7)	O(3)-Rh(1)-N(1)	90.37(17)
		O(1)-Rh(1)-N(1)	93.11(17)
		O(1)-Rh(1)-Rh(1)#1	87.52(11)
		N(1)-Rh(1)-Rh(1)#1	173.57(13)
Symmetry transformations used to generate equivalent atoms: #1 -x,-y+1,-z+1			

Table 3.14 Selected bond lengths [Å] and angles [°] for **3-8**.

Rh(1)-O(4)	2.028(4)	O(4)-Rh(1)-O(1)	89.79(15)
Rh(1)-O(1)	2.041(4)	O(1)-Rh(1)-O(2)	89.24(15)
Rh(1)-O(3)	2.041(4)	O(1)-Rh(1)-O(3)	176.52(13)
Rh(1)-O(2)	2.045(4)	O(4)-Rh(1)-N(1)	85.18(14)
Rh(1)-N(1)	2.318(4)	O(1)-Rh(1)-N(1)	92.02(14)
Rh(1)-Rh(1)#1	2.3948(8)	O(3)-Rh(1)-N(1)	91.38(14)
		O(2)-Rh(1)-N(1)	98.49(14)
		O(1)-Rh(1)-Rh(1)#1	88.43(10)
		N(1)-Rh(1)-Rh(1)#1	173.74(10)

Symmetry transformations used to generate equivalent atoms: #1 -x,-y+1,-z+1

Table 3.15 Selected bond lengths [Å] and angles [°] for **3-9**.

Rh(1)-O(3)	2.039(3)	O(3)-Rh(1)-O(1)	88.47(11)
Rh(1)-O(2)	2.043(3)	O(2)-Rh(1)-O(1)	91.79(11)
Rh(1)-O(1)	2.044(2)	O(1)-Rh(1)-O(4)	175.61(10)
Rh(1)-O(4)	2.049(3)	O(3)-Rh(1)-N(1)	94.77(10)
Rh(1)-N(1)	2.322(3)	O(2)-Rh(1)-N(1)	89.28(10)
Rh(1)-Rh(1)#1	2.4059(6)	O(1)-Rh(1)-N(1)	97.82(11)
		O(4)-Rh(1)-N(1)	86.57(11)
		O(1)-Rh(1)-Rh(1)#1	87.20(7)
		N(1)-Rh(1)-Rh(1)#1	174.59(7)

Symmetry transformations used to generate equivalent atoms: #1 -x+2,-y,-z

Table 3.16 Selected bond lengths [Å] and angles [°] for **3-10**.

Rh(1)-O(1)	2.036(6)	O(1)-Rh(1)-O(3)	90.4(3)
Rh(1)-O(3)	2.045(7)	O(1)-Rh(1)-O(2)	89.2(3)
Rh(1)-O(2)	2.046(7)	O(1)-Rh(1)-O(4)	175.7(2)
Rh(1)-O(4)	2.049(6)	O(1)-Rh(1)-N(1)	98.5(3)
Rh(1)-N(1)	2.266(7)	O(3)-Rh(1)-N(1)	91.1(3)
Rh(1)-Rh(1)#1	2.4012(14)	O(2)-Rh(1)-N(1)	92.8(3)
		O(4)-Rh(1)-N(1)	85.7(3)
		N(1)-Rh(1)-Rh(1)#1	173.82(19)
		C(6)-N(2)-N(1)	112.7(8)

Symmetry transformations used to generate equivalent atoms: #1 -x+3/2,-y+1/2,-z

Table 3.17 Selected bond lengths [Å] and angles [°] for **3-11**.

Rh(1)-O(5)	2.032(7)	O(5)-Rh(1)-O(1)	176.0(3)
Rh(1)-O(7)	2.035(6)	O(7)-Rh(1)-O(1)	90.9(3)
Rh(1)-O(3)	2.040(6)	O(3)-Rh(1)-O(1)	89.3(3)
Rh(1)-O(1)	2.046(6)	O(5)-Rh(1)-N(1)	94.3(3)
Rh(1)-N(1)	2.248(7)	O(7)-Rh(1)-N(1)	97.1(3)
Rh(1)-Rh(2)	2.4117(10)	O(3)-Rh(1)-N(1)	87.6(3)
		O(1)-Rh(1)-N(1)	89.6(3)
		O(1)-Rh(1)-Rh(2)	88.57(17)
		N(1)-Rh(1)-Rh(2)	175.38(19)

Table 3.18 Selected bond lengths [Å] and angles [°] for **3-12**.

Rh(1)-O(2)	2.034(9)	O(2)-Rh(1)-O(1)	89.9(3)
Rh(1)-O(4)	2.043(8)	O(4)-Rh(1)-O(1)	89.1(3)
Rh(1)-O(3)	2.053(7)	O(3)-Rh(1)-O(1)	174.9(3)
Rh(1)-O(1)	2.064(8)	O(2)-Rh(1)-N(1)	89.5(3)
Rh(1)-N(1)	2.300(8)	O(4)-Rh(1)-N(1)	95.0(3)
Rh(1)-Rh(1)#1	2.4310(17)	O(3)-Rh(1)-N(1)	98.5(3)
		O(1)-Rh(1)-N(1)	86.6(3)
		O(1)-Rh(1)-Rh(1)#1	88.3(2)
		N(1)-Rh(1)-Rh(1)#1	174.3(2)

Symmetry transformations used to generate equivalent atoms: #1 -x+1,-y,-z+2

Table 3.19 Intramolecular hydrogen bonds for complexes **3-7 – 3-12** [Å and °].

Complex	D-H...A	d(D-H)	d(H...A)	d(D...A)	<(DHA)
3-7	N(2)-H(2)...O(4)	0.86	2.10	2.705(6)	127.3
3-8	N(2)-H(2)...O(4)	0.86	2.10	2.689(5)	125.0
3-9	N(2)-H(2)...O(4)	0.86	2.20	2.783(4)	124.9
3-10	N(2)-H(2)...O(4)	0.86	2.17	2.752(11)	124.5
3-11	N-H...O	0.86	2.18	3.077(14)	124.6
3-12	N(2)-H(2)...O(1)	0.86	2.16	2.778(12)	128.3

Table 3.20 Selected bond lengths [Å] and angles [°] for **3-13**.

Rh(1)-N(2)	2.037(3)	N(2)-Rh(1)-N(7)	178.11(12)
Rh(1)-N(7)	2.039(3)	N(2)-Rh(1)-N(4)	90.33(12)
Rh(1)-N(4)	2.054(3)	N(7)-Rh(1)-N(4)	91.47(12)
Rh(1)-N(6)	2.061(3)	N(2)-Rh(1)-N(6)	89.38(12)
Rh(1)-Cl(2)	2.3638(11)	N(7)-Rh(1)-N(6)	91.20(12)
Rh(1)-Cl(1)	2.3711(10)	N(4)-Rh(1)-N(6)	90.41(13)
N(1)-H(1A)	0.86	N(2)-Rh(1)-Cl(2)	89.69(9)
		N(7)-Rh(1)-Cl(2)	89.65(9)
		N(4)-Rh(1)-Cl(2)	92.17(9)
		N(6)-Rh(1)-Cl(2)	177.26(9)
		N(2)-Rh(1)-Cl(1)	88.15(9)
		N(7)-Rh(1)-Cl(1)	90.05(9)
		N(4)-Rh(1)-Cl(1)	178.40(9)
		N(6)-Rh(1)-Cl(1)	90.06(10)

Table 3.21 Hydrogen bonds for **3-13** [Å and °].

D-H...A	d(D-H)	d(H...A)	d(D...A)	<(DHA)
N(3)-H(1)...N(5)	1.03(6)	1.66(6)	2.563(5)	145(5)

Table 3.22 Selected bond lengths [Å] and angles [°] for **3-14**.

N(1)-Rh(1)	2.0971(14)	N(1)-Rh(1)-P(3)	176.49(4)
P(1)-Rh(1)	2.3084(4)	N(1)-Rh(1)-P(2)	86.73(4)
P(2)-Rh(1)	2.2994(4)	P(3)-Rh(1)-P(2)	96.194(17)
P(3)-Rh(1)	2.2290(5)	N(1)-Rh(1)-P(1)	82.94(4)
		P(3)-Rh(1)-P(1)	94.510(17)
		P(2)-Rh(1)-P(1)	165.602(17)

Table 3.23 Selected bond lengths [Å] and angles [°] for **3-15**.

N(1)-Rh(1)	2.078(4)	N(1)-Rh(1)-P(1)	175.13(13)
P(1)-Rh(1)	2.2258(16)	N(1)-Rh(1)-P(2)	85.50(14)
P(2)-Rh(1)	2.3048(17)	P(1)-Rh(1)-P(2)	96.77(6)
P(3)-Rh(1)	2.3202(17)	N(1)-Rh(1)-P(3)	83.79(14)
		P(1)-Rh(1)-P(3)	94.23(6)
		P(2)-Rh(1)-P(3)	168.48(6)

Table 3.24 Hydrogen bonds for **3-15** [Å and °].

D-H...A	d(D-H)	d(H...A)	d(D...A)	<(DHA)
N(3)-H(3A)...N(2)	0.86	2.00	2.832(7)	161.2

Table 3.25 Selected bond lengths [Å] and angles [°] for **3-16**.

N(1)-Rh(1)	2.108(3)	N(1)-Rh(1)-P(3)	179.43(9)
Rh(1)-P(3)	2.2293(13)	N(1)-Rh(1)-P(1)	86.27(9)
Rh(1)-P(2)	2.3068(12)	N(1)-Rh(1)-P(2)	87.29(9)
Rh(1)-P(1)	2.3140(12)	P(3)-Rh(1)-P(1)	93.46(4)
		P(2)-Rh(1)-P(1)	170.12(4)
		P(3)-Rh(1)-P(2)	93.05(5)

REFERENCES

1. (a) Hass, G. *J. Opt. Soc. Am.* **1982**, 72, 27. (b) Marot, L.; De Temmerman, G.; Thommen, V.; Mathys, D.; Oelhafen, P. *Surf. Coat. Tech.* **2008**, **202**, 2837.
2. (a) Dal Santo, V.; Mondelli, C.; De Grandi, V.; Gallo, A.; Recchia, S.; Sordelli, L.; Psaro, R. *Appl. Catal. A – Gen.* **2008**, 346, 126. (b) Williams, F. J.; Tikhov, M. S.; Palermo, A.; Macleod, N.; Lambert, R. M. *J. Phys. Chem. B* **2001**, 105, 2800.
3. (a) Lane, M. W.; Murray, C. E.; McFeely, F. R.; Vereecken, P. M.; Rosenberg, R. *Appl. Phys. Lett.* **2003**, 83, 2330. (b) Goswami, I.; Laxman, R. *Semicond. Int.* **2004**, 27, 49.
4. Renzas, J. R.; Somorjai, G. A. *J. Phys. Chem. C* **2010**, 114, 17660.
5. (a) Lu, J.-P.; Chu, P. W.; Raj, R.; Gysling, H. *Thin Solid Films* **1992**, 208, 172. (b) Flint, E. B.; Messelhaeuser, J.; Suhr, H. *Appl. Surf. Sci.* **1992**, 54, 56. (c) Crane, E. L.; You, Y.; Nuzzo, R. G.; Girolami, G. S. *J. Am. Chem. Soc.* **2000**, 122, 3422.
6. (a) Kumar, R.; Puddephatt, R. J. *Can. J. Chem.* **1991**, 69, 108. (b) Cohan, J. S.; Yuan, H.; Williams, R. S.; Zink, J. I. *Appl. Phys. Lett.* **1992**, 60, 1402. (c) Aaltonen, T.; Ritala, M.; Leskelae, M. *Electrochem. Solid St.* **2005**, 8, C99.
7. (a) Trofimenko, S. *Chem. Rev.* **1972**, 72, 497. (b) Halcrow, M. A. *J. Chem. Soc., Dalton Trans.* **2009**, 12, 2059.
8. (a) Waheed, A.; Jones, R. A.; Agapiou, K.; Yang, X.; Moore, J. A.; Ekerdt, J. G. *Organometallics* **2007**, 26, 6778. (b) Wang, Z.; Abernethy, C. D.; Cowley, A. H.; Jones, J. N.; Jones, R. A.; Macdonald, C. L. B.; Zhang, L. *J. Organomet. Chem.* **2003**, 666, 35. (c) Song, Y.-H.; Chen, Y.-L.; Chi, Y.; Liu, C.-S.; Ching, W.-L.; Kai, J.-J.; Chen, R.-S.; Huang, Y.-S.; Carty, A. J. *Chem. Vap. Deposition* **2003**, 9, 162. (d) Chi, Y.; Yu, H.-L.; Ching, W.-L.; Liu, C.-S.; Chen, Y.-L.; Chou, T.-Y.; Peng, S.-M.; Lee, G.-H. *J. Mater. Chem.* **2002**, 12, 1363. (e) El-Kadri, O. E.; Heeg, M. J.; Winter, C. H. *Dalton Trans.* **2006**, 16, 1943.
9. Balley, J. A.; Grundy, S. L.; Stobart, S. R. *Organometallics* **1990**, 9, 536.
10. Beveridge, K. A.; Bushnell, G. W.; Stobart, S. R.; Atwood, J. L.; Zaworotko, M. *J. Organometallics* **1983**, 2, 1447.
11. Holland *et al.* *Angew. Chem. Int. Ed.* **2006**, 45, 1607. (b) Winter *et al.* *Angew. Chem. Int. Ed.* **2002**, 41, 1591.

12. (a) Tejel, C.; Bordonaba, M.; Ciriano, M. A.; Edwards, A. J.; Clegg, W.; Lahoz, F. J.; Oro, L. A. *Inorg. Chem.* **1999**, *38*, 1108. (b) Barcelo, F.; Lahuerta, P.; Ubeda, M. A.; Foces-Foces, C.; Cano, F. H.; Martinez-Ripoll, M. *J. Chem. Soc. Chem. Commun.* **1985**, *1*, 43. (c) Tejel, C.; Ciriano, M. A.; Oro, L. A.; Tiripicchio, A.; Ugozzoli, F. *Organometallics* **2001**, *20*, 1676.
13. Billig, E.; Shupack, S. I.; Waters, J. H.; Williams, R.; Gray, H. B. *J. Am. Chem. Soc.* **1964**, *86*, 926.
14. (a) Cui, W.; Li, S.; Wayland, B. B. *J. Organomet. Chem.* **2007**, *692*, 3198. (b) Wayland, B. B.; Sherry, A. E.; Bunn, A. G. *J. Am. Chem. Soc.* **1993**, *115*, 7675. (c) Grass, V.; Lexa, D.; Momenteau, M.; Saveant, J.-M. *J. Am. Chem. Soc.* **1997**, *119*, 3536. (d) Collman, J. P.; Boulatov, R. *J. Am. Chem. Soc.* **2000**, *122*, 11812. (e) Anderson, J. E.; Yao, C. L.; Kadish, K. M. *J. Am. Chem. Soc.* **1987**, *109*, 1106.
15. (a) Paul, P.; Tyagi, B.; Bilakhiya, A. K.; Bhadbhade, M. M.; Suresh, E. *J. Chem. Soc. Dalton Trans.* **1999**, *12*, 2009. (b) Anderson, J. E.; Gregory, T. P. *Inorg. Chem.* **1989**, *28*, 3905.
16. Rawle, S. C.; Yagbasan, R.; Prout, K.; Cooper, S. R. *J. Am. Chem. Soc.* **1987**, *109*, 6181.
17. (a) Haefner, S. C.; Dunbar, K. R.; Bender, C. *J. Am. Chem. Soc.* **1991**, *113*, 9540. (b) Chen, S. J.; Dunbar, K. R. *Inorg. Chem.* **1991**, *30*, 2018.
18. Hay-Motherwell, R. S.; Koschmieder, S. U.; Wilkinson, G.; Hussain-Bates, B.; Hursthouse, M. B. *J. Chem. Soc. Dalton Trans.* **1991**, *11*, 2821.
19. (a) Connelly, N. G.; Emslie, D. J. H.; Geiger, W. E.; Hayward, O. D.; Linehan, E. B.; Orpen, A. G.; Quayle, M. J.; Rieger, P. H. *J. Chem. Soc. Dalton Trans.* **2001**, *5*, 670. (b) Dixon, F. M.; Farrell, J. R.; Doan, P. E.; Williamson, A.; Weinberger, D. A.; Mirkin, C. A.; Stern, C.; Incarvito, C. D.; Liable-Sands, L. M.; Zakharov, L. N.; Rheingold, A. L. *Organometallics* **2002**, *21*, 3091.
20. Koh, Y. B.; Cristoph, G. G. *Inorg. Chem.* **1978**, *17*, 2590.
21. (a) Kaim, W.; Reinhardt, R.; Greulich, S.; Fiedler, J. *Organometallics* **2003**, *22*, 2240. (b) Gerisch, M.; Krumper, J. R.; Bergman, R. G.; Tilley, T. D. *Organometallics* **2003**, *22*, 47.
22. Barron, A. R.; Wilkinson, G.; Motevalli, M.; Hursthouse, M. B. *Polyhedron* **1985**, *4*, 1131.

23. Breher, F.; Rueegger, H. *Angew. Chem. Int. Ed.* **2005**, *44*, 473.
24. Garcia, R.; Adams, H.; Patmore, N. J. *Dalton Trans.* **2009**, *2*, 259.
25. Cotton, F. A.; Walton, R. A. *Multiple Bonds Between Metal Atoms*; John Wiley and Sons, 1982; pp. 311-323.
26. Cotton, F. A.; Felthouse, T. R. *Inorg. Chem.* **1981**, *20*, 584.
27. Hu, Z.; Loas, A.; Gorun, S. M. *Inorg. Chim. Acta* **2009**, *362*, 4639.
28. (a) Johnson, S. A.; Hunt, H. R.; Neumann, H. M. *Inorg. Chem.* **1963**, *2*, 960. (b) Bear, J. L.; Kitchens, J.; Wilcotte, M. R. *Inorg. Nucl. Chem.* **1971**, *33*, 3479.
29. Cotton, F. A.; Felthouse, T. R. *Inorg. Chem.* **1982**, *21*, 2667.
30. (a) Norman, J. G.; Renzoni, G. E.; Case, D. A. *J. Am. Chem. Soc.* **1979**, *101*, 5256. (b) Cotton, F. A.; Felthouse, T. R. *Inorg. Chem.* **1981**, *20*, 600.
31. Lopez, C.; Claramunt, C. A.; Trofimenko, S. Elguero, J. *Can. J. Chem.* **1993**, *71*, 678.
32. Cotton, F. A.; Dikarev, E. V.; Feng, X. *Inorg. Chim. Acta* **1995**, *237*, 19.
33. Cushing, G. W.; Howard, W. A.; Pang, K. *J. Mol. Struct.* **2006**, *797*, 165.
34. (a) Kruck, T.; Baur, K. *Angew. Chem. Int. Ed. Engl.* **1965**, *4*, 521. (b) Yuan, Z.; Jiang, D.; Naftel, S.J.; Sham, T.-K.; Puddephatt, R.J. *Chem. Mater.* **1994**, *6*, 2151. (c) Park, S.; Lim, S.; Choi, H. *Chem. Mater.* **2006**, *18*, 5150. (d) Bennett, M. A.; Patmore, D. J. *Inorg. Chem.* **1971**, *10*, 2387.
35. Rivers, J. H., *Novel Organometallic Precursors for the Chemical Vapor Deposition of Metal Thin Films*. Ph.D. Dissertation, University of Texas, Austin, TX, 2010.
36. Claire, P. P. K.; Coe, P. L.; Jones, C. J.; McCleverty, J. A. *J. Fluorine Chem.* **1991**, *51*, 283.
37. Fernandez-Castano, C.; Foces-Foces, C.; Jagerovic, N.; Elguero, J. *J. Mol. Struct.* **1995**, *355*, 265.

38. Zelenin, K. N.; Tugusheva, A. R.; Yakimovich, S. I.; Alekseev, V. V.; Zerova, E. V. *Chem. Heterocyc. Compd.* **2002**, 38, 668.
39. M. J. Frisch, *et al.* *Gaussian 03*, Revision E.01.; Gaussian: Pittsburgh, 2003.
40. (a) Becke, A. D. *Phys. Rev. A* **1988**, 38, 3098. (b) Becke, A. D. *J. Chem. Phys.* **1993**, 98, 5648. (c) Lee, C. T.; Yang, W. T.; Parr, R. G. *Phys. Rev. B* **1988**, 37, 785.
41. (a) Wadt, W. R.; Hay, P. J. *J. Chem. Phys.* **1985**, 82, 284. (b) Hay, P. J.; Wadt, W. R. *J. Chem. Phys.* **1985**, 82, 299.

Chapter 4: A tungsten pyrazolate complex

INTRODUCTION

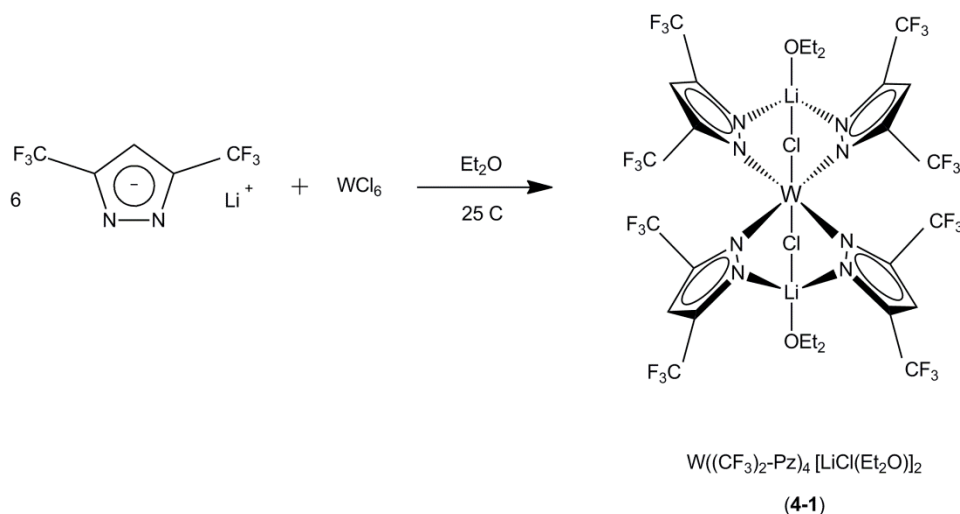
The high melting point (3410 °C) and low electrical resistivity (5.3 $\mu\Omega$ cm at 27 °C) of tungsten make it a desirable metal for many applications.¹ Thin films of W are used extensively as an interconnect material in very-large-scale integration (VLSI) devices.² Current deposition techniques involve use of WF_6 with a reducing carrier gas such as H_2 or SiH_4 to afford deposition.³ High purity films with conformal step coverage are obtained under these conditions, although the formation of HF as a corrosive by-product poses potential safety issues. The use of volatile complexes such as $W(CO)_6$ and $CpW(CO)_3CH_3$ as CVD precursors eliminates the formation of HF, but leads to films with high levels of C and O contamination from decomposition of the ligands.⁴ Aside from binary tungsten halide compounds, development of CVD precursors has been limited.⁵

While the chemistry of tungsten with tris(pyrazolyl)borate “scorpionate” ligands is quite developed,^{6,7} there exist relatively few examples of mononuclear or bridged tungsten pyrazolate species. Winter *et al.* have studied mononuclear tungsten pyrazolate derivatives for the chemical vapor deposition of tungsten nitride thin films using 3,5-dimethylpyrazole.⁸ Amongst homoleptic and mixed ligand tungsten pyrazolate complexes, there exist no examples of coordination of 3,5-bis(trifluoromethyl)pyrazole to a tungsten center.

RESULTS AND DISCUSSION

Addition of six equivalents of 3,5-(CF_3)₂PzLi to a suspension of WCl_6 in Et_2O resulted in a deep green heterogeneous mixture (Scheme 4.1). After filtration, several

crops of large green X-ray quality crystals were grown from an ether solution upon cooling to -30 °C. The product $[\text{LiCl}(\text{Et}_2\text{O})]_2\text{W}(\mu\text{-}3,5\text{-(CF}_3)_2\text{Pz})_4$ (**4-1**) is soluble in a variety of organic solvents and is extremely air and moisture sensitive.



Scheme 4.1 Synthesis of $[\text{LiCl}(\text{Et}_2\text{O})]_2\text{W}(\mu\text{-}3,5\text{-(CF}_3)_2\text{Pz})_4$ (**4-1**).

The X-ray crystal structure of complex **4-1** is depicted in Figure 4.1. Selected bond lengths and angles are presented in Table 4.2, while additional crystallographic data are presented in Table 4.1. The complex crystallizes in the triclinic space group $P\bar{1}$ with one half of a molecule comprising the asymmetric unit and one molecule per unit cell.

The central tungsten atom resides on an inversion center in a *pseudo* octahedral coordination environment. It forms a plane with four pyrazolate N atoms, and is axially coordinated to two chloride atoms above and below the W-N₄ plane. The four 3,5-bis(trifluoromethyl)pyrazolate ligands bridge the central W ion as well as two lithium ions in a $\kappa^1:\kappa^1\text{-}\mu$ coordination mode common for this ligand. The Cl atoms also bridge the W and Li atoms, forming a near right angle ($90.8(3)^\circ$) between them. The coordination

sphere of each Li ion is further filled by the oxygen atom of a diethyl ether solvent molecule. The W-N and W-Cl bond lengths (2.160(3) Å av. and 2.289(3) Å, respectively) are in close agreement with those reported for other tungsten pyrazolate complexes.¹⁰ The large bite angle of the pyrazolate ligand allows for bridging of metal centers across rather large distances, and the non-bonding distance between the W and Li atoms in the complex is 3.344 Å. The pyrazolate ligands are tilted slightly with respect to the W-N4 plane of the molecule ($\text{N1}^{\text{i}}\text{-W1-N3-N4} = -118.5^\circ$) giving each half of the molecule a boat like configuration.

The X-ray crystal structure suggests tungsten(IV), and while the exact nature of the reducing agent is uncertain, the mechanism may be similar to that seen in the reduction of RhCl_3 upon reaction with 3,5-(CF_3)₂PzLi to give the Rh(II) species $[\text{Li}(\text{THF})]_2 \text{Rh}(\mu\text{-3,5-(CF}_3)_2\text{Pz})_4$ (**3-1**) as discussed in Chapter 3. The structural similarity of these complexes is striking (Figure 4.2), with both complexes showing a square planar arrangement of coordinated Pz ligands around the central metal ion as well as the presence of two Li ions in each structure, which allow the pyrazolate ligands to bridge two metal centers. This further illustrates the reluctance of the pyrazolate ligand to coordinate to heavier late transition metal centers in a bidentate η^2 fashion.

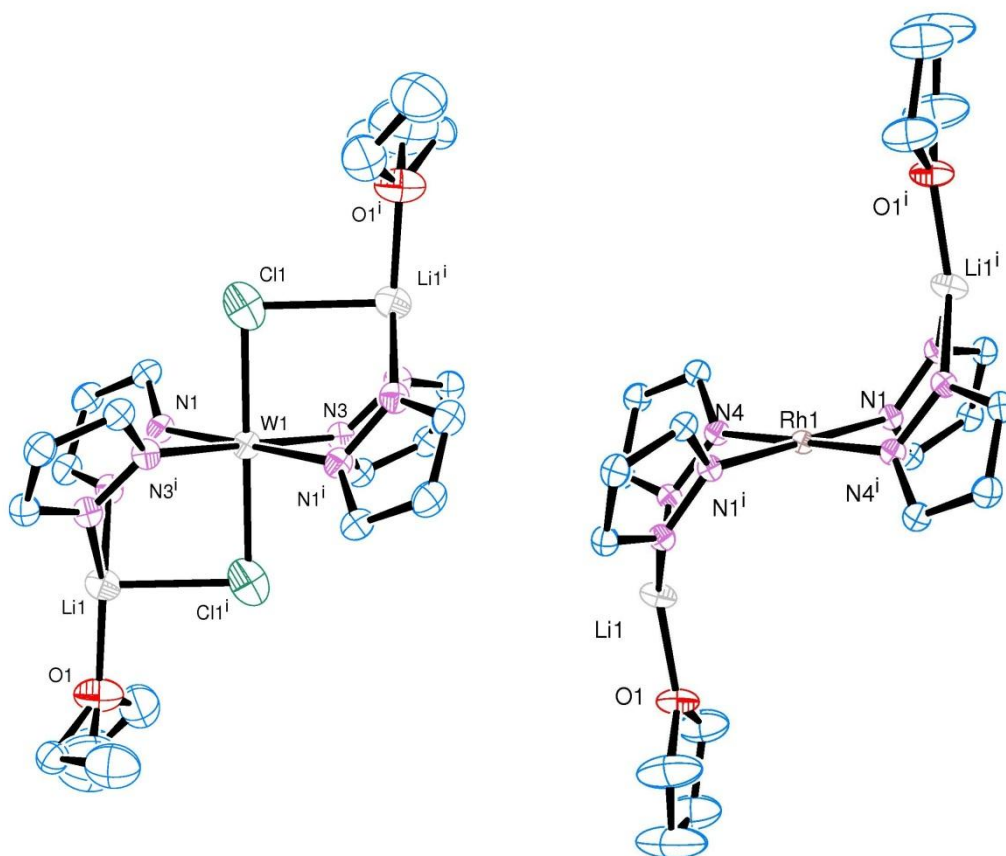


Figure 4.2 ORTEP diagrams of **4-1** (left) and **3-1** (right) highlighting the similarities in the square planar arrangement of pyrazolate ligands of both complexes. The (CF₃) functional groups of the Pz ligands and all hydrogen atoms have been omitted for clarity.

CONCLUSIONS

The tungsten pyrazolate complex $[\text{LiCl}(\text{Et}_2\text{O})]_2\text{W}(\mu\text{-}3,5\text{-(CF}_3)_2\text{Pz})_4$ has been synthesized and structurally characterized. The compound presents a unique example of a homoleptic tungsten pyrazolate complex, with the vast majority of structurally similar tungsten complexes are based on boron containing tris-pyrazolylborate ligands. Although its reactivity and involatility limit its potential as a CVD precursor, its isolation offers interesting possibilities for further development of volatile tungsten complexes with nitrogen-containing ligands.

EXPERIMENTAL DETAILS

General synthesis

Unless otherwise noted, all reactions were performed under a dry, oxygen-free nitrogen atmosphere or under vacuum using standard Schlenk line and dry box techniques. All solvents were dried prior to use by distillation from molten sodium or sodium benzophenone ketyl under nitrogen. 3,5-bis(trifluoromethyl) pyrazole,⁹ was prepared according to literature procedures. Microanalyses (C, H, N) were performed by Galbraith Laboratories of Knoxville, TN. Melting points were determined in sealed capillaries under N_2 (1 atm.) on an Electrothermal Melting Point apparatus and are uncorrected. ESI mass spectra were collected on a Finnigan MAT TSQ 700 mass spectrometer. NMR spectra were recorded on a Varian 300 Unity Plus spectrometer (300 MHz at 298 K). Chemical shifts are referenced to the deuterated solvent. Infrared spectra were taken on a Nicolet IR 200 FTIR spectrometer between KBr plates.

Single crystal X-ray crystallography

A single crystal of **4-1** was collected under flowing N₂, covered in mineral oil and mounted on a nylon thread loop. Crystallographic data was collected on a Rigaku AFC12 diffractometer with a Saturn 724+ CCD using a graphite monochromator with MoK α radiation at reduced temperature using a Rigaku XStream low temperature device. Data reduction was performed with DENZO-SMN. The structure was solved by direct methods using SIR2004 and refined by full-matrix least squares on F² with anisotropic displacement parameters for the non-H atoms using SHELXL-97.

Synthesis of [LiCl(Et₂O)]₂W(μ -3,5-(CF₃)₂Pz)₄ (**4-1**)

To a solution of 3,5-bis(trifluoromethyl)pyrazole (0.324 g, 1.59 mmol) in Et₂O (150 mL) was added dropwise ⁿBu-Li in hexane (1 mL, 1.6 M) at -78 °C. The mixture was stirred cold for 30 minutes and then allowed to warm to room temperature. This solution was quantitatively transferred to a suspension of WCl₆ (0.105 g, 0.26 mmol) in Et₂O (50 mL) at 25 °C. The dark red mixture immediately became yellow green. After stirring overnight, a light precipitate had formed. The resulting solution was filtered through a short bed of Celite (2 cm), and bright green crystals of **4-1** formed upon cooling the solution to -30 °C. Isolated: 0.07 g, 22 %; mp 45-50 °C. (dec., 1 atm N₂); ¹H-NMR (300 MHz, δ , CDCl₃): 6.13 (s, 4 H), 3.34 (s, 8 H), 1.16 (s, 12H); ¹⁹F{¹H}-NMR (CDCl₃): δ -60.36 (s), -62.20 (s); Calcd. for C₂₈H₂₄Cl₂F₂₄Li₂N₈O₂W: C, 27.36; H, 1.97; N, 9.12 %. Found: C, 26.09; H, 1.69; N, 9.22 %.

X-RAY CRYSTALLOGRAPHIC DETAILS

Table 4.1 Crystallographic details and refinement data for **4-1**.

Empirical formula	C ₁₄ H ₁₂ Cl F ₁₂ Li N ₄ O W _{0.5}
Formula weight	614.59
Temperature	153(2) K
Wavelength	0.71073 Å
Crystal system	triclinic
Space group	<i>P</i> $\bar{1}$
Unit cell dimensions	a = 8.432 Å b = 11.036 Å c = 12.156 Å α = 74.43° β = 72.05° γ = 85.17°
Volume	1036.6(9) Å ³
Z	2
Density (calculated)	1.969 Mg/m ³
Absorption coefficient	3.063 mm ⁻¹
F(000)	594
Theta range for data collection	1.92 to 27.46°
Index ranges	-10 ≤ h ≤ 10, -12 ≤ k ≤ 14, -15 ≤ l ≤ 15
Reflections collected	7875
Independent reflections	4664 [R(int) = 0.0276]
Refinement method	Full-matrix least-squares on F ²
Data / restraints / parameters	4664 / 204 / 304
Goodness-of-fit on F ²	1.055
Final R ^a indices	R1 = 0.0534
[I > 2σ(I)]	wR2 = 0.1322
R ^a indices (all data)	R1 = 0.0557
	wR2 = 0.1356
Largest diff. peak and hole	2.629 and -2.965 e.Å ⁻³

$$^a R_1 = \sum_{hkl} (|F_o| - |F_c|) / \sum_{hkl} |F_o|; wR_2 = [\sum w(|F_o| - |F_c|)^2 / \sum w|F_o|^2]^{1/2}$$

Table 4.2 Selected bond lengths [Å] and angles [°] for **4-1**.

Li(1)-O(1)	1.906(14)	W(1)-Cl(1)-Li(1)	90.9(3)
Li(1)-N(4) ⁱ	2.029(14)	N(1) ⁱ -W(1)-N(3)	90.19(19)
Li(1)-N(2)	2.044(14)	N(1)-W(1)-N(3)	89.81(19)
Li(1)-Cl(1)	2.409(14)	N(1) ⁱ -W(1)-N(3) ⁱ	89.81(19)
Li(1)-F(11) ⁱ	2.642(15)	N(1)-W(1)-N(3) ⁱ	90.19(19)
Li(1)-W(1)	3.348(13)	N(3)-W(1)-N(3) ⁱ	180.0(3)
N(1)-N(2)	1.368(7)	N(1) ⁱ -W(1)-Cl(1) ⁱ	91.93(15)
N(1)-W(1)	2.158(5)	N(1)-W(1)-Cl(1) ⁱ	88.07(15)
N(3)-N(4)	1.369(7)	N(3)-W(1)-Cl(1) ⁱ	92.43(16)
N(3)-W(1)	2.163(5)	N(3) ⁱ -W(1)-Cl(1) ⁱ	87.57(16)
N(4)-Li(1) ⁱ	2.029(14)	N(1) ⁱ -W(1)-Cl(1)	88.07(15)
Cl(1)-W(1)	2.287(3)	N(1)-W(1)-Cl(1)	91.93(15)
W(1)-N(1) ⁱ	2.158(5)	N(3)-W(1)-Cl(1)	87.57(16)
W(1)-N(3) ⁱ	2.163(5)	N(3) ⁱ -W(1)-Cl(1)	92.43(16)
W(1)-Cl(1) ⁱ	2.287(3)	Cl(1) ⁱ -W(1)-Cl(1)	180.00(13)
W(1)-Li(1) ⁱ	3.348(13)	N(1) ⁱ -W(1)-Li(1) ⁱ	61.0(3)
F(11)-Li(1) ⁱ	2.642(15)	N(1)-W(1)-Li(1) ⁱ	119.0(3)
		N(3)-W(1)-Li(1) ⁱ	61.5(3)
		N(3) ⁱ -W(1)-Li(1) ⁱ	118.5(3)
		Cl(1) ⁱ -W(1)-Li(1) ⁱ	46.0(2)
		Cl(1)-W(1)-Li(1) ⁱ	134.0(2)
		N(1) ⁱ -W(1)-Li(1)	119.0(3)
		N(1)-W(1)-Li(1)	61.0(3)
		N(3)-W(1)-Li(1)	118.5(3)
		N(3) ⁱ -W(1)-Li(1)	61.5(3)
		Cl(1) ⁱ -W(1)-Li(1)	134.0(2)
		Cl(1)-W(1)-Li(1)	46.0(2)
		Li(1) ⁱ -W(1)-Li(1)	180.000(1)
		C(10)-F(11)-Li(1) ⁱ	111.3(5)

Symmetry transformations used to generate equivalent atoms: i -x,-y,-z+1

REFERENCES

1. (a) Cezairliyan, A. *High Temp. Sci.* **1972**, *4*, 248-252. (b) *ASM Handbook online, Properties and Selection-Nonferrous Alloys and Pure Metals*. Vol. 2.
2. Liu, R; Pai, C.-S.; Martinez, E. *Solid-State Electron.* **1999**, *43*, 1003.
3. (a) Barber, E. J.; Cady, G. H. *J. Phys. Chem.* **1956**, *60*, 505-506. (b) Ireland, P. J. *Thin Solid Films* **1997**, *304*, 1.
4. Kodas, T. T.; Hampden-Smith, M. J. *The Chemistry of Metal CVD*, 1994, VCH, Weinheim and New York.
5. (a) Buchanan, D. A.; McFeeley, F. R.; Yurkas, J. *J. Appl. Phys. Lett.* **1998**, *73*, 1676. (b) Lai, K. K.; Lamb, H. H. *Thin Solid Films* **2000**, *370*, 114. (c) Jeon, S.; Yong, K.; Park, S.-G.; Rhee, S.-W. *J. Vac. Sci. Tech. B* **2006**, *24*, 1428.
6. (a) Garner, M.; Lehmann, M.-A.; Reglinski, J.; Spicer, M. D. *Organometallics* **2001**, *20*, 5233. (b) Ahn, S.; Mayr, A. *J. Am. Chem. Soc.* **1996**, *118*, 7408.
7. Vogeley, N. J.; Templeton, J. L. *Polyhedron* **2004**, *23*, 311.
8. El-Kadri, O. M.; Heeg, M. J.; Winter, C. H. *Dalton Trans.* **2006**, *16*, 1943.
9. Claire, P. P. K.; Coe, P. L.; Jones, C. J.; McCleverty, J. A. *J. Fluorine Chem.* **1991**, *51*, 283.
10. (a) Jia, W.-L.; Tang, L.-F.; Wang, Z.-H.; Chai, J.-F.; Wang, J.-T. *Transit. Metal Chem.* **2001**, *26*, 400-403. (b) Baker, P. K.; van Kampen, M.; Roos, C.; Spaeth, J. *Transit. Metal Chem.* **1994**, *19*, 165.

Chapter 5: Synthesis and characterization of palladium pyrazolate complexes

INTRODUCTION

Thin films of palladium have many potential applications in the microelectronics industry owing to the high electrical conductivity, resistance to oxidation, and economic advantages of palladium over other platinum group metals.¹ While thin films of Pd have been deposited by electroplating and vacuum sputtering, relatively few studies utilizing CVD techniques have been reported. Examples of organometallic complexes with volatilities suitable for CVD of palladium thin films include (η^3 -allyl) complexes, as well as methyl (Me) and cyclopentadienyl (Cp) derivatives. A variety of allyl derivatives such as $\text{Pd}(\eta^3\text{-allyl})(\text{Cp})$,² $\text{Pd}(\eta^3\text{-allyl})_2$,³ $\text{Pd}(\eta^3\text{-methyl-2-allyl})(\text{acac})$ ⁴ and $\text{Pd}(\eta^3\text{-allyl})(\text{hfacac})$ ⁵ may be similarly prepared from $[\text{Pd}(\eta^3\text{-allyl})\text{Cl}]_2$ in high yield (acac = acetylacetonate; hfacac = hexafluoroacetylacetonate). The air and moisture stability of these complexes varies, and most show high volatility under mild conditions. The incorporation of a direct Pd-C bond may contribute to carbon impurities in the resultant films. For example, deposition studies of $\text{Pd}(\eta^3\text{-allyl})(\text{Cp})$ at 250 °C at 10^{-4} Torr resulted in Pd films with up to 5% carbon,⁶ although use of H_2 or O_2 as a reactive carrier gas significantly reduced this contamination.⁷

Several complexes of the general formula $\text{Pd}(\text{Me})_2(\text{PR}_3)_2$ are known, though only a few are volatile. $\text{Pd}(\text{Me})_2(\text{PMe}_3)_2$ and $\text{Pd}(\text{Me})_2(\text{PEt}_3)_2$ have been shown to deposit Pd films at 200 °C at 10^{-3} Torr.⁸ Resultant films from these precursors contained roughly 10% C. Use of H_2 carrier gas under similar deposition conditions reduced the carbon content, but led to significant P incorporation into the films.^{8b} Use of β -diketonato ligands to fill the coordination sphere of the metal center is advantageous since the chelating

ability of the ligand allows a higher metal to ligand ratio in the resultant complexes. $\text{Pd}(\text{acac})_2$ and $\text{Pd}(\text{hfacac})_2$ are prepared in moderate yield from aqueous solutions of PdCl_2 and the corresponding acetylacetonate salt.⁹ Both complexes have been used to deposit Pd films in the presence of hydrogen gas.¹⁰

Pyrazolate ligands present potential advantages for chemical vapor deposition precursors because they support a variety of coordination modes, the volatility can be tuned by substitution of functional groups at various positions of the ring, and they display high thermal stabilities similar to that of acetylacetonato ligands. Several homoleptic trinuclear pyrazolate complexes of the coinage metals¹¹ have been structurally characterized and thin films of Ag have been grown under CVD conditions from a series of complexes of the form $[\text{Ag}(3\text{-R},5\text{-R}'\text{Pz})]_3$ ($\text{R}=\text{R}'=\text{CF}_3$, $\text{R}=\text{CF}_3$, $\text{R}'=\text{tBu}$, $\text{R}=\text{R}'=\text{tBu}$).¹² Homoleptic pyrazolate complexes are especially attractive due to their ease of synthesis. Mononuclear,¹³ dinuclear,¹⁴ and trinuclear¹⁵ homoleptic palladium complexes have been studied with various substituted pyrazole and pyrazolate ligands.

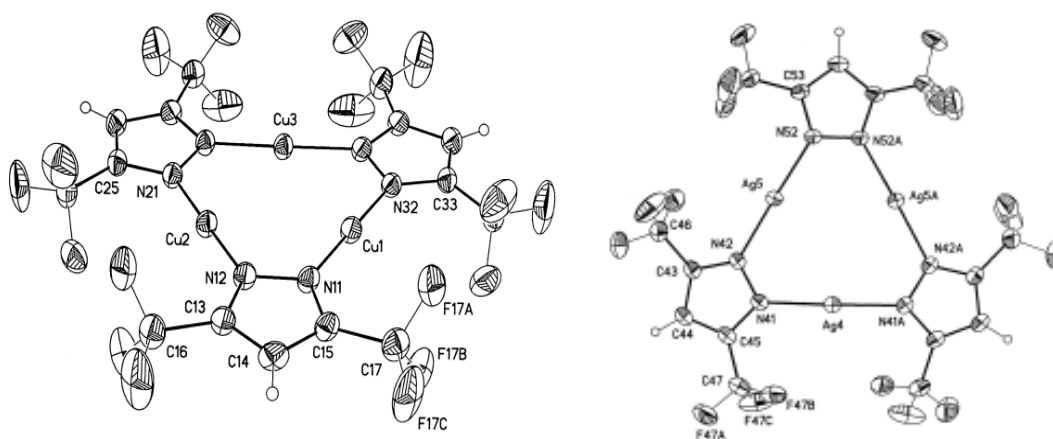


Figure 5.0 Examples of volatile homoleptic metal pyrazolate complexes appropriate for CVD applications.¹¹

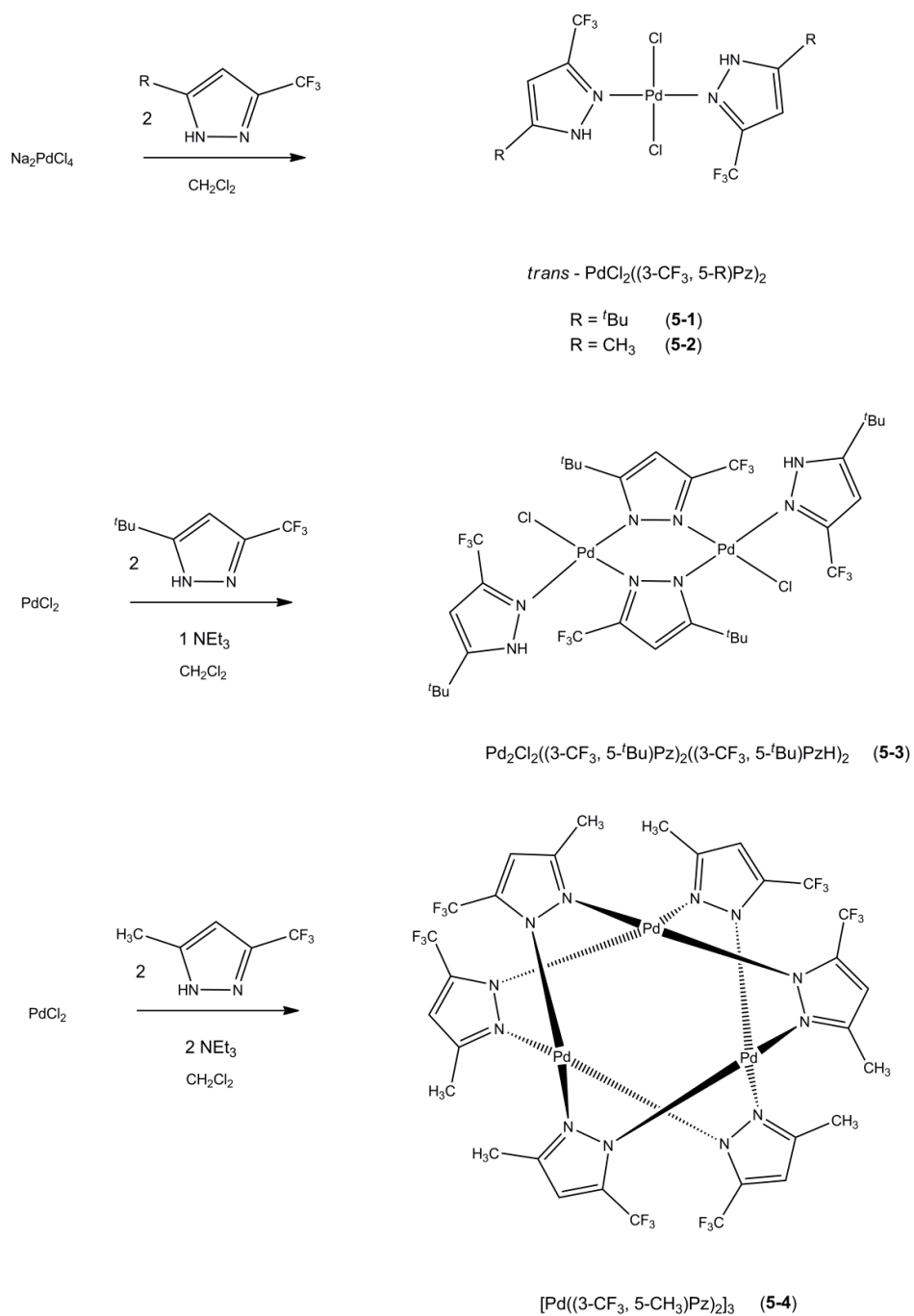
Synthesis of palladium pyrazolate complexes

The synthetic routes involved in the research presented in this chapter are shown in Scheme 5.1. Pyrazole adducts of formula *trans*-Cl₂Pd(3-R,5-R'-PzH)₂ (R = CF₃, R' = ^tBu (**5-1**), R = CF₃, R' = CH₃ (**5-2**)) were isolated from the interaction of Na₂PdCl₄ with the appropriate pyrazole in CH₂Cl₂. Both complexes feature intermolecular hydrogen-bonding interactions in the solid state. Under similar reaction conditions, the dinuclear bridging pyrazolate complex Cl₂Pd₂(μ-3-(CF₃),5-(^tBu)Pz)₂(3-(CF₃),5-(^tBu)PzH)₂ (**5-3**) is formed upon the addition of one molar equivalent of base to a mixture of Na₂PdCl₄ and 3-(CF₃),5-(^tBu)PzH, while addition of excess base to Na₂PdCl₄ and 3-(CF₃),5-(CH₃)PzH leads to the homoleptic pyrazolate-bridged Pd(II) trimer [Pd(μ-3-(CF₃),5-(CH₃))Pz]₃ (**5-4**).

RESULTS AND DISCUSSION

Pyrazole adducts

Addition of two equivalents of (3-(CF₃),5-(^tBu))PzH to anhydrous Na₂PdCl₄ in THF led to a gradual color change of the solution from brown to yellow. Evaporation of the solvent followed by recrystallization of the residue from methylene chloride gave yellow crystals of the dimeric species **5-1** in moderate yield. Several other isostructural pyrazole adducts of PdCl₂ are known which have varying substitution of the pyrazole ring.¹³



Scheme 5.1 Synthesis of palladium pyrazolate complexes.

Complex **5-1** crystallizes in the space group $C2/c$ with four dimeric $[\text{PdCl}_2(\text{PzH})_2]_2$ units as well as one non-coordinating methylene chloride solvent per unit cell. The dimeric units are formed via hydrogen bonding interactions between two $\text{PdCl}_2(\text{PzH})_2$ molecules. The structure is shown in Figure 5.1 and selected bond lengths and angles are listed in Table 5.3. Each palladium atom is in a distorted square planar coordination environment with the pyrazole molecules in a *trans* configuration. The deviation from square planarity is evident from the complimentary bowing of the ligands in and out of the Pd-L_4 plane ($\text{N}(1)\text{-Pd}(1)\text{-N}(1)^i = 175.4(3)^\circ$, $\text{Cl}(1)\text{-Pd}(1)\text{-Cl}(1)^i = 175.07(8)^\circ$). The planes formed by the pyrazole rings are twisted out of plane with the Cl-Pd-Cl axis, with a $\text{N}(1)\text{-N}(2)\text{-N}(2)^i\text{-N}(1)^i$ torsion angle of $54.65(9)^\circ$. This results in the placement of the trifluoromethyl groups on the same side of each complex, and the two $\text{PdCl}_2(\text{PzH})_2$ complexes thus interact via intermolecular hydrogen bonding interactions formed from a pyrazole NH hydrogen on one unit and a metal-coordinated chlorine atom from the other molecular unit. The average $\text{N}\cdots\text{H-Cl}$ distances of $3.22(5)$ Å and $\angle\text{N}\cdots\text{H-Cl}$ angles of $175(2)^\circ$ are typical of hydrogen bonds exhibited in other complexes of Pd with $\text{N}\cdots\text{H-Cl}$ interactions.^{13b} A list of hydrogen bonding interactions for **5-1** is presented in Table 5.7.

The ^1H NMR spectrum of **5-1** in C_6D_6 shows resonances at 6.34 ppm and 1.09 ppm, indicative of the aromatic and ^tBu protons, respectively, while a broad singlet at 12.83 ppm corresponds to the PzH protons involved in hydrogen bonding. The $^{19}\text{F}\{^1\text{H}\}$ NMR spectrum contains a singlet at -58.5 ppm, indicating a single magnetic environment for the CF_3 fluorine atoms. The IR spectrum of **5-1** shows a sharp band at 3144 cm^{-1} , characteristic of an N-H stretch.

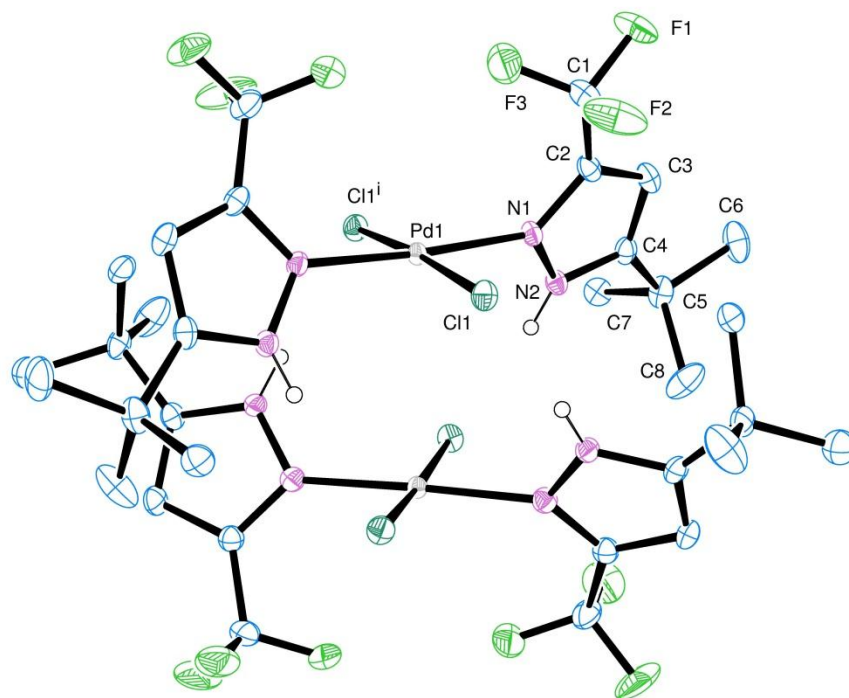


Figure 5.1 ORTEP diagram and partial atom numbering scheme of $[\text{PdCl}_2(3\text{-(CF}_3\text{)}, 5\text{-(tBu)PzH})_2]_2$ (**5-1**). Thermal ellipsoids are drawn at the 30% probability level. Selected hydrogen atoms have been omitted for clarity.

Reaction of Na_2PdCl_4 with two molar equivalents of 3-(CF_3),5-(CH_3)PzH in THF produces complex **5-2**, which may be isolated as X-ray quality crystals from slow evaporation of a CH_2Cl_2 extract of the crude reaction product. The complex crystallizes as a pyrazole adduct of the formula *trans*- $\text{PdCl}_2(\text{PzH})_2 \cdot 2 \text{ PzH}$ and a view of the asymmetric unit is shown in Figure 5.2. The solid state structure of complex **5-2** consists of a simple $\text{PdCl}_2(\text{PzH})_2$ monomer complex stabilized by two pyrazole molecules through hydrogen bonding interactions. The partial atom numbering scheme is shown in Figure 5.2, while selected bond lengths and angles are reported in Table 5.4. The coordination environment of the palladium atom is nearly square planar, with Pd-N and Pd-Cl distances within typical ranges for complexes of this type. The N-Pd-N angle is

179.1(2)°, while the Cl-Pd-Cl angle deviates from linearity (172.32(8)°) such that the two chlorine atoms are closer to the non-coordinating pyrazole molecules. The two metal-coordinated pyrazole units are angled out of plane slightly in order to achieve a shorter N...H-N distance with the two non-coordinated pyrazole molecules. Thus the two sets of unique hydrogen bonding interactions of N...H-N ($d(D\cdots A) = 2.822(9) \text{ \AA}$, $\angle(DHA) = 163(7)^\circ$) and N...H-Cl ($d(D\cdots A) = 3.397(7) \text{ \AA}$, $\angle(DHA) = 150(8)^\circ$) are responsible for the deviation of the $\text{PdCl}_2(\text{PzH})_2$ unit from perfect square planarity.

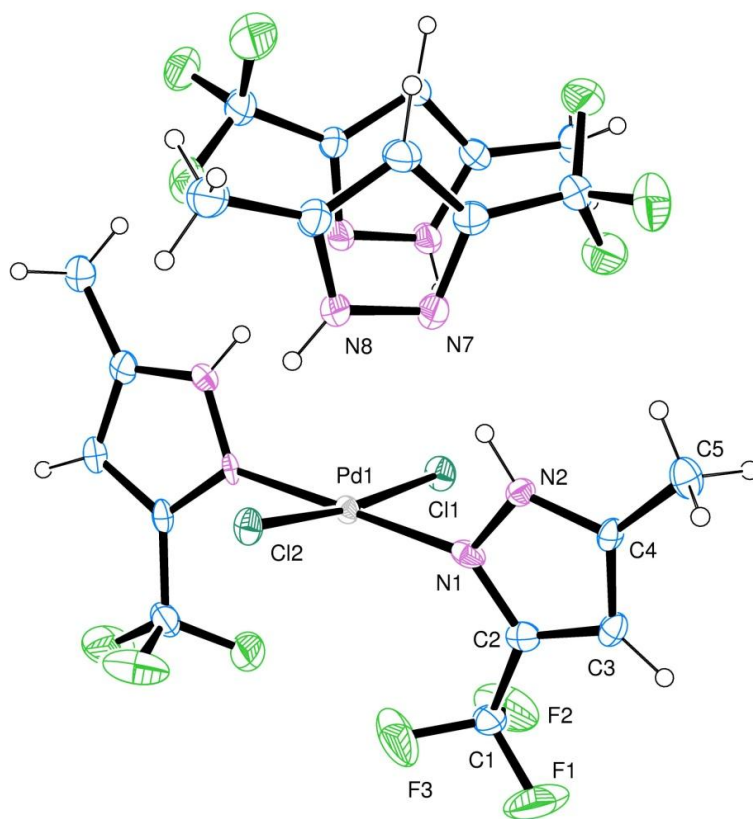


Figure 5.2 ORTEP diagram and partial atom numbering scheme of *trans*-Cl₂Pd(3-(CF₃),5-(CH₃)PzH)₂ • 2 (3-(CF₃),5-(CH₃)PzH) (**5-2**). Thermal ellipsoids are drawn at the 30% probability level.

Interestingly, the ^1H NMR spectrum of **5-2** in C_6D_6 shows several resonances in the regions corresponding to the protons of the coordinated pyrazole ligands. The $^{19}\text{F}\{^1\text{H}\}$ NMR spectrum is equally complex, with three distinct magnetic environments showing an approximate 1:3:6 peak intensity ratio. These data may be consistent with **5-2** existing as a mixture of species in solution, such as a monomer, a dimer, or as a pyrazole adduct, all of which may give rise to separate NMR signals. In addition, complex **5-2** may exist as a mixture of conformational isomers, corresponding to the *syn* and *anti* orientations of the PzH ligands allowed by rotation about the Pd-N bonds (Figure 5.3). The increased complexity of the spectra may also be due to species formed via exchange reactions between free and coordinated PzH molecules in solution. Spectroscopic detection of configurational isomers in similar *trans*- $\text{Cl}_2\text{Pd}(\text{polyetherpyrazole})_2$ complexes has been reported.^{13c} Thus as a result of the many different possible chemical environments for the NMR active nuclei, the ^1H and $^{19}\text{F}\{^1\text{H}\}$ NMR spectra of **5-2** are complex, with specific contributions from each isomeric species difficult to assign.

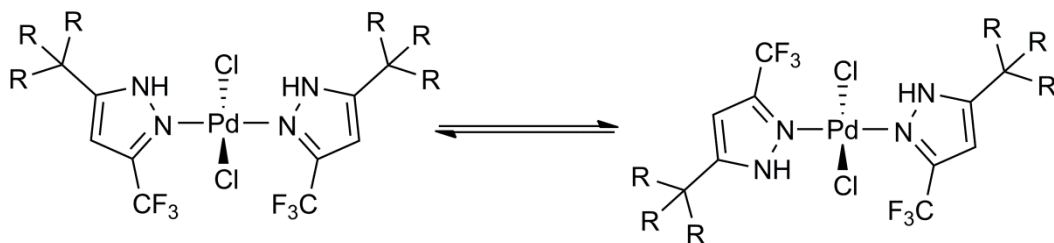


Figure 5.3 Conformational isomers of *trans*- $\text{Cl}_2\text{Pd}(\text{PzH})_2$ due to the rotational freedom of the pyrazole ligand along the Pd-N(2) bond.

Gentle heating of **5-2** under vacuum (70 °C) removes the two noncoordinated PzH molecules. Crystals of formula $[\text{PdCl}_2(\text{PzH})_2]_2$ (**5-2(a)**) may be obtained by crystallization of the residue from chloroform/hexane. The solid state structure (not shown) confirms the removal of two moles of free pyrazole allowing dimerization of two $\text{PdCl}_2(\text{PzH})_2$ units via intermolecular H-bonding interactions, resulting in a bonding configuration similar to that seen in complex **5-1**. ^1H NMR of samples of **5-2(a)** that were dried *in vacuo* at 70 °C for several hours show two sets of closely spaced signals with a peak intensity ratio of 0.7:1, indicating the presence of two configurational isomers. Elemental analysis of the thermally treated samples corresponds to $\text{Cl}_2\text{Pd}(\text{PzH})_2$, while high resolution mass spectral data suggest that the complex exists as discrete monomeric units in the gas phase. A large peak centered at m/e 442 in the mass spectrum indicates that the complex loses a Cl^- ion and exists as a $[\text{M}-\text{Cl}]^+$. Furthermore, no peak corresponding to $\text{Cl}_2\text{Pd}(\text{PzH}) \cdot 2 \text{PzH}$ (m/e 777) was detected.

Reaction of PdCl_2 with two molar equivalents of 3-(CF_3),5-($t\text{Bu}$)PzH followed by addition of one molar equivalent of triethylamine in THF results in a color change of the solution from orange to light yellow and formation of an insoluble light precipitate. Filtration and evaporation of volatiles from the filtrate leaves $\text{Cl}_2\text{Pd}_2(\mu\text{-(3-(CF}_3\text{),5-(}t\text{Bu)Pz))}_2(3\text{-(CF}_3\text{),5-(}t\text{Bu)PzH})_2$ (**5-3**) in moderate yield.

Complex **5-3** crystallizes in the monoclinic space group $P21/c$ with four molecules per unit cell. The X-ray crystal structure of the complex is presented in Figure 5.4. Key bond lengths and angles are presented in Table 5.5 and additional crystallographic data are presented in Table 5.2. The complex is comprised of two palladium ions bridged by two η^2 -pyrazolate ligands arranged such that the CF_3 functionality on each ring faces opposite directions. Each palladium atom is further coordinated by one chloride ion as well as one molecule of neutral, monodentate 3-

(CF₃),5-(^tBu)PzH, thus giving each palladium center an approximate *pseudo*-square planar coordination geometry (N(3)-Pd(1)-N(2) = 89.63(19)°; N(2)-Pd(1)-Cl(1) = 91.79(14)°). The two neutral PzH ligands coordinate to the metal centers through the nitrogen atom proximal to the CF₃ functionality of the ring, and there is no significant difference in Pd-N bond distances between the pyrazolate and pyrazole ligands. The Pd...Pd non-bonding interaction of 2.9315(6) Å is similar to the distance found in [Pd(μ-OAc)₂]₃ but ca. 0.4 Å shorter than interactions found in similar bridged pyrazolate species.¹⁴ The monodentate pyrazole molecule bound to one palladium ion and a chloride ion bound to the other metal center have appropriate geometry to form intramolecular N-H...Cl hydrogen bonds. This interaction may be responsible for the slight distortion of the arrangement of ligands from a perfect square plane around each Pd. A list of hydrogen bonding interactions for **5-3** is presented in Table 5.9.

The ¹H NMR spectrum of **5-3** in C₆D₆ shows two resonances of equal intensity at 1.63 ppm and 1.12 ppm corresponding to the two distinct magnetic environments of the ^tBu functionalities of the pyrazole and pyrazolate ligands, and a broad singlet at 12.81 ppm indicative of the pyrazole-bound N-H protons. The ¹⁹F{¹H} NMR spectrum is composed of two resonances of equal intensity centered at -58.63 ppm and -60.47 ppm, indicating non-equivalence of the CF₃ functionalities of the pyrazolate and pyrazole ligands. The IR spectrum of **5-3** shows a medium intensity band at 3157 cm⁻¹ corresponding to the N-H stretch of the pyrazole ligands.

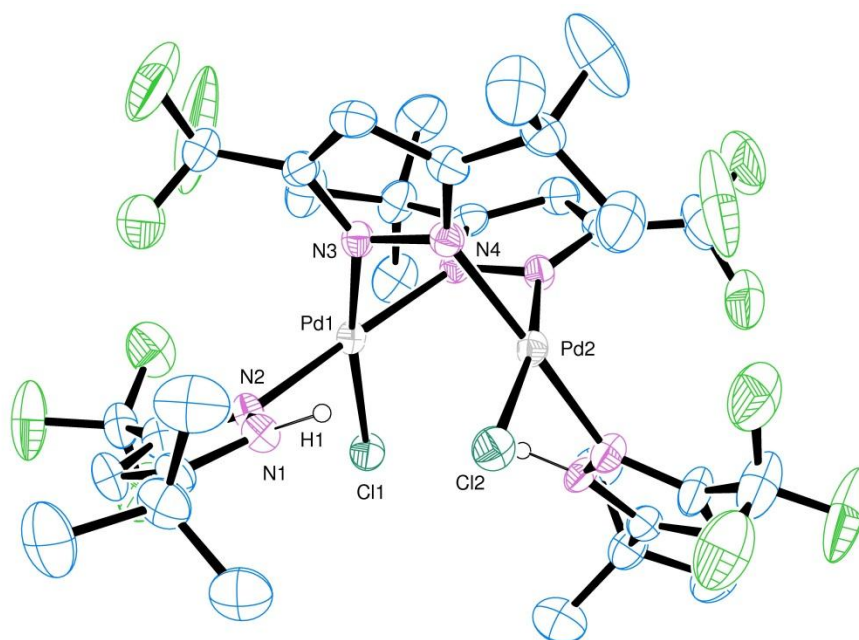


Figure 5.4 ORTEP diagram and partial atom numbering scheme of $\text{Cl}_2\text{Pd}_2(\mu\text{-(3-(CF}_3\text{),5-(tBu)Pz)})_2(3\text{-(CF}_3\text{),5-(tBu)PzH})_2$ (**5-3**). Thermal ellipsoids are drawn at the 30% probability level. Selected hydrogen atoms have been omitted for clarity.

A binary palladium pyrazolate complex

Reaction of PdCl_2 and two molar equivalents of 3-(CF_3),5-(CH_3)PzH with excess NEt_3 in a one-pot synthesis resulted in the formation of the homoleptic pyrazolato-bridged cyclic trinuclear complex $[\text{Pd}(\mu\text{-(3-(CF}_3\text{),5-(CH}_3\text{)Pz})_2)]_3$ (**5-4**). This complex has been characterized in solution and in the solid state and is structurally similar to other trinuclear Pd(II) complexes with various pyrazolate ligands (e.g. Pz, 3-PhPz, 4-MePz).¹⁵ The X-ray crystal structure of **5-4** is shown in Figure 5.5. Key bond angles and distances are presented in Table 5.6 and additional crystallographic data are listed in Table 5.2. The complex crystallizes in the monoclinic space group $P\bar{1}$ with two molecules in the unit

cell. The complex shows approximate D_3 symmetry, with the pyrazolate ligands coordinating in a one-directional, head to tail arrangement around the Pd_3 plane. Each Pd center has near square planar coordination geometry, while the unequal non-bonding Pd...Pd spacing ($\text{Pd}(1)\cdots\text{Pd}(3) = 3.0586(16) \text{ \AA}$, $\text{Pd}(1)\cdots\text{Pd}(2) = 3.0621(16) \text{ \AA}$, $\text{Pd}(2)\cdots\text{Pd}(3) = 3.0277(16) \text{ \AA}$) is similar to that observed in other $[\text{Pd}(\text{Pz})_2]_3$ systems. The Pd-N distances and N-Pd-N angles are in the ranges $2.015(13) \text{ \AA} - 2.049(14) \text{ \AA}$, and $82.3(5)^\circ - 97.8(5)^\circ$, respectively.

The ^1H NMR spectrum of **5-4** consists of two peaks centered at 5.68 ppm and 1.59 ppm, corresponding to the aromatic and methyl protons of the Pz ligand. The single peak at -61.51 ppm in the $^{19}\text{F}\{^1\text{H}\}$ NMR spectrum is consistent with the solid state structure. It is expected that similar complexes may be formed from analogous reactions of PdCl_2 with other substituted Pz moieties. Indeed, preliminary X-ray crystal data support the formation of $[\text{Pd}(\mu\text{-(3,5-(CF}_3)_2\text{Pz))}_2]_3$ from 3,5-(CF_3) $_2$ Pz. However, severe disorder present in the Pz ligand system prevents unambiguous structure solution, but there is a clear triangular arrangement of Pd centers with similar metrical parameters to complex **5-4**. The $[\text{Pd}(\mu\text{-(3-(CF}_3)_5\text{-(}^t\text{Bu)Pz))}_2]_3$ analog is supported by spectroscopic data. Complex **5-4** was not further investigated for use as a CVD reagent as it remains involatile upon heating to 300°C in a sealed tube under vacuum (10^{-2} Torr).

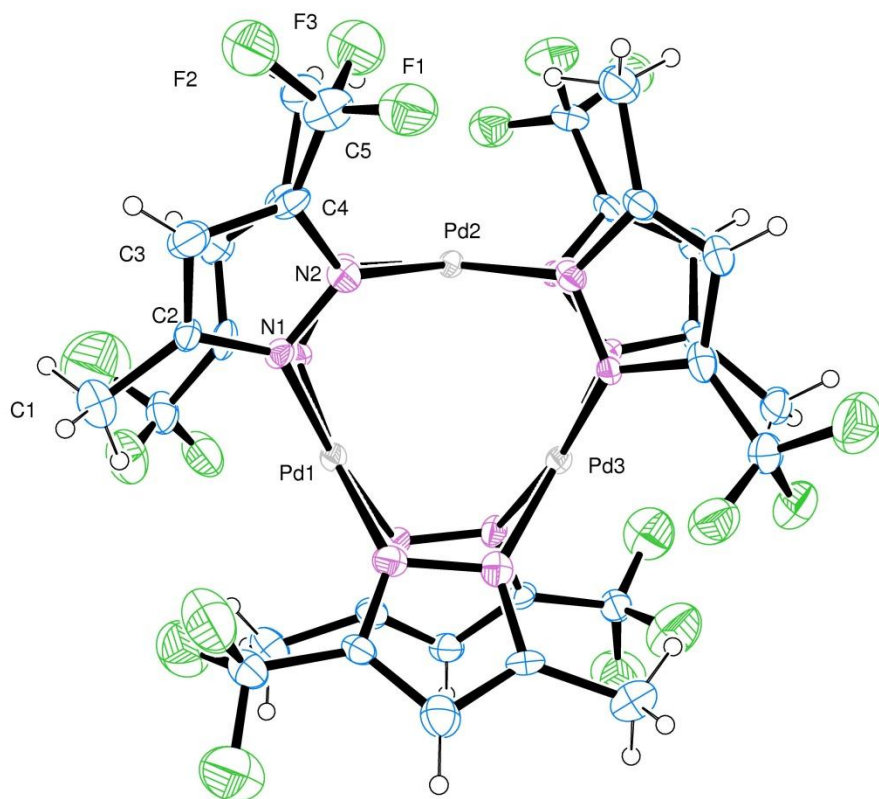


Figure 5.5 ORTEP diagram and partial atom numbering scheme of $[\text{Pd}(\mu\text{-(3-(CF}_3\text{), 5-(CH}_3\text{)Pz)}_2)_3]$ (**5-4**). Thermal ellipsoids are drawn at the 30% probability level.

CONCLUSIONS AND FUTURE STUDIES

This chapter outlines a synthetic scheme for the stepwise removal of halide ligands from PdCl_2 starting material with the goal of isolating homoleptic palladium pyrazolate complexes. Future studies are warranted, which involve the extension of this synthetic approach to other Group 10 metals (Ni, Pt), as well as mixed metal systems (Pd,-Ag; Pt,-Au). Furthermore, since the $[\text{Pd}(\mu\text{-Pz)}_2)_3$ structural motif may prove too involatile for CVD applications, it would be of interest to attempt to break up this

molecular framework into lower molecular weight units by addition of coordinating small molecules. For example, reaction of $[\text{Pd}(\mu\text{-Pz})_2]_3$ with PMe_3 may result in the formation of $\text{Pd}(\text{PMe}_3)_2\text{Pz}_2$. Alternatively, reaction of $\text{Cl}_2\text{Pd}(\text{PMe}_3)_2$ with 2 LiPz may afford similar mononuclear complexes. Further extension of the chemistry explored in this chapter with a variety of other symmetrically and asymmetrically substituted pyrazole and pyrazolate moieties would be of interest.

EXPERIMENTAL DETAILS

General synthesis

Unless otherwise noted, all reactions were performed under a dry, oxygen-free nitrogen atmosphere or under vacuum using standard Schlenk line and dry box techniques. All solvents were dried prior to use by distillation from molten sodium or sodium benzophenone ketyl under nitrogen. 3,5-bis(trifluoromethyl) pyrazole,¹⁶ 3,5-di-*tert*-butylpyrazole,¹⁷ 3-trifluoromethyl, 5-methyl pyrazole,¹⁸ and 3-trifluoromethyl, 5-*tert*-butyl pyrazole¹⁹ were prepared according to literature procedures. Microanalyses (C, H, N) were performed by Galbraith Laboratories of Knoxville, TN or QTI Labs of Whitehouse, NJ. Melting points were determined in sealed capillaries under N_2 (1 atm.) on an Electrothermal Melting Point apparatus and are uncorrected. ESI mass spectra were collected on a Finnigan MAT TSQ 700 mass spectrometer. NMR spectra were recorded on a Varian 300 Unity Plus spectrometer (300 MHz at 298 K). Chemical shifts are referenced to the deuterated solvent. Infrared spectra were taken on a Nicolet IR 200 FTIR spectrometer between KBr plates.

Single crystal X-ray crystallography

All crystals were covered in mineral oil and mounted on a nylon thread loop. Crystallographic data were collected on either a Nonius Kappa CCD diffractometer using a graphite monochromator with MoK α radiation ($\lambda = 0.71073\text{\AA}$) at reduced temperature using an Oxford Cryostream low temperature device or a Rigaku AFC12 diffractometer with a Saturn 724+ CCD using a graphite monochromator with MoK α radiation at reduced temperature using a Rigaku XStream low temperature device. Data reduction was performed with either DENZO-SMN or Rigaku Americas Corporation's Crystal Clear version 1.40. All structures were solved by direct methods using SIR2004 and refined by full-matrix least squares on F^2 with anisotropic displacement parameters for the non-H atoms using SHELXL-97. Hydrogen atoms on carbon were calculated in idealized positions with isotropic displacement parameters set to $1.2 \times U_{eq}$ of the attached atom ($1.5 \times U_{eq}$ for methyl hydrogen atoms). The function $\Sigma w(|F_o|^2 - |F_c|^2)^2$, was minimized, where $w = 1/[(\sigma(F_o))^2 + (0.0528*P)^2 + (0.685*P)]$ and $P = (|F_o|^2 + 2|F_c|^2)/3$. Neutral atom scattering factors and values used to calculate the linear absorption coefficient are from the International Tables for X-ray Crystallography. All figures were generated using SHELXTL/PC.

Synthesis of *trans*-Cl₂Pd(3-(CF₃),5-(*t*Bu)PzH)₂ (5-1)

To Na₂PdCl₄ (0.1 g, 0.34 mmol) in THF (30 mL) was added a solution of 3-trifluoromethyl,5-*tert*-butylpyrazole (0.13 g, 0.67 mmol) in THF (30 mL). The dark orange solution lightened and became more homogeneous. The mixture was stirred for 30 minutes at room temperature and then filtered. Solvent was removed *in vacuo* and the residue was taken up in methylene chloride (10 mL). Yellow X-ray quality crystals were

grown by slow evaporation of the methylene chloride solution. Isolated: 0.12 g, 64 %; mp 220-222 °C. (dec., 1 atm. N₂); ¹H-NMR (400 MHz, δ, CDCl₃): 12.83 (s, 2H, N-*H*), 6.34 (s, 2H, Pz-*H*), 1.09 (s, 18H, *t*Bu-*H*); ¹⁹F{¹H}-NMR (282 MHz, δ, CDCl₃): -58.53 (s, CF₃). FT-IR (KBr, cm⁻¹): 3144 (w), 2970 (w), 2872 (w), 1498-1471 (br, m), 1256 (m), 1219 (w), 1142 (s), 819 (w), 770 (s). HRMS (chemical ionization) *m/e*: 525.0459 [M⁺ - Cl]; Calcd. for C₁₆H₂₂F₆N₄ClPd: 525.04665. Anal. calcd. for C₁₆H₂₂F₆N₄Cl₂Pd: C, 34.21; H, 3.95; N, 9.97 %. Found: C, 34.19; H, 3.74; N, 9.61 %.

Synthesis of *trans*-Cl₂Pd(3-(CF₃),5-(CH₃)PzH)₂ (5-2)

To Na₂PdCl₄ (0.1 g, 0.34 mmol) in THF (30 mL) was added a solution of 3-trifluoromethyl, 5-methylpyrazole (0.10 g, 0.67 mmol) in THF (30 mL). The dark orange solution lightened and became more homogeneous. The mixture was stirred for 30 minutes at room temperature and then filtered. Solvent was removed *in vacuo* and the residue was taken up in methylene chloride (10 mL). Yellow X-ray quality crystals were grown by slow evaporation of the methylene chloride solution. Isolated: 0.08 g, 51 %; mp 208-211 °C. (dec., 1 atm. N₂); ¹H-NMR (400 MHz, δ, CDCl₃): 12.98 (br m, 4H, N-*H*), 6.39, 6.38, 6.35 (m, 4H, Pz-*H*), 2.89, 2.87, 2.07 (m, 12H, CH₃); ¹⁹F{¹H}-NMR (282 MHz, δ, CDCl₃): -60.89, -60.95 (m, CF₃). FT-IR (KBr, cm⁻¹): 3126 (w), 2926 (w), 1585 (m), 1435 (br, m), 1301 (w), 1247 (s), 1148 (vs), 821 (m). HRMS (chemical ionization) *m/e*: 440.9533. Calcd. for C₁₀H₁₀F₆N₄ClPd: 440.95275 [M⁺ - Cl]; Anal. calcd. for C₁₀H₁₀F₆N₄Cl₂Pd: C, 25.15; H, 2.11; N, 11.73 %. Found: C, 25.45; H, 2.11; N, 11.50 %.

Synthesis of $\text{Cl}_2\text{Pd}_2(\mu\text{-(3-(CF}_3\text{),5-(tBu)Pz)})_2(3\text{-(CF}_3\text{), 5-(tBu)PzH})_2$ (5-3)

A Schlenk flask was charged with PdCl_2 (0.063 g, 0.35 mmol) and anhydrous LiCl (0.03 g, 0.70 mmol) in the glove box and THF (50 mL) was added, resulting in a red homogeneous solution. A solution of 3-trifluoromethyl, 5-*tert*-butylpyrazole (0.138 g, 0.70 mmol) in THF (20 mL) was added to this solution, resulting a color change to yellow. This was allowed to stir for 30 minutes, and then triethylamine (0.05 mL, 0.35 mmol) was added. The resulting mixture immediately became lighter yellow and a precipitate developed. This was allowed to stir overnight at room temperature. The mixture was filtered, and the solvent removed completely *in vacuo*. The orange residue was then extracted into hexane (20 mL) and filtered. Yellow X-ray quality crystals were grown from slow evaporation of the hexane solution. Isolated: 0.04 g, 21 %; mp > 300 °C. (1 atm. N_2); $^1\text{H-NMR}$ (400 MHz, δ , C_6D_6): 12.32 (s, 2H, N-*H*), 6.34 (s, 2H, Pz-*H*), 6.08 (s, 2H, Pz-*H*), 1.63 (s, 18H, *t*Bu-*H*), 1.12 (s, 18H, *t*Bu-*H*); $^{19}\text{F}\{^1\text{H}\}$ -NMR (282 MHz, δ , C_6D_6): -58.63 (s, 6F, CF_3), -60.47 (s, 6F, CF_3); FT-IR (KBr, cm^{-1}): 3157 (m), 3108 (m), 2969 (s), 1717 (m), 1574 (s), 1500 (m), 1371 (m), 1258 (m), 1168 (s), 1134 (s), 1010 (m), 805 (m).

Synthesis of $[\text{Pd}(\mu\text{-(3-(CF}_3\text{),5-(CH}_3\text{)Pz)})_2]_3$ (5-4)

A Schlenk flask was charged with PdCl_2 (0.05 g, 0.28 mmol) and anhydrous LiCl (0.024 g, 0.56 mmol) in the glove box and THF (50 mL) was added, resulting in a red homogeneous solution. In a separate flask, triethylamine (0.15 mL) was added to a solution of 3-trifluoromethyl, 5-methylpyrazole (0.085 g, 0.59 mmol). The pyrazole was allowed to stir with base for 30 minutes, and then this solution was quantitatively transferred to the solution of the palladium salt. The resulting mixture immediately

became light yellow orange and a precipitate developed. This was allowed to stir overnight at room temperature. The mixture was filtered, and the solvent removed completely *in vacuo*. The orange residue was then extracted into hexane (20 mL) and filtered. Yellow X-ray quality crystals were grown from slow evaporation of the hexane solution. Isolated: 0.03 g, 25 %; mp > 300 °C. (dec., 1 atm. N₂); ¹H-NMR (400 MHz, δ, C₆D₆): 5.68 (s, 6H, Pz-*H*), 1.59 (s, 18H, CH₃); ¹⁹F{¹H}-NMR (282 MHz, δ, C₆D₆): -61.51 (s, CF₃); FT-IR (KBr, cm⁻¹): 2924 (m, br), 2850 (m), 1637 (s), 1460 (br, m), 1244 (m), 1132 (br, m), 796 (m). MS (chemical ionization) *m/e*: 1214 [M⁺], 1065 [M⁺ - Pz], 958 [M⁺ - Pz - Pd].

X-RAY CRYSTALLOGRAPHIC DETAILS

Table 5.1 Crystallographic details and refinement data for **5-1** and **5-2**.

	5-1	5-2
Empirical formula	C ₃₃ H ₄₂ Cl ₅ F ₁₂ N ₈ Pd ₂	C ₂₀ H ₁₆ Cl ₂ F ₁₂ N ₈ Pd
Formula weight	1168.8	773.71
Temperature	100(2) K	100(2) K
Wavelength	0.71073 Å	0.71073 Å
Crystal system	monoclinic	monoclinic
Space group	<i>C2/c</i>	<i>P2₁/n</i>
Unit cell dimensions	a = 15.379 Å b = 16.413 Å c = 21.751 Å $\alpha = 90^\circ$ $\beta = 110.66^\circ$ $\gamma = 90^\circ$	a = 8.807 Å b = 23.399 Å c = 14.275 Å $\alpha = 90^\circ$ $\beta = 101.89^\circ$ $\gamma = 90^\circ$
Volume	5137.3 Å ³	2878.6 Å ³
Z	4	4
Density (calculated)	1.511 Mg/m ³	1.785 Mg/m ³
Absorption coefficient	1.035 mm ⁻¹	0.935 mm ⁻¹
F(000)	2324	1520
Theta range for data collection	3.09 to 27.48°	2.99 to 27.48°
Index ranges	-19 ≤ h ≤ 19, -21 ≤ k ≤ 21, -28 ≤ l ≤ 28	-11 ≤ h ≤ 11, -30 ≤ k ≤ 30, -18 ≤ l ≤ 18
Reflections collected	26858	27797
Independent reflections	5897 [R(int) = 0.0439]	6572 [R(int) = 0.1109]
Refinement method	Full-matrix least-squares on F ²	Full-matrix least-squares on F ²
Data / restraints / parameters	5897 / 0 / 265	6572 / 0 / 400
Goodness-of-fit on F ²	1.016	1.112
Final R ^a indices [I > 2σ(I)]	R ₁ = 0.0696 wR ₂ = 0.1914	R ₁ = 0.0976 wR ₂ = 0.1786
R ^a indices (all data)	R ₁ = 0.0827 wR ₂ = 0.2024	R ₁ = 0.1287 wR ₂ = 0.1939
Largest diff. peak and hole	4.871 and -2.520 e.Å ⁻³	1.254 and -2.442 e.Å ⁻³

^a R₁ = Σ_{hkl}(|F_o| - |F_c|) / Σ_{hkl}|F_o|; wR₂ = [Σ w(|F_o| - |F_c|)² / Σ w|F_o|²]^{1/2}

Table 5.2 Crystallographic details and refinement data for **5-3** and **5-4**.

	5-3	5-4
Empirical formula	C ₃₂ H ₄₂ Cl ₂ F ₁₂ N ₈ Pd ₂	C ₃₀ H ₂₄ F ₁₈ N ₁₂ Pd ₃
Formula weight	1050.44	1213.81
Temperature	100(2) K	100(2) K
Wavelength	0.71073 Å	0.71073 Å
Crystal system	monoclinic	triclinic
Space group	<i>P</i> 2 ₁ / <i>c</i>	<i>P</i> $\bar{1}$
Unit cell dimensions	a = 11.196 Å b = 21.521 Å c = 17.939 Å α = 90° β = 102.33° γ = 90°	a = 11.825 Å b = 11.828 Å c = 15.675 Å α = 106.54° β = 91.77° γ = 111.33°
Volume	4222.7 Å ³	1935.5 Å ³
Z	4	2
Density (calculated)	1.652 Mg/m ³	2.083 Mg/m ³
Absorption coefficient	1.065 mm ⁻¹	1.509 mm ⁻¹
F(000)	2096	1176
Theta range for data collection	3.00 to 27.48°	3.08 to 27.48°
Index ranges	-14 ≤ h ≤ 14, -27 ≤ k ≤ 27, -23 ≤ l ≤ 23	-15 ≤ h ≤ 12, -15 ≤ k ≤ 15, -20 ≤ l ≤ 19
Reflections collected	69235	14030
Independent reflections	9679 [R(int) = 0.0977]	8688 [R(int) = 0.0782]
Refinement method	Full-matrix least-squares on F ²	Full-matrix least-squares on F ²
Data / restraints / parameters	9679 / 0 / 519	8688 / 381 / 550
Goodness-of-fit on F ²	1.069	1.279
Final R ^a indices [I > 2σ(I)]	R ₁ = 0.0638 wR ₂ = 0.1330	R ₁ = 0.1228 wR ₂ = 0.3415
R ^a indices (all data)	R ₁ = 0.1029 wR ₂ = 0.1480	R ₁ = 0.1809 wR ₂ = 0.3886
Largest diff. peak and hole	0.916 and -0.626 e.Å ⁻³	5.043 and -3.101 e.Å ⁻³

^a $R_1 = \sum_{\text{hkl}} (|F_o| - |F_c|) / \sum_{\text{hkl}} |F_o|$; $wR_2 = [\sum w(|F_o| - |F_c|)^2 / \sum w|F_o|^2]^{1/2}$

Table 5.3 Selected bond lengths [Å] and angles [°] for **5-1**.

Pd(1)-N(1)#1	2.012(5)	N(1)#1-Pd(1)-N(1)	175.4(3)
Pd(1)-N(1)	2.012(5)	N(1)#1-Pd(1)-Cl(1)	87.24(15)
Pd(1)-Cl(1)	2.2959(15)	N(1)-Pd(1)-Cl(1)	92.96(15)
Pd(1)-Cl(1)#1	2.2959(15)	N(1)#1-Pd(1)-Cl(1)#1	92.96(15)
Pd(2)-N(3)	2.019(5)	N(1)-Pd(1)-Cl(1)#1	87.24(15)
Pd(2)-N(3)#1	2.019(5)	Cl(1)-Pd(1)-Cl(1)#1	175.07(8)
Pd(2)-Cl(2)	2.2917(15)	N(3)-Pd(2)-N(3)#1	177.8(3)
Pd(2)-Cl(2)#1	2.2917(15)	N(3)-Pd(2)-Cl(2)	89.17(16)
		N(3)#1-Pd(2)-Cl(2)	90.91(16)
		N(3)-Pd(2)-Cl(2)#1	90.91(16)
		N(3)#1-Pd(2)-Cl(2)#1	89.17(16)
		Cl(2)-Pd(2)-Cl(2)#1	175.72(9)

Symmetry transformations used to generate equivalent atoms: #1 -x,y,-z+3/2

Table 5.4 Selected bond lengths [Å] and angles [°] for **5-2**.

N(1)-Pd(1)	2.000(8)	N(1)-Pd(1)-N(3)	179.1(2)
N(3)-Pd(1)	2.017(6)	N(1)-Pd(1)-Cl(2)	91.83(19)
Cl(1)-Pd(1)	2.295(2)	N(3)-Pd(1)-Cl(2)	88.64(17)
Cl(2)-Pd(1)	2.2910(19)	N(1)-Pd(1)-Cl(1)	88.84(19)
		N(3)-Pd(1)-Cl(1)	90.79(18)
		Cl(2)-Pd(1)-Cl(1)	172.32(8)

Table 5.5 Selected bond lengths [Å] and angles [°] for **5-3**.

Pd(1)-N(5)	2.022(5)	N(5)-Pd(1)-N(2)	175.26(19)
Pd(1)-N(2)	2.022(5)	N(5)-Pd(1)-N(3)	87.27(19)
Pd(1)-N(3)	2.045(5)	N(2)-Pd(1)-N(3)	89.63(19)
Pd(1)-Cl(2)	2.2938(15)	N(5)-Pd(1)-Cl(2)	90.62(14)
Pd(1)-Pd(2)	2.9315(6)	N(2)-Pd(1)-Cl(2)	91.79(14)
Pd(2)-N(4)	2.006(5)	N(3)-Pd(1)-Cl(2)	169.59(14)
Pd(2)-N(8)	2.031(5)	N(5)-Pd(1)-Pd(2)	67.51(14)
Pd(2)-N(6)	2.034(5)	N(2)-Pd(1)-Pd(2)	107.92(14)
Pd(2)-Cl(1)	2.3038(17)	N(3)-Pd(1)-Pd(2)	66.23(13)

		Cl(2)-Pd(1)-Pd(2)	103.57(4)
N(6)-Pd(2)-Cl(1)	169.33(14)	N(4)-Pd(2)-N(8)	174.0(2)
N(4)-Pd(2)-Pd(1)	68.27(14)	N(4)-Pd(2)-N(6)	86.70(19)
N(8)-Pd(2)-Pd(1)	106.28(15)	N(8)-Pd(2)-N(6)	88.7(2)
N(6)-Pd(2)-Pd(1)	66.95(13)	N(4)-Pd(2)-Cl(1)	90.28(14)
Cl(1)-Pd(2)-Pd(1)	102.43(5)	N(8)-Pd(2)-Cl(1)	93.54(16)

Table 5.6 Selected bond lengths [Å] and angles [°] for **5-4**.

N(1)-N(2)	1.358(18)	Pd(1)-Pd(3)	3.0586(16)
N(1)-Pd(1)	2.024(13)	Pd(1)-Pd(2)	3.0621(16)
N(2)-Pd(2)	2.026(13)	Pd(2)-Pd(3)	3.0277(16)
N(3)-N(4)	1.343(18)		
N(3)-Pd(2)	2.015(13)	N(7)-Pd(1)-N(12)	94.7(5)
N(4)-Pd(3)	2.045(12)	N(7)-Pd(1)-N(1)	82.3(5)
N(5)-N(6)	1.42(2)	N(12)-Pd(1)-N(1)	172.9(5)
N(5)-Pd(3)	2.019(14)	N(7)-Pd(1)-N(6)	173.3(6)
N(6)-Pd(1)	2.049(14)	N(12)-Pd(1)-N(6)	84.5(5)
N(7)-N(8)	1.397(18)	N(1)-Pd(1)-N(6)	97.8(5)
N(7)-Pd(1)	2.003(13)	N(7)-Pd(1)-Pd(3)	107.1(4)
N(8)-Pd(2)	1.956(14)	N(12)-Pd(1)-Pd(3)	65.4(4)
N(9)-N(10)	1.343(16)	N(1)-Pd(1)-Pd(3)	109.2(4)
N(9)-Pd(2)	2.053(11)	N(6)-Pd(1)-Pd(3)	66.5(4)
N(10)-Pd(3)	2.019(12)	N(7)-Pd(1)-Pd(2)	65.6(4)
N(11)-N(12)	1.388(18)	N(12)-Pd(1)-Pd(2)	109.4(4)
N(11)-Pd(3)	2.055(13)	N(1)-Pd(1)-Pd(2)	63.5(4)
N(12)-Pd(1)	2.014(13)	N(6)-Pd(1)-Pd(2)	108.4(4)
		Pd(3)-Pd(1)-Pd(2)	59.29(4)
		Pd(2)-Pd(3)-Pd(1)	60.41(4)

Table 5.7 Hydrogen bonds for **5-1** [Å and °].

D-H...A	d(D-H)	d(H...A)	d(D...A)	<(DHA)
N(4)-H(4)...Cl(1)	0.86	2.36	3.222(5)	177.9
N(2)-H(2)...Cl(2)#1	0.86	2.38	3.232(5)	173.5

Symmetry transformations used to generate equivalent atoms: #1 -x,y,-z+3/2

Table 5.8 Hydrogen bonds for **5-2** [Å and °].

D-H...A	d(D-H)	d(H...A)	d(D...A)	<(DHA)
N(4)-H(2)...N(5)	0.88(8)	1.97(8)	2.822(9)	163(7)
N(6)-H(3)...Cl(1)	0.84(9)	2.64(9)	3.419(8)	156(8)
N(8)-H(8A)...Cl(2)	0.86	2.64	3.375(7)	144.9
N(2)-H(1)...N(7)	0.94(10)	1.92(10)	2.822(10)	162(9)

Table 5.9 Hydrogen bonds for **5-3** [Å and °].

D-H...A	d(D-H)	d(H...A)	d(D...A)	<(DHA)
N(7)-H(100)...Cl(2)	0.957(5)	2.3389(16)	3.242(5)	157.1(3)
N(1)-H(101)...Cl(1)	1.015(5)	2.3507(17)	3.247(5)	146.7(3)

REFERENCES

1. Hierso, J.C.; Feurer, R.; Kalck, P. *Coordination Chemistry Reviews* **1998**, 178-180, 1811.
2. McClellan, W.R.; Hoen, H.H.; Cripps, H.N.; Mutterties, E.L.; Howk, B.W. *J. Am. Chem. Soc.* **1961**, 83, 1601.
3. Becconsall, J.K.; Job, B.E.; O'Brien, S. *J. Chem. Soc. A* **1967**, 423.
4. (a) Robinson, S.D.; Shaw, B.L. *J. Chem. Soc.* **1963**, 4806. (b) Imamura, S.; Kajimoto, T.; Kitano, Y.; Tsuji, J. *Bull. Chem. Soc. Jpn.* **1969**, 42, 805.
5. Yuan, Z.; Puddephatt, R.J. *Adv. Mater.* **1994**, 1, 6.
6. Gozum, J.E.; Pollina, D.M.; Jensen, J.A.; Girolami, G.S. *J. Am. Chem. Soc.* **1988**, 110, 2688.
7. Hierso, J.-C.; Satto, C.; Feurer, R.; Kalck, P. *Chem. Mater.* **1996**, 8, 2481.
8. (a) Calvin, G.; Coates, G.E. *J. Chem. Soc.* **1960**, 2008. (b) Yuan, Z.; Jiang, D.; Naftel, S.J.; Sham, T.-K.; Puddephatt, R.J. *Chem. Mater.* **1994**, 6, 2151.
9. (a) Gibson, D.; *Coord. Chem. Rev.* **4** **1969**, 225. (b) Baba, S.; Oguri, T.; Kawaguchi, S. *Bull. Chem. Soc. Jpn.* **1974**, 47, 665. (c) Siedle, A.R.; Newmark, R.A.; Kruger, A.A.; Pignolet, L.H. *Inorg. Chem.* **1981**, 20, 3399. (d) Siedle, A.R. *Inorg. Synth.* **1990**, 27, 317.
10. (a) Lin, W.; Wiegand, B.C.; Nuzzo, R.G.; Girolami, G.S. *J. Am. Chem. Soc.* **1996**, 118, 5977. (b) Lin, W.; Nuzzo, R.G.; Girolami, G.S. *J. Am. Chem. Soc.* **1996**, 118, 5988. (c) Bhaskaran, V.; Hampden-Smith, M.J.; Kodas, T.T. *Chem. Vapor Depos.* **1997**, 3, 85.
11. (a) Dias, H. V. R.; Gamage, C. S. P.; Keltner, J.; Diyabalanage, H. V. K.; Omari, I.; Eyobo, Y.; Dias, N. R.; Roehr, N.; McKinney, L.; Poth, T. *Inorg. Chem.* **2007**, 46, 2979. (b) Dias, H. V. R.; Singh, S.; Campana, C. F. *Inorg. Chem.* **2008**, 47, 3943.
12. Song, Y.-H.; Chen, Y.-L.; Chi, Y.; Liu, C.-S.; Ching, W.-L.; Kai, J.-J.; Chen, R.-S.; Huang, Y.-S.; Carty, A. J. *Chem. Vapor. Deposition* **2003**, 9, 162. (b) Chi, Y.; Lay, E.; Chou, T.-Y.; Song, Y.-H.; Carty, A. J. *Chemical Vapor Deposition* **2005**, 11, 206.

13. (a) Spencer, L. C.; Guzei, I.A.; Ojwach, S.O.; Darkwa, J. *Acta Cryst. C* **2006**, 62, m421. (b) Cheng, C.-H.; Lain, J.-S.; Wu, Y.-J.; Wang, S.-L. *Acta Cryst. C* **1990**, 46, 208. (c) Boixassa, A.; Pons, J.; Solans, X., Font-Bardia, M.; Ros, J *Inorganica Chimica Acta* **2003**, 346, 151.
14. (a) Ara, I.; Falvello, L.R.; Fornies, J.; Lasheras, R.; Martin, A.; Oliva, O.; Sicilia, V. *Inorganica Chimica Acta* **2006**, 359, 4574-4584. (b) Ara, I.; Fornies, J.; Lasheras, R.; Martin, A.; Sicilia, V. *Eur. J. Inorg. Chem.* **2006**, 5, 948. (c) Jain, V.K.; Kannan, S.; Tiekink, E.R.T. *J. Chem. Soc. Dalton Trans.* **1992**, 14, 2231.
15. (a) Baran, P.; Marrero, C.M.; Perez, S.; Raptis, R.G. *Chem. Commun.* **2002**, 9, 1012-1013. (b) Umakoshi, K.; Yamauchi, Y.; Nakamiya, K.; Kojima, T.; Yamasaki, M.; Kawano, H.; Onishi, M. *Inorganic Chemistry* **2003**, 42, 3907.
16. Claire, P. P. K.; Coe, P. L.; Jones, C. J.; McCleverty, J. A. *J. Fluorine Chem.* **1991**, 51, 283-89. (b) Threadgill, M. D.; Heer, A. K.; Jones, B. G. *J. Fluorine Chem.* **1993**, 65, 21.
17. Zelenin, K. N.; Alekseyev, V. V.; Tygysheva, A. R.; Yakimovitch, S. I. *Tetrahedron* **1995**, 51, 11251.
18. Hu, Z.; Loas, A.; Gorun, S.M. *Inorganica Chimica Acta* **2009**, 362, 4639.
19. Foces-Foces, C.; Alkorta, I.; Elguero, J. *Acta Cryst. B* **2000**, B56, 1018.

Chapter 6: Low-temperature synthetic routes to transition metal phosphides and borates for Li-ion battery applications

INTRODUCTION

Li-ion batteries

Lithium-ion batteries are a promising power source for Hybrid Electric Vehicles, the widespread use of which is predicted to greatly reduce CO₂ emissions as well as dependence on foreign oil.¹ Current battery technology must progress, however, in order to produce safer, cheaper and lighter high-capacity battery solutions for the next generation of electric vehicles. Towards this goal, considerable research has been carried out on improving Li-ion battery anode and cathode materials by discovering novel materials with morphologies and chemical compositions that allow for fast charge/discharge rates and high capacity.

Early batteries based on Li⁺ ion technology initially incorporated lithium metal as the anode material due to its low atomic weight and high reactivity, though serious safety issues were quickly discovered which limited its further use.² As an alternative to lithium electrodes, intercalation compounds based on a variety of different materials and composites have since been investigated, as they allow insertion/de-insertion of lithium ions at low potentials relative to the Li/Li⁺ redox couple and avoid the potential safety hazards associated with use of elemental lithium.

In a typical Li-ion battery system (Figure 6.1), the negative electrode releases Li⁺ ions upon discharging, concomitant with the flow of an equal number of moles of electrons to the cathode. Because the electrolyte used in the cell is ionically conductive and not electrically conductive, the electrons travel through an external connection (where they can be used to do work), while the lithium ions travel through the electrolyte to the cathode. The reversal of this process upon charging changes the direction of travel

of the ions and current, and must be driven by an externally applied voltage that is higher than the difference in electrochemical potential between the anode and cathode.

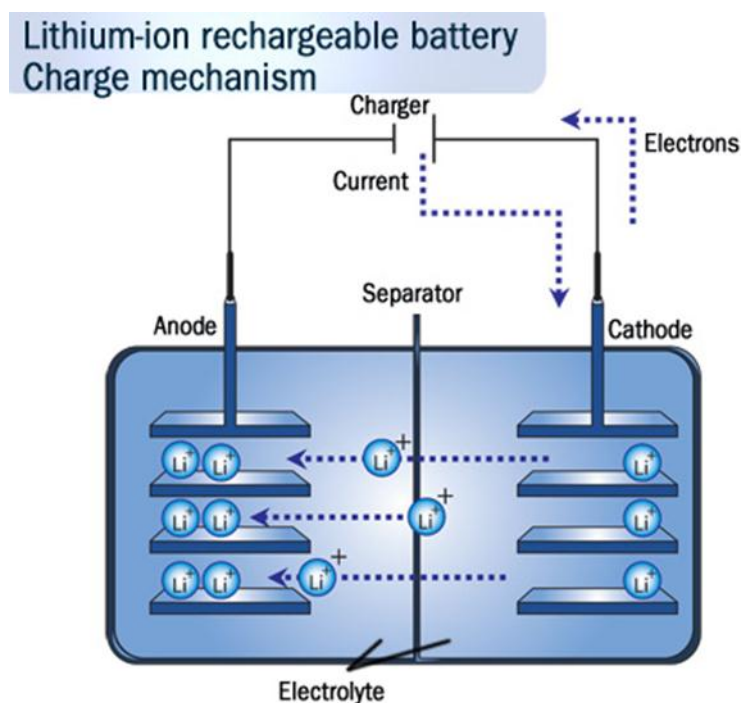


Figure 6.1 Schematic representation of a lithium ion battery.

Use of intercalation materials for both electrodes in an electrochemical cell has become the basis for modern lithium ion batteries, and a great deal of current research into the improvement of battery performance has been directed toward the development of novel anode and cathode materials. Suitable electrode materials must meet several important criteria: (i) low molecular weight, (ii) high conductivity, (iii) high charge density, (iv) reversibility, (v) stability, (vi) low cost and (vii) low toxicity. Graphitic carbon has emerged as the standard active anode material in commercial batteries as it meets many of the requirements mentioned above. The high gravimetric capacity of ca.

370 mAhg⁻¹ arises from the ability of Li⁺ ions to occupy space between individual two-dimensional graphene sheets. The electrostatic repulsion exhibited by two neighboring positively charged Li⁺ centers is less than the energy required to separate the sheets, allowing a maximum stoichiometry of one Li per six carbons (LiC₆). Upon discharge, the lithium ions leave the interstitial space, and while the overall structure allows for facile re-insertion, cycling performance is usually limited by the buildup of a barrier layer that is formed from the decomposition of electrolyte upon repeated cycling. This inhibits further Li intercalation, limiting device performance.

Metal phosphides

Attractive candidates for anode materials in lithium-ion batteries should exhibit low molecular weight, low redox potential relative to the Li/Li⁺ couple and reversible lithium insertion/de-insertion reactions. Novel materials that meet these criteria have been investigated as substitutes for graphitic carbon. Due to their high gravimetric capacities upon reaction with Li, transition metal phosphides (TMP) have emerged as a promising class of compounds suitable for improved high capacity anode materials. Several studies of TMPs such as TiP₂,³ VP₄,⁴ NiP₂,⁵ CuP₂,⁶ Cu₃P,⁷ and CoP₃⁸ have produced promising results. For example, Li₇TiP₄, LiMnP₄, and FeP have been shown to exhibit initial charge/discharge capacities of 625, 1400, and 970 mAhg⁻¹, respectively.⁹⁻¹¹ This is a significant improvement in capacity compared to the currently utilized material LiC₆, which shows reversible capacity on the order of 370 mAh/g.¹² Some TMPs have been shown to operate via a metal alloying step with formation of Li₃P (Equation 2). Much higher gravimetric capacities have been realized with materials that undergo this type of reaction, the mechanism of which involves both a Faradaic contribution from the

Li^+ insertion process (intercalation), and a contribution from the charge-transfer process associated with surface alloying processes (capacitive). These intercalative and capacitive alloying effects have been observed for other high surface area metal oxide materials and demonstrate that significantly higher energy density can be achieved when both charge storage processes are operative. It is hypothesized that as crystallite size decreases and as the material becomes more porous, the latter surface alloying mechanism will contribute to a larger extent.



One drawback of transition metal phosphides for battery applications is the large irreversible volume changes that accompany charge transfer reactions. Upon repeated cycling, these structural changes introduce stress into the lattice of the material, causing particle aggregation and degradation, eventually leading to significant overall capacity loss. Efforts to mitigate capacity dampening by modification of the ratio of active anode material and various binder excipients, additives, etc. has been somewhat successful.¹³ Another approach to limit the magnitude of the volume change associated with cycling is to tune the morphology of the electrode materials by utilizing porous or nanostructured architectures.

Synthesis of transition metal phosphides

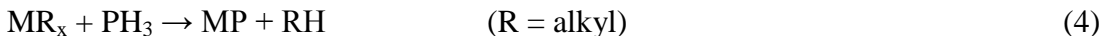
This chapter highlights the development of a novel synthetic approach which has proven versatile for the formation of transition metal phosphides with a variety of metals. Key advantages of the synthetic method are its low-energy requirements and facile, near quantitative yield. Current methods of preparing nanostructured TMP's include solvothermal and arrested precipitation processes which employ relatively high temperatures.¹⁴ For example, use of trioctylphosphine (TOP) and trioctylphosphine oxide (TOPO) at temperatures generally in the range of 200 - 300 °C have yielded a variety of late transition metal phosphides as nanoparticles and nanorods,¹⁵ while other materials such as VP,¹⁶ Ti_xP_y ¹⁷ and CoP_3 ¹⁸ have been synthesized by heating stoichiometric amounts of the elements anaerobically in sealed tubes or by mechanochemical grinding. In contrast to these high temperature methods which, in most cases provide the most thermodynamically stable, well known crystalline phase, the synthetic strategy employed in this chapter involves low temperature reactions (most performed at -78 °C) of transition metal organometallic species with phosphine gas (PH_3) allowing the formation of both amorphous and crystalline phases of TMPs with hitherto unknown stoichiometries and morphologies.

Reactions of PH_3 with a variety of different transition metal complexes have been reported and a number of compounds containing coordinated PH_3 are known.¹⁹ The focus of the synthetic studies described herein is the interaction of PH_3 with *d*-block transition metal organometallic derivatives including σ -bonded metal alkyls and dialkylamide derivatives, an area of research which does not appear to have been previously investigated. Of related interest, for the *p*-block elements, tertiary butyl derivatives of Ga and In ($t\text{Bu}_3\text{M}$, M= Ga, In) react with phosphine under mild conditions to give phosphido ($\mu\text{-PH}_2$) complexes of formula $[t\text{Bu}_2\text{M}(\mu\text{-PH}_2)]_3$ by loss of *iso*-butane. The chemistry of

the Ga derivatives was first described previously in these laboratories.²⁰ Subsequent heating of these compounds, either during CVD processes, or in the condensed phase gives excellent yields of the corresponding binary semiconductor materials GaP or InP. Similarly, InMe₃ reacts with PH₃ to give InP (eq. 3). This is a high temperature reaction, typically carried out in the gas phase on a heated substrate under low pressure and can produce thin films of ultra high purity InP.²¹



Studies described in this chapter show that reactions of PH₃ with suitable organometallic derivatives of the appropriate transition metal, conducted at low temperatures, can ultimately lead to metal TMP's with nanostructured architectures (equations 4 and 5).



One of the key goals is to learn what factors affect TMP morphology and to produce nanostructured architectures that will permit facile Li⁺ ion transport. Materials with small particle size and high surface area are hypothesized to better tolerate volumetric changes associated with the Li⁺ insertion/redox reactions and should therefore show improved performance in terms of energy storage. As described below, our initial investigations have allowed us to identify materials that show great promise. In this chapter, the specific objectives are focused on the low temperature preparation,

evaluation and optimization of mesoporous MnP and Li_3MnP_2 for use as anode materials in lithium-ion batteries. Since electrochemical activity is known to be crucially dependent on size, morphology, and composition, critical structure-activity relationships are evaluated using *ex situ* structural and chemical surface analysis tools (XRD, SEM, BET surface area).

RESULTS AND DISCUSSION

TMPs with varying morphologies and chemical compositions were synthesized from a facile, low-temperature synthetic route involving interaction of phosphine gas with reactive metal alkyl and bis(trimethylsilyl)amido complexes. These materials were structurally characterized by electron microscopy and X-ray powder diffraction. Additionally their electrochemical properties were evaluated in battery cells between 0.1 and 2.2 V for use as negative electrode materials for lithium ion batteries (by collaborators Jing Wu and Nellymar Membreno in the Stevenson lab at the Center for Electrochemistry). Also discussed are some promising results with other metal systems, namely iron and manganese borates, which were prepared in an analogous manner.

Synthesis of manganese phosphide and lithium manganese phosphide

Manganese phosphide was synthesized by direct reaction of dimethylmanganese with phosphine gas at low temperature. In a typical synthesis, a freshly prepared solution of dimethylmanganese in Et_2O was prepared and quantitatively transferred to a Fischer-Porter bottle equipped with a pressure regulator. The solution was cooled to $-78\text{ }^\circ\text{C}$ and then PH_3 (ca. 1 atm.) was introduced, causing an instantaneous darkening of the bright orange solution, and within several minutes, formation of dark precipitate. After stirring

for several hours and warming to room temperature, the solution became colorless and a large amount of black solid had precipitated. Under similar reactions conditions, but with the use of Li_2MnMe_4 as the starting metal alkyl reagent, a mixed phase material consisting of MnP and Li_3MnP_2 was isolated as a black amorphous solid. The formation of a ternary phase containing lithium has interesting implications for Li reactivity of the material since prior incorporation of lithium in the material may reduce the drastic structural change associated with lithium intercalation. Regardless of the starting reagent, the reactions were quantitative with recovered yields generally (>90%).

Due to the extreme reactivity of phosphine gas, reactions were initiated at reduced temperatures and allowed to slowly warm to room temperature. This was followed by subsequent heating (120-150 °C), either under PH_3 or under vacuum to help drive the M-R + P-H reaction to completion and to remove any other ancillary ligands or solvent that might still be present after the first step. The resulting mesostructured materials retained considerable amorphous character and could be rendered more crystalline upon annealing at higher temperatures. Both the phase-pure MnP and mixed phase material were considerably air and moisture reactive, quickly forming MnO_2 upon exposure to atmosphere.

Characterization

Scanning electron microscopy

The morphology of the synthesized material was found to vary with specific reaction conditions. For example, synthesis of MnP by a solution-based reaction method described above resulted in small particles (50-100 nm) as shown in the SEM images in Figure 6.2 (top). Alternatively, complete removal of solvent *in vacuo* prior to reaction

with PH_3 led to material with a microstructure consisting of a porous framework (Figure 6.2, bottom). The pores ranged in size from 20 to 500 nm with a fairly wide size distribution as visually determined by SEM. This porous morphology observed in material synthesized from the solid-gas reaction is hypothesized to originate from the formation of gaseous methane upon reaction of MnMe_2 with PH_3 .

The porous material exhibited a high surface area as determined by N_2 adsorption-desorption isothermal analysis (BET method) as shown in Figure 6.3. Surface areas as high as $251 \text{ m}^2\text{g}^{-1}$ were found for material formed from the solid-gas reaction, while surface areas for materials synthesized through solution methods were observed to be lower. The average pore size for the mesoporous materials were on the order of 2 nm as determined by multipoint BET pore size distribution analysis. The ability to control morphology by altering reaction conditions leads to interesting possibilities for potential tailoring of electrochemical properties. Higher surface area and smaller particle size of the electrode material is desirable as this leads to more direct contact with the electrolyte and shortens the diffusion path of Li upon intercalation.

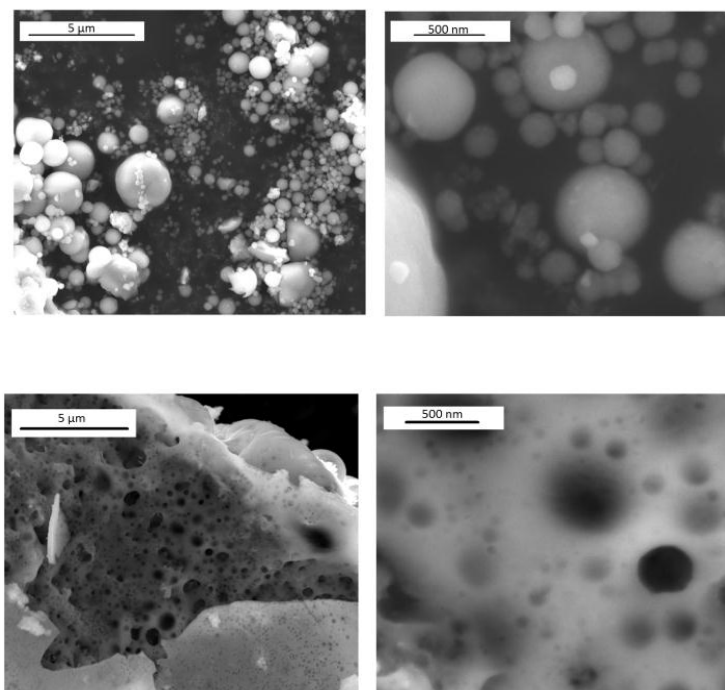


Figure 6.2 SEM images of MnP. Reaction of $\text{Mn}(\text{CH}_3)_2$ with PH_3 in solution leads to small (ca. 100 nm) particles (top) whereas the same reaction performed without solvent yields material with a porous microstructure (bottom).

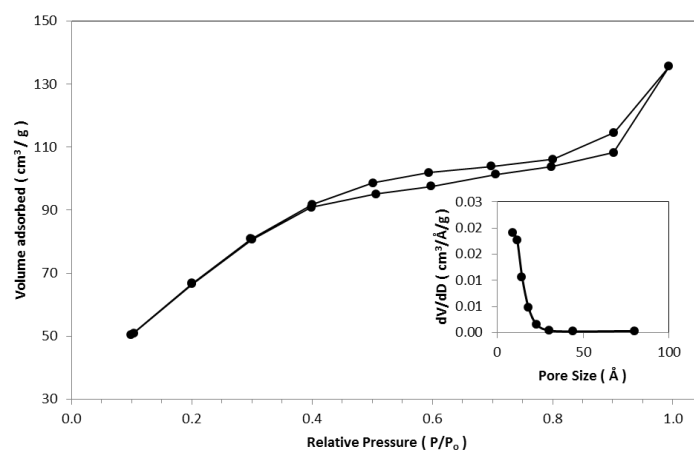


Figure 6.3 N_2 adsorption-desorption isotherm for MnP.

X-ray diffraction

Powder X-ray diffraction studies were used as a means to characterize the specific crystalline phase of the material upon annealing, as well as reveal information about average crystallite size. All as-synthesized materials were found to be X-ray amorphous, and subsequent thermal treatment of the material resulted in larger crystallite formation and appearance of well-resolved peaks in XRD patterns, as shown in Figures 6.4 and 6.5.

MnP was found to remain amorphous at temperatures up to 400 °C. Upon crystallization, the only observed diffraction peaks corresponded to binary MnP (PDF# 01-078-0029). Indexing the XRD power pattern showed that the compound crystallized in the orthorhombic crystal system, space group Pnma (No. 62) with lattice parameters $a = 5.259 \text{ \AA}$, $c = 3.173 \text{ \AA}$, $b = 5.918 \text{ \AA}$ and $D = 5.776 \text{ g/cm}^3$. The full width at half-maximum (FWHM) of three representative reflections, namely (211), (220), and (121), were determined using profile fitting software and are listed in Table 6.1 at various annealing temperatures for comparison. Crystallite sizes were estimated from the Scherrer equation²² and increase in size to roughly 250 Å after annealing at 600 °C.

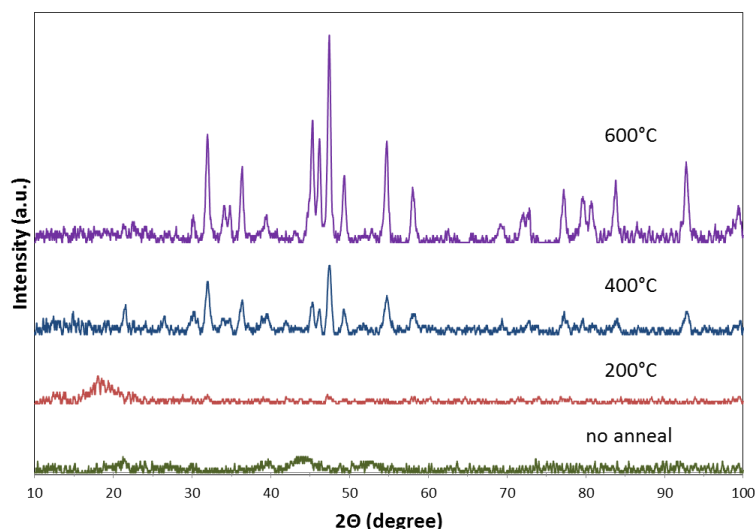


Figure 6.4 Powder XRD patterns of MnP annealed at different temperatures *in vacuo*. The patterns are vertically shifted for comparison.

The XRD pattern of the as-synthesized mixed-phase lithiated material was similarly featureless, with the exception of two broad peaks centered at $2\Theta = 27^\circ$ and 43° . These diffraction peaks indicate the presence of microcrystalline Li_3MnP_2 . Analysis of material that was subjected to further annealing showed a greater number of high intensity peaks corresponding to Li_3MnP_2 , as well as the appearance of additional peaks corresponding to MnP. Figure 6.5 shows a series of X-ray diffraction patterns of the lithiated material at various annealing temperatures. Peaks indicated by a star (*) were indexed to the tetragonal cell of the Li_3MnP_2 phase (PDF# 01-076-1697) with space group P4/nmm (No. 129), lattice constant $a = b = 4.1634 \text{ \AA}$ and $c = 5.983 \text{ \AA}$, and $D = 2.205 \text{ g/cm}^3$, while peaks marked with a plus (+) were indexed to the orthorhombic cell of the MnP phase (PDF# 01-078-0029). Upon annealing, a clear increase in crystallite size was observed for the mixed phase material, as illustrated in the right-hand column of Table 6.1.

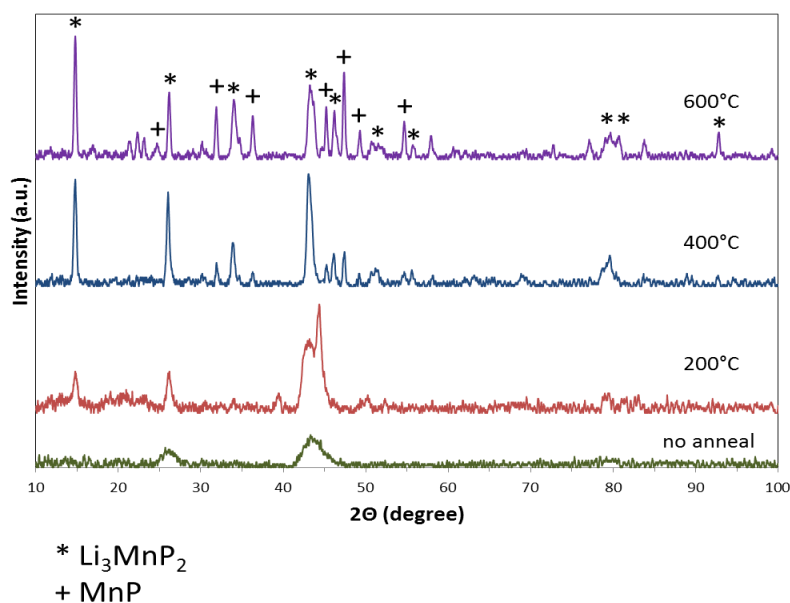


Figure 6.5 Powder XRD patterns of the mixed phase material ($\text{Li}_3\text{MnP}_2 + \text{MnP}$) annealed at different temperatures *in vacuo*. The patterns are vertically shifted for comparison.

MnP				Li_3MnP_2			
Position 2θ (hkl)	FWHM	Crystallite size (\AA)	T ($^\circ\text{C}$)	Position 2θ (hkl)	FWHM	Crystallite size (\AA)	T ($^\circ\text{C}$)
45.16 (211)	0.99	90	200	14.75 (001)	0.51	174	200
	0.89	100	400		0.39	233	400
	0.40	245	600		0.33	288	600
46.05 (220)	0.71	129	200	26.02 (111)	0.68	127	200
	0.67	137	400		0.41	224	400
	0.38	262	600		0.35	273	600
47.28 (121)	0.81	113	200				
	0.70	132	400				
	0.39	250	600				

Table 6.1 Comparison of the FWHM values determined for selected reflections in the powder X-ray diffraction patterns of MnP (left) and the mixed phase material (right).

Electrochemical studies

Following synthesis and structural characterization, the materials described above were tested in battery cells composed of 1.0 M LiPF₆ electrolyte dissolved in a 1:1 mixture of ethylene carbonate (EC) and dimethyl carbonate (DMC). The as-synthesized and annealed materials were evaluated as anode materials using various electrochemical methods in order to determine charge-discharge capacity and rate capability. The electrochemical properties of MnP and the mixed phase lithiated material were similar, showing charge/discharge capacities of several hundred mAhg⁻¹ between 0.2 and 2.5 V over a range of galvanic rates. For the lithiated material, peak discharge capacities of ca. 350 mAhg⁻¹ were observed initially and then quickly diminished after several cycles. Although not extremely high, this reversible capacity is comparable to that observed for commercial carbon anodes (372 mAhg⁻¹) and alternative materials such as alloys and oxides.²³ These numbers suggest that the electrochemical processes are limited to intercalative Li insertion mechanisms as opposed to conversion reactions, for which much higher theoretical capacities would be expected.

For both the phase-pure MnP and mixed phase material, charge/discharge capacities of the amorphous, as-synthesized material were compared to that of annealed material to determine the role of crystallite size with respect to electrochemical activity. It was hypothesized that the amorphous material would show marked improvement over the annealed material, but this was not the case. This is illustrated in the voltage profile for the mixed phase lithium manganese phosphide shown in Figure 6.6, which shows only minimal (ca. 40 mAhg⁻¹) improvement of initial discharge capacity observed for the annealed material compared to amorphous.

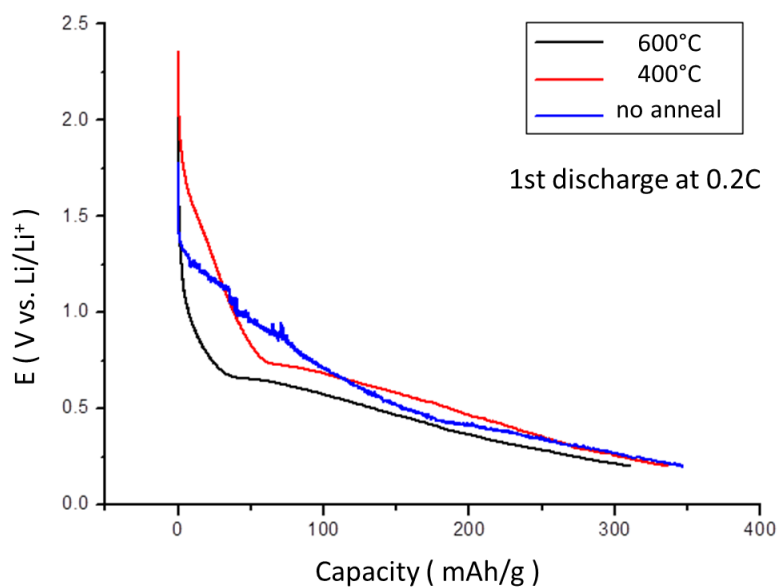


Figure 6.6 Initial discharge capacity of $(\text{MnP} + \text{Li}_3\text{MnP}_2)$ annealed at different temperatures.

The chemical composition of the material appeared to have more significant effects on the electrochemical activity. In general, the mixed phase material showed higher capacities after several charge/discharge cycles compared to phase-pure MnP. This is illustrated in the comparative voltage profiles in Figure 6.7. The extra lithium ions initially present in the mixed phase material may reduce the drastic structural changes associated with Li^+ insertion, thus diminishing the capacitive dampening observed upon successive charge/discharge cycles.

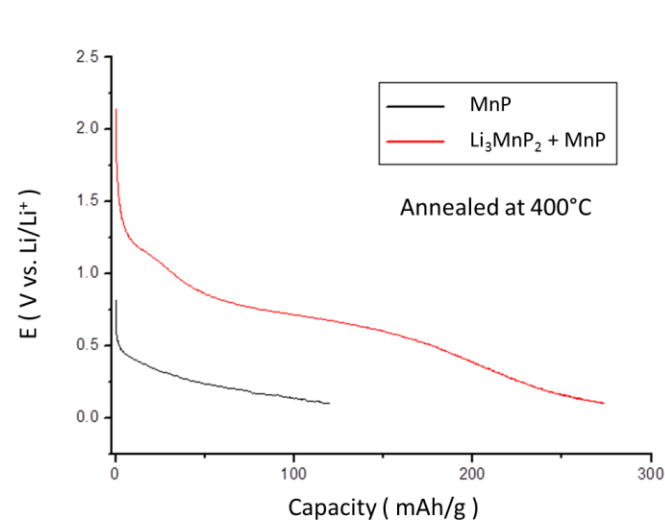


Figure 6.7 Comparison of the 6th discharge cycles of MnP (blue) and the mixed phase material (red).

Other metal systems

The synthetic scheme described in this chapter is applicable to a wide range of metal compounds because (i) stable, isolable metal-alkyl and dialkylamido complexes exist for a large number of first row transition metals and (ii) these complexes are generally reactive enough to abstract even a slightly acidic proton from an available source. Thus use of other gases such as ammonia (NH_3) or water vapor (H_2O) as well as inorganic acids, such as sulfuric (H_2SO_4), phosphoric (H_3PO_4), boric (H_3BO_3) or carbonic (H_2CO_3) may be combined with transition metal alkyl or dialkylamido complexes to form a wide variety of M^+X^- binary compounds appropriate for Li-ion electrode applications. Synthetic details as well as preliminary electrochemical results of a few promising compounds are described below.

Iron phosphide

The relatively flat charge/discharge capacity exhibited by the manganese phosphide system is in stark contrast to capacities observed for FeP, synthesized through analogous routes using PH_3 gas and $\text{Fe}(\text{N}(\text{SiMe}_3)_2)_3$ as the iron source. An initial discharge capacity of 1750 mAhg^{-1} is observed for this material, which, despite a marked drop-off after 5 cycles to ca. 850 mAhg^{-1} , shows great promise for use as a high-capacity anode material.

Titanium phosphide

The thermal stabilities of the alkyl or aryl derivatives of Ti(IV) cover a wide range. For example TiMe_4 is only stable below -78°C , whereas $\text{Ti}(\text{CH}_2\text{Ph})_4$, and $\text{Ti}(\text{Ph})_4$ are stable at room temperature. These compounds are also extremely air and moisture sensitive. Initial studies have examined the reaction of PH_3 with the following compounds: TiMe_4 (at -78°C), $\text{Ti}(\text{CH}_2\text{Ph})_4$, $\text{Ti}(\text{Ph})_4$, as well as commercially available $\text{Ti}(\text{NEt}_2)_4$ and $\text{Ti}(\text{NMe}_2)_4$. For each reaction, dark black materials are rapidly produced and XPS analysis indicates that they are binary titanium phosphides. Interestingly, XPS data for material produced from $\text{Ti}(\text{NMe}_2)_4$ is consistent with Ti:P ratio of 5:2 i.e. Ti_5P_2 , while that from $\text{Ti}(\text{NEt}_2)_4$ is closer to Ti_3P_2 . In both cases, powder XRD data show that the materials are amorphous.

Manganese and iron borates as cathode materials

Li-ion battery cathode materials are commonly produced in the lithiated form and act as an initial source of lithium when used with graphite anodes. The most studied and widely utilized cathode materials are transition metal oxides.²⁴ Other anions such as

phosphates (PO_4^{3-}), sulfates (SO_4^{2-}) and borates (BO_3^{3-}) have also been utilized with a wide variety of first row transition metals to form low molecular weight, stable compounds with open structures capable of Li insertion and removal. Examples include LiFeBO_3 , LiFePO_4 , $\text{Fe}_2(\text{SO}_4)_3$, $\text{Li}_3\text{V}_2(\text{PO}_4)_3$, and LiCoPO_4 .²⁵⁻²⁹ These materials intercalate lithium ions at higher potentials than their oxide analogs, and this has the advantage of increasing the voltage range available for resultant Li-ion cells.

Transition metal borates have been investigated as promising Li-ion battery cathode materials, in part due to the significantly smaller and lighter (BO_3^{3-}) unit as compared to other commonly studied oxyanions such as sulfate or phosphate. This, coupled with similar redox behavior of the metal and high electrical conductivities (e.g. 3.9×10^{-7} S/cm for LiFeBO_3), has prompted a great deal of interest in transition metal borates as cathodes with high theoretical gravimetric capacities.³⁰ Attempts to reduce particle size and increase surface area may result in shortened Li^+ ion diffusion paths and better cycleability. Thus a low-temperature synthetic route, analogous to that discussed above for transition metal phosphides was attempted for the formation of manganese and iron borates.

Reaction of Li_2MnMe_4 with boric acid (H_3BO_3) in a 3:4 molar ratio in a Et_2O /dioxane mixture resulted in immediate formation of gas bubbles and precipitation of a tan solid. As shown in Figure 6.8, the air stable solid, upon annealing under vacuum at 400 °C, showed diffraction peaks characteristic of two separate phases of LiMnBO_3 (PDF# 01-073-4014 and PDF# 01-070-8322). The electrochemical performance of this material was rather poor, showing charge/discharge capacities of less than 50 mAhg^{-1} over a range of cycling rates. Furthermore, no significant differences in the electrochemical properties were observed between amorphous and annealed material.

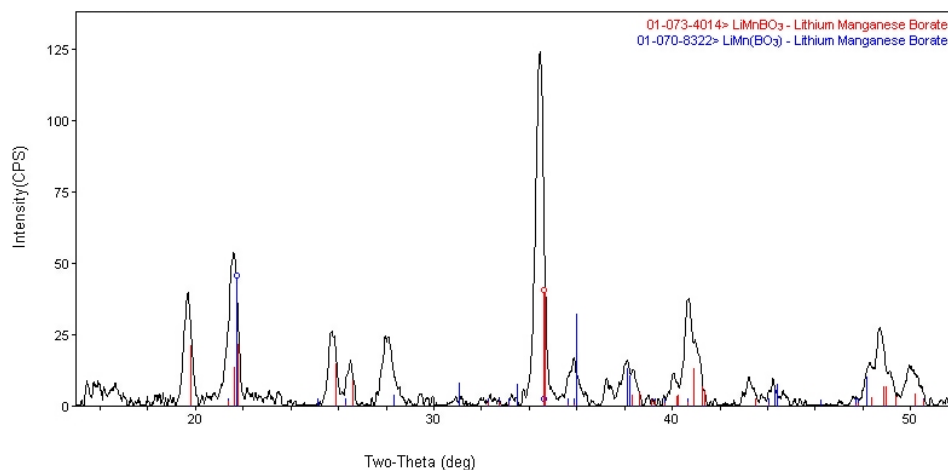


Figure 6.8 XRD pattern of LiMnBO_3 annealed at 400 °C for 4 hr.

Reaction of $\text{Fe}(\text{N}(\text{SiMe}_3)_2)_3$ with a stoichiometric amount of boric acid in a 1:1 mixture of Et_2O and dioxane resulted in the formation of a light brown precipitate. After filtration and washing to remove trimethylsilylamine, the solid was dried *in vacuo* to give FeBO_3 in near quantitative yield. XRD of the as-synthesized material revealed an amorphous microstructure, whereas annealing at 400 °C under vacuum for 4 hr. led to diffraction peaks corresponding to $\text{Fe}_3\text{O}_2(\text{BO}_3)$. This oxyborate has been observed as a by-product in other iron borate syntheses and shows a diminished electrochemical response compared to FeBO_3 .³¹ The source of oxygen in this system is not readily apparent, as great measures were taken to exclude air and moisture in all stages of the reaction, and the material was annealed *in vacuo*. One possible source is from excess boric acid, which decomposes upon heating above 170 °C to form metaboric acid (HBO_2) and water, which if present in the system upon annealing, may oxidize FeBO_3 to $\text{Fe}_3\text{O}_2(\text{BO}_3)$. The iron oxyborate phase shows ability to react with lithium, however, and the cycling performance for the amorphous and annealed materials are compared in Figure 6.9. The observed initial discharge capacity of $\text{Fe}_3\text{O}_2(\text{BO}_3)$ approaches 320 mAhg⁻¹

¹, while the annealed material shows an initial capacity of 110 mAhg⁻¹. Furthermore, the amorphous material shows slightly better capacity retention as compared to the annealed material (25 mAhg⁻¹ vs. 10 mAhg⁻¹ after 5 cycles). The improvement in electrochemical performance of the amorphous material compared to the annealed material may be directly related to the smaller crystallite size as well as the chemical composition. While the cycling performances of both materials are low, the high initial charge/discharge capacities are encouraging, and are comparable to those seen in other metal borate systems.³²

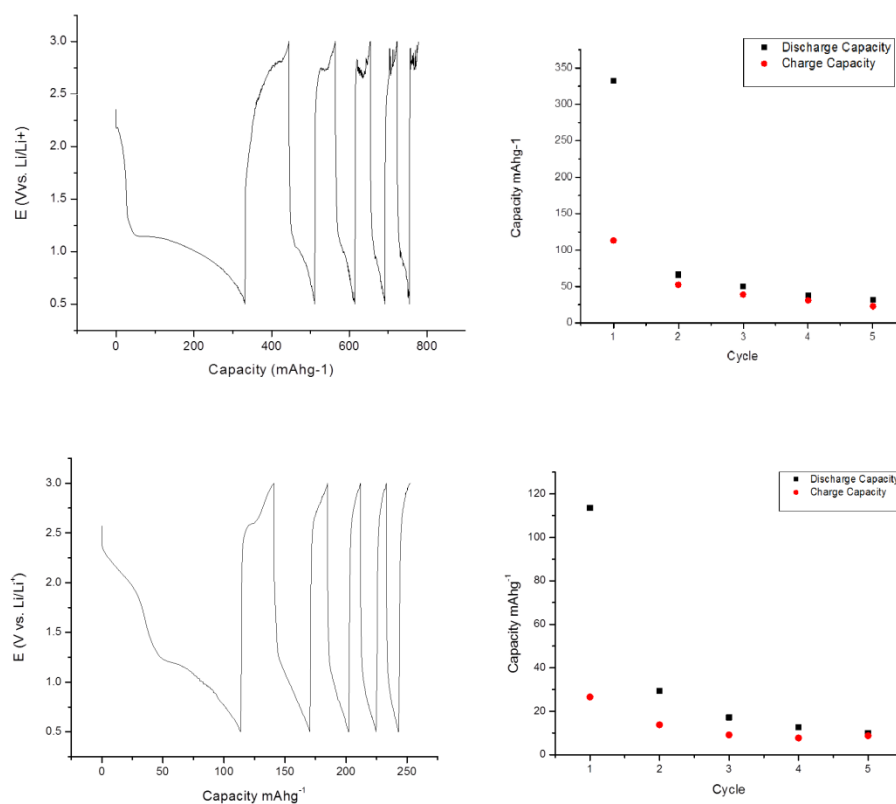


Figure 6.9 Electrochemical behavior of amorphous iron borate (top) and material annealed to 400 °C (bottom). Efficiency performance for the first 5 cycles is shown on the left and cycling performance is shown on the right.

CONCLUSIONS AND FUTURE STUDIES

This study has shown that MnP and Li_3MnP_2 may be synthesized by a novel low-temperature synthetic route by direct reaction of various methylmanganese complexes with phosphine gas. These materials exhibit similar behavior toward electrochemical reaction with lithium, namely a predominantly intercalative process and not a conversion reaction. The mixed phase material showed higher initial capacity and better cycleability compared to MnP. Furthermore, no clear trend in annealing temperature (crystallite size) versus charge/discharge capacity could be established with these materials, indicating that perhaps the effects of particle size are more pronounced for electrochemical conversion processes. Modification of specific reaction conditions allowed control over composition and morphology of the bulk material, resulting in materials composed of small discrete particles or mesostructured porous frameworks. Further investigation of factors that control composition and morphology of the resulting material may optimize the performance in terms of energy storage.

This synthetic strategy was also applied to iron and titanium systems, with FeP showing extremely high gravimetric capacities. Reaction of boric acid with $\text{Fe}(\text{N}(\text{SiMe}_3)_2)_3$ resulted in the formation of an iron oxyborate that shows relatively high initial charge/discharge capacities, and may have interesting applications as a cathode material in Li-ion batteries.

The use of tri-block copolymers and long chain tertiary alkylamine species as structure directing or capping agents was attempted through the course of these studies in order to control the morphology of the resultant metal phosphides. Use of these compounds as structure directing templates for metal oxides with various sol-gel processing techniques has been demonstrated to result in highly ordered mesoporous materials that exhibit remarkably high surface areas.³³ This strategy has not translated to

the traditionally used synthesis of metal phosphides, however, primarily due to the higher temperatures commonly employed for TMP formation, which likely creates more disordered packing situations for the polymers. The low temperature routes employed in reactions discussed in this work would not interfere with self-assembled block copolymer structure formation, and use of these in a one-pot synthesis of metal alkyl and PH_3 may have interesting possibilities.

EXPERIMENTAL DETAILS

General synthesis

Unless otherwise noted, all reactions were performed under a dry, oxygen-free nitrogen atmosphere or under vacuum using standard Schlenk line and dry box techniques. All solvents were dried prior to use by distillation from molten sodium or sodium benzophenone ketyl under nitrogen. Anhydrous manganese(II) chloride and iron(III) chloride, and solutions of phenyllithium, benzylmagnesium bromide, lithium bis(trimethylsilyl)amine and methyllithium were purchased and were used without further purification. Dimethylmanganese,^{34a} dilithium tetramethylmanganate,^{34a} and $\text{Fe}(\text{N}(\text{SiMe}_3)_2)_3$ ^{34b} were synthesized according to literature procedures.

Synthesis of manganese phosphide

A solution of freshly prepared dimethylmanganese (ca. 8 mmol) was dissolved in diethyl ether (100 mL) and transferred to a Fischer-Porter bottle via cannula. The solution was cooled to $-78\text{ }^\circ\text{C}$ and an excess of phosphine gas was condensed into the bottle, with the resultant pressure of the system set to ca. 1 atm. The bottle was sealed and the mixture was allowed to stir overnight under PH_3 . A dark precipitate began to form immediately, and after several hours, the orange color of the solution began to disappear.

Solvent and excess phosphine gas were removed *in vacuo* and the black precipitate was washed with diethyl ether (3×100 mL) and then dried under vacuum. The bottle was taken into the dry box where black solid was collected. Isolated: 0.65 g.

Synthesis of mixed phase manganese phosphide (MnP + Li₃MnP₂)

A solution of freshly prepared dilithium tetramethylmanganate (ca. 8 mmol) was dissolved in diethyl ether (100 mL) and transferred to a Fischer-Porter bottle via cannula. The solution was cooled to -78 °C and an excess of phosphine gas was condensed into the bottle, with the resultant pressure of the system set to ca. 1 atm. The bottle was sealed and the mixture was allowed to stir overnight under PH₃. A dark precipitate began to form immediately, and after several hours, the orange color of the solution began to disappear. Solvent and excess phosphine gas were removed *in vacuo* and the black precipitate was washed with diethyl ether (3×100 mL) and then dried under vacuum. The bottle was taken into the dry box where black solid was collected. Isolated: 0.3 g.

Synthesis of iron phosphide

Fe(N(SiMe₃)₂)₃ (0.51 g, 0.95 mmol) was dissolved in Et₂O (100 mL) and then transferred to a Fischer-Porter bottle via cannula. The filtrate was cooled to -78 °C and an excess of phosphine gas was condensed into the bottle, with the resultant pressure of the system set to ca. 1 atm. The bottle was sealed and the mixture was allowed to stir overnight under PH₃. Solvent and excess phosphine gas were removed *in vacuo* and the black precipitate was washed with diethyl ether (3×100 mL) and then dried under vacuum. Isolated: 0.06 g, 72%.

Synthesis of titanium phosphide

In a typical synthesis using tetrakis(dimethylamino)titanium(IV) (TDMAT) as the starting titanium reagent; a Fisher-Porter bottle was filled with dry, degassed diethyl ether (200 mL) and neat TDMAT (0.2 mL) was added via syringe. The orange solution was cooled to -78 °C and an excess of phosphine gas was condensed into the bottle, with the resultant pressure of the system set to ca. 1 atm. The bottle was sealed and the mixture was allowed to stir overnight under PH_3 at room temperature. Solvent and excess phosphine gas were removed *in vacuo* and the black precipitate was washed with diethyl ether (3×100 mL) and then dried under vacuum. Isolated: 0.08g.

Synthesis of lithium manganese borate

Anhydrous manganese(II) chloride (0.693g, 5.5 mmol) was suspended in dry diethyl ether (100 mL) and a solution of methyllithium (13.8 mL, 1.6 M in Et_2O) was added at room temperature with stirring. The reaction mixture was allowed to stir overnight in the dark. During this time, the solution became orange yellow and remained heterogeneous. The mixture was filtered through a short bed of Celite (2 cm) and then filtered. To this mixture was added a solution of boric acid (0.368 g, 5.95 mmol) dissolved in dioxane (50 mL). Gas evolved and a light tan precipitate formed after stirring for several minutes at room temperature. This was allowed to further stir overnight. During this time, the solution became colorless and a large amount of tan solid formed. The solvent was decanted and the solid was washed several times with dioxane and diethyl ether (3×100 mL each), and then dried *in vacuo*. Isolated: 0.6 g, 90%.

Synthesis of iron borate

$\text{Fe}(\text{N}(\text{SiMe}_3)_2)_3$ (0.76 g, 1.4 mmol) was dissolved in dry diethyl ether (100 mL) and boric acid (0.088 g, 1.4 mmol) was dissolved in dry, degassed dioxane (100 mL). The solution of $\text{Fe}(\text{N}(\text{SiMe}_3)_2)_3$ was added dropwise to the solution of boric acid at room temperature. The resulting solution became lighter, evolved gas bubbles, and developed a light brown precipitate. This mixture was allowed to stir overnight. During this time, the solution became colorless and a large amount of brown solid formed. The solvent was decanted and the solid was washed consecutively with dioxane and diethyl ether (3×100 mL each), and then dried *in vacuo*. Isolated: 0.14 g, 86%.

REFERENCES

1. (a) Scrosati, B.; Garche, J. *J. Power Sources* **2010**, *195*, 2419. (b) Kang, B.; Ceder, G.; *Nature* **2009**, *458*, 190.
2. Dahn, J.; Sleight, A.; Shi, H.; Way, B.; Weydanz, W.; Reimers, J.; Zhong, Q.; von Sacken, U. *Lithium Batteries - New Materials, Developments and Perspectives*, Elsevier: Amsterdam, 1994.
3. Bichatt, M.-P.; Gillot, F.; Monconduit, L.; Favier, F.; Morcrette, M.; Lemoigno, F.; Doublet, M.-L. *Chem. Mat.* **2004**, *16*, 1002.
4. Kim, Y.-U.; Cho, B. W.; Sohn, H. *J. Electrochem. Soc.* **2005**, *152*, A1475.
5. Gillot, F.; Boyanov, S.; Dupont, L.; Doublet, M.-L.; Morcrette, M.; Monconduit, L.; Tarrascon, J.-M. *Chem. Mat.* **2005**, *17*, 6327.
6. Wang, K.; Yang, J.; Xie, J.; Wang, B.; Wen, Z. *Electrochem. Comm.* **2003**, *5*, 480.
7. Pfeiffer, H.; Tancret, F.; Bichatt, M.-P.; Monconduit, L.; Favier, F.; Brousse, T. *Electrochem. Comm.* **2004**, *6*, 263.
8. Alcantara, R.; Tirado, J.; Jumas, J.; Monconduit, L.; Ollier-Fourcade, J. *J. Power Sources* **2002**, *109*, 308.
9. Mauchamp, V.; Moreau, P.; Monconduit, L.; Doublet, M.; Boucher, F.; Ouvard, G.; *J. Phys. Chem. C* **2007**, *111*, 3996.
10. Gillot, F.; Monconduit, L.; Doublet, M.-L. *Chem. Mater.* **2005**, *17*, 5817.
11. Boyanov, S.; Bernardi, J.; Gillot, F.; Dupont, L.; Womes, M.; Tarascon, J.-M.; Monconduit, L.; Doublet, M.-L.; *Chem. Mater.* **2006**, *18*, 3531.
12. Dahn, J. *Phys. Rev. B* **1991**, *44*, 9170.
13. (a) Bruce, P. G.; Scrosati, B.; Tarascon, J.-M.; *Angew. Chem. Int. Ed.* **2008**, *47*, 2930. (b) Guo, Y.-G.; Hu, J.-S.; Wan, L.-J. *Adv. Mater.* **2008**, *20*, 2878. (c) Wang, Y.; Cao, G. *Adv. Mater.* **2008**, *20*, 2251.

14. (a) Henkes, A. E.; Schaak, R. E. *Inorg. Chem.* **2008**, *47*, 671. (b) Henkes, A. E.; Vasquez, Y.; Schaak, R. E. *J. Am. Chem. Soc.* **2007**, *129*, 1896. (c) Henkes, A. E.; Schaak, R. E. *Chem. Mater.* **2007**, *19*, 4234.
15. Qian, C.; Kim, F.; Ma, L.; Tsui, F.; Yang, P.; Liu, J. *J. Am. Chem. Soc.* **2004**, *126*, 1195.
16. Park, C.-M.; Kim, Y.-U.; Sohn, H.-J. *Chem. Mater.* **2009**, *21*, 5566.
17. Woo, S.-G.; Jung, J.-H.; Kim, H.; Kim, M.G.; Lee, C.K.; Sohn, H.-J.; Cho, B.W. *J. Electrochem. Soc.* **2006**, *153*, A1979.
18. Zhang, Z.; Yang, J.; Nuli, Y.; Wang, B.; Xu, J. *Solid State Ionics* **2005**, *176*, 693.
19. (a) Fischer, E. O.; Louis, E.; Bathelt, W.; Moser, E.; Mueller, J. *J. Organomet. Chem.* **1968**, *14*, P9. (b) Fischer, E. O.; Louis, E.; Kreiter, C. G. *Angew. Chem. Int. Ed.* **1969**, *8*, 377. (c) Moser, E.; Fischer, E. O.; Bathelt, W.; Gretner, W.; Knauss, L.; Louis, E. *J. Organomet. Chem.* **1969**, *19*, 377. (d) Huttner, G.; Schelle, S. *J. Organomet. Chem.* **1969**, *19*, P9.
20. (a) Cowley, A. H.; Harris, P. R.; Jones, R. A.; Nunn, C. M. *Organometallics* **1991**, *10*, 652. (b) Atwood, D. A.; Cowley, A. H.; Harris, P. R.; Jones, R. A.; Koschmieder, S. U.; Nunn, C. M.; Atwood, J. L.; Bott, S. G. *Organometallics* **1993**, *12*, 24. (c) Trentler, T. J.; Goel, S. C.; Hickman, K. M.; Viano, A. M.; Chiang, M. Y.; Beatty, A. M.; Gibbons, P. C.; Buhro, W. E. *J. Am. Chem. Soc.* **1997**, *119*, 2172.
21. Pierson, H. O. *Handbook of Chemical Vapor Deposition (CVD)*; Noyes Publications: Westwood, 1992.
22. Scherrer, P. *Zsigmondy's Kolloidchemie*, 3rd. ed.; Verlag: Berlin, 1920.
23. Tirado, J. L. *Mater. Sci. Eng.* **2003**, *40*, 103.
24. The Structural Stability of Transition Metal Oxide Insertion Electrodes for Lithium Batteries. *Handbook of Battery Materials*, Besenhard, J.ed.; Wiley-VCH: Weinheim, 2000.
25. Rowsell, J.L.C.; Gaubicher, J.; Nazar, L.F. *J. Power Sources* **2001**, *97*, 254.
26. Padhi, A.K.; Nanjundaswamy, K.S.; Goodenough, J.B. *J. Electrochem. Soc.* **1997**, *144*, 1188.

27. Manthiram, A.; Goodenough, J.B. *J. Power Sources* **1989**, *26*, 403.
28. Saidi, M. Y. ; Barker, J.; Huang, H.; Swoyer, J. L.; Adamson, G. *Electrochem. Solid-State Lett.* **2002**, *5*, A149.
29. Amine, K.; Asuda, H.; Yamachi, M. *Electrochem. Soc. St. Lett.* **2000**, *3*, 178.
30. Dong, Y.Z.; Zhao, Y.M.; Shi, Z.D.; An, X.N.; Fu, P.; Chen, L. *Electrochimica Acta* **2007**, *53*, 2339.
31. Shi, X.; Chang, C.; Xiang, J.; Xiao, Y.; Yuan, L.; Sun, J. *J. Solid State Chem.* **2008**, *181*, 2231.
32. (a) Ibarra-Palos, A.; Darie, C.; Proux, O.; Hazemann, J.L.; Aldon, L.; Jumas, J.C.; Morcrette, M.; Strobel, P. *Chem. Mater.* **2002**, *14*, 1166. (b) Ibarra-Palos, A.; Morcrette, M.; Strobel, P. *J. Solid State Electrochem.* **2002**, *6*, 134. (c) Chen, L.; Zhao, Y.; An, X.; Liu, J.; Dong, Y.; Chen, Y.; Kuang, Q. *J. Alloy Compd.* **2010**, *494*, 415.
33. (a) Warren, S. C.; Messina, L. C.; Slaughter, L. S; Kamperman, M.; Zhou, Q.; Gruner, S. M.; DiSalvo, F. J.; Wiesner, U. *Science* **2008**, *320*, 1748. (b) Aizawa, M.; Buriak, J. M. *Chem. Mater.* **2007**, *19*, 5090. (c) Yang, X.-Y.; Li, Y.; Lemaire, A.; Yu, J.-G.; Su, B.-L. *Pure Appl. Chem.* **2009**, *81*, 2265.
34. (a) Andersen, R. A.; Carmona-Guzman, E.; Gibson, J. F.; Wilkinson, G. *J. Chem. Soc. Dalton Trans.* **1976**, 2204-2211. (b) Aylea, E. C.; Bradley, D. C.; Copperthwaite, R. G. *J. Chem. Soc. Dalton Trans.* **1972**, *14*, 1580.

Glossary

κ	relative dielectric constant
θ	angle between the incident X-ray beam and the substrate surface
acac	2,4-pentanedionato, acetylacetonato
AFM	atomic force microscopy
ALD	atomic layer deposition
BE	binding energy
CMOS	complementary metal-oxide-semiconductor
COD	cyclooctadiene
Cp	cyclopentadienyl
CVD	chemical vapor deposition
EDX	dispersive X-ray spectroscopy
EPR	electron paramagnetic resonance
ESI	electrospray ionization
Et	ethyl
fcc	face-centered cubic
FET	field effect transistor
FRAM	ferroelectric random access memory
hcp	hexagonal close packed
hfacac	1,1,1,5,5,5-hexafluoro-2,4-pentanedionato, hexafluoroacetylacetonato
IC	integrated circuit
Me	methyl
NEt ₃	triethylamine
ppm	parts per million
PMe ₃	trimethylphosphine
PVD	physical vapor deposition
Pz	pyrazolate
RF-ID	radio frequency identification
RT	room temperature
sccm	standard cubic centimeters per minute
SEM	scanning electron microscopy
TEM	transmission electron microscopy
THF	tetrahydrofuran
tfac	1,1,1 -trifluoro-2,4-pentanedionato, trifluoroacetylacetonato
thd	2,2,6,6-tetramethyl-3,5-heptanedionato
TOF-ERDA	time-of-flight elastic recoil detection analysis
XPS	X-ray photoelectron spectroscopy
XRD	X-ray diffraction
XRR	X-ray reflectivity

Vita

William Jeffrey McCarty was born in Austin, Texas on October 26th, 1982, the son of Wade and Carol McCarty. After graduating from L. C. Anderson High School in Austin, TX in May 2001, he attended the University of Texas at Austin to pursue a degree in Chemistry. There he conducted undergraduate research under the guidance of Professor Richard A. Jones. After graduating with a Bachelor of Science degree in Chemistry in 2005, he continued to work in the Jones Group upon enrollment into the Ph.D. program in 2006.

Permanent address: 20024 Hallbrook Lane
Pflugerville, TX 78660

This dissertation was typed by the author.